

Experimental analysis of the influence of elevated operating pressures on Solid Oxide Cell stacks during steam, co- and CO₂ electrolysis

Von der Fakultät Energie-, Verfahrens- und Biotechnik der
Universität Stuttgart zur Erlangung der Würde eines Doktors der
Ingenieurwissenschaften (Dr.-Ing.) genehmigte Abhandlung

vorgelegt von

Marc Riedel

aus Nürtingen

Hauptberichter: Prof. Dr. rer. nat. K. Andreas Friedrich

Mitberichter: Prof. Dr. rer. nat. habil. Rüdiger-A. Eichel

Tag der mündlichen Prüfung: 13.01.2022

Universität Stuttgart

Institut für Gebäudeenergetik, Thermotechnik und Energiespeicherung

2022

Acknowledgements

First, I would like to thank Prof. K. Andreas Friedrich for giving me the opportunity to carry out my research within the department of Electrochemical Energy Technology of the Institute of Engineering Thermodynamics at DLR, Stuttgart. In particular, I would like to thank him for his supervision during my doctorate. I highly appreciated every discussion with him and thank him a lot for his valuable feedbacks.

Second, I would like to thank Dr. Marc P. Heddrich, who supported and encouraged me during my thesis and significantly contributed to the development of my personality and me as a scientist. I appreciated his valuable criticisms during my daily work, the preparation of my publications, presentations and finally this thesis.

Third, I would like to thank all of my teammates, but especially Dr. Srikanth Santhanam and Marius Tomberg for the numerous discussions during the development and validation of the stack simulation model described in this work. I am particularly pleased that the experimental data I have obtained during my work will continue to be used after completing my thesis and that a valuable contribution for the perspective scientific research within the SOC field will be generated.

Finally, this thesis would not have been possible without the support of the most important people in my private life. I would like to express my honest gratitude to my family and especially to my beloved wife who always supported and motivated me with their positivity and love during the time of preparation. You were crucial for the success I achieved so far.

Abstract

Moving towards a renewable energy powered society, the solid oxide electrolysis cell (SOEC) technology can be an essential constituent for the efficient supply of molecules like hydrogen and carbon monoxide for various synthesis routes in the chemical industry from renewable electricity. However, downstream synthesis reactors for the production of chemicals like methane, ammonia, dimethyl ether (DME), methanol or jet fuel are typically operated at elevated pressures in the range of 10-60 bar to achieve high conversion or high yield. Furthermore, storage and transportation of gaseous products also require a certain pressurization of the electrolysis products. The operation of the electrolyzer at an elevated pressure can therefore be highly beneficial since additional compression work of the produced molecules can be significantly reduced or omitted. As for polymer electrolyte membrane and alkaline electrolyzers pressurized operation is already state of the art, the research and developments associated with the operation of pressurized solid oxide electrolyzers is rare. However, SOECs have the potential to be operated significantly more efficient than the low-temperature electrolyzers.

In this thesis, the pressurized operation of SOEC stacks during steam, co- and CO₂ electrolysis is investigated experimentally. The experiments were carried out using a test rig that was adapted for the electrolysis operation of different stack types. It enables stack characterizations in an operating pressure range of 1.4 to 8 bar. Thus, the influence of increased partial pressures as additional experimental parameters can provide scientific knowledge. 10-layer stacks having either electrolyte supported cells (ESC) or fuel electrode supported cells (in electrolysis: cathode supported cell, CSC) were used for the scientific investigations.

The ohmic resistances of both stack types were quantified over a wide temperature range and provided to the literature via parameterized mathematical expressions. Since the ohmic resistance was found to be the dominant cell resistance of the ESC, it was theoretically investigated with a simplified model. A deviation of 15-20 % between the theoretically and experimentally obtained ohmic resistance value was found which indicates a considerable amount of unaccounted resistance that can be attributed to contact resistances occurring within the stack.

The overall performance and the influence of an elevated operating pressure were found to be significantly different by operating a stack with electrolyte supported or fuel electrode supported cells. The stack using the latter cell concept showed a significantly lower ohmic resistance and almost twice as high achievable current densities compared to the stack with electrolyte supported cells. A significantly decreased area specific resistance (ASR) at higher pressures was observed for the CSC stack that was attributed to reduced activation and diffusion resistances. This phenomenon led to a crossing of the current-voltage characteristics within the endothermic operating regime during the studied steam, co- and CO₂ electrolysis operations. Hence, a noticeable performance gain was observed for the pressurized operation of the CSC stack. In contrast, the performance of the ESC stack was hardly influenced by an increased operating pressure. Rather, it was found to be primarily dictated by the operating temperature due to predominant contribution of the ohmic resistance to the overall performance. Gas analysis was used during the co-electrolysis operations and showed that the thermodynamic equilibrium is reached with both stack types. Consequently, both the reverse water-gas shift (rWGS) and the methanation reaction occur stack-internally which indicates that the chemical reactions are fast and the catalytic surfaces of the stacks are sufficiently active and available in relation to the gas hourly space velocity. For high operating pressures, methane contents of up to 7 % were found. The ASR of both stack types was quantified with the help of several steady-state and dynamically recorded current-voltage curves at different pressures. Consequently, detailed relations about the temperature and pressure dependent performance characteristics of both the CSC and the ESC stacks were provided to the literature by this thesis.

Electrochemical impedance spectroscopy (EIS) analyses were used to identify the characteristic frequencies of the electrochemical processes that occur within both stack types. The influence of an elevated operating pressure on the electrochemical processes was closely investigated for both steam and CO₂ electrolysis operation. By investigating the pressurized co-electrolysis operation, it could be shown that the main reaction path for the CO production can be attributed to the rWGS reaction. The amount of CO that is generated by the rWGS reaction or by the electrochemical CO₂ reduction process during co-electrolysis operation represents still a scientific gap to which the current thesis contributes.

Moreover, this work presents an in-depth analysis of the long-term degradation of three ESC stacks operated under pressurized steam and co-electrolysis mode. The operating

durations were 1,000-2,000 hours at a constant current with high conversions of 70 %, thus representing the first published experimental analysis of the SOEC stack degradation behavior under relevant pressurized operations for more than 200 hours. It was observed that the degradation is predominantly dictated by a time dependent increase of the ohmic resistance. The experimental results furthermore revealed that an increased operating pressure leads to increased performance loss and that co-electrolysis operation has an additionally worsening effect on the long-term stability of the stacks. Detailed post-test analyses of the electrodes and the bipolar plates were carried out. A noticeably higher degree of nickel depletion was found within the fuel electrode of the stack that was operated at the highest pressure. Observed delamination, contamination and oxide layer formation within the post-test analyses of the stacks are discussed.

Based on an existing numerical model of one repeating unit, a 1D+1D stack model was developed and parameterized with experimental data to predict the performance and temperature gradients during the pressurized stack operation of the ESC. The validity of the model was shown for several operating conditions at different pressures. The relations of the predominant resistance contribution and the pressure dependent activation energy of the electrochemical steam reduction process were used as input parameters for the mathematical equations. Beside the electrochemistry, the model includes a proper heat transfer model according to the structure of the experimental test setup.

Zusammenfassung

Bei der zunehmenden Nutzung von erneuerbarer Energie können Festoxidelektrolysezellen (solid oxide electrolysis cell, SOEC) ein essentieller Bestandteil für die effiziente Bereitstellung von Molekülen wie Wasserstoff und Kohlenmonoxid für unterschiedlichste Synthesen in der chemischen Industrie werden. Dem Elektrolyseur nachgeschaltete Synthesereaktoren zur Herstellung von Chemikalien wie Methan, Ammoniak, Dimethylether (DME), Methanol oder Kerosin werden jedoch typischerweise bei Drücken von 10 bis 60 bar betrieben, um hohe Umsätze und Ausbeuten zu erzielen. Darüber hinaus können auch die Speicherung und der Transport eine Kompression der gasförmigen Elektrolyseprodukte erforderlich machen. Der druckaufgeladene Betrieb von Elektrolyseuren kann daher insofern vorteilhaft sein, da zusätzlich aufzuwendende Kompressionsarbeit hinsichtlich der erzeugten Gase signifikant reduziert oder vermieden werden kann. Bei Polymerelektrolytmembran- und alkalischen Elektrolyseuren ist der druckaufgeladene Betrieb bereits Stand der Technik, der Betrieb von druckaufgeladenen Festoxidelektrolyseuren ist dagegen kaum erforscht.

In dieser Arbeit wird der druckaufgeladene Betrieb von SOEC Stacks während der Dampf-, Co- und CO₂-Elektrolyse experimentell untersucht. Die Versuche wurden mit einem Prüfstand durchgeführt, der für den Elektrolysebetrieb verschiedener Stacktypen angepasst wurde. Dieser ermöglicht Stackcharakterisierungen in einem Betriebsdruckbereich von 1.4 bis 8 bar. Somit kann der Einfluss erhöhter Partialdrücke als zusätzlicher experimenteller Parameter genutzt werden, um wissenschaftliche Erkenntnisse zu generieren. Für die wissenschaftlichen Untersuchungen wurden Stacks mit 10-Ebenen verwendet, die entweder elektrolytgestützte Zellen (ESC) oder brenngaselektrodengestützte Zellen (bei Elektrolyse: cathode supported cell, CSC) enthielten.

Die ohmschen Widerstände beider Stacktypen wurden über einen weiten Temperaturbereich quantifiziert und mittels mathematischer Ausdrücke in der Literatur zur Verfügung gestellt. Da sich der ohmsche Widerstand als der dominierende Zellwiderstand des ESC herausstellte, wurde er mit einem vereinfachten Modell theoretisch untersucht. Zwischen dem theoretisch und dem experimentell ermittelten ohmschen Widerstandswert wurde eine Abweichung von 15-20 % festgestellt, was auf nennenswerte Kontaktwiderstände innerhalb des Stacks hindeutet.

Es konnte gezeigt werden, dass sich die Gesamtleistung und der Einfluss eines erhöhten Betriebsdrucks deutlich beim Betrieb eines Stacks mit elektrolytgestützten Zellen von dem eines Stacks mit brenngaselektroden gestützten Zellen unterscheidet. Der Stack mit letztgenanntem Zellkonzept zeigte im Vergleich zum Stack mit elektrolytgestützten Zellen einen deutlich niedrigeren ohmschen Widerstand und erreichte fast doppelt so hohe Stromdichten. Für den CSC-Stack wurde außerdem ein signifikant verringerter flächenspezifischer Widerstand (ASR) bei höheren Drücken beobachtet, welcher auf reduzierte Aktivierungs- und Diffusionswiderstände zurückgeführt werden konnte. Diese Eigenschaft führte innerhalb des untersuchten Dampf-, Co- und CO₂-Elektrolysebetriebs zu einem Kreuzen der Strom-Spannungs-Kennlinien innerhalb des endothermen Betriebsregimes. Für den Druckbetrieb des CSC-Stacks konnte somit ein deutlicher Leistungsgewinn bei erhöhtem Betriebsdruck beobachtet werden. Im Gegensatz dazu, zeigte sich die Leistung des ESC-Stacks durch einen erhöhten Betriebsdruck kaum beeinflusst, sondern war aufgrund des dominierenden ohmschen Widerstands in erster Linie von der Betriebstemperatur abhängig. Eine Gasanalyse wurde während des Co-Elektrolysebetriebs eingesetzt und zeigte, dass das thermodynamische Gleichgewicht bei beiden Stacktypen erreicht wird. Folglich finden innerhalb des Stacks sowohl die umgekehrte Wassergas Shift (rWGS) als auch die Methanisierungsreaktion statt. Beides deutet darauf hin, dass die chemischen Reaktionen entsprechend schnell ablaufen und die katalytischen Oberflächen der Stacks bezogen auf die Raumgeschwindigkeit der Gase ausreichend aktiv und verfügbar sind. Darüber hinaus wurden bei hohen Betriebsdrücken Methangehalte von bis zu 7 % gemessen. Der ASR beider Stacktypen wurde mit Hilfe mehrerer stationärer und dynamisch aufgenommener Strom-Spannungs-Kennlinien bei unterschiedlichen Betriebsdrücken quantifiziert. Somit konnten in dieser Arbeit detaillierte Zusammenhänge über die temperatur- und druckabhängige Leistungscharakteristik sowohl des CSC- als auch des ESC-Stacks bereitgestellt werden.

Mit Hilfe der Analyse elektrochemischer Impedanzspektren wurden die charakteristischen Frequenzen der in den beiden Stacks ablaufenden elektrochemischen Prozesse identifiziert. Der Einfluss eines erhöhten Betriebsdrucks auf die elektrochemischen Prozesse wurde sowohl für den Dampf- als auch für den CO₂-Elektrolysebetrieb detailliert untersucht. Die Untersuchung des druckaufgeladenen Co-Elektrolysebetriebs zeigte weiter, dass die Produktion von Kohlenmonoxid hauptsächlich auf die rWGS-Reaktion zurückzuführen ist. Inwiefern CO vorwiegend durch die rWGS-Reaktion oder über die

elektrochemische CO₂-Reduktion während des Co-Elektrolysebetriebs erzeugt wird, stellt derzeit noch eine wissenschaftliche Lücke dar, zu der die vorliegende Arbeit einen Beitrag leistet.

Darüber hinaus stellt diese Arbeit eine eingehende Analyse der Langzeitdegradation von drei ESC-Stacks vor, welche im druckaufgeladenen Dampf und Co-Elektrolysemodus betrieben wurden. Mit den Betriebsdauern von 1000 bis 2000 Stunden bei konstanter Stromdichte und hohen Umsätzen von 70 % stellen diese Experimente somit die ersten veröffentlichten Analysen des Degradationsverhaltens von SOEC-Stacks unter relevantem Druckbetrieb für mehr als 200 Stunden dar. Die Degradation zeigte sich dabei überwiegend durch einen Anstieg des ohmschen Widerstands bestimmt. Außerdem deuten die experimentellen Ergebnisse darauf hin, dass ein höherer Betriebsdruck zu einem erhöhten Leistungsverlust führt und der Co-Elektrolysebetrieb darüber hinaus einen zusätzlich negativen Effekt auf die Langzeitstabilität der Stacks hat. Im Anschluss an die experimentellen Versuche wurden detaillierte Analysen der Elektroden und der Bipolarplatten durchgeführt. In der Brenngaselektrode des Stacks, der mit dem höchsten Druck betrieben wurde, wurde ein deutlich größerer Verlust von Nickel festgestellt. Beobachtete Delaminationen, Kontaminationen und Oxidschichtbildungen im Rahmen der Stackanalysen werden in dieser Arbeit diskutiert.

Basierend auf einem bestehenden numerischen Modell einer Wiederholeinheit wurde ein 1D+1D-Stackmodell entwickelt und mit experimentellen Daten parametrisiert, um die Leistung und die auftretenden Temperaturgradienten während des Betriebs des ESC-Stacks unter Druck vorhersagen zu können. Das Modell wurde mittels verschiedener Betriebsbedingungen bei unterschiedlichen Betriebsdrücken validiert. Als Eingangsparameter für die mathematischen Gleichungen wurden die dominierenden Widerstandsbeiträge und die druckabhängige Aktivierungsenergie der elektrochemischen Dampfreduktion verwendet. Neben der Elektrochemie beinhaltet das Modell ein geeignetes Wärmeübergangsmodell entsprechend dem Aufbau des Teststands.

Author's declaration

I declare that I have written this dissertation with the title “Experimental analysis of the influence of elevated operating pressures on solid oxide cell stacks during steam, co- and CO₂ electrolysis” independently and that it has not been submitted for any other academic award. Except where indicated by specific reference in the text, the work is the candidate's own work.

Marc Riedel
Stuttgart, 13.01.2022

Table of Contents

List of Tables	xi
List of Figures	xii
List of Acronyms	xv
List of Symbols	xvii
List of Scientific Publications	xx
1 Introduction	1
1.1 Background - Energy storage and sector coupling	1
1.2 Pressurized operation of solid oxide electrolyzers	2
1.3 Thesis structure.....	3
2 Research motivation	5
2.1 Current state of solid oxide electrolyzers	5
2.2 Scientific research gap.....	7
2.3 Scientific research approach.....	10
3 Solid oxide electrolyzer technology	12
3.1 Operating principle of solid oxide electrolyzers	12
3.2 Electrochemical fundamentals.....	14
3.2.1 Thermodynamics	14
3.2.2 Electrochemical losses	16
4 Experimental Methodologies	18
4.1 Pressurized test setup.....	18
4.2 Investigated SOEC stacks.....	19
4.2.1 10-layer stack with electrolyte supported cells.....	20
4.2.2 10-layer stack with fuel electrode supported cells.....	22
4.3 Electrochemical characterization methods	23
4.3.1 Current-voltage characteristics and the area specific resistance.....	23
4.3.2 Electrochemical impedance analysis	25
4.3.3 Measurement errors	26
4.4 Physical characterization methods	28
4.4.1 Gas analysis	28

4.4.2	Scanning Electron Microscopy (SEM) and Energy Dispersive X-ray spectroscopy (EDX).....	28
5	Results and discussion	29
5.1	Numerical cell and stack model.....	29
5.1.1	Model description.....	29
5.1.2	Parameterization of the stack model	33
5.1.3	Simulation results.....	35
5.2	Article I: Analysis of the pressurized steam electrolysis operation of an ESC stack.....	38
5.2.1	Research questions	38
5.2.2	Experimental	39
5.2.3	Results and discussion.....	40
5.3	Article II: Analysis of the pressurized co- and CO ₂ electrolysis operation of an ESC stack.....	46
5.3.1	Research questions	46
5.3.2	Experimental	47
5.3.3	Results	47
5.4	Article III: Analysis of the long-term stability of stacks operated at elevated pressure in steam and co-electrolysis mode	54
5.4.1	Research questions	54
5.4.2	Experimental	54
5.4.3	Results	55
5.5	Article IV: Comparison of the performance of stacks with different cell concepts at elevated operating pressure	61
5.5.1	Research questions	61
5.5.2	Experimental	61
5.5.3	Results	62
5.6	General context of the results	68
6	Publications	73
7	Conclusion	131
8	Future work.....	136
9	References	139

List of Tables

Table 1: Summary of the obtained ASR values out of the dynamically recorded U(i)- curves for 1.4, 4 and 8 bar.	44
Table 2: Summary of the obtained fit parameters for calculating the temperature dependent ASR for steam and co-electrolysis operation of the ESC stack with the equation: $ASR=A \cdot \exp(B \cdot T)$	50

List of Figures

Figure 1: Number of publications related to the operation of SOEC stacks. Distinction is made between theoretical and experimental publications for stack operation in electrolysis mode. The given numbers are based on scopus database (date: 09/2020).	8
Figure 2: Schematic of a solid oxide cell operated in electrolysis mode.	12
Figure 3: Energy demand of the reduction reaction from H ₂ O to H ₂ and CO ₂ to CO with the total energy demand (reaction enthalpy ΔH , squares), the electricity demand (Gibbs free reaction energy ΔG , points) and heat demand ($T\Delta S$, triangles). [63].	14
Figure 4: Influence of the operating pressure on the Nernst voltage. The values are calculated for relevant feed gas mixtures at 800 °C: Steam electrolysis 90/10 H ₂ O/H ₂ ; co-electrolysis 60/30/10 H ₂ O/CO ₂ /H ₂ ; CO ₂ electrolysis 90/10 CO ₂ /CO.	15
Figure 5: Schematic of the pressurized test rig used for the experimental studies of this thesis. The main units of the rig are marked with the letters A-E. [63].	19
Figure 6: Schematic of the electrolyte supported cell structure.	20
Figure 7: Complete repeating unit of the ESC stack. The visible area of the active surface represents the air electrode. The glass sealing around the active electrode is highlighted in red.	21
Figure 8: Manufactured stack box at the beginning of the study.	21
Figure 9: Schematic of the fuel electrode supported cell structure used in the F10-design stack.	22
Figure 10: Schematic of one repeating unit of the F10-design CSC stack provided by Forschungszentrum Jülich.	23
Figure 11: Equivalent circuit model used for the fitting procedures of the recorded impedance spectra.	25
Figure 12: Schematic of an infinitesimal control volume considered for the 1D model of a single repeating unit.	30
Figure 13: Schematic of the structure of the test rig with the integrated stack and the associated heat transfers between stack and surroundings [72].	32
Figure 14: Determination of the a) parameter a as a function of the hydrogen partial pressure and b) parameter b as a function of the steam partial pressure on a double-logarithmic scale. The obtained parameters are used for equation 5.2 and are implemented into the stack model. The linear fits achieved a) $R^2=0.94$ and b) $R^2= 0.96$	34

Figure 15: a) activation energies obtained for the operating pressures of 1.4, 4 and 8 bar. b) shows the fit and the corresponding equation associated with the experimentally obtained activation energies shown in a) for a pressure range from 1.4 to 30 bar. The activation energies are implemented into the stack model.	35
Figure 16: a) Comparison of the simulated and measured voltage behavior of the middle cell of the ESC stack. b) shows the corresponding simulated U(i)-curve for 30 bar.	36
Figure 17: a) temperature profile of the middle cell of the ESC stack during co-electrolysis operation at 1.4 and 8 bar. The cell is discretized into ten units along the length. The simulated data is compared with experimentally obtained temperatures presented in Article II. b) simulated temperature profile of the same cell at a pressure of 30 bar.	37
Figure 18: a) temperature distribution within the stack during the steady-state U(i)-curves recorded at 1.4 bar. The sensor location is indicated by the colored crosses in the scheme. b) shows the cell voltages of specific cells of the same experiment. The cells shown in the graph are indicated by colors. [80].	41
Figure 19: Temperature dependency of the ohmic resistance obtained for the middle cell of the stack. [80].	42
Figure 20: a) Simplified sketch of one single repeating unit of the ESC stack. Arrows represent the electrical (ρ_e) and ionic (ρ_{ionic}) resistivities of each material and the contact resistances (R_{contact}) between each component. Neglected resistivities and resistances for the presented modeling approach are scored out with diagonal bars. b) Comparison between the measured ohmic resistance of one cell of the stack with the theoretical resistance based on the resistivities of the used materials. [80].	43
Figure 21: Analysis of the temperature and pressure dependency of the polarization resistances obtained out of the dynamically recorded U(i)-curves. [80].	44
Figure 22: ASR values derived from steady-state and dynamically recorded U(i)-characteristics for co-electrolysis (a), (b) and pure steam-electrolysis (c). (d) shows the fitted ASR curves of a-c. Values of the temperature-dependency of the ohmic resistance are derived from Article I. [63].	49
Figure 23: Comparison of five gas compositions for steam, co- and CO ₂ electrolysis at 1.4 (a) and 8 bar (b). [63].	51
Figure 24: Comparison of EIS spectra during steam and CO ₂ electrolysis at 700 °C and 850 °C respectively and 1.4 and 8 bar of pressure. RC is 30 % at a current density of $-0.20 \text{ A} \cdot \text{cm}^{-2}$. [63].	52
Figure 25: Constant-current steam electrolysis operation over a) 1,000 h at 1.4 bar and b) 2,000 h at 8 bar. [83].	56

- Figure 26: Recorded impedance spectra of the steam electrolysis operation over a) 1,000 h at 1.4 bar and b) 2,000 h at 8 bar. [83]. 57
- Figure 27: Cross section showing the fuel electrode and electrolyte of the stacks that were operated at a) 1.4 bar over 1,000 h and b) 8 bar over 2,000 h. [83]. 58
- Figure 28: a) Constant-current operation in steam and co-electrolysis mode over 1,000 h at 1.4 bar and 8 bar. b) Overview of the temperature corrected increase of the ohmic resistance observed for the three independently operated stacks. [83]. . 59
- Figure 29: Characterization of the ohmic resistance of the ESC and CSC stacks. The values were obtained from impedance measurements at 1.4 bar for the middle cell of each stack. Data of the ESC can be found in Article I. [69]. 63
- Figure 30: Steady-state $U(i)$ -curves recorded for the co-electrolysis operation for a) the CSC stack and b) the ESC stack at 1.4, 4 and 8 bar. Inlet gas composition is 60/30/10 ($H_2O/CO_2/H_2$) with a reactant conversion of 70 % at every measuring point. [69]. 64
- Figure 31: Temperature and pressure dependent total ASR of the CSC and the ESC stack. The ASR of the ESC stack is plotted jointly with values obtained with a different but identically constructed stack used in Article II (unfilled squares). [69]. 65
- Figure 32: EIS spectra of the CSC during a) pure steam and b) pure CO_2 electrolysis at pressures of 1.4, 4, and 8 bar at 750 °C. c) and d) show the same experiment for the ESC stack at a temperature of 700 °C. [69]. 66
- Figure 33: Pressure dependency of the voltage efficiencies of the ESC and CSC stack for an endothermal, exothermal and close to thermoneutral operation during steam and co-electrolysis. 68

List of Acronyms

ASR	Area Specific Resistance
BoP	Balance of Plant
CSC	Cathode Supported Cell
CSTR	Continuously Stirred Tank Reactor
DME	Dimethyl Ether
ECM	Equivalent Circuit Model
EDX	Energy Dispersive X-ray
EIS	Electrochemical Impedance Spectroscopy
ESC	Electrolyte Supported Cells
GDC	Gadolinium-Doped Ceria
HTSE	High Temperature Steam Electrolysis
ICVT	Institute for Chemical Process Engineering
LCA	Life Cycle Assessment
LSCF	Lanthanum Strontium Cobalt Ferrite
LSCM	Lanthanum Strontium Chromo-Manganite
LSMC	Lanthanum Strontium Manganese Chromium
MCF	Manganese Cobalt Ferrite
MEA	Membrane Electrode Assembly
MFC	Mass Flow Controller
NDIR	Nondispersive Infrared Sensor
Ni	Nickel
OCV	Open Circuit Voltage
PTA	Post-Test Analysis
PtG	Power to Gas
PtL	Power to Liquid
PtX	Power to Chemicals
RC	Reactant Conversion
rSOC	Reversible Solid Oxide Cell
rWGS	Reverse Water-Gas Shift
SEM	Scanning Electron Microscopy
SFM	Strontium Iron Molybdenum
SOC	Solid Oxide Cell

SOEC	Solid Oxide Electrolysis Cell
TEA	Techno-Economic Analysis
TPB	Triple Phase Boundary
YSZ	Yttria-Stabilized Zirconia

List of Symbols

Latin letters:

Symbol	Description	Unit
a	Activity of a species in a reaction	
a	Exponent for H ₂ partial pressure dependency	
A	Effective area	m ²
ASR_{act}	Activation contribution to ASR	Ω m ²
ASR_{diff}	Diffusion contribution to ASR	Ω m ²
ASR_{Ω}	Ohmic contribution to ASR	Ω m ²
b	Exponent for H ₂ O partial pressure dependency	
D_{eff}	Effective diffusion coefficient	m ² s ⁻¹
d_p	Pore diameter	m
E_{act}	Activation energy	J mol ⁻¹
f	Frequency	Hz
F	Faraday constant = 96485 C mol ⁻¹	C mol ⁻¹
ΔG_0	Standard Gibbs reaction enthalpy	J mol ⁻¹
ΔH	Enthalpy of the reaction	J mol ⁻¹
$\Delta_r h^0$	Standard molar reaction enthalpy	J mol ⁻¹
i	Current density	A m ⁻²
i_0	Exchange current density	A m ⁻²
J	Area specific inlet gas flux	mol cm ⁻² s ⁻¹
k_B	Boltzmann constant	J K ⁻¹
Kn	Knudsen number	
L	Inductivity	H
m	Exponent for O ₂ partial pressure dependency	
\dot{m}	Mass flow	kg s ⁻¹
p	Pressure	bar
p_0	Standard pressure	bar
\dot{Q}	Heat flow	J s ⁻¹
Q	Non-ideal capacitance	F
R	Resistance	Ω
R	Universal gas constant	J mol ⁻¹ K ⁻¹
R^2	Coefficient of determination	

RC	Reactant conversion	%
$slpm$	Standard liters per minute	$l\ min^{-1}$
T	Temperature	K or $^{\circ}C$
U	Voltage	V
V	Reactor volume	m^3
X	Mole fraction of a gas species in a mixture	
z	Number of transferred electrons	
Z'	Real part of the complex impedance	$\Omega\ m^2$
Z''	Imaginary part of the complex impedance	$\Omega\ m^2$

Greek letters:

Symbol	Description	Unit
α	Charge transfer coefficient of anode or cathode	
Δ	Operator representing a change in quantity	
\square	Emissivity of a material or medium	
ε	Porosity	%
η_U	Voltage efficiency	%
γ	Pre-exponential factor of an electrode	$A\ m^{-2}$
λ	Molecular mean free path	m
σ	Conductivity of a material	$S\ m^{-1}$
ρ	Resistivity of a material	$\Omega\ m$
ν_j	Stoichiometric coefficient of chemical species j	

Subscripts:

Symbol	Description	Unit
act	Activation	
ae	Air electrode	
avg	Average	
cl	Contact layer	
$cond$	Conduction	
$contact$	Contact	
$conv$	Convection	
crb	Chromium barrier layer	
e^-	Electrical	

<i>diff</i>	Diffusion resistance
<i>el</i>	Electrolyte
<i>fe</i>	Fuel electrode
<i>i</i>	Reaction index
<i>ic</i>	Interconnect
<i>ionic</i>	Ionic
<i>LF</i>	Low frequency
<i>max</i>	Maximum
<i>MEA</i>	Membrane electrode assembly
<i>mesh</i>	Mesh
<i>MF</i>	Middle frequency
<i>OCV</i>	Open circuit voltage
<i>ohm</i>	Ohmic resistance
<i>pol</i>	Polarization
<i>prod</i>	Product
<i>R</i>	Reaction
<i>rad</i>	Radiation
<i>react</i>	Reactant
<i>s</i>	Solid
<i>tot</i>	Total

List of Scientific Publications

This is a cumulative thesis, which is based on four scientific articles listed below.

First author:

Article I: Analysis of pressurized operation of 10 layer solid oxide electrolysis stacks.
M. Riedel, M.P. Heddrich, K.A. Friedrich,
International Journal of Hydrogen Energy, Vol. 44 (2019), 4570–4581.
DOI: <https://doi.org/10.1016/j.ijhydene.2018.12.168>.

Article II: Experimental Analysis of the Co-Electrolysis Operation under Pressurized Conditions with a 10 Layer SOC Stack.
M. Riedel, M.P. Heddrich, K.A. Friedrich, Journal of The Electrochemical Society, 167 (2020), 024504.
DOI: <https://doi.org/10.1149/1945-7111/ab6820>.

Article III: Investigation of the Long-term Stability of Solid Oxide Electrolysis Stacks under Pressurized Conditions in Exothermic Steam and Co-electrolysis Mode.
M. Riedel, M.P. Heddrich, K.A. Friedrich, Fuel Cells. Vol. 20 (2020), 592-607.
DOI: <https://doi.org/10.1002/fuce.202000011>.

Article IV: Pressurized operation of solid oxide electrolysis stacks : An experimental comparison of the performance of 10-layer stacks with fuel electrode and electrolyte supported cell concepts.
M. Riedel, M.P. Heddrich, A. Ansar, Q. Fang, L. Blum, K.A. Friedrich,
Journal of Power Sources, Vol. 475 (2020), 228682.
DOI: <https://doi.org/10.1016/j.jpowsour.2020.228682>.

Co-author and acknowledged contributions:

Article V: Theoretical and experimental study of Reversible Solid Oxide Cell (r-SOC) systems for energy storage.
S. Santhanam, M.P. Heddrich, M. Riedel, K.A. Friedrich, Energy, Vol. 141 (2017).
DOI: <https://doi.org/10.1016/j.energy.2017.09.081>.

Article VI: Process design study of reversible solid oxide cell (r-SOC) system for coupling energy storage and hydrogen economy supply chain.
S. Santhanam, M.P. Heddrich, M. Riedel, K.A. Friedrich, ECS Trans., Vol. 78 (2017).
DOI: <https://doi.org/10.1149/07801.2925ecst>.

Article VII: High Temperature Co₂ electrolysis for Power₂to₂X.
D.M.A. Dueñas, M. Riedel, M. Riegraf, R. Costa, K.A. Friedrich, Chemie Ing. Tech. 92 (2020), 45–52.
DOI: <https://doi.org/10.1002/cite.201900119>.

Article VIII: Transient reversible solid oxide cell reactor operation – Experimentally validated modeling and analysis.
S. Srikanth, M.P. Heddrich, S. Gupta, K.A. Friedrich, Appl. Energy. 232 (2018), 473–

488.

DOI: <https://doi.org/10.1016/j.apenergy.2018.09.186>.

Article IX: Gas recirculation at the hydrogen electrode of solid oxide fuel cell and solid oxide electrolysis cell systems.

M. Henke, S. Hillius, M. Riedel, J. Kallo, K. A. Friedrich, *Fuel Cells*. Vol. 16 (2016), 584-590.

DOI: <https://doi.org/10.1002/fuce.201500114>

Scientific presentations:

Oral presentations:

- M. Riedel, R. Nitsche, M.P. Heddrich, K.A. Friedrich, „Electrochemical Characterization of a 10 layer SOEC Stack under pressurized conditions”, *1st International Conference on Electrolysis, Copenhagen, Denmark (2017)*
- M. Riedel, M.P. Heddrich, K.A. Friedrich, „Performance and Durability of a 10 layer SOE Stack operated under pressurized conditions”, *13th European SOFC & SOE Forum, Lucerne, Switzerland (2018)*
- M. Riedel, M.P. Heddrich, K.A. Friedrich, „Experimental analysis of SOE stacks under pressurized operation”, *2nd International Conference on Electrolysis, Loen, Norway (2019)*
- M. Riedel, M.P. Heddrich, K.A. Friedrich, „Experimental analysis of SOE stacks under pressurized co- and CO₂ electrolysis operation”, *14th European SOFC & SOE Forum, Lucerne, Switzerland (2020)*

Poster presentations:

- M. Riedel, R. Nitsche, M. Henke, M.P. Heddrich, K.A. Friedrich “Pressurized Operation of a 10-layer Solid Oxide Electrolysis Stack”, *12th European SOFC & SOE Forum, Lucerne, Switzerland (2016)*
- M. Riedel, R. Nitsche, M.P. Heddrich, „Electrochemical Characterization of a Solid Oxide Electrolysis Stack operated under pressurized conditions”, *7th International Conference on Fundamentals & Development of Fuel Cells, Stuttgart, Germany (2017)*
- M. Riedel, C. Schnegelberger, S. Santhanam, M.P. Heddrich, K.A. Friedrich, „High temperature steam electrolysis at DLR – from stack to system level”, *2nd International Conference on Electrolysis, Loen, Norway (2019)*

1 Introduction

1.1 Background - Energy storage and sector coupling

Global warming induced by the extensive emission of greenhouse gases in modern industry is considered to be one of the most threatening and challenging topics of our time. In order to mitigate the corresponding climate change, the transition towards a more renewable energy powered society is crucial. However, an increased use of renewable energy raises new challenges within the power grid and requests smart power management and storage options. Since the main production of basic chemicals today is based on fossil fuels, an increased use of renewable energy is becoming a further challenge for this industry sector. Renewable energy sources like solar and wind are intermittent in nature and their production varies significantly with time and natural conditions. Furthermore, the electricity production is oftentimes not congruent with the temporal energy demand. In order to ensure a continuous and stable power supply, effective and highly efficient storage options for renewable electrical energy have to be investigated and established [1–3]. Since a stringent reduction of the proportion of fossil fuels has to be considered within all industrial fields, especially the cross-sectoral use of renewable energy in the area of combined heat and power, transport and chemical industry will be of essential importance [4,5].

One promising method of storing electrical energy is the conversion into valuable chemicals. Storing chemical energy is very attractive and beneficial due the high storage capacities [6–9]. Additionally, the electricity-based conversion offers opportunities for alternative syntheses of industrial chemicals and fuels that are currently produced from fossil fuels. The conversion processes are commonly referred to as Power to Chemicals (PtX) or depending on the final product more specifically to Power to Gas (PtG) or Power to Liquid (PtL). The opportunity to couple the synthesis of valuable commodity chemicals like hydrogen or synthesis gas (H_2+CO) via PtX with the energy storage industry is enabled by technologies such as electrolysis.

There are several different types of electrolyzers operating at different temperatures. Depending on the type, it is able to convert liquid water or steam into hydrogen, CO_2 into CO or even both reactions simultaneously into a synthesis gas (or syngas). Syngas itself

can be seen as one of the major commodity chemicals for various chemical and fuel syntheses in modern industry [10,11]. However, a high yield production of gaseous or more complex liquid chemicals and fuels such as methane, ammonia, dimethyl ether (DME), methanol or jet fuel requires further downstream processes subsequent to the electrolyzer. For example, a conventional process for methanol synthesis with a copper-based catalyst is operated at 45-60 bar whereas Fischer-Tropsch reactors are operated in a wide range between 10-60 bar depending on the used metal catalyst and the desired product [12–18]. Furthermore, for storage or transportation of synthesized gases certain pressurization is needed. In order to that, the products of the electrolyzer (H_2 , CO or syngas) have to be pressurized to fulfill the requirements of the respective downstream or storage option. However, the compression of gas is generally energy consuming which might consequently not lead to the beneficial synergy the coupling of an electrolyzer with a storage or fuel production step could have. Therefore, considerable advantages might be achieved if electrolyzers are operated at elevated pressures and thus produce pressurized gases that can be fed directly to the downstream option [13,19–22]. Hence, this option provides the opportunity to couple the energy storage industry with chemical synthesis industry sector via electrolysis.

1.2 Pressurized operation of solid oxide electrolyzers

Solid oxide electrolysis cells (SOEC) use solid ion-conducting electrolytes which enable the operation at high temperatures between 650 and 1,000 °C. The high operating temperature leads to reduced electrochemical losses, fast kinetics and high reaction rates without requiring noble catalysts. In contrast to the low-temperature electrolyzers, SOECs can be operated in endothermic, thermoneutral and exothermic electrolysis mode due to the generally low voltage of the electrolysis reaction at high temperatures. Additionally, these types of electrolyzers can be used for hydrogen and carbon monoxide production or for the conversion of steam and carbon dioxide into synthesis gas during co-electrolysis operation.

The pressurization of the SOEC product gas can either be achieved via electric compression or by pressurizing the whole electrolysis step. The latter offers the possibility for increased process intensification since the related PtX systems can be built with a higher grade of integration. Furthermore, costs for the auxiliary compressors of the product gas can be significantly reduced or omitted [13,23]. For instance, an operation of the

electrolyzer at 20 bar reduces the subsequently required compression energy for hydrogen by approximately 40 % when aiming at 900 bar for dispenser stations [20]. At the same time, the power required for pressurizing the liquid water for generating steam does not increase significantly which consequently leads to increased system efficiencies. Furthermore, elevated pressure also supports higher mass flow rates for the same size components due to lower flow velocities of the media. On the electrochemical side, elevated pressures lead to decreased electrochemical losses within an SOEC and thus a decreased power consumption of the electrolyzer can be achieved [24–31].

However, certain challenges within the operation of SOECs at elevated pressures have to be overcome. Since solid oxide cells consist of ceramic materials which are sensitive towards mechanical forces, appropriate pressure controls have to be provided within pressurized systems in order to prevent differential pressures between anode, cathode or the surrounding atmosphere. However, this pressure control is in fact not trivial due to the often unequal gas volumes between the fuel and the air sides of stacks and larger stack modules and the high probability of destruction as a consequence of malfunctions. Furthermore, a precise management of a constant and stable steam supply is required since condensations within the electrolyzer system lead to pressure fluctuations, influence the mechanical robustness of the cell and stack components and can thus lead to increased degradation or malfunction of the electrochemical device.

1.3 Thesis structure

This cumulative thesis is divided into seven chapters. A brief overview about the specific contents is given below:

Chapter 1: A brief introduction into the scientific field and research topic is provided in this section.

Chapter 2: The current state of the scientific research is described. The identified scientific gap is addressed and the scientific approach is highlighted.

Chapter 3: The solid oxide electrolyzer technology and the associated electrochemical fundamentals are briefly presented in this section.

Chapter 4: The experimental methodologies are highlighted in this chapter. The used experimental facility, the used solid oxide cell stacks, and both the electrochemical and physical characterization methods are described.

Chapter 5: The numerical stack model is briefly described at the beginning of this chapter. Furthermore, the contribution of the thesis to the model and some simulation results are presented in order to show the general capabilities and the achieved agreement between simulation and experiment.

Furthermore, this chapter summarizes the addressed research questions and the used experimental methodologies of the four publications. The main results are highlighted.

Chapter 6: The four published articles are listed in this chapter.

Chapter 7: The conclusion of the thesis is presented in this section.

Chapter 8: Possible follow up activities to continue the research of this thesis are described in the last chapter.

2 Research motivation

The scientific motivation behind the thesis is presented in this chapter. The current state of the art of the pressurized operation of SOECs is listed within the section 2.1. A brief overview of the scientific research in the field and the identified scientific gap in the research is addressed in section 2.2. Finally, the scientific approach and the thesis structure are presented in section 2.3 and 1.3.

2.1 Current state of solid oxide electrolyzers

The SOEC technology for producing hydrogen, carbon monoxide, or syngas has developed rapidly in recent years. Developments on material-, cell- and stack levels, to demonstration, operation and commercialization of larger systems have been intensified [32–36].

The first time the SOEC technology attracted considerable attention was in the early 1980s where Dönitz et al. reported about steam electrolysis results achieved within the HotElly project from Dornier Systems GmbH [37]. Additionally, Westinghouse Electric Corporation Research and Development Center made substantial progress within the cell and stack developments due to proper selection of the used materials in terms of their thermal, mechanical, and chemical characteristics [38]. However, the research work within the high temperature electrolysis field decreased within the 1990s where remarkable work was solely done in Japan [39,40]. Due to the upcoming demand for efficient energy storage options and the considerable potential of the SOEC technology within this field of application, the research work increased within the last two decades significantly [34]. Next to experimental investigations examined on pure steam electrolysis, co-electrolysis of steam and carbon dioxide and even pure CO₂ electrolysis on cell, stack and system level were reported [41–45]. In addition, a large number of theoretical and modeling studies including SOECs were provided in literature.

The majority of published work based on experimental studies are examined on half or single cells focusing on material development, novel manufacturing techniques, alternative designs or degradation and operational phenomena [45–50]. However, experimental investigations of stacks got more attraction within recent years since the stack performance and degradation can highly differ to single cell tests. Furthermore, to be able to design possible plants and to identify operational strategies, detailed performance characteristics and understandings of the operational behavior of stacks have

to be prior investigated. Leading research centers and universities in the US, CEA¹ in France, EIFER², FZJ³, and DLR⁴ in Germany and DTU⁵ in Denmark are just a few examples of institutions that intensified their research work on SOEC stack level within the last decade. Most of the published studies investigate the performance characteristics during different operating modes and the degradation behavior. Furthermore, companies like Haldor Topsoe in Denmark, sunfire GmbH in Germany or SolidPower in Italy enhance their developments towards components and products for SOEC system applications [32,51–53]. The limiting factors of the currently available stacks are the considerably high degradation rates which restrict the operational boundaries in terms of current density, temperature gradients or the dynamical operation. Furthermore, the relatively high investment costs of the stacks in combination with the still small production numbers did not help the SOEC technology to get significantly beyond the prototype status of >150 kilowatt demonstrations yet. As a minor exception, Haldor Topsoe developed the commercially available “eCOs” plant which allows the production of CO from CO₂ directly at the site of facilities where the gas is needed [33]. However, currently only two plants that can deliver up to 96 m³/h CO are in operation in the USA. Data about the degradation of the stacks, the operating strategy or the system concept are not published. Sunfire GmbH will start the operation of a steam electrolysis system in Salzgitter at the end of 2020 that is planned to have a nominal power input of 720 kW. In the near future, the same company wants to build the first commercial plant for hydrogen-based renewable aviation fuel in Europe. The plant with its significant relevance of 20 MW electrical power input is planned to start in 2023 [54,55]. These examples show that the SOEC technology continues to target the mass market entry and several manufacturers are rapidly accelerating their production capacities and scale-up. Note that all these applications run at atmospheric operating pressures.

Research and developments in the field of pressurized SOEC operation are thus currently considerably less available than for the operation at atmospheric pressures. Consequently, scientific publications on the experimental behavior of cells, stacks or systems are rare. However, the few publications that are available found considerable advantages in operating SOECs at elevated pressures. On button cells, oxygen and fuel electrodes have been

¹ CEA: The French Alternative Energies and Atomic Energy Commission

² EiFER: European Institute for Energy Research

³ FZJ: Forschungszentrum Jülich

⁴ DLR: German Aerospace Center

⁵ DTU: Danish Technical University

independently studied in symmetrical cell setups at elevated pressures [31,56]. Both studies found a decreased electrode resistance with increasing pressure and concluded a significant potential for the pressurized operation in fuel cell or electrolysis mode. Bernadet et al. investigated a circular single cell with an active area of 3.14 cm^2 between 1 and 10 bar in steam and co-electrolysis mode [25–27]. Similar studies were conducted by Jensen et al., Momma et al. and Sun et al. for pressure ranges between 0.1 and 10 bar [13,28,29]. However, the used gas compositions of these studies contained significantly high hydrogen or nitrogen proportions which might not be of relevance for perspective hydrogen or syngas production applications.

First remarkable research work in the field of pressurized electrolysis mode on stack level was examined by O'Brien et al. in 2012 [57]. The authors used a 10-cell stack and operated it at pressures of up to 15 bar in steam electrolysis mode. Although the steam utilization was just 40 %, the authors were able to successfully demonstrate the functionality and performance of the stack at elevated pressures. Jensen et al. reported experimental results by using an 11-cell stack from Haldor Topsoe in steam electrolysis mode between 1.2 and 25 bar in 2016 [20,58]. Subsequent investigations were examined by the same authors with a 30-cell stack in reversible mode by furthermore performing some co-electrolysis experiments [30,59]. The first system approach regarding the pressurized hydrogen production with SOECs has been reported in 2017 by sunfire GmbH [23]. Three 30-cell stacks with a nominal input power of 10 kW were operated up to 15 bar and were coupled with several balance-of-plant (BoP) components like an evaporator, electrical heaters and heat exchangers. However, challenges like thermal management of the stack, pressure control, stable steam supply and considerable heat losses towards the surroundings were observed and must be safely addressed for future approaches.

2.2 Scientific research gap

The scientific work performed on the topic of experimental investigations of SOEC stacks is rare and by far dominated by non-pressurized operations. The available studies mainly focus on dynamical performance characterizations with different gas compositions in the feed or the long-term operation in steam and co-electrolysis mode combined with post-mortem analyses of the stacks.

Figure 1 illustrates the quantity of relevant publications that have been published for the atmospheric and pressurized operation of SOEC stacks. A distinction is made between

theoretical and experimental studies. At the time this PhD thesis is written, there are five relevant publications that experimentally investigated SOEC stack behaviors at elevated pressures [20,23,57–59]. Note that the four publications added in brackets to Figure 1 come from this cumulative thesis (Article I-IV).

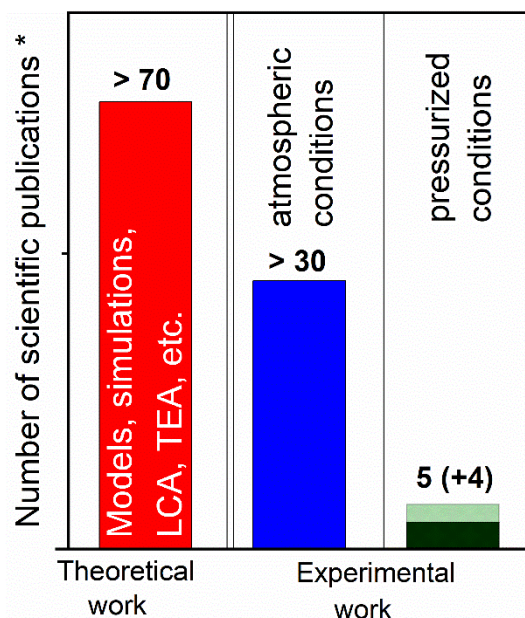


Figure 1: Number of publications related to the operation of SOEC stacks. Distinction is made between theoretical and experimental publications for stack operation in electrolysis mode. The given numbers are based on scopus database (date: 09/2020).

With the exception of the author's publications, the other studies primarily investigated the dynamical performance characteristics with gas compositions for pure steam electrolysis or the reversible SOC (rSOC) mode, which includes fuel cell and steam electrolysis operation. However, for the latter a considerably high proportion of hydrogen in the feed was used which would not be reasonable for hydrogen production applications. Within the single publication from Jensen et al. examining the co-electrolysis operation at elevated pressure, a gas composition with an H/C ratio of almost seven was used [59]. However, for relevant downstream processes like Fischer-Tropsch H/C ratios of one to two are required [60]. None of the available studies focused on the performance of pressurized CO₂ electrolysis or the influence of elevated pressures on the differences during steam, co- or CO₂ electrolysis so far. Moreover, the longest operation on stationary steam electrolysis was studied within the publication of Jensen et al. over 200 hours [58]. Unfortunately, several test incidents occurred during this experiment. Hence, the significance of the found degradation behavior is limited and post-test analyses of the cells were not carried out. The long-term stability of a stack during pressurized co-electrolysis was not

studied in any publications. Within most of the published experiments planar stacks with cathode supported cells were used, though stacks with electrolyte supported cells might be reasonable for pressurized systems due to better mechanical and redox stability of the cells [61]. Only one publication treated the behavior of a stack with electrolyte supported cells during steam electrolysis operation, though a considerable amount of nitrogen was used in the feed during the study. A direct comparison of the pressure influences on the performance and electrochemical characteristics of different stack concepts operated on relevant electrolysis conditions was missing. Furthermore, experimentally validated numerical stack models were not developed. The available pressurized SOEC models are designed for single cell operation or a single repeating unit of a stack [27,62].

Consequently, the resulting gap within the scientific research on the pressurized operation of SOEC stacks was addressed within the current thesis. Experimental data about the influence of elevated operating pressures on the occurring electrochemical processes, on the dynamical and stationary performance and on the long-term stability of SOEC stacks are provided. The direct comparison of the performance of two different stack concepts that are operated in pressurized steam, co- and CO₂ electrolysis and thus the quantification of the pressure and temperature dependency of the specific resistances was not yet investigated in previous studies. Hence, the identification, quantification and analysis of the dominating physical and electrochemical resistances provide scientific novelty by varying the partial pressures of the media in a much larger range than it is possible within atmospheric pressure operations. The development of a unique numerical stack model and its parameterization and validation with experimental results can be used as basis for perspective developments of suitable control, operation and integration strategies of pressurized SOEC systems. To increase the scientific knowledge and simultaneously support the developments of pressurized solid oxide electrolysis systems by delivering highly required experimental data and analyses, a significant scientific gap is identified and filled.

2.3 Scientific research approach

For the current thesis, the electrochemical behavior of two types of planar 10-layer SOEC stacks with having either fuel electrode supported cells (in electrolysis: cathode supported cells, CSC) or electrolyte supported cells (ESC), were examined under steam, co- and CO₂ electrolysis at elevated pressures of up to 8 bar. The ESC stack is a commercial product from sunfire GmbH whereas the stack with cathode supported cells (CSC) is a

research prototype from Forschungszentrum Jülich. Both stacks are presented in detail in section 4.2 and Article IV. In order to bridge the scientific gap identified in section 2.2, the following methodologies for the experimental investigations were used. Note that two CSC stacks were available whereas a number of eight ESC stacks were used for the studies of this thesis.

Characteristic physical and electrochemical resistances of the stacks were determined with electrochemical impedance spectroscopy (EIS) analyses under different operating temperatures, gas compositions and pressures. The quantification of the identified cell resistances by using an appropriate equivalent circuit model (ECM) offers scientific knowledge about the relationship between the operating conditions and the observed differences during steam, co- and CO₂ electrolysis operation of the stacks. The methodology related to the process identification and quantification via EIS is explained in section 4.3.2, whereas experimental results are presented in the Articles II and IV.

Detailed electrochemical characterizations were carried out with the help of steady-state and dynamically recorded current-voltage curves. The steady-state characterization offers the possibility to investigate the influence of occurring temperature gradients on the voltage and area specific resistance of the stacks at a constant conversion. For the co-electrolysis operation, the analysis of the produced gas composition in dependence of the operating pressure was investigated. The methodology of steady-state current-voltage characteristics is not commonly used within the scientific research and is introduced in this thesis as a profound characterization technique. In contrast, dynamically recorded current-voltage curves with fast current ramps were conducted for a quasi-isothermal characterization of the stack without having dominant horizontal or vertical temperature gradients. Hence, the stack performance is evaluated for one specific stack temperature. Both electrochemical characterization methods are presented in detail in section 4.3.

The long-term stability during the pressurized operation of stacks was investigated during steam and co-electrolysis mode. The influence of the operating pressure on the stack degradation was quantified and was compared with published single cell experiments and stack operations at atmospheric conditions. In contrast to the current state of the pressurized research activities, significantly increased experimental durations of 1,000-2,000 hours were used. Furthermore, post-test analyses were used to examine the influence of the operating conditions on the stack components and cell microstructures.

The long-term experiments were conducted with the ESC stack concept due to limited availability of the CSC stacks.

A 1D-simulation model was developed and was parameterized with quantified electrochemical and physical data of the stacks. Furthermore, heat losses according to the structure of the test rig and the used material properties of the setup are considered. Furthermore, the experimental results related to the current-voltage curves, the area specific resistance (ASR) and the quantified resistance values of the stacks were used for the validation of the simulation results. The 1D model was used to support the experimental characterizations and to predict the operational behavior beyond the experimental possibilities of the test rig.

3 Solid oxide electrolyzer technology

In this section the basic structure of SOECs and the electrochemical reactions are described.

3.1 Operating principle of solid oxide electrolyzers

A solid oxide electrolysis cell is an electrochemical device where electrical energy is converted into chemical energy via redox reactions. An SOEC consists of two spatially separated electrode compartments and a ceramic membrane as the electrolyte. Figure 2 shows a schematic of an SOEC in which the electrolyte acts as an ion conductor and simultaneously as an electronic insulator between the two electrode compartments. The electrolyte permits the transport of oxygen ions (O^{2-}) from the fuel electrode (cathode) to the oxygen electrode (anode) whereas the electrons are forced to go through an external circuit.

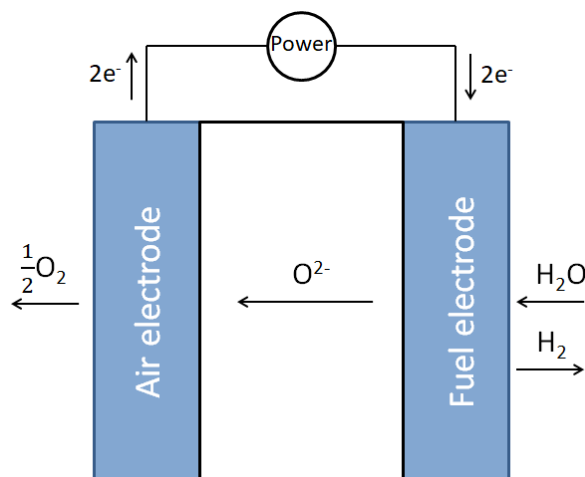
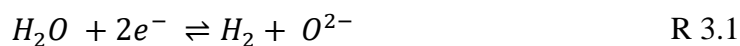


Figure 2: Schematic of a solid oxide cell operated in electrolysis mode.

The reduction reaction of water and/or carbon dioxide takes place at the fuel electrode when a current is applied to the electrochemical device. As a consequence of the applied current, the resulting potential difference between both electrode compartments drives the oxygen ion towards the air electrode.



The oxygen ion migrates through the electrolyte and becomes oxidized at the air electrode.



In addition to the redox reactions, various synthesis reactions can furthermore occur within the SOEC depending on the operating mode. Due to the high operating temperatures and the catalytic property of the commonly used fuel gas electrode and support materials, the kinetics of the respective reactions are fast.

The co-electrolysis operation of steam and CO₂ favors the reverse water-gas shift reaction (rWGS, R 3.4) that can significantly contribute to the production of CO in co-electrolysis mode. High H₂/CO₂ ratios and high temperatures favor this endothermic reaction. Furthermore, the methanation reaction (R 3.5) can occur that is favored at high pressures and low SOEC operating temperatures (above 650 °C). The co- and CO₂ electrolysis operation implies the use of carbonaceous species, with the risk of solid carbon deposition at the fuel electrode due to the Boudouard reaction (R 3.6). Furthermore, CO can be furthermore electrolyzed towards solid carbon within the SOEC at high operating voltages or high conversion rates (R 3.7). The formation of solid carbon within the fuel electrode compartment can lead to a reduced number of active sites, thus leading to a reduced activity and cell performance. Moreover, the formation of larger amounts within the fuel electrode support or the porous active electrode material can in worst case cause structural damage due to volume expansion and nickel dusting.



3.2 Electrochemical fundamentals

3.2.1 Thermodynamics

The electrochemical reduction of H₂O and/or CO₂ occurs at the fuel electrode and requires energy supply due to the endothermic properties of the reactions R 3.1 and R 3.2. The

reaction enthalpies of the reduction reactions from H_2O to H_2 and CO_2 to CO are shown in Figure 3 as a function of temperature.

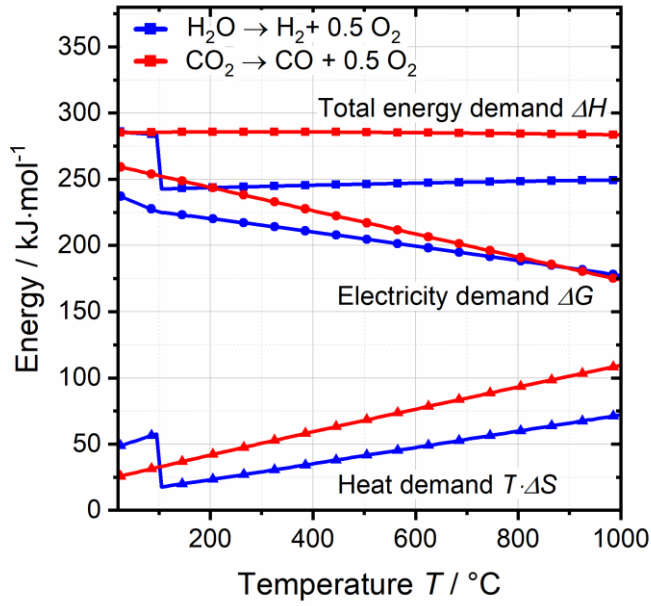


Figure 3: Energy demand of the reduction reaction from H_2O to H_2 and CO_2 to CO with the total energy demand (reaction enthalpy ΔH , squares), the electricity demand (Gibbs free reaction energy ΔG , points) and heat demand ($T\Delta S$, triangles). [63].

The overall required energy of an electrolysis reaction corresponds to the value of the reaction enthalpy ΔH . The Gibbs free energy ΔG corresponds to the electrical energy whereas $T\Delta S$ corresponds to the part of energy that can be supplied by external thermal energy to an SOEC. Consequently, from a thermodynamic point of view it is advantageous to operate at high temperatures since a part of the required energy for the electrolysis can be obtained from the thermal energy produced within the cell during operation (as a result of cell's internal resistances) and/or from renewable or waste heat sources.

The cell voltage of an SOEC can be calculated according to the Nernst equation that describes a theoretical voltage under non-loaded conditions:

$$U_{Nernst} = -\frac{\Delta G_0}{zF} - \frac{RT}{zF} \ln \prod_{i=1}^k a_i^{v_i} \quad 3.8$$

Where U_{Nernst} is the Nernst voltage, ΔG_0 is the Gibbs reaction enthalpy at standard state, R the ideal gas constant, T the temperature, z the number of transferred electrons, F the Faraday constant, a_i the activities of product and reactant species and v_i the stoichiometric coefficients of the participating species. Using the definition of the mole fraction with $X_i = p_i/p$ and ideal gas $a_i = p/p_0$, equation 3.8 yields to the pressure dependent form of the Nernst equation for the H_2O and CO_2 electrolysis reactions:

$$U_{Nernst} = U^0 - \frac{RT}{zF} \ln \frac{X_{react,fuel}}{X_{prod,fuel} + X_{O_2}^{0.5}} + \frac{RT}{2zF} \ln \frac{p}{p_0} \quad 3.9$$

where $X_{react,fuel}$ is the reactant H_2O or CO_2 and $X_{prod,fuel}$ is the produced species H_2 or CO . The pressure dependency of the theoretical Nernst voltage is illustrated in Figure 4. Since the ΔG values for steam and carbon dioxide reduction are highly similar in the temperature range between 700-900 °C, the pressure dependent Nernst voltages show similar values.

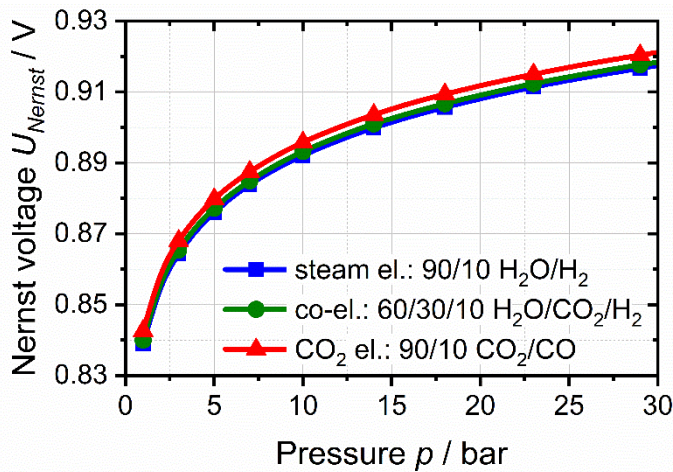


Figure 4: Influence of the operating pressure on the Nernst voltage. The values are calculated for relevant feed gas mixtures at 800 °C: Steam electrolysis 90/10 H_2O/H_2 ; co-electrolysis 60/30/10 $H_2O/CO_2/H_2$; CO_2 electrolysis 90/10 CO_2/CO .

A higher operating pressure leads to an increased open circuit voltage of the SOEC, which is disadvantageous due to the associated higher power consumption. However, this negative effect on thermodynamics can be compensated or exceeded by decreasing activation and diffusion resistances when conversion takes place. Furthermore, the effect of pressure is most dominant at low pressures and becomes less at higher operating pressures and is in general weak due to the logarithmic function in the Nernst equation.

3.2.2 Electrochemical losses

The main loss mechanisms in a SOEC are the ohmic, activation and diffusion losses that lead to increased voltages and heat production within the electrochemical device. Consequently, the higher the losses of the electrochemical cell are, the more power needs to be supplied to the electrolyzer that leads to a decreased overall process efficiency.

The ohmic loss is due to the resistivity associated with the charge carriers. The main contributor to the ohmic resistance originates from the electrolyte material and the oxygen ion transport. Furthermore, the resistance of electrodes to electron transport and contact resistances between the different functional layers in a cell or stack can significantly contribute to the ohmic loss. Consequently, the ohmic resistance can show a temperature-dependency but is not influenced by the operating pressure.

Activation losses occur due to the charge transfer reactions at the electrode-electrolyte interfaces. In particular, the losses are dictated by the electrode reaction kinetics and the specific mechanisms of the reactions. With higher operating pressures, the activation resistances decrease due to increased adsorption rates of the reactants at active sites and the overall enhanced surface coverage with reactant species.

Diffusion losses occur predominantly at high conversion rates when a lower concentration of reactants at the active surface is present due to the limited diffusion of gases through the porous electrodes. Consequently, the diffusion becomes dominant with increased electrode thicknesses and reduced porosities. The diffusion process within a porous electrode is assumed to be governed by both the Knudsen and the ordinary diffusion mechanism. At low operating pressures the diffusion mechanism is dominated by Knudsen diffusion, thus expecting the collision between molecules and wall to be predominantly occurring. Since Knudsen diffusion itself is independent of pressure, the mass flow of the reactants from the gas channel to the active sites is governed by the concentration gradient perpendicular to the porous electrode. It is important to note that the concentration gradient itself is proportional to pressure. The importance of Knudsen diffusion can be expressed with the Knudsen number Kn that is calculated as

$$Kn = \frac{\lambda}{d_p} \quad 3.10$$

with the molecular mean free path λ and the pore diameter d_p . Hence, equation 3.10 indicates that a small pore size increases the contribution of Knudsen diffusion to the overall diffusion process within an SOC electrode. For a typical SOC and the operation at atmospheric pressure, the Knudsen number was shown to be approximately one [64]. Furthermore, Yang et al. showed that for a SOC with an averaged pore size of $<3 \mu\text{m}$, Knudsen diffusion significantly contributes to the effective diffusion of hydrogen within the fuel electrode [65]. However, with larger pore sizes ($>4 \mu\text{m}$), the influence of Knudsen diffusion on the effective diffusion coefficient was shown to decrease considerably. Since

typical pore sizes of SOC fuel electrode materials are in the range of 0.5-2 μm , Knudsen diffusion must be taken into account due to its significant contribution to the overall diffusion process within SOC electrodes [65–68].

At high operating pressures ($\text{Kn} \ll 1$), diffusion becomes dominated by ordinary diffusion, thus inter-molecular collisions become predominant. Since ordinary diffusion is reciprocally proportional to the pressure, the influence of the concentration gradient perpendicular to the electrode becomes less. Consequently, the highest influence of an elevated operating pressure on the diffusion mechanism takes place within the transition region from Knudsen to ordinary diffusion mechanism.

4 Experimental Methodologies

In this section, the test setup, the utilized stack types and the electrochemical and physical characterization methods are presented.

4.1 Pressurized test setup

The test rig for the scientific investigations on high-temperature SOC stacks at the German Aerospace Center can be divided into five sub-areas. The functions are described within the Articles I and II where a picture of the bench can furthermore be found. It includes the pressure vessel with the integrated furnace, the fuel and oxide gas supply, the quench water supply, the equalizing tanks and the gas analysis system. The main component is the pressure vessel with an integrated furnace that enables experimental investigations in both fuel cell and electrolysis mode up to an operating pressure of 8 bar and a temperature of up to 950 °C. The vessel includes an electrical preheater and the furnace environment. In the preheater area, the process gases flow through several pipe loops and are thus brought to the desired process temperature. The furnace environment contains the stack as well as its media inlets and outlets and is flushed with compressed air, with which the surrounding operating pressure is set. The connections for the temperature and pressure sensors as well as the power connections are located under the removable base plate of the pressure vessel.

The test rig was adapted for the investigations of the electrolysis mode within the present thesis. As one of the major challenges during the operation at elevated pressures, a functional and precise pressure control between the both electrode compartments and the furnace environment had to be implemented. In order to enable a detailed and fast responding pressure control, differential pressure sensors were positioned directly at the outlet of the media pipes from the pressure vessel, hence as close as possible to the stack. However, care had to be taken to ensure that the steam does not condense there, as this would lead to considerable pressure fluctuations. Another challenge of the operation in pressurized electrolysis mode is the supply of a stable and pulsation-free steam mass flow to the stack. Steam pulsations or sudden pressure surges or drops due to condensation can lead to fluctuations in the cell voltage or even to cell ruptures and stack failures. Within the test rig an inlet-cooled water evaporator was installed that was developed at the Institute for Chemical Process Engineering (ICVT) at the University of Stuttgart. Compressed air is used to cool the liquid water inlet directly below the heated area in which the water is

evaporated. The sharp transition between the liquid water and heated evaporation area successfully prevents pulsations over the entire operating pressure range of the test rig. In order to prevent solid carbon deposition in the outlet pipes during co- or CO₂ electrolysis studies, an additional evaporator was installed that injects steam into the fuel gas pipe directly behind the stack. The underlying principle of this method is described in detail in Article II and proved its successful effect during the pressurized studies of this thesis. These adaptations were crucial for the successful examination of the pressurized electrolysis studies of the current thesis.

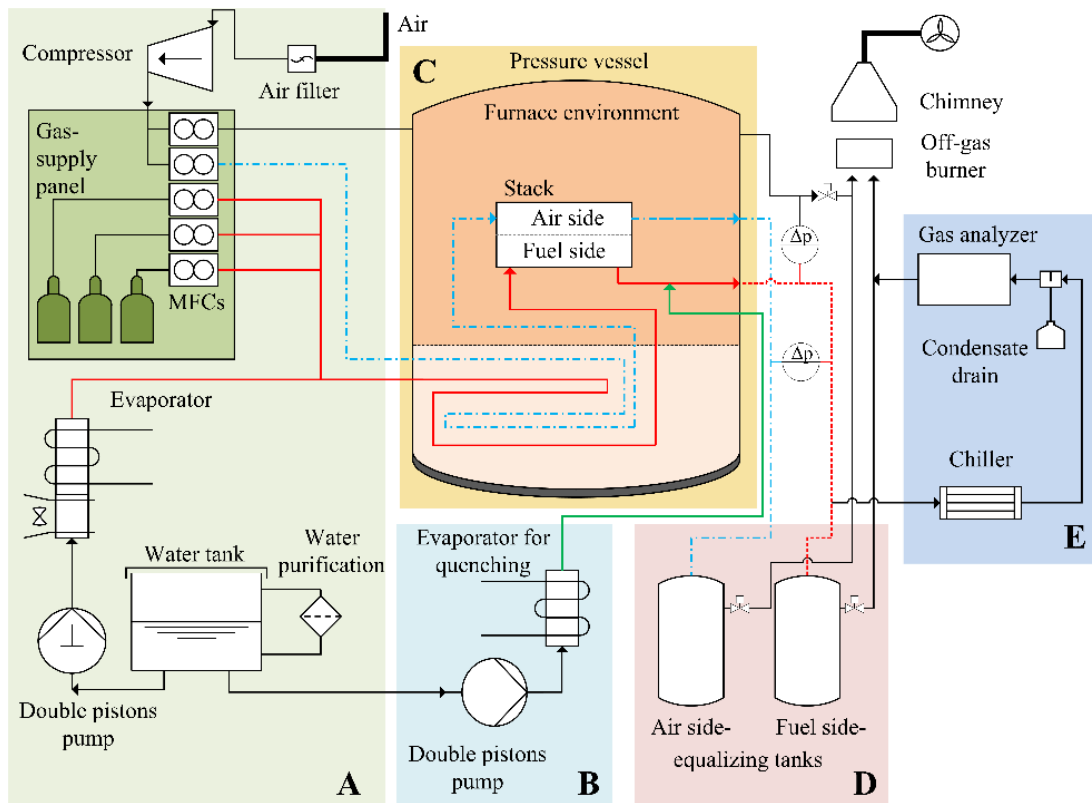


Figure 5: Schematic of the pressurized test rig used for the experimental studies of this thesis. The main units of the rig are marked with the letters A-E. [63].

4.2 Investigated SOEC stacks

The investigated solid oxide 10-layer stacks are briefly introduced in this section. Detailed explanations regarding the setup and the integration into the pressurized test rig can be found in Article II and IV.

4.2.1 10-layer stack with electrolyte supported cells

The ESC stacks used in this thesis were produced by the company sunfire GmbH. The stacks consist of ten electrolyte-supported cells, each with an active area of 127.8 cm².

The fuel electrodes consist of Nickel (Ni) and gadolinium-doped ceria (GDC) that form a composite electrode referred to as Ni-GDC. The electrolyte consists of 3 mol% yttria-stabilized zirconia (3YSZ) and the air electrode of lanthanum strontium cobalt ferrite composite (LSCF) material. Thin GDC layers are implemented between the electrolyte and the air electrode and between the electrolyte and the fuel electrode due to chemical and thermomechanical reasons. The contact layer on the air side is of lanthanum strontium manganese chromium (LSMC) material. A schematic of the cell structure with its layer thicknesses is shown in Figure 6.

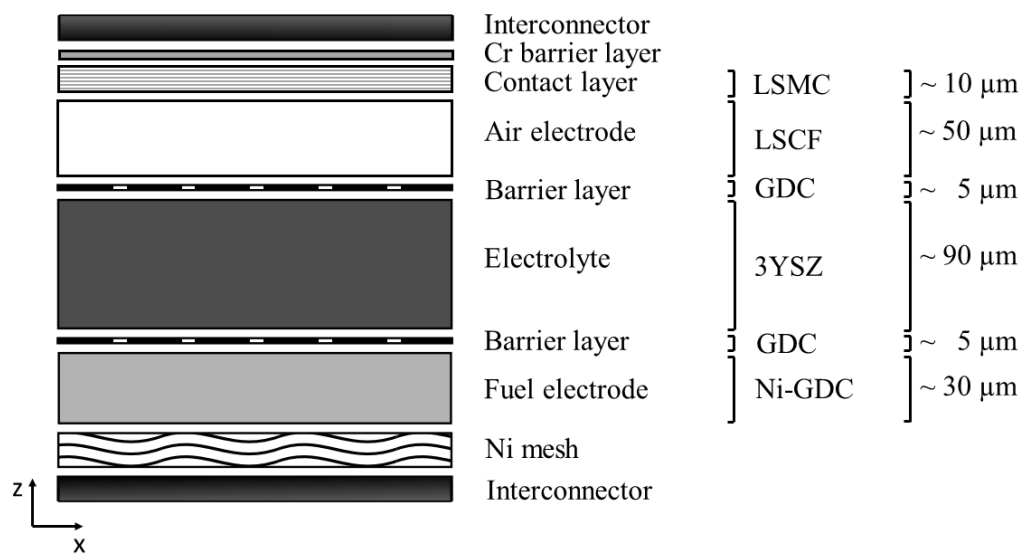


Figure 6: Schematic of the electrolyte supported cell structure.

The stack has an open external air manifold design. The inlet media are passed over the active cell surface of the stack in co-flow direction. One complete repeating unit of the stack is shown in Figure 7. The fuel gas inlet and outlet channels are separated by ceramic spacers and glass sealings from the air electrode compartment. Furthermore, the electrochemically active cell is attached and sealed with glass on the bipolar plate to prevent the crossover of gas or air.

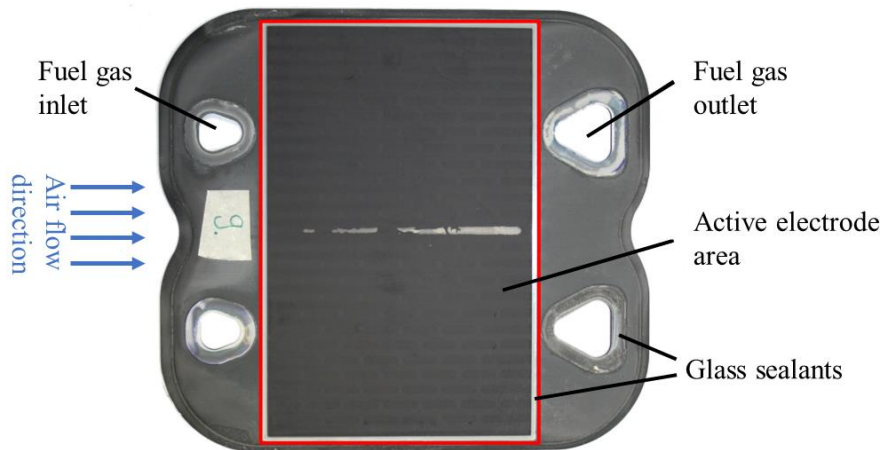


Figure 7: Complete repeating unit of the ESC stack. The visible area of the active surface represents the air electrode. The glass sealing around the active electrode is highlighted in red.

The ESC stack is housed in a gas tight steel box which was engineered collaboratively with sunfire GmbH at the beginning of this thesis (shown in Figure 8). Due to the open external air manifold design, the box enables a precise pressure control of the oxygen electrode compartment. Furthermore, it prevents the generated oxygen and, in case of a leakage, other gases from entering the furnace environment. A thin transfer plate at top of the box enables the supply of the required compression force of 100 kg to the stack. An overall number of five thermocouples are integrated on the air electrodes of cell 1, 5 and 10 of the stack. In addition, four thermocouples are implemented into the inlet and outlet gas pipes of the steel box. Further description of this setup of the ESC stack is given in Article I.

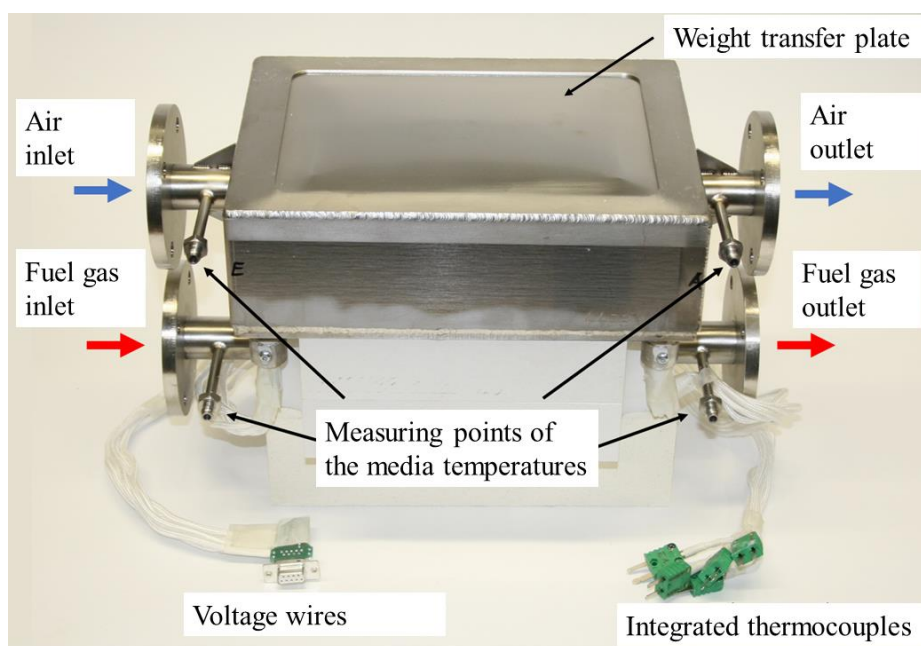


Figure 8: Manufactured stack box at the beginning of the study.

4.2.2 10-layer stack with fuel electrode supported cells

The F10-design CSC stacks used in this thesis were produced and provided by Forschungszentrum Jülich. The stacks consist of ten fuel electrode-supported cells, each with an active area of 80 cm^2 . Figure 9 shows the schematic of the cell structure. The fuel electrodes consist of a Ni-YSZ composite material, the electrolyte of 8YSZ and the air electrode of LSCF material. A thin GDC layer is implemented between the electrolyte and the air electrode. Manganese chromium ferrite (MCF) is implemented as a chromium barrier layer between the air electrode and the interconnector. In contrast to the ESC stacks, the CSC stacks operate in counterflow. Furthermore, the stacks have a closed manifold design, hence do not require an enclosing stack box for the investigations in the pressurized test rig [69].

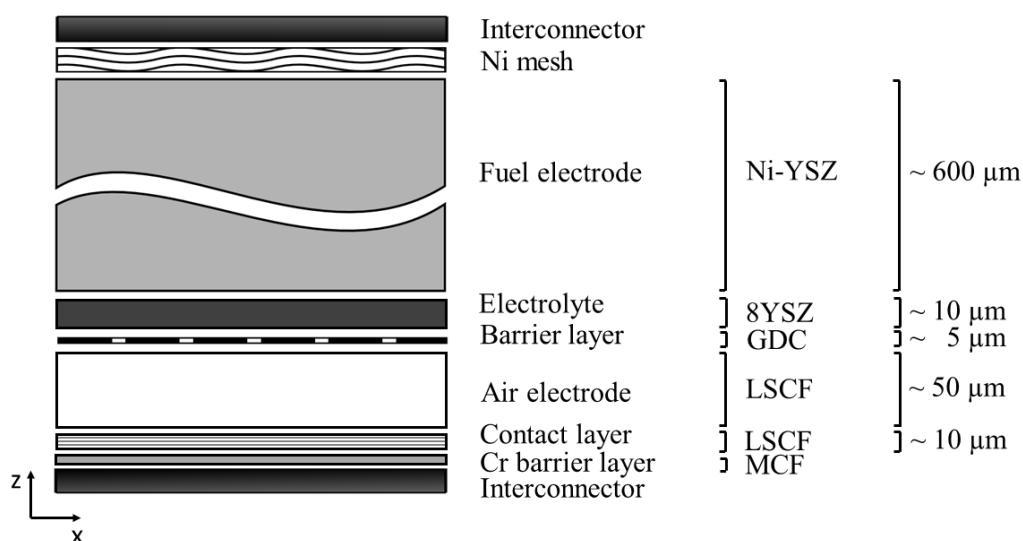


Figure 9: Schematic of the fuel electrode supported cell structure used in the F10-design stack.

The media are supplied via holes in the base plate of the stack. Figure 10 shows a repeating unit of the F10-design stack with the inlet and outlet channels. A photo of a repeating unit can furthermore be found in [70].

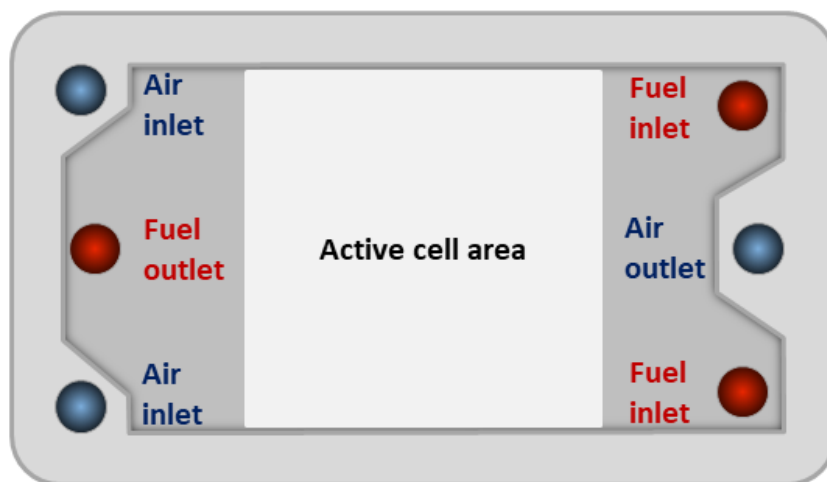


Figure 10: Schematic of one repeating unit of the F10-design CSC stack provided by Forschungszentrum Jülich.

For the implementation of the stack into the pressurized test rig, an adapter plate was designed in collaboration with Forschungszentrum Jülich to meet the required media connection points of the test rig. Shaped mica gaskets were used for the electrical insulation between the stack and the adapter plate. For temperature measurements during the operation, three thermocouples were inserted into the central interconnector of the stack whereas one thermocouple was inserted into the top and bottom plate of the stack respectively. Detailed description of the setup can be found in Article IV.

4.3 Electrochemical characterization methods

4.3.1 Current-voltage characteristics and the area specific resistance

Steady state and dynamically recorded current-voltage characteristics were used for the performance investigations in this thesis. The main differences are described in this section. Furthermore, the area specific resistance was used as a performance indicator that offers the possibility to compare and investigate the pressure influence on different stack concepts.

For steady-state $U(i)$ -curves, the current density is increased stepwise. Due to the formed temperature gradients in the stacks during operation and the different heat capacity of the stacks and the weights on top, reaching stationary conditions takes at least 90 min depending on the operating point. The gas flows for the predefined inlet gas compositions are set at every current density point for a constant reactant conversion (RC) at the cells. The RC is defined according to the overall inlet mass flow of convertible reactants. The

methodology of steady-state current-voltage characteristics is not commonly used within the scientific research. However, it has the significant advantage that the temperature profile in the stack and its influence on the voltage and area specific resistance can be determined in detail. With this method it is possible to record $U(i)$ -characteristics with a current density dependent vertical and horizontal temperature profile at a constant and relevant reactant conversion rate. Consequently, the steady-state experiments offer the possibility to gain insights into the perspective stack operation behavior under different operating modes in larger systems. In contrast, the commonly used dynamically recorded $U(i)$ -characteristics are limited in their suitability for these purposes.

However, dynamically recorded $U(i)$ -curves offer a quasi-isothermal characterization of the stack since a fast current ramp is used that leads to a low temperature change over the complete range of current density. For this method of stack characterization, the gas flows are set for a predefined RC at a respective current density. The advantage of this characterization method is the possible analysis of the ASR at a certain and almost constant stack temperature, while horizontal and vertical temperature gradients are insignificant.

The performance of SOCs can generally be described with the help of the area specific resistance value. Since it is a normalized value, it provides the possibility to compare the performance of SOCs that are operated at different conditions. The general definition of the ASR is given in equation 4.1. In this work, ΔU is calculated via subtracting the reactant conversion dependent ideal Nernst voltage ($U_{Nernst, avg}$) from the measured voltage ($U_{measured}$). $U_{Nernst, avg}$ is calculated with the actual measured characteristic temperature and the averaged gas composition between the inlet and the outlet of the cell, consequently assuming a linear conversion along the cell length. This assumption was shown to be sufficiently precise and valid in [71].

$$ASR = \frac{\Delta U}{i} = \frac{U_{measured} - U_{Nernst, avg}}{i} \quad 4.1$$

In particular, the ideal voltage and thus the ASR associated with the steady-state $U(i)$ -curves is calculated with the aforementioned procedure for every current density step. In case of the dynamically recorded $U(i)$ -curves, the gas composition changes for every current density point due to the varying conversion caused by the current ramp. Consequently, the present gas composition and the related Nernst voltage has to be calculated for each current density step. These calculations were performed with MATLAB in this thesis. The ASR of the dynamically recorded $U(i)$ -curves is thus determined by linearizing over the current density range from $-0.1 \text{ A} \cdot \text{cm}^{-2}$ to i_{max} .

4.3.2 Electrochemical impedance analysis

In this thesis EIS was performed to identify and quantify the influence of an elevated operating pressure and various operating conditions on the electrochemical processes of the ESC and CSC stacks. The analyses were examined with a measurement setup consisting of a TDK Lambda electric power supply, a Zahner Zennium potentiostat and a Zahner EL1000 electronic load. The setup allows the measurement of up to five cells of the stacks simultaneously. The electrochemical impedance spectra were recorded in a frequency range between 50 mHz and 20 kHz or 100 kHz respectively. Depending on the operating conditions, current amplitudes of 0.38 A and 0.96 A were used, whereby linear EIS measurements were generally ensured. Nyquist and $-Z''(f)$ diagrams were used for the graphical analyses of the spectra. The first intersection of the recorded spectra with the abscissa in the Nyquist diagram correlates to the ohmic resistance of the investigated cell. Furthermore, semicircles can be correlated to the additional electrochemical resistances in the spectra. The frequency dependent $-Z''(f)$ plot was used to determine the characteristic frequencies of the remaining contributions to the overall cell resistance. Furthermore, a changing peak height by varying the operating conditions can graphically indicate a changing resistance in such a graph. The Thales software was used for the analyses of the recorded spectra. For the performed quantifications of the electrochemical resistances, the spectra were fitted with a suitable electrochemical circuit model shown in Figure 11.

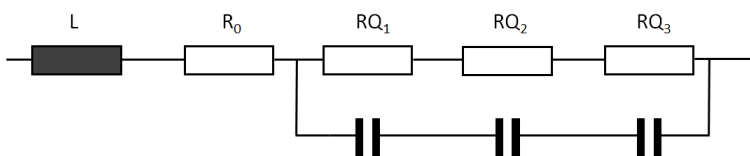


Figure 11: Equivalent circuit model used for the fitting procedures of the recorded impedance spectra.

The ECM consists of one inductive unit (L), a serial resistor to determine the ohmic resistance (R₀) and three RQ elements connected in series that correlate to the fuel electrode, the air electrode and the concentration resistances. Care is taken that the fit quality was generally greater than 99.0 % and that the obtained values were sensible and in accordance with the graphical analyses.

For the scientific EIS investigations in this thesis, the characteristic frequencies of the ohmic, activation, diffusion and conversion impedance were determined by varying the experimental operating parameters as a first step. Subsequently, resistances were

quantified with the appropriate ECM under varying electrolysis modes and different operating pressures. Consequently, the relationships between experimental parameters, the quantified resistances and the performance of the stacks enabled the investigation of the observed differences during steam, co- and CO₂ electrolysis operation of the stacks.

4.3.3 Measurement errors

The author is aware that experimental measurements generally underlie inaccuracies. Therefore, a short discussion of possible measurement errors is provided in this section:

1. Test rig: The test rig was calibrated before the commissioning of each stack with regard to the furnace temperature, the integrated thermocouples and the measurement devices for the absolute pressure. The latter have a specified accuracy of ± 0.3 % of the set value.
2. Temperature measurement: The thermocouples that were implemented in the ESC stacks were positioned at quarter, half and three-fourths of the length of the cell. Since these sensors were positioned manually at the manufacturer, a certain inaccuracy is expected but not quantifiable. However, the impact of the positioning on the experimental results is expected to be small. Furthermore, a temperature measurement always includes inaccuracies due to the thermocouples used and the transmission of the thermoelectric voltage. For the type K thermocouples used in the test rig an accuracy of approximately ± 3 °C is given by the manufacturer for 800 °C operating temperature.
3. Mass flows: The gas flow rates were controlled with industrial standard mass flow controllers. The mass flow controllers were regularly calibrated. Furthermore, the correctly set gas compositions were evaluated based on the measured open circuit voltage (OCV) of the stacks. With this method the leakage of the stacks could furthermore be evaluated. However, the mass flow controllers have an error of 0.05 % that significantly increases at the flow boundaries. A discussion about the impact of this inaccuracy on the ASR was addressed in Article II.
4. Voltage measurement: The voltages were measured using a Siemens SPS unit. However, the specified error of these units is 0.2 % and should therefore not be significant for the measured voltage range of 0.7-1.5 V.
5. Gas analysis: The gas analyzer was calibrated before starting each experimental campaign. Due to its measuring principle, the gas analyzer has a specified inaccuracy of ± 1 % of the measured value for each species.

6. **EIS:** When recording the impedance spectra, care was taken to meet the required conditions of stability, causality and linearity of the measurements for valid impedance data as precisely as possible. However, inaccuracies within the measured voltage or current responses can be induced by the measurement equipment itself (Zahner Zennium, see section 4.3.2), the cables or the plugs. Furthermore, poor electromagnetic compatibility between e.g. the furnace and the sensible impedance setup can lead to undesirable influences. Although these possible influences were considered when connecting the measurement system with the test rig, these inaccuracies are still difficult to quantify. The input voltage accuracy of the potentiostat is specified by the manufacturer with $\pm 50\text{-}100\mu\text{V}$ whereas the current accuracy of the electronic load (EL1000) is specified with $\pm 0.25\%$ of the set value.

In this work, great effort was put into the exactness of measurements. The measurement errors caused by the used hardware were not studied in detail, though. In general, largest discrepancies could arise with the temperature measurement that is used for the ASR calculation. With an assumed maximum temperature inaccuracy of 3 K, the error would be greatest in the lower current density range where $\Delta U = U_{\text{measured}} - U_{\text{Nernst,avg}}$ is smallest. To exemplify, a stack temperature of 790 °C was measured at a current density of $-0.078\text{ A}\cdot\text{cm}^{-2}$ during steam electrolysis operation with the ESC stack (see Article I). Thus, a 3 K higher or lower temperature would lead to a change of the calculated Nernst voltage of approximately 2 mV considering the used operating conditions. The ASR consequently changes by $11\text{ m}\Omega\text{cm}^2$ that corresponds to a deviation of $<1\%$ in this worst-case scenario. Hence, the impact of the measurement inaccuracies on the qualitative and quantitative results of this thesis is expected to be low.

4.4 Physical characterization methods

4.4.1 Gas analysis

An online gas analyzer was used to determine the product gas composition during the co- and CO_2 electrolysis studies. A stream of approximately 1 slpm was taken from the off-gas of the stack and was continuously analyzed by a Rosemount X-STREAM X2GP gas analyzer. The analyzer offers the possibility to determine the molar proportions of H_2 , CO , CO_2 and CH_4 during operation. The proportions of the carbon-containing molecules are measured via a nondispersive infrared sensor (NDIR) whereas the hydrogen content is measured via a thermal conductivity sensor. Since the measuring principle of the

analyzer is not suitable for determining the H₂O content in the gas stream, steam is condensed in the upstream with a compressor chiller operated at 3 °C. Hence, the steam content of the outlet gas composition was calculated via a mass balance for the analyses carried out in this thesis.

4.4.2 Scanning Electron Microscopy (SEM) and Energy Dispersive X-ray spectroscopy (EDX)

For the post-test analyses of the degradation tests shown in Article III, the stacks were disassembled and cross sections of certain areas of different cells and bipolar plates were prepared. Therefore, samples with approximately 1x1 cm² were cut and embedded in resin. The SEM analyses were carried out with a Zeiss UltraPlus, providing an electron beam range of 2.0 to 10 kV. Combined with SEM measurements, the energy dispersive x-ray spectroscopy allowed the identification and quantification of the chemical elements.

5 Results and discussion

The most important results of this thesis are presented in this chapter. First, the parameterized and validated numerical stack model and the author's contribution to it are described. Second, the four publications (Article I-IV) are summarized. Each publication is treated separately in a sub-chapter that is divided into the underlying scientific research questions, the experimental procedure and the presentation of the most important results.

5.1 Numerical cell and stack model

A model built by S. Santhanam for a single repeating unit was the starting point for the development of the presented stack model [62]. The model was used by R. Lin to create a stack model in collaboration with the author to accurately simulate the stack operation within the experimental test rig [72]. The author supported the theoretical stack model developments by providing material properties, experimental parameters and specially designed experiments for the parameterizations (see section 5.1.2). The identified and quantified relations obtained from the electrochemical characterizations of the ESC stack were implemented into the stack model that can therefore support the experimental characterization and predict the operation behavior beyond the experimental possibilities. Results are presented in section 5.1.3 in order to show the general possibilities of the model and the agreement between simulated and experimentally obtained data.

5.1.1 Model description

The stack model is implemented into the open source equation-based and object-oriented software language Modelica. It is hierarchically built and consists of different sub-models for the electrochemical and physical parts that are interlinked to form a complete stack.

One essential part of the stack model is the underlying model that was developed by S. Santhanam for a single repeating unit of an SOC stack [62]. This 1D model considers the geometrical axis parallel to the gas flow direction. Hence, it is assumed that the fluid, thermodynamic and electrical properties along the other two axes are distributed uniformly. A schematic representation of the control volume considered for the 1D model is shown in Figure 12. It consists of five parts which are treated in the corresponding sub-models: The fuel and air chamber, the electrochemical cell compound and two half-width interconnectors. Several infinitesimal control volumes as shown in Figure 12 can be arranged in row to form a complete cell with multiple discretization units.

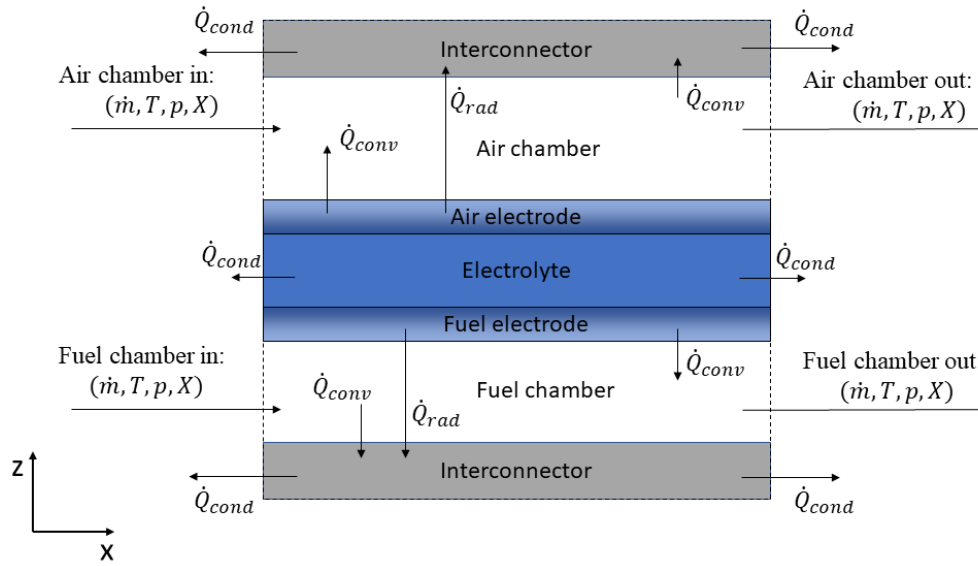


Figure 12: Schematic of an infinitesimal control volume considered for the 1D model of a single repeating unit.

The figure shows the parameters for the inlets and outlets of both the fuel and air chamber of the control volume with the mass flow \dot{m} , temperature T , pressure p and gas composition X . Furthermore, the directions of the conductive heat transfer \dot{Q}_{cond} , the radiative heat transfer \dot{Q}_{rad} and the convective heat transfer \dot{Q}_{conv} are described. Hence, the model for the repeating unit lays the foundation for the entire stack modeling task. The sub-models and their main assumptions are briefly summarized below:

Within the 1D model, the air electrode, electrolyte and fuel electrode are assembled in a triple layer referred to as membrane electrode assembly (MEA). This model primarily calculates the cell voltage and the irreversible losses that arise from electrochemical reaction kinetic, charge transfer and mass transfer. The cell voltage is calculated using the equation

$$U_{cell} = U_{OCV} - i \cdot (ASR_{\Omega} - ASR_{act} - ASR_{diff}) \quad 5.1$$

where U_{OCV} describes the theoretical voltage, i the applied current density, ASR_{Ω} the normalized serial resistance, ASR_{act} the activation losses and ASR_{diff} the diffusion losses. The activation resistance within the MEA sub-model is described by a Butler-Volmer equation. The corresponding equation for the exchange current density i_0 of each electrode has the following form [73,74]:

$$i_{0,fe} = \gamma_{fe} T_{MEA} \cdot \left(\frac{p \cdot X_{H_2,fe}}{p_0} \right)^a \cdot \left(\frac{p \cdot X_{H_2O,fe}}{p_0} \right)^b \cdot \exp\left(\frac{-E_{act,fe}}{R \cdot T_{MEA}} \right) \quad 5.2$$

$$i_{0,ae} = \gamma_{ae} T_{MEA} \cdot \left(\frac{p \cdot X_{O_2,ae}}{p_0} \right)^m \cdot \exp \left(\frac{-E_{act,ae}}{R \cdot T_{MEA}} \right) \quad 5.3$$

with the fuel and air electrode prefactors γ_{fe} and γ_{ae} , the exponents for the partial pressure dependencies a , b , and m as well as the activation energies $E_{act,fe}$ and $E_{act,ae}$.

The serial resistance behavior was determined experimentally and corresponds directly to the actual temperature of the electrochemical device (see 5.1.2 and Article I). The activation losses are evaluated using a parameterized Butler-Volmer equation. The diffusion losses related to the mass transport through the porous electrode material are modeled using extended Fick's law model with Knudsen diffusion employment. The theoretical equations according to the activation and diffusion losses can be found in [62,72,75].

The relevant phenomena that are accounted for in the fuel gas and air channel sub-models are mass storage, energy balance and pressure loss. Furthermore, both the methanation and water-gas shift reaction and their reverse reactions are considered within the fuel gas sub-model. To simplify the model routines, electrochemical steam reduction is assumed to take place at the fuel electrode-electrolyte interface whereas CO/CO₂ reactions proceed via the rWGS/WGS reaction. The experiments that were carried out in this work underline this assumption as being sufficiently precise for relevant co-electrolysis operations (see Article II). The interconnectors are modeled as solid components where only thermal energy accumulation is accounted. Its function as an electrical conductor with certain electrical losses is not considered, since ohmic losses are considered within the MEA sub-model. By connecting the different sub-models, the convective, conductive and radiative heat transfer rates between the MEA and the interconnector sub-models are considered.

The stack model is developed on the basis of the above described model of a single repeating unit. Each repeating unit interacts with adjacent units or the surrounding via gas flow, electric flow and heat flow. The stack model is resolved in the gas flow direction (x) and in the vertical orientation (z), hence resolved as a 1D+1D model.

For the stack modeling purpose, it is assumed that the inlet gas is equally distributed among all cells. The discretized units of the single repeating unit model are electrically connected in parallel to form a complete cell and multiple cells are connected in series to form a stack. The heat conduction between adjacent repeating units and the heat flow into or out of the stack is implemented in x and z direction (see Figure 13). Therefore, a model attached to every discretized unit of a single repeating unit and between adjacent interconnectors is implemented that calculates the heat conduction rate between the

infinitesimal control volumes. Furthermore, the heat transfer between the stack and its surrounding along y direction is considered.

Since the stack model is used to support the characterization of SOEC stacks in the pressurized test rig, it had to be adapted according to the structure of the test bench. In particular, proper heat transfer must be considered due to its large influence on the modeling accuracy. This includes the geometric properties as well as the consideration of the components integrated in the test setup, such as the weights on top of the stack box or the support structure underneath the stack. Figure 13 shows the general heat transfer scheme.

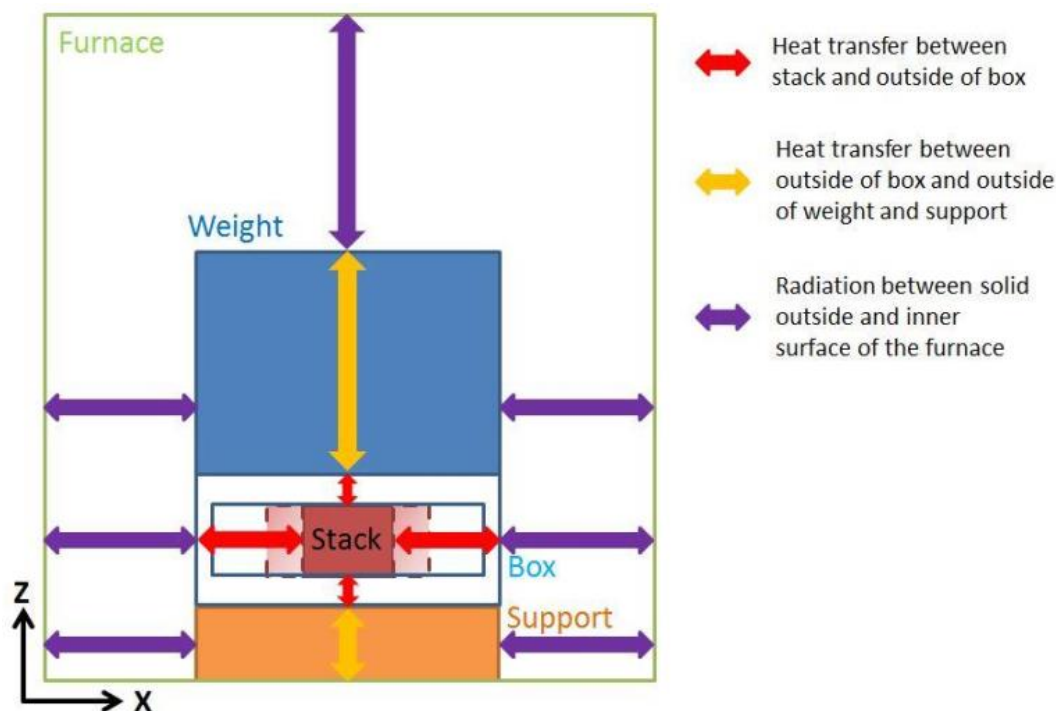


Figure 13: Schematic of the structure of the test rig with the integrated stack and the associated heat transfers between stack and surroundings [72].

Except for radiation, the heat transfer paths in x and z direction is modeled as a series connection of transfer resistances and heat capacities in order to preserve the simplicity of the model. Furthermore, a pressure dependency of the heat transfer through porous insulation materials in x, y or z direction could be neglected due to the operation of the stack within a furnace environment. Note that this aspect can additionally be integrated into the model, as the pressure dependency of the heat transfer through insulation materials significantly affects the simulation accuracy when the model is applied to pressurized non-furnace test environments. Radiation between the solid parts and the outer furnace environment is calculated with the assumption that the furnace area is much larger

than the parts attached to the stack. Consequently, the equation of the radiative heat transfer is implemented into the model via

$$\dot{Q} = \mathcal{E}_i \cdot k_B \cdot (T_{furnace}^4 - T_k^4) \cdot A_i \quad 5.4$$

where k stands for the stack box, the support underneath the stack or the weights on top, \mathcal{E} for the emissivity and k_B for the Stefan-Boltzmann constant. The thermal properties of the stack components and the materials that are implemented in the furnace environment are derived from literature [72,76–78].

5.1.2 Parameterization of the stack model

The experimental investigations of the current thesis were used to obtain several values for the parameterization of the stack model. Since the ESC stack concept was mainly used for the experiments carried out in this thesis, the model is set and validated for this concept. However, the basis for modeling of the CSC stack concept was furthermore laid since the temperature and pressure dependency of the ohmic resistance and the overall ASR was quantified and provided to the literature (see Article IV).

The ohmic resistance was identified as the major loss of the ESC. It was extensively studied in Article I via EIS for operating temperatures between 650-850 °C. Furthermore, the correlation between a theoretical resistance based on the used materials in the stack and the actual measured stack resistance was shown. The temperature dependency of the ohmic resistance was directly implemented into the MEA model via the normalized ASR_{Ω} value in equation 5.1. Furthermore, a possible degradation of the stack can be simulated via the pressure and time dependency of the ohmic resistance as shown and quantified in Article III. However, note that this specific correlation is valid for the experimentally tested operating temperatures, current densities and RC during steam and co-electrolysis modes. Hence, different operating parameters might lead to a different evolution of the time dependent ohmic resistance behavior and degradation.

Several parameters for the equation of the exchange current density related to the Butler-Volmer equation were obtained experimentally. The exponents a and b of the terms of equation 5.2 that describe the partial pressure dependencies were obtained via the electrode resistance during a separate variation of the partial pressures of H_2 and H_2O . The parameters were obtained from the slope within the double logarithmic diagram of the resistance versus the partial pressure.

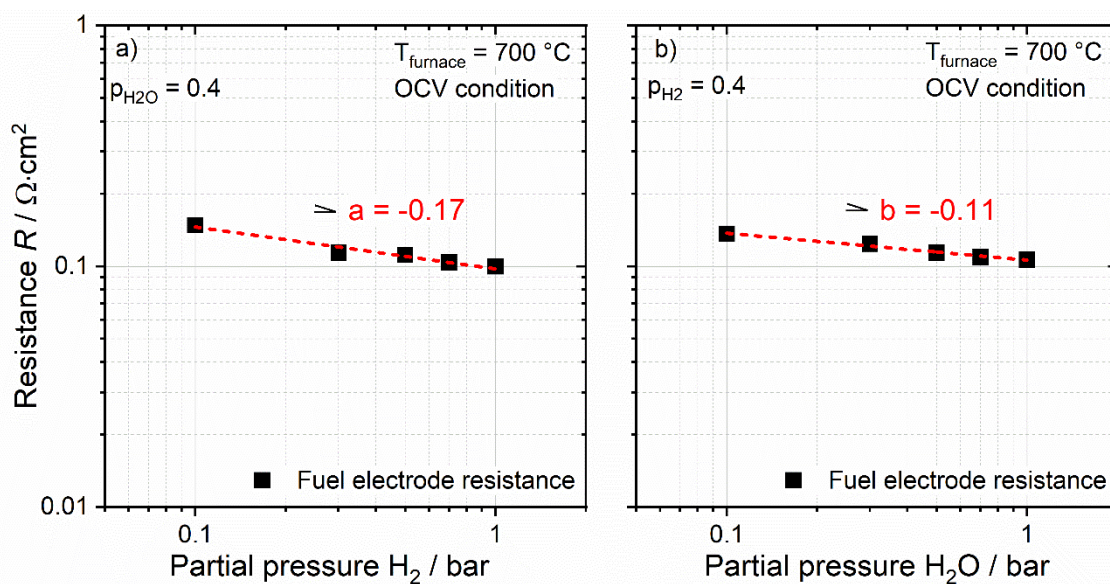


Figure 14: Determination of the a) parameter a as a function of the hydrogen partial pressure and b) parameter b as a function of the steam partial pressure on a double-logarithmic scale. The obtained parameters are used for equation 5.2 and are implemented into the stack model. The linear fits achieved a) $R^2=0.94$ and b) $R^2=0.96$.

The exponent m related to the oxygen partial pressure dependency of the exchange current density was used from literature ($m=0.22$) due to limitations of the pressurized test rig [79]. The behavior of the air electrode and the commonly used LSCF material are well investigated within the scientific literature for the fuel cell and electrolysis operation.

The activation energy of the fuel electrode was obtained via the quantification of the fuel electrode resistance during a temperature variation. The value is reflected by the slope within an Arrhenius approach. Since the activation energy is pressure dependent, it was experimentally investigated at three different operating pressures of 1.4, 4 and 8 bar. The values were fitted to an exponential expression in order to implement the relation via a pressure dependent equation into the model. Consequently, it is assumed that the values of the activation energy follow this expression for operating pressures >8 bar.

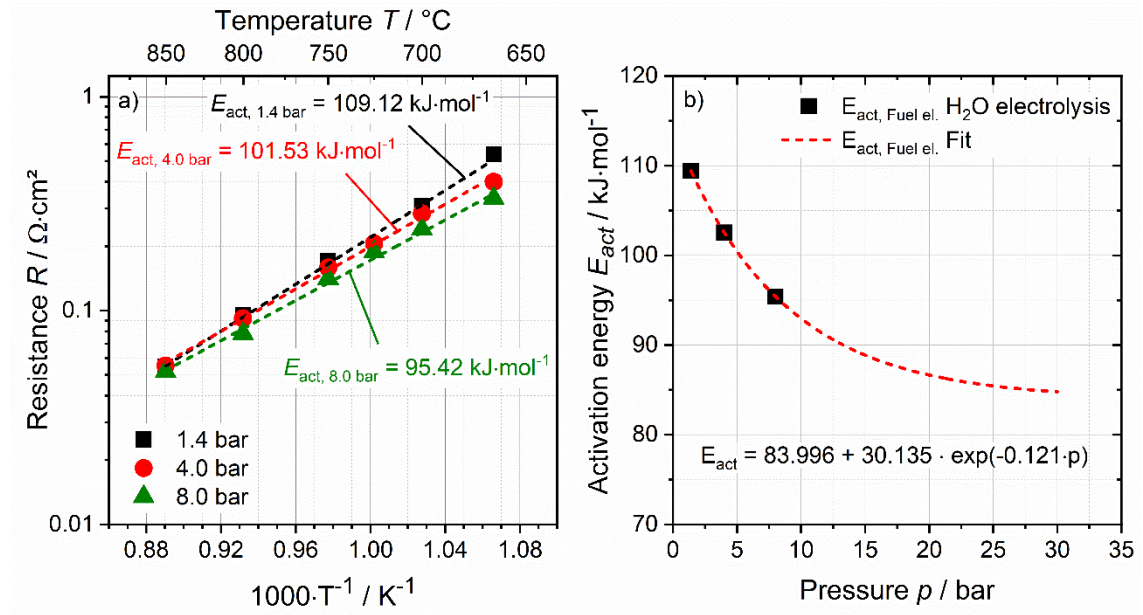


Figure 15: a) activation energies obtained for the operating pressures of 1.4, 4 and 8 bar. b) shows the fit and the corresponding equation associated with the experimentally obtained activation energies shown in a) for a pressure range from 1.4 to 30 bar. The activation energies are implemented into the stack model.

The temperature dependent prefactors γ_{fe} and γ_{ae} of the exchange current densities were determined according to Leonide et al. with the found activation energies for the operating pressures of 1.4, 4 and 8 bar [79]. The charge transfer coefficients α_{FE} and α_{AE} of the Butler-Volmer equation were taken as 0.5, thus assuming reversible reactions.

5.1.3 Simulation results

Figure 16 shows the simulated $U(i)$ -curve for the middle cell of the ESC stack during co-electrolysis operation with an inlet gas composition of 60/30/10 ($\text{H}_2\text{O}/\text{CO}_2/\text{H}_2$) for a) 1.4, 8 bar and b) 30 bar. The furnace temperature of 800 °C and the RC of 70 % are constant throughout the current density range. The simulated data is furthermore compared with the experimentally obtained data shown in Article II.

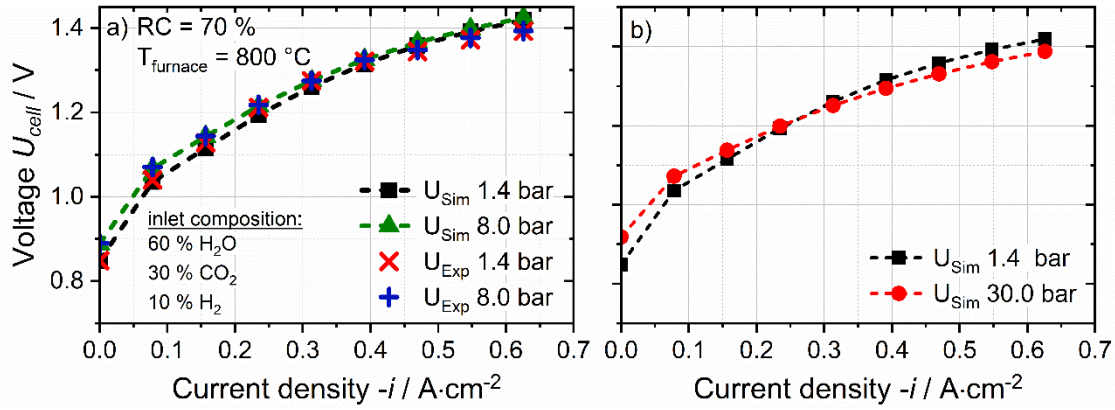


Figure 16: a) Comparison of the simulated and measured voltage behavior of the middle cell of the ESC stack. b) shows the corresponding simulated $U(i)$ -curve for 30 bar.

As can be seen in the diagrams, the voltage behavior of the simulated data is generally in good agreement with the measured values. However, at highly exothermic operation, a slight deviation between the experimentally obtained and simulated voltage is found. This phenomenon can be attributed to a deviation of the simulated stack temperature as discussed below (see Figure 17). However, compared to the simulated voltage at 1.4 bar the voltage reduces by 31 mV at a pressure 30 bar. Note that the stack temperature also changes significantly with pressure and contributes to the decreased voltage (see Figure 17).

Generally, horizontal or vertical temperature profiles within the stack can be simulated with the parameterized stack model in order to determine critical operating conditions or the dynamic changes. Figure 17 shows the temperature profiles within the middle cell for pressures of 1.4, 8 and 30 bar according to the operating conditions shown in Figure 16. The measured temperatures for the operating pressures of 1.4 and 8 bar are furthermore shown within the diagram according to the experiment presented in Article II. For the simulation, the cell length of 90 mm was discretized into ten units and temperature profiles for two steady-state current density points were modeled. The current density of $-0.16 A \cdot cm^{-2}$ corresponds to an endothermic operation mode of the ESC stack at 1.4 and 8 bar whereas a current density of $-0.47 A \cdot cm^{-2}$ is associated with an exothermic behavior. Note that the corresponding voltages for these current density points can be found in Figure 16.

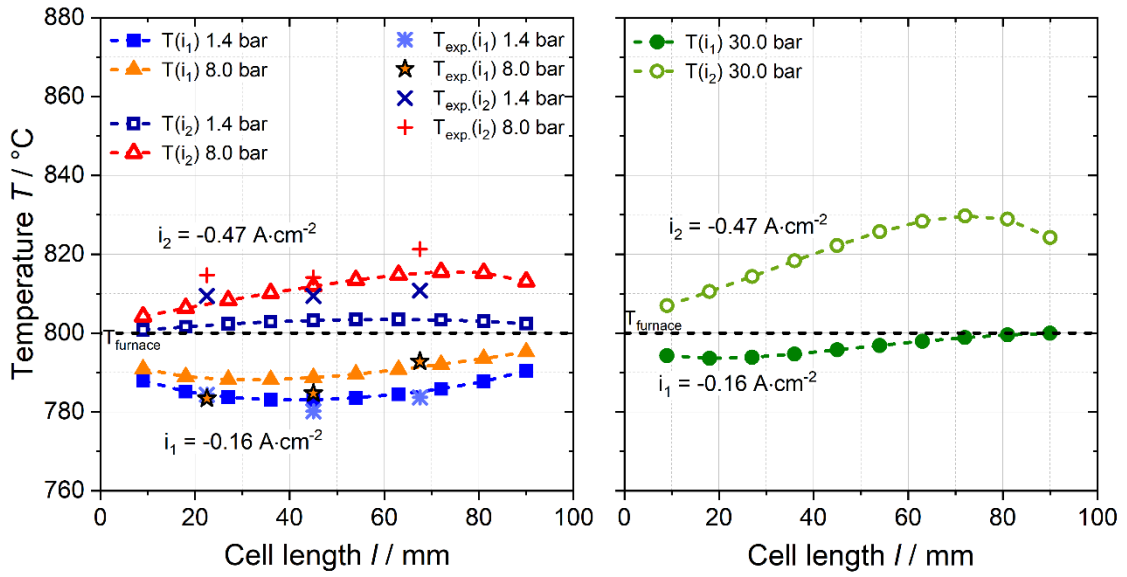


Figure 17: a) temperature profile of the middle cell of the ESC stack during co-electrolysis operation at 1.4 and 8 bar. The cell is discretized into ten units along the length. The simulated data is compared with experimentally obtained temperatures presented in Article II. b) simulated temperature profile of the same cell at a pressure of 30 bar.

As already observed during the co-electrolysis studies of the ESC stack shown in Article II, the decreased voltage at 8 bar is predominantly related to an increased temperature and thus a decreased ohmic resistance. The temperature during the pressurized operation increases due to the occurring exothermic methanation reaction. The simulated temperatures of the stack model are generally in good agreement with the measured values for 1.4 and 8 bar. However, a slight deviation between the simulated and measured temperature data can be observed for the exothermic operation. This phenomenon can be attributed to inaccuracies associated with the heat capacities considered for the materials inside the furnace environment or a poor uniformity of the furnace heating that can consequently lead to slightly different heat transfers. However, the deviations do not lead to qualitatively different results. At a pressure of 30 bar, the operation of the stack at a current density of $-0.16 \text{ A}\cdot\text{cm}^{-2}$ shifts close to a thermoneutral behavior. It can be assumed that the extent of methanation is approximately four times higher than during the operation at 8 bar. In particular, the chosen operating conditions would lead to a methane content of up to 10 % assuming that the gases reach thermodynamic equilibrium as it was already shown for the operation at lower pressures (see Article II and IV). Figure 16 shows that applying a higher current density leads to a more significant temperature gradient along the cell length which might affect the mechanical robustness of stacks over long-term operations.

As a consequence, the successful parameterization and experimental validation of the stack model offers the possibility to investigate operating conditions that go beyond the experimental feasibilities. For instance, the investigation of temperature gradients along the cell or the vertical temperature profile of larger stacks can be investigated in detail and offer a significant value for the safe operation of SOECs. The unique model can thus serve as a basis for the development and optimization of suitable control, operation and integration strategies of pressurized SOEC systems. Consequently, the development and experimental validation of a stack model for the pressurized SOEC operation addressed the identified scientific gap described in section 2.2.

5.2 Article I: Analysis of the pressurized steam electrolysis operation of an ESC stack

5.2.1 Research questions

The research needs identified in section 2.2 about the performance characterization of the ESC stack and the quantification of its dominant cell resistances during the pressurized operation in steam electrolysis with high steam contents in the feed and high electrochemical conversions are addressed within Article I.

The scientific study evaluated the influence of the increased partial pressures of the supplied gases on the behavior of both the cell voltages and the temperatures in the stack. In particular, the temperature behavior and the resulting horizontal and vertical temperature gradients in endothermic, thermoneutral and exothermic operation were examined for the pressurized steam electrolysis mode. The voltage behavior of the ESC stack at elevated pressure was examined in detail since a performance gain could already be observed for CSCs at higher operating pressures in literature [58].

The detailed performance characterization and the influence of the elevated pressure have been quantified in Article I over a wide temperature range using the ASR. This normalized value offers the possibility to compare different stacks under different operating conditions and is furthermore a valuable input parameter for stack and system simulation studies. Since the ohmic resistance was expected to make a significant contribution to the overall resistance of the ESC, a detailed study of its contribution was carried out over a wide temperature range. The quantification of this temperature dependent proportion of the total ASR was directly implemented into the stack model of the current work.

Additionally, the measured ohmic resistance of one repeating unit of the ESC stack was compared with a theoretical one that is based on the resistivity of the used materials. This investigation could indicate the amount of the contact resistances encountered in a stack and could point out perspective paths for improvements.

The long-term stability of a second ESC stack operated close to atmospheric pressure with relevant current density and high steam conversion was investigated. This experiment could serve as a basis for the perspective investigation of the influence of an elevated operating pressure on the degradation behavior. Consequently, a 1,000 hours test was carried out with each proportion of the cell resistance being resolved in detail every 200 hours by means of EIS.

5.2.2 Experimental

Two 10-layer ESC stacks were used in this study. Both were equipped with temperature sensors that were placed according to the description in 4.2.1. One stack was used for the characterization of the pressure influence on the performance via $U(i)$ -curves and the quantification of the above described cell resistances. The second stack was used for the investigation of the long-term stability over 1,000 hours during steam electrolysis operation close to an atmospheric operating pressure of 1.4 bar.

In order to evaluate the influence of an elevated pressure on the voltage and temperature behavior, steady-state and dynamically recorded $U(i)$ -curves were performed. In particular, the steady-state $U(i)$ -curves were used to investigate the resulting horizontal and vertical temperatures in the stack during the endothermic, thermoneutral and exothermic operation. The characteristics were performed according to the description in chapter 4.3.1 with a stepwise increase of the current density. The furnace temperature was 800 °C. The inlet gas composition with high steam content of 90 % (with 10 % H_2) was chosen due to its relevance for perspective system applications. The reactant conversion was 60 % for every measuring point of the steady-state curves that were recorded at 1.4, 4 and 8 bar. Dynamically recorded $U(i)$ -curves were furthermore used for the characterization of the stack and the quantification of the ASR under quasi-isothermal operation. The characteristics were recorded with an increase of the current density of $1.96 \cdot 10^{-3} \text{ A} \cdot \text{cm}^{-2} \cdot \text{s}^{-1}$. The gas flows were defined for a RC of 60 % at $-0.8 \text{ A} \cdot \text{cm}^{-2}$. The stack was operated at the same pressure levels as for the steady-state characteristics and at three temperatures of 750 °C, 800 °C and 850 °C. The ASR values were calculated according to the equation 4.1 by linearizing the dynamically recorded $U(i)$ -curves. The quantification of the

temperature dependent ohmic resistance was carried out via impedance spectra that were recorded close to the open circuit voltage. The resistance was quantified within the temperature range of 650-850 °C. It was ensured that the stack temperature was equal to the furnace temperature. With the help of the quantified ASR and the ohmic resistance values, the polarization resistance was calculated in dependence of the temperature and pressure. For all of the recorded U(i)-curves 1 slpm per cell air was used at the anode sides of the stack.

The long-term steam electrolysis experiment was carried out over 1,000 hours at an operating pressure of 1.4 bar using the second ESC stack of this study. The applied current density was $-0.5 \text{ A}\cdot\text{cm}^{-2}$ with a RC of 70 %. EIS was performed at the same current density for every 200 hours of the experiment in a frequency range of 100 kHz to 50 mHz.

5.2.3 Results and discussion

The characterization of the stack showed a higher OCV at higher pressure and thus a good agreement with thermodynamics' theory. The core temperature of the stack decreased at low current densities due to the endothermic steam reduction reaction. The steady-state curves showed a minimum stack temperature of approximately 782 °C at around $-0.15 \text{ A}\cdot\text{cm}^{-2}$. At a voltage of 1.28 V for thermoneutral operation, the current density showed values of -0.36 to $-0.4 \text{ A}\cdot\text{cm}^{-2}$ depending on the operating pressure. By further increasing the current density, the stack showed an exothermic behavior whereby the temperatures at the maximum operating point of $-0.63 \text{ A}\cdot\text{cm}^{-2}$ reached close to 850 °C. The U(i)-curves recorded at 4 and 8 bar showed a slight decrease of the slope with higher current densities compared to the U(i)-curve recorded at 1.4 bar. Associated is a slight convergence, but a crossing of the U(i)-curves and thus a performance gain was not observed within the investigation of the ESC stack. Consequently, the performance of the stack was shown to be dominantly dictated by the ohmic resistance. Despite the fact that the ESC stack does not show a significant pressure influence on the performance, the electrical power applied for the electrolysis operation at 8 bar is almost the same as at low pressure due to the convergence of the U(i)-curves at high currents. Thus, the advantage of obtaining pressurized hydrogen at the outlet remains.

Figure 18 a) shows the temperature profile in the stack during the recorded steady-state curves. Within the endothermic operating mode, the center cell of the stack was found to be the coldest and the outer layers of the stack to be the warmest. The vertical temperature gradient in the 10-layer stack was 5 K, whereas it was about 10 K in exothermic

operation. Consequently, the horizontal temperature gradient that formed during these experiments was small and thus did not pose a risk to the stack during steam electrolysis. The cell voltages depicted in Figure 18 b) furthermore show the thermal influence of the surrounding furnace that acts as a heat sink during the exothermic operation of the stack. Consequently, the outer layers of the stack showed the highest voltage due to their low temperature when compared to the inner cells of the stack.

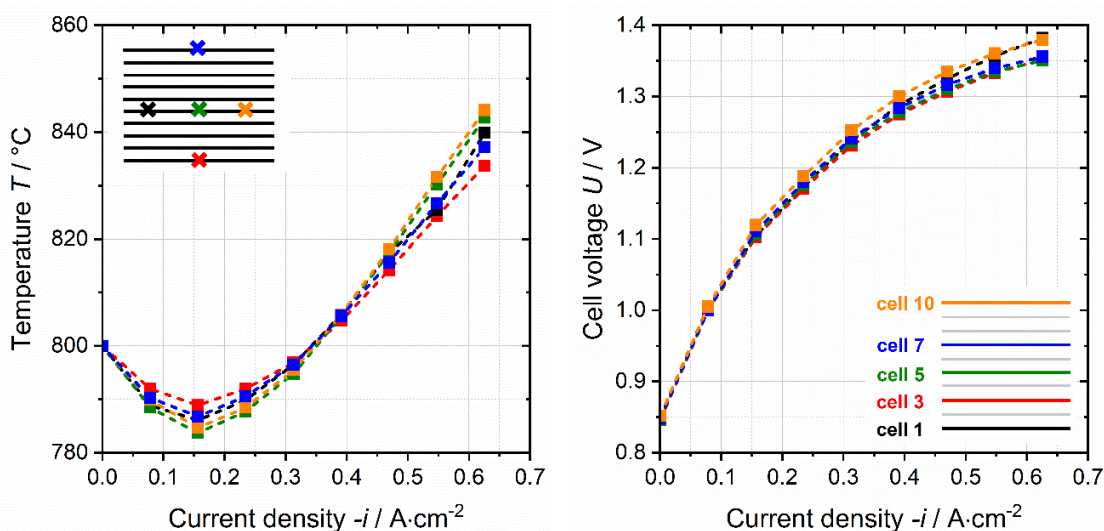


Figure 18: a) temperature distribution within the stack during the steady-state $U(i)$ -curves recorded at 1.4 bar. The sensor location is indicated by the colored crosses in the scheme. b) shows the cell voltages of specific cells of the same experiment. The cells shown in the graph are indicated by colors. [80].

A detailed investigation of the ohmic resistance was carried out via recorded EIS spectra in a temperature range between 650 $^\circ\text{C}$ and 850 $^\circ\text{C}$. The obtained relation of the ohmic resistance followed the exponential expression of $\text{ASR}_\Omega = y_0 + A \cdot \exp(B \cdot T)$. The quantification of this temperature-dependent proportion of the total ASR was furthermore directly implemented into the stack model of the current work (see chapter 5.1.2). Furthermore, values of the ohmic resistance obtained out of impedance spectra recorded at steady-state conditions under current (blue triangles in Figure 19) were compared to the ones obtained from the measurements close to OCV. Under operating conditions, the cells of the stack have a distinct horizontal temperature profile that has a significant impact on their local ionic transport conductivity. However, the steady-state measured points nevertheless fit very well with the temperature dependent ohmic resistance curve analyzed before. Hence, this behavior indicates that the measured core temperature of the ESC stack reflects a good average and can thus be used as the characteristic temperature within the electrolysis mode. This observation could thus be applied to stack modules where multiple stacks are implemented. Instead of measuring temperatures via thermocouples that are generally

implemented and distributed in many stacks, the ohmic resistance value could be used. This opens up a possibility for a significant saving of costs and working time which are incurred for the placement and manual installation of the temperature measurement sensors in large modules.

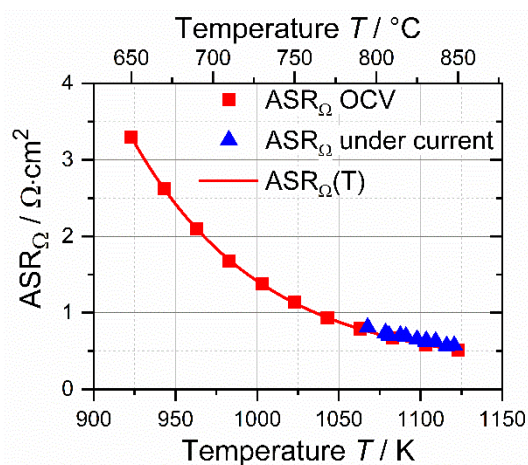


Figure 19: Temperature dependency of the ohmic resistance obtained for the middle cell of the stack. [80].

Since the ohmic resistance was found to have a major influence on the ESC stack performance, it was theoretically analyzed based on the structure and used materials of one repeating unit. Figure 20 a) shows the schematic of the structure and highlights the simplifications for the presented modeling approach. The components with very low total resistivities ($<10^3 \Omega \cdot \text{m}$) are assumed to be negligible and were scored out with diagonal bars. The resistivities of the considered layers are taken from literature (see Article I).

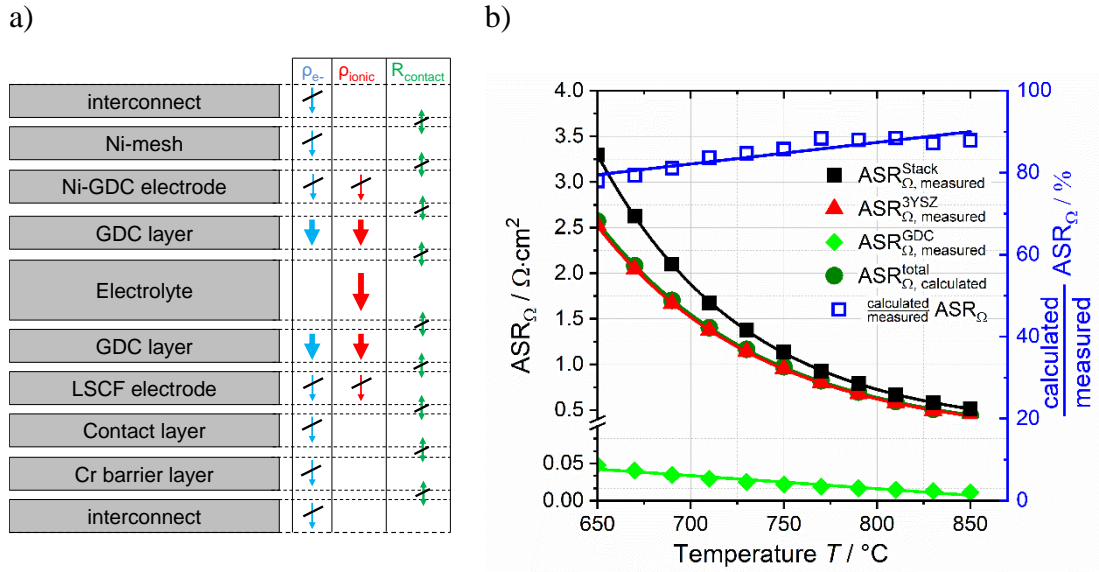


Figure 20: a) Simplified sketch of one single repeating unit of the ESC stack. Arrows represent the electrical (ρ_{e-}) and ionic (ρ_{ionic}) resistivities of each material and the contact resistances (R_{contact}) between each component. Neglected resistivities and resistances for the presented modeling approach are scored out with diagonal bars. b) Comparison between the measured ohmic resistance of one cell of the stack with the theoretical resistance based on the resistivities of the used materials. [80].

It was observed that the experimentally obtained values of the ohmic resistances are higher than the calculated ones of the total ASR. In the considered temperature range from 650 °C to 850 °C a deviation of 15-20 % between the modeled and experimentally obtained ohmic resistance was found. Since contact resistances were not considered in this simplified model, it is likely that the origin of one or more additional resistances in the repeating unit can be attributed to a poor contact between the electrochemically active cell materials and the electronically conductive parts. Consequently, it could be a promising path for perspective improvements of the ESC stack to reduce these additional resistances and thus increase its performance. Additionally, an increased performance can furthermore be obtained by decreasing the electrolyte thickness or using an electrolyte material with higher oxygen ion conductivity (e.g. 8YSZ). However, the mechanical properties must be considered and the robustness of the ESC must be maintained.

Out of the performed dynamically recorded $U(i)$ curves shown in Article I, the ASR values were obtained. The found values are summarized within Table 1. In addition to the successful quantification of the total ASR for different temperatures and pressures, the values show that the largest pressure effect can be observed at lower temperatures. There, the pressure dependent activation and diffusion losses are more dominant than at high temperatures. However, even at the low temperatures, the decrease of the ASR at 8 bar is

not sufficient to compensate completely for the thermodynamic effect of the higher voltage at higher pressure. Consequently, a performance gain at an elevated operating pressure was not observed for either the steady-state characteristics or the dynamically recorded ones.

Table 1: Summary of the obtained ASR values out of the dynamically recorded $U(i)$ -curves for 1.4, 4 and 8 bar.

<u>ASR / $\Omega\cdot\text{cm}^2$</u>	<u>1.4 bar</u>	<u>4.0 bar</u>	<u>8.0 bar</u>
750 °C	1.674	1.615	1.588
800 °C	1.069	1.018	1.003
850 °C	0.681	0.662	0.660

With the information about the temperature relation of the ohmic resistance, the polarization resistances from the dynamically recorded $U(i)$ -curves could be analyzed. Figure 21 shows the significant dependency of the polarization resistances from the operating temperature. As the resistance at 750 °C was approximately $0.5 \Omega\cdot\text{cm}^2$, it was more than halved when the temperature increased up to 850 °C. As already observed within the analysis of the ASR values obtained from the dynamically recorded $U(i)$ -curves, the pressure dependency is more significant especially at lower temperatures. In contrast, the polarization resistance at a high operating temperature showed hardly any pressure dependency.

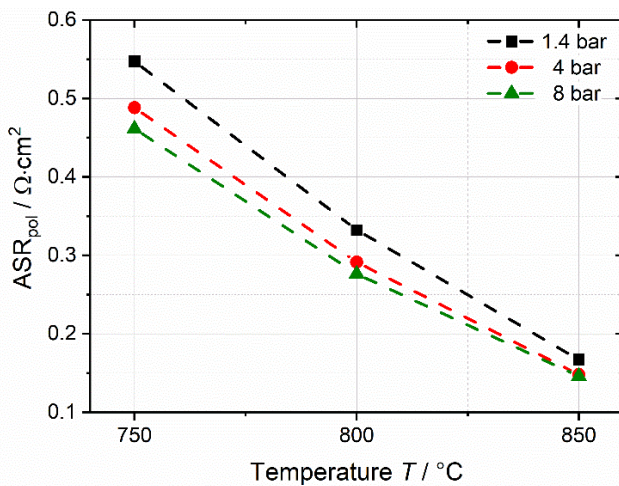


Figure 21: Analysis of the temperature and pressure dependency of the polarization resistances obtained out of the dynamically recorded $U(i)$ -curves. [80].

The second stack of this study was successfully operated over 1,000 hours at 1.4 bar in steam electrolysis and showed a promising low degradation. A detailed analysis of the

results with a comparison to the steam electrolysis operation at 8 bar is presented in Article III. Hence, it is referred to section 5.4.

Consequently, the experimental data on pressurized steam electrolysis presented in this publication significantly complement to the scientific field of electrochemical performance characterization of the ESC stack and the quantification and investigation of its dominant cell resistances.

5.3 Article II: Analysis of the pressurized co- and CO₂ electrolysis operation of an ESC stack

5.3.1 Research questions

The research questions described in section 2.2 that are related to the performance characterization of the ESC stack during the pressurized operation in co- and CO₂ electrolysis are addressed within Article II. Furthermore, the major differences between the steam electrolysis performance investigated in Article I and the co- and CO₂ electrolysis provide scientific knowledge in terms of the electrochemical characteristics that are influenced.

The research questions related to the stack performance are similar to the ones described in Article I. However, the influence of the co-electrolysis operation with two different inlet gas compositions that result in different H₂/CO ratios of the produced synthesis gas were evaluated. In particular, H₂/CO ratios of 1-2 are considered to be of major relevance for Fischer-Tropsch downstream processes [60]. The associated scientific question was whether the stack shows a significantly difference in performance with the different inlet gas compositions or whether the carbon formation limit in the stack restricts the mode of operation under increased operating pressures. Since rWGS reaction and CO₂ reduction have an influence on the thermal behavior of the stack, the horizontal and vertical temperature profiles were investigated during the pressurized co-electrolysis operation. An analysis of the produced synthesis gas evaluated if the thermodynamic equilibrium can be reached at endothermic and highly exothermic operating points for every pressure level.

The major influences of the operating condition of steam, co- and CO₂ electrolysis and the influence of an elevated operating pressure on the electrochemical resistances were determined experimentally. In particular, different hypotheses on the processes taking place during the co-electrolysis operation can be found in literature. From an exclusively and parallel occurring electrochemical reduction of steam and CO₂ up to an exclusively running rWGS equilibrium reaction is reported [43,81,82]. The stack measurements carried out in this study should contribute to provide sound investigations on this particular scientific question. Furthermore, the influence of an elevated operating pressure on the difference between characteristic processes during pure steam and pure CO₂ electrolysis were investigated and quantified.

5.3.2 Experimental

A 10-layer ESC stack was used for the characterization of the pressure influence on the performance under co-electrolysis operation. Steady-state and dynamically recorded $U(i)$ -curves were performed in order to evaluate the performance over a wide temperature range and to quantify the ASR at the pressures of 1.4, 4 and 8 bar. The steady-state $U(i)$ -characteristics were performed according to the description in chapter 4.3.1 with a step-wise increase of the current density of $78.24 \text{ mA}\cdot\text{cm}^{-2}$ and at $800 \text{ }^\circ\text{C}$ furnace temperature. Furthermore, the outlet gas composition at different current densities was analyzed and compared with the calculated thermodynamic equilibrium. Two different inlet gas compositions were used. The first composition consisted of 60 % H_2O , 30 % CO_2 and 10 % H_2 whereas the second one consisted of 45 % H_2O , 45 % CO_2 and 10 % H_2 . With an RC of 70 % and assuming thermodynamic equilibrium at the outlet of the stack, these compositions were expected to lead to H_2/CO ratios of 2 and 1 respectively.

EIS was used to investigate the influence of different proportions of CO_2 in the inlet gas on the resistances that become visible in the impedance spectra. An overall number of five gas compositions was used. Pure steam electrolysis with a 90/10 ($\text{H}_2\text{O}/\text{H}_2$) mixture, co-electrolysis compositions with 60/30/10 and 45/45/10 ($\text{H}_2\text{O}/\text{CO}_2/\text{H}_2$) and CO_2 -electrolysis with 90/10 (CO_2/H_2 and CO_2/CO) were investigated. For the co-electrolysis and the CO_2/H_2 compositions rWGS reaction can occur, whereas for the CO_2/CO mixture electrochemical reduction of CO_2 is ensured. The outlet gas composition of the stack was close to a 60/40 reactant/product mixture where the concentration impedance is highly reduced due to the more balanced composition between reactants and products in the cells. Furthermore, a direct comparison between pure steam and pure CO_2 electrolysis operation was carried out for temperatures of $700 \text{ }^\circ\text{C}$ and $850 \text{ }^\circ\text{C}$ in order to investigate the influence of the operating temperature on the characteristic resistances at two pressures. The impedance spectra were fitted with the ECM described in chapter 4.3.2 in order to quantify and compare the resistances.

5.3.3 Results

The steady-state characteristics with the two predefined co-electrolysis inlet gas compositions (60/30/10 and 45/45/10 $\text{H}_2\text{O}/\text{CO}_2/\text{H}_2$) show comparable cell voltages during operation. A significant pressure effect was not observed with either the steam or the two co-electrolysis mixtures. However, the steady-state characteristics of the co-electrolysis

mode show a more significant convergence of the $U(i)$ -curves at higher operating pressures. A difference in the cell voltage is not observed for current densities $< -0.3 \text{ A} \cdot \text{cm}^{-2}$. Consequently, the electrical energy required at 1.4, 4 and 8 bar is equal. However, this effect was found not to be related to an electrochemical pressure effect, but to the methanation reaction that takes place within the stack. Methanation primarily occurs at high pressures and low temperatures. This exothermic reaction leads to an increased stack temperature and consequently to reduced cell resistances. As shown within Article I, the performance of the ESC stack is strongly associated with the operating temperature due to the high proportion of the ohmic resistance. In addition, the gas analysis carried out for the steady-state characteristics shows a good agreement between the measured gas concentration of H_2 , CO_2 , CO and CH_4 and the equilibrium composition that is calculated on the basis of the measured stack temperature. As expected, a slightly higher methane concentration was shown for the used 60/30/10 ($\text{H}_2\text{O}/\text{CO}_2/\text{H}_2$) mixture due to the higher H_2/CO ratio. Consequently, for a high-pressure operation with a high amount of stack-internally produced methane, the stack is operated at higher temperatures and larger temperature gradients form along the cell lengths. This is in agreement with 5.1.3, where the simulated temperature profile for the co-electrolysis operation at 30 bar is shown. Hence, temperature control strategies such as decreased applied current densities or active cooling via the air side might be required for high pressure co-electrolysis applications.

The comparison of the dynamically recorded $U(i)$ -curves between steam and co-electrolysis show a comparable behavior at both operating temperatures. The voltage shows an almost linear behavior up to the maximum current density with a slightly reduced slope of the $U(i)$ curves that were recorded at increased pressure.

The ASR values obtained from the steady-state and dynamically recorded $U(i)$ -curves were compared with one another for the steam and the two co-electrolysis mixtures. Figure 22 shows that during steam electrolysis operation the ASR follows the characteristic of the ohmic resistance with an additional and temperature dependent resistance.

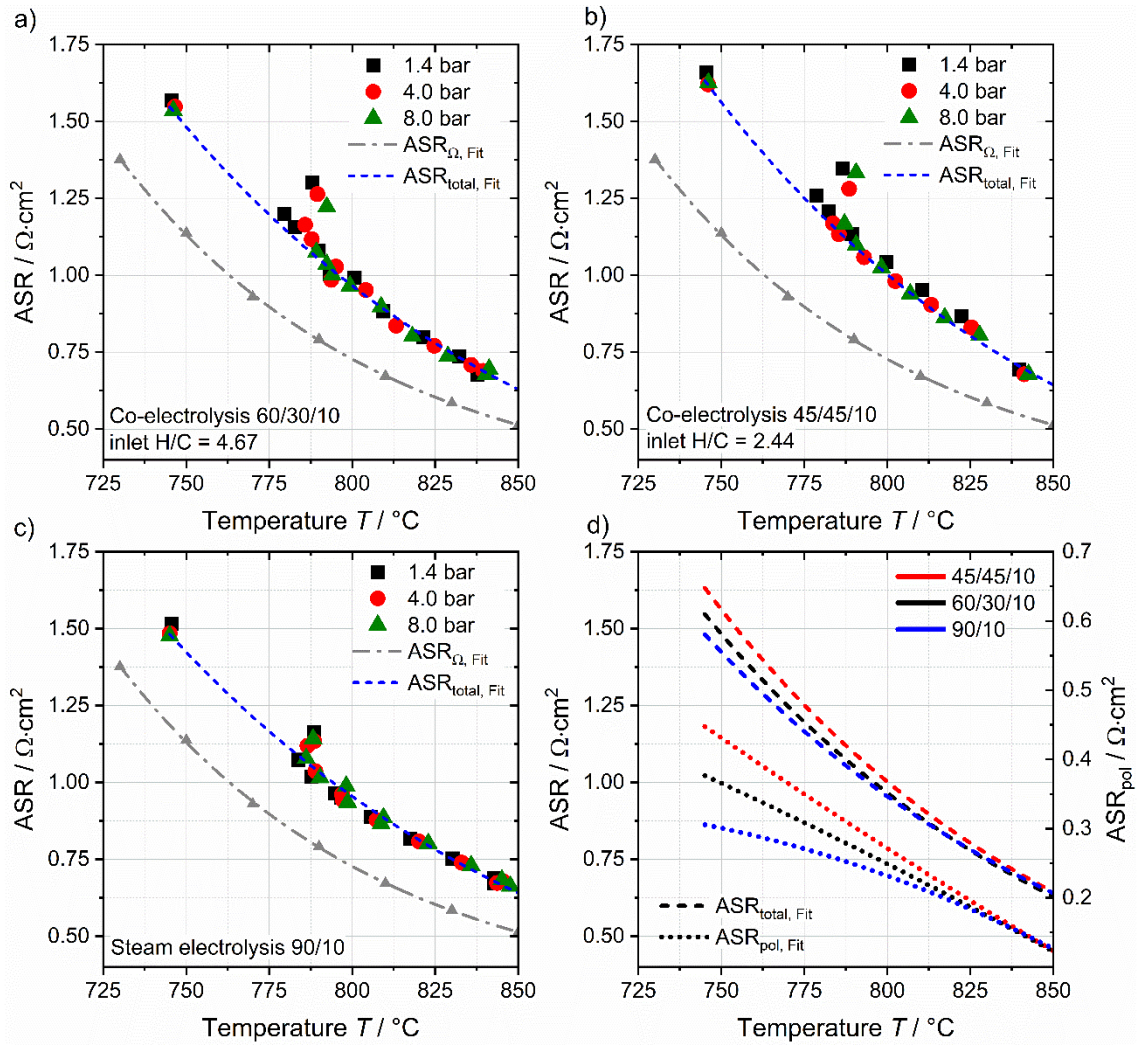


Figure 22: ASR values derived from steady-state and dynamically recorded $U(i)$ -characteristics for co-electrolysis (a), (b) and pure steam-electrolysis (c). (d) shows the fitted ASR curves of a-c. Values of the temperature-dependency of the ohmic resistance are derived from Article I. [63].

This additional part can be attributed to the polarization resistance. Note that the fitted curves shown in Figure 22 have slight inaccuracies due to the fit across different pressures, but are able to elucidate the general trend of the relation of the ASR with temperature. The obtained parameters for the mathematical expression of the ASR ($\text{ASR} = A \cdot \exp(B \cdot T)$) are summarized in Table 2.

Table 2: Summary of the obtained fit parameters for calculating the temperature dependent ASR for steam and co-electrolysis operation of the ESC stack with the equation: $ASR=A \cdot \exp(B \cdot T)$.

<u>ASR / $\Omega \cdot \text{cm}^2$</u>	<u>A · 10³ / $\Omega \cdot \text{cm}^2$</u>	<u>B · 10⁻³ / $^{\circ}\text{K}^{-1}$</u>
Steam electrolysis 90/10	5.05	-7.99
Co-electrolysis 60/30/10	9.52	-8.57
Co-electrolysis 45/45/10	13.63	-8.87

In case of co-electrolysis operation, the polarization resistance shows a higher temperature dependency. At low temperatures, the ASR shows a higher proportion of the polarization resistance while at high temperatures ($>820^{\circ}\text{C}$) a significant difference between steam- and co-electrolysis is not observed. Thus, the increasing partial pressure of CO_2 has a worsening influence on the cell and stack performance during co-electrolysis especially at lower temperatures. An influence of the presence of CO_2 was hypothesized within Article II and was confirmed with EIS measurements shown in Figure 23 and Figure 24.

The recorded EIS spectra of the five gas compositions with steam, co- and CO_2 electrolysis compositions show an apparent influence of the operating pressure. The peak in the $-Z''(f)$ diagram attributable to the concentration resistance at a characteristic frequency of 0.1-0.5 Hz becomes less prominent and shows a decreased frequency at elevated pressure. This can be attributed to a decreasing diffusion resistance. For the detailed explanation of the relationship and the made conclusion, it is referred to the section within Article II.

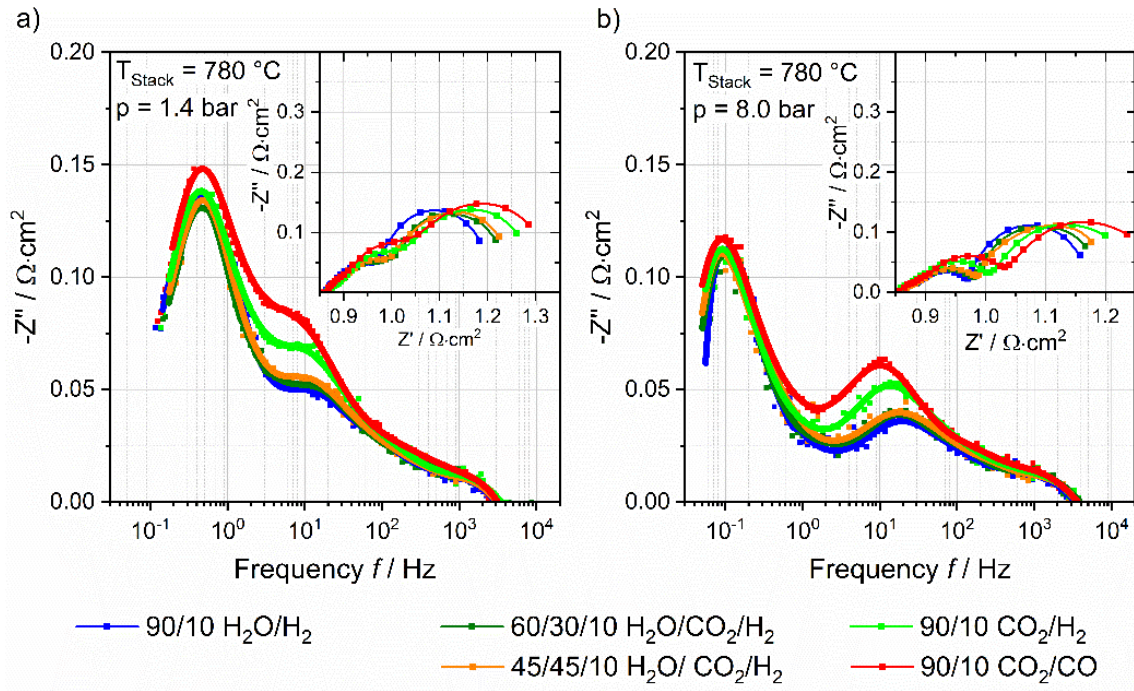


Figure 23: Comparison of five gas compositions for steam, co- and CO₂ electrolysis at 1.4 (a) and 8 bar (b). [63].

The process related to the frequency of 10–20 Hz can be attributed to a surface process at the fuel electrode since it highly depends on the partial pressures of the reactants. With higher pressure the resistance and the characteristic frequency decreases due to the increased concentration of reactants at active sites. Additionally, the peak and the resistance can be observed to get more prominent with an increasing content of CO₂ in the feed gas. Since the activation energy of electrochemical CO₂ reduction is reported to be higher than that for steam reduction, it strongly indicates that CO₂ is reduced electrochemically to some extent during co-electrolysis operation. However, it is shown by the results of Article II that the hypothesis that the main reaction pathway for the production of CO during relevant co-electrolysis operations (for H₂/CO ratios of 1-2) at relevant operating temperatures of the ESC stack via the rWGS reaction is valid.

Since a temperature dependency of the ASR is found to be associated with the CO₂ content in the feed gas for low temperatures, the difference between steam and CO₂ electrolysis was examined for a comparison at 700 °C and 850 °C. At 700 °C the difference between steam and CO₂ electrolysis is significant for both the fuel electrode and the concentration impedance. The difference can be attributed to a more significant diffusion resistance for CO₂ electrolysis operation. At higher pressure the diffusion resistance decreases due to superior mass transport and the peaks are shifted towards lower resistance values and lower frequencies. The fuel electrode process shows higher values for CO₂

electrolysis and consequently a decreased frequency. The decrease of the resistance at elevated pressure was observed to be more significant for the CO₂ electrolysis. This indicates a higher pressure sensitivity during CO₂ electrolysis compared to pure steam electrolysis operation. Note that for the dynamically recorded U(i)-curves presented in Article IV, an increased pressure sensitivity was indeed shown for the CO₂ electrolysis operation.

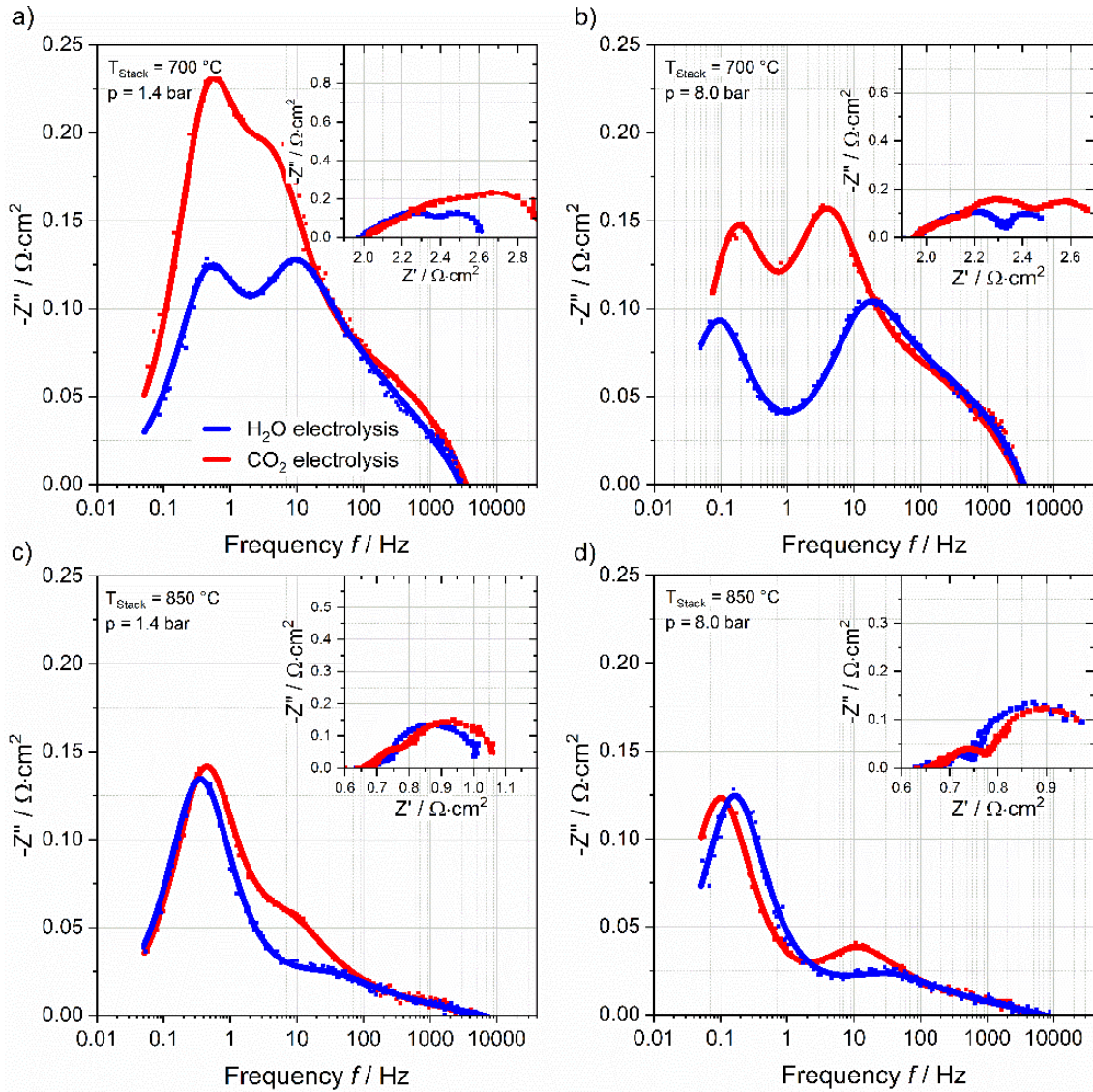


Figure 24: Comparison of EIS spectra during steam and CO₂ electrolysis at 700 °C and 850 °C respectively and 1.4 and 8 bar of pressure. RC is 30 % at a current density of $-0.20 \text{ A}\cdot\text{cm}^{-2}$. [63].

At a stack temperature of 850 °C the observed resistances at 1.4 and 8 bar show lower values due to the generally faster kinetics at higher temperatures. The concentration process is observed to be similar for both steam and CO₂ electrolysis, which indicates an equal diffusion rate of the reactants through the porous layer at these conditions. The frequency of the fuel electrode process shows slightly higher resistances for CO₂ reduction compared to steam reduction at both 1.4 and 8 bar. However, in relation to the total

ASR, the proportion of the fuel electrode process resistance is marginal in both operation modes and at both pressures whereas the concentration part takes almost a proportion of one fourth of the total ASR at 850 °C and at the studied conditions.

To conclude, Article II presents detailed investigations about the performance characteristics during co- and CO₂ electrolysis via steady-state and dynamically recorded U(i)-curves. The influence of the rWGS and methanation reactions on the characteristic stack performance was elucidated. Furthermore, the dependency of the total ASR and the occurring electrochemical processes from the CO₂ content in feed for relevant co-electrolysis mixtures was quantified for a wide temperature range and different operating pressures. The direct comparison between steam and CO₂ electrolysis provided further scientific knowledge about the pressure sensitivity of different operating modes. These findings significantly contribute to the addressed research questions described in section 2.2 for the pressurized co- and CO₂ electrolysis operation of an ESC stack.

5.4 Article III: Analysis of the long-term stability of stacks operated at elevated pressure in steam and co-electrolysis mode

5.4.1 Research questions

The research questions that were addressed by Article III are associated with the long-term stability of ESC stacks under pressurized steam and co-electrolysis operation. Since experimental data on the long-term performance of stacks are highly required for the further development of the SOEC technology and its usability in perspective applications, several scientific institutions are investigating this topic. However, a research gap as discussed in section 2.2 for the pressurized operation was identified, since the longest degradation test that has been published was for about 200 hours where several test incidents occurred. Consequently, a sound investigation about the influence of an elevated pressure on the degradation was missing within the scientific research.

In this study, the degradation rates during pressurized steam and co-electrolysis under constant-current operation was investigated and quantified over durations of $\geq 1,000$ hours. In order to increase the relevance of the obtained results, gas compositions, current densities and reactant conversions were used that have a high probability to be used within perspective SOEC system applications. The influence of the elevated operating pressure on the stability of the cell and stack components was investigated in detail within post-test analyses. In particular, the stacks were investigated with regard to formed oxide layers in the stacks, delamination, contamination or material depletion effects that might have contributed to the observed degradation behavior.

5.4.2 Experimental

In this study, three 10-layer ESC stacks were used that were evaluated via EIS before the beginning of the tests regarding comparable resistances. Constant-current tests at a furnace temperature of 800 °C were performed. Two stacks were used for the investigation of the stability during pressurized steam electrolysis operation at 1.4 (stack A) and 8 bar (stack B) respectively. An inlet gas composition of 90 % H₂O with 10 % H₂ was used with a RC of 70 % and at a constant current density of $-0.5 \text{ A}\cdot\text{cm}^{-2}$. The test at 1.4 bar was examined over a duration of 1,000 hours. The experiment at 8 bar was examined over 2,000 hours whereas a short operation in fuel cell mode was performed in between. The

third stack (stack C) was used for the co-electrolysis experiment over 1,000 hours. In order to compare the performances, the first 160 hours were carried out in steam electrolysis at 1.4 bar with this stack. Subsequently, co-electrolysis with an inlet gas composition of 63.7 % H₂O, 31.3 % CO₂, 3.3 % of H₂, and 1.7 % CO was performed. After 500 hours of testing at 1.4 bar, the operating pressure was increased to 8 bar for the rest of the test duration. The current density and the RC were the same as for the steam electrolysis tests. Furthermore, the outlet gas composition was monitored throughout the test duration.

At the beginning of the tests and several times within the experiments, EIS was carried out at the operating points, in order to evaluate the time-dependent change of the resistances. After the degradation tests, the three stacks were disassembled and the middle cells of the stacks were used for post-test analyses with the help of SEM and EDX.

5.4.3 Results

All stacks showed highly similar resistances according to their respective temperature dependency at the beginning of the tests, indicating a high level of accuracy and repeatability during manufacturing.

Figure 25 shows the test results of both steam electrolysis experiments at 1.4 bar and 8 bar. With the chosen values for the conversion and current density, both stacks were operated exothermically. The diagrams show the increase of the voltage, of the characteristic temperature and of the total ASR per kh. Furthermore, the ohmic resistances received from the EIS measurements are shown in the lower graphs. The depicted polarization resistances ASR_{pol} were thus calculated with the difference between the total ASR and the measured ASR_{Ω} .

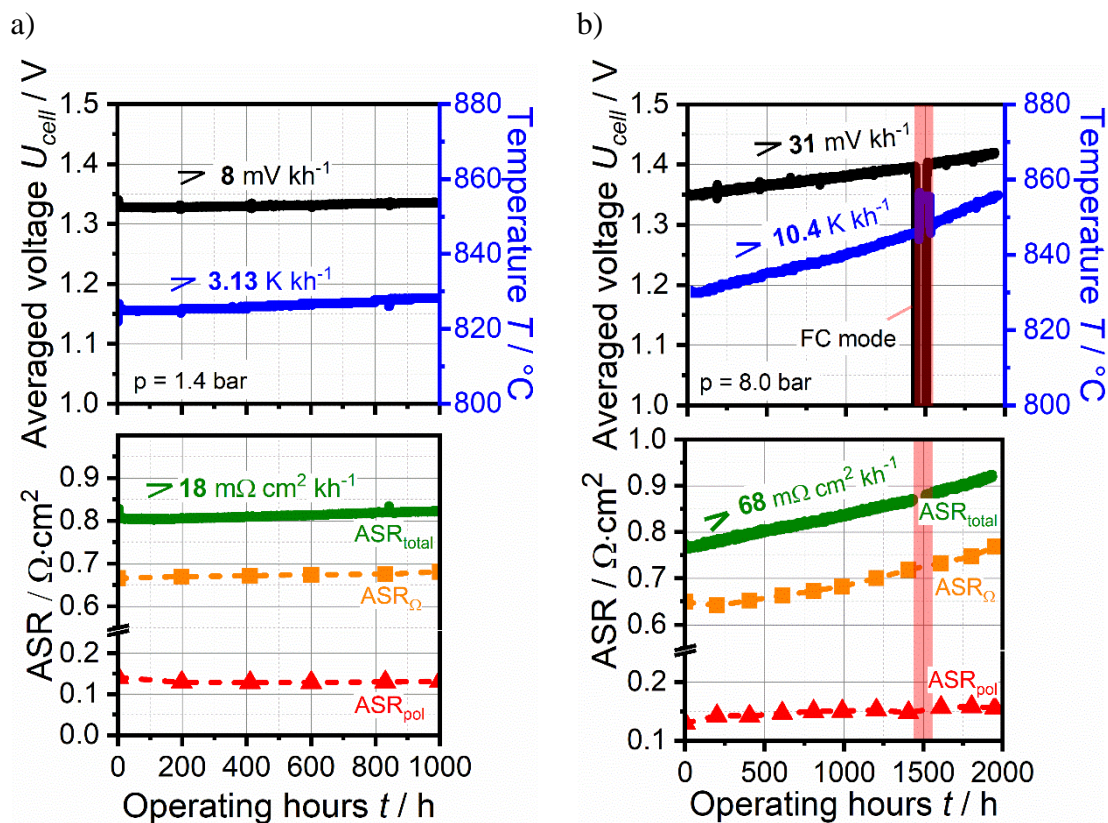


Figure 25: Constant-current steam electrolysis operation over a) 1,000 h at 1.4 bar and b) 2,000 h at 8 bar. [83].

Comparing both experiments shown in Figure 25, it can be seen that the voltage and characteristic stack temperature related to the 8 bar test increased rapidly. The ASR showed a degradation rate almost four times higher compared to the 1.4 bar test. Figure 26 shows the EIS measurements that were regularly recorded during the 1,000 h and 2,000 h experiments. The spectra show a dominant increase of the ohmic resistance in both cases. However, the increase of the ohmic resistance was more apparent within the 8 bar test than at 1.4 bar. Furthermore, the degradation was found to be primarily associated with an increase of the ohmic resistance. In comparison to that, the polarization resistances were hardly affected.

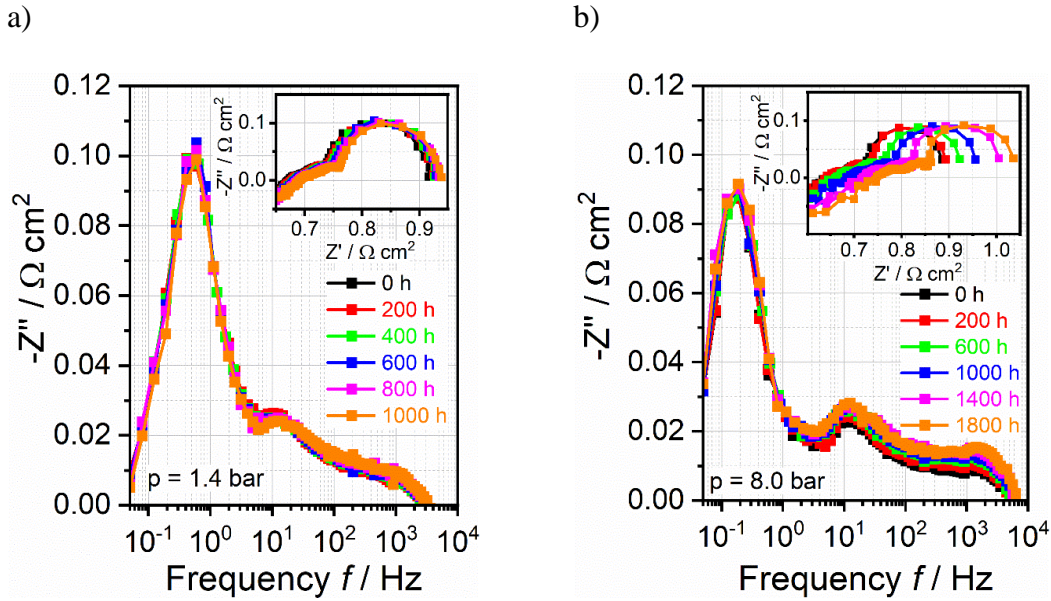


Figure 26: Recorded impedance spectra of the steam electrolysis operation over a) 1,000 h at 1.4 bar and b) 2,000 h at 8 bar. [83].

The observed degradation of stack A is in a similar range to relevant stack investigations at ambient pressure [35,84]. Furthermore, published results about the CSC and the ESC long-term stability at ambient pressure showed that the ohmic resistance predominantly increased [84,85]. This phenomenon can be attributed to considerable oxide layer formation, delamination, contamination or a decreased contact between the electrically and oxide ion conducting materials in the cells. These observations were also made within the post-test analyses of the stacks within Article III, whereas the extents were different in dependence of the operating conditions and test durations.

Within the post-test analyses of the two stacks, the bipolar plates and the electrodes of the middle cells were investigated with the help of SEM and EDX. Apparent formation of oxide layers on the bipolar plates towards the air chambers was observed, with the bipolar plates of the stack operated at 8 bar having oxide layers almost twice as thick as observed for stack A. However, the oxide layer formation is attributable to the duration of the experiment and not to the increased partial pressure of oxygen, since the growth of oxide layers generally follows a parabolic time law in the temperature range of 750-950 °C [86]. Figure 27 shows the cross section of the fuel electrode (Ni-GDC) and partly of the electrolyte (3YSZ) of the stacks that were operated in steam electrolysis at a) 1.4 bar and b) 8 bar. Coarsening and depletion of Nickel are apparent within the fuel electrode of the stack that was operated at 8 bar. Furthermore, a comparably denser layer of Nickel on the surface of the electrode was observed. Since these observations were particularly made

at the inlet of the stack where the partial pressure of H_2O was highest during operation, the results indicate a direct correlation between steam partial pressure and Ni depletion rate. The mobility of Nickel can most likely be attributed to the occurring hydroxide species $\text{Ni}(\text{OH})_2$ whose concentration shows a linear dependency on the partial pressure of steam. Consequently, the mobility of Nickel increases with the operating pressure and leads to the observed depletion within the fuel electrode operated at 8 bar. The loss of Nickel in the porous electrode can furthermore lead to the observed increased ohmic resistance since the ionic conduction pathway of the O^{2-} ions becomes longer. This effect was also shown in literature for Ni-YSZ electrodes before [87–89].

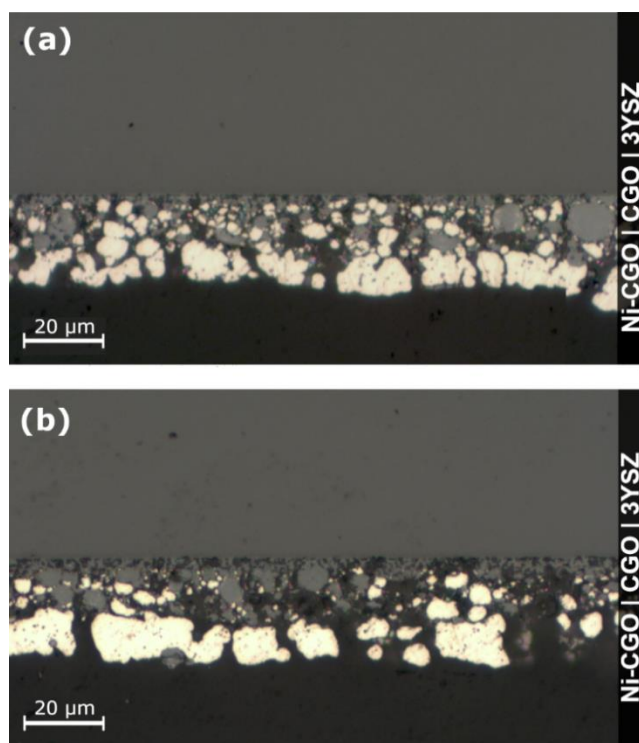


Figure 27: Cross section showing the fuel electrode and electrolyte of the stacks that were operated at a) 1.4 bar over 1,000 h and b) 8 bar over 2,000 h. [83].

Furthermore, a partial delamination of the air electrode was observed particularly at the outlet of the stack that was operated at the highest pressure for 2,000 hours. Although this delamination could significantly contribute to the observed degradation behavior, it could not be confidently attributed to the operating conditions, since it may have occurred during the disassembly of the stack.

The third stack used in this study (stack C) was initially operated in steam electrolysis mode at 1.4 bar and showed a similar degradation as the operation of stack A within the first 160 hours. The degradation was found to increase noticeably within the subsequent operation over 500 h in co-electrolysis mode at 1.4 bar. The ohmic resistance was

identified again to be the dominant cause of the performance loss. Furthermore, the co-electrolysis operation at an elevated pressure of 8 bar showed that the degradation increases. However, the stack failed after a total operating time of 930 h due to a steam starvation incident that caused a detrimental increase of the ohmic resistance. Figure 28 a) shows the experimental results with the voltage, temperature and quantified ASR development for the co-electrolysis operation.

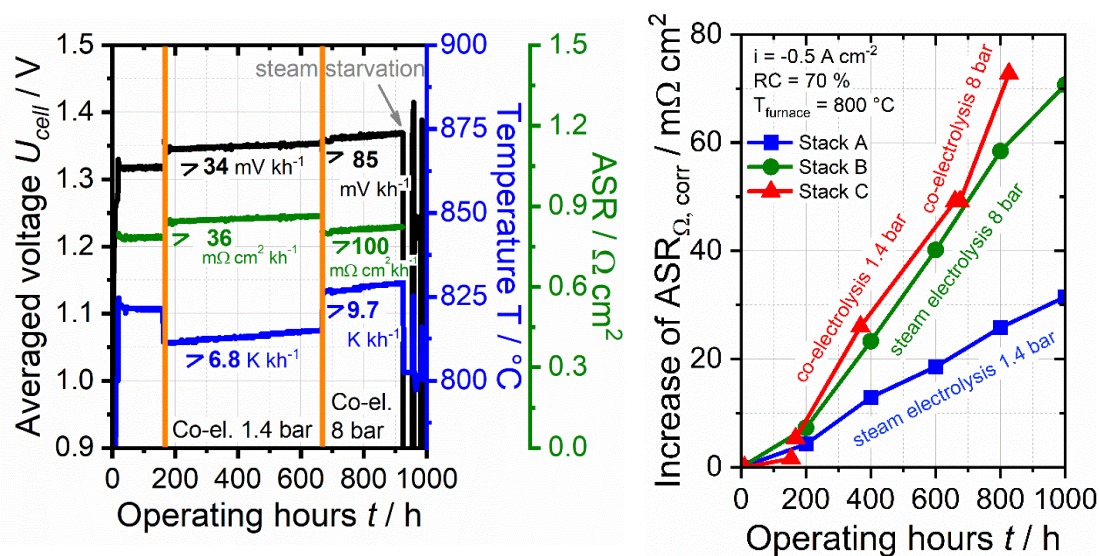


Figure 28: a) Constant-current operation in steam and co-electrolysis mode over 1,000 h at 1.4 bar and 8 bar. b) Overview of the temperature corrected increase of the ohmic resistance observed for the three independently operated stacks. [83].

Figure 28 b) shows the development and a direct comparison of the normalized ohmic resistances of the three independently operated stack experiments. Due to the slightly different operating voltages and different degradation rates, the ASR $_{\Omega}$ development was temperature corrected in order to obtain a sound comparison. Consequently, the experiments indicate a significantly pressure dependency of the degradation behavior. Furthermore, the results indicate a negative influence of the used CO $_2$ or CO on the long-term performance. A higher degradation during co-electrolysis operation has already been observed within single cell and stack tests and was ascribed to additional contaminants like sulfur which can be brought in by the carbonaceous gas leading to an inactivation of the catalyst [90–92]. The possible contamination brought in by the CO $_2$ or CO feed was identified as a topic for perspective research needs.

To conclude, Article III shows the degradation phenomena of three identically constructed stacks that were operated at different pressurized conditions. These tests thus represent the first experimental results about the long-term stability during relevant

pressurized electrolysis operations. The results showed that higher operating pressures lead to a higher degradation and that co-electrolysis has furthermore a detrimental effect on the stack stability. Correlations between the steam partial pressure and Ni depletion as well as increased oxide layer formation with test durations were obtained. Overall, the ohmic resistance was found to be the most dominating cell resistance that contributes to the performance loss. However, an increased number of experiments with post-test analyses have to be conducted in order to reproduce the results shown in this Article and in order to increase the statistical significance. Nonetheless, the experiments and analyses carried out in this article addressed and helped to fill the scientific gap described in section 2.2 about the stack stability during pressurized electrolysis operations.

5.5 Article IV: Comparison of the performance of stacks with different cell concepts at elevated operating pressure

5.5.1 Research questions

As described in section 2.2, extended research needs were identified for the comparison of the pressure influence on the performance and characteristic cell resistances of stacks using different cell concepts. Hence, these research questions were addressed within Article IV.

Stacks with either electrolyte supported or fuel electrode supported cells were investigated and were compared during pressurized steam, co- and CO₂ electrolysis operation. The experiments carried out with the ESC stack were intended to show whether the results agree with those of the steam and co-electrolysis shown in the Articles I and II and thus reflect the reproducibility and accuracy during the production process of the cells and stacks. This attribute is of major interest of the SOC technology suppliers since similar stack performances are important for efficient operating strategies of large modules containing multiple stacks. The stack with fuel electrode supported cells, referred to as CSC stack, was provided by Forschungszentrum Jülich. Its investigation is the first scientific study at elevated pressure. Hence, the main purpose of this work was to provide experimental data about the quantified temperature and pressure dependent ASR and the general performance data associated with the CSC stack architecture. The impedance study and the direct comparison of the recorded spectra provides scientific knowledge about the influence of an elevated operating pressure during steam and CO₂ electrolysis related to the different cell concepts and electrode materials used within both stack types. Furthermore, the results provide the basis for perspective stack and system modeling activities associated with the CSC concept where experimental data are crucial for the reliability of the simulation results.

5.5.2 Experimental

The structure, the sensor equipment and the integration into the test rig of both stacks can be found in chapter 4.2. In order to investigate the pressure influence on the performance, steady state U(i)-curves were carried out in steam and co-electrolysis with both stack types. A fuel gas flow for a constant RC of 70 % at each current density point was used. Steam electrolysis operation was performed with an inlet gas composition of 90/10

(H₂O/H₂), whereas co-electrolysis operation was performed with an inlet gas composition of 60/30/10 (H₂O/CO₂/H₂). Due to thermal operating limits of the stacks, the CSC type was operated at a furnace temperature of 750 °C whereas the ESC stack was operated at a furnace temperature of 800 °C.

For the dynamically recorded U(i)-curves the fuel gas flows were set according to a RC of 70 % at a current density of -0.75 A·cm⁻² for each gas composition. Due to a current ramp of -0.16 A·cm⁻²·min⁻¹ a quasi-isothermally recorded U(i)-curve was performed with each stack. In order to quantify the ohmic resistance of the CSC stack, impedance spectra were recorded close to OCV conditions in a temperature range from 650 to 820 °C. The furnace temperature was increased in 20 K steps.

The impedance measurements for analyzing the differences during the performed electrolysis modes were recorded galvanostatically at -0.2 A·cm⁻² and a current amplitude of 0.38 A. For all experiments a constant air flow of 1 slpm air per cell was used for the air side of the stacks.

5.5.3 Results

The observed ohmic resistance of the CSC stack is shown in Figure 29 a) together with data of the ESC stack published in Article I. Due to the thinner electrolyte and the enhanced oxide ion conductivity of the 8YSZ material, the CSC shows a significantly lower ohmic resistance. Thus, the temperature dependency of this loss contribution is limited whereas it is predominant for the ESC stack.

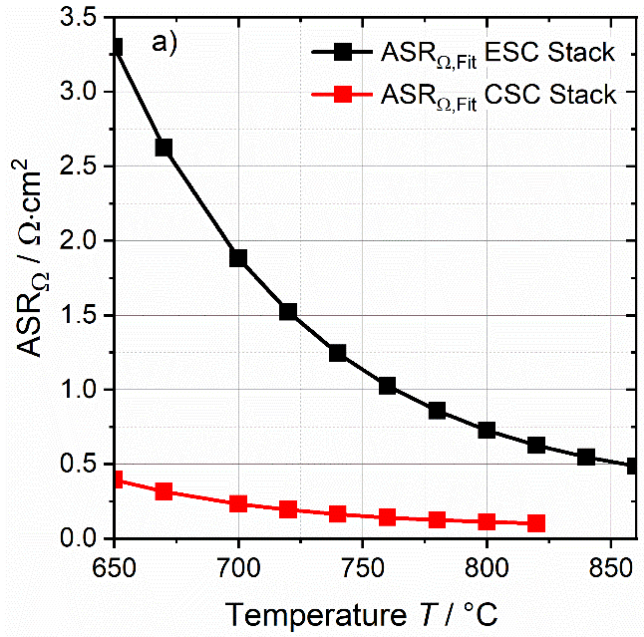


Figure 29: Characterization of the ohmic resistance of the ESC and CSC stacks. The values were obtained from impedance measurements at 1.4 bar for the middle cell of each stack. Data of the ESC can be found in Article I. [69].

The comparison of the pressure influence on the performance of each stack during different electrolysis modes shows that the overall performance is significantly different due to the different cell types. A performance gain that is reflected by crossing $U(i)$ -curves was observed for current densities lower than $-0.5 \text{ A} \cdot \text{cm}^{-2}$ in case of the CSC stack whereas a significant pressure influence on the ESC stack was not observed. Furthermore, the achieved current density of the CSC stack is almost twice as high as for the ESC stack although both stacks were operated at close to their system relevant operating temperatures. During the performed co-electrolysis operation, the gas analysis showed that the outlet gas compositions of the stacks are in good agreement with the thermodynamic equilibrium and methane contents of up to 7% at a pressure of 8 bar were found.

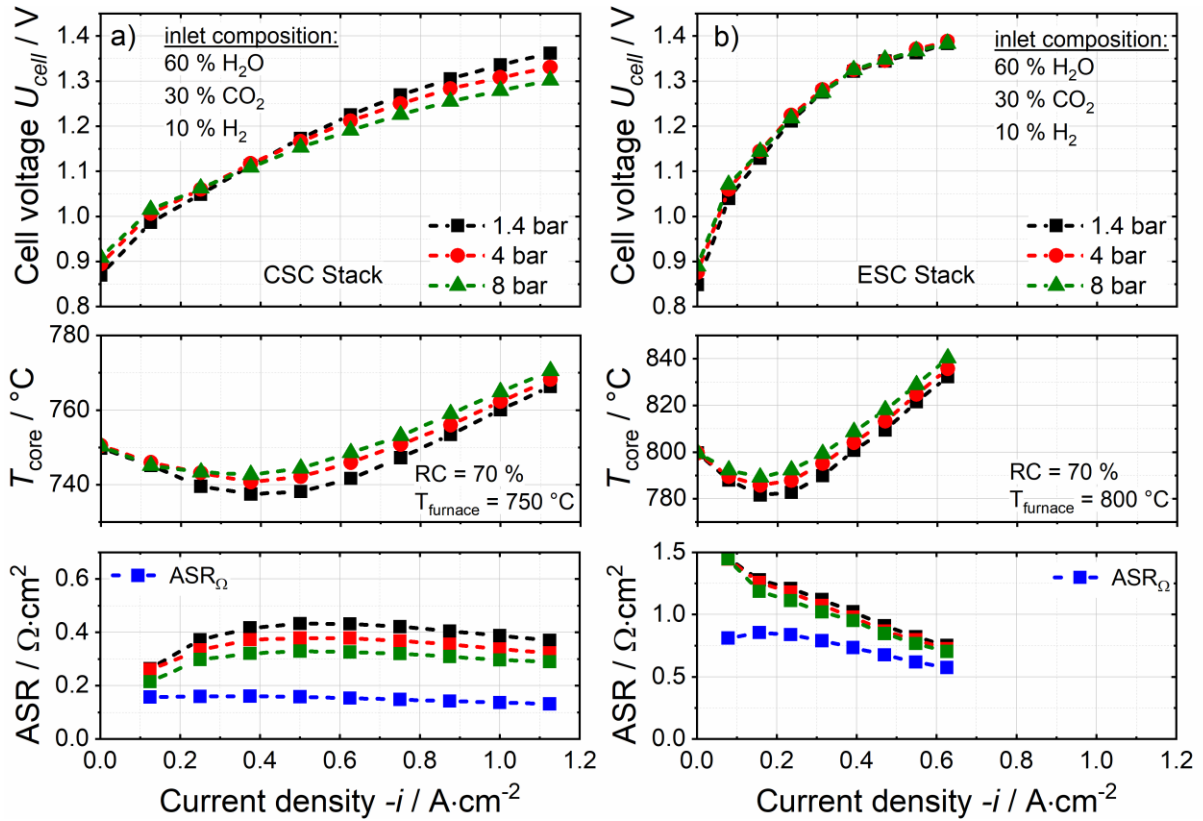


Figure 30: Steady-state $U(i)$ -curves recorded for the co-electrolysis operation for a) the CSC stack and b) the ESC stack at 1.4, 4 and 8 bar. Inlet gas composition is 60/30/10 ($\text{H}_2\text{O}/\text{CO}_2/\text{H}_2$) with a reactant conversion of 70 % at every measuring point. [69].

The increase of pressure from 1.4 bar to 8 bar leads to a decrease of the ASR of the CSC stack of approximately 20 % at the highest current density point. Out of the performed steady-state and dynamically recorded $U(i)$ -curves, a temperature and pressure dependent ASR relation was quantified for 1.4, 4 and 8 bar. The values were fitted to an exponential expression that can be used as an input parameter for stack and system studies of both stack architectures. The parameters can be found in table 2 of Article IV. The pressure effect on both the CSC and the ESC stack was found to be more prominent at lower temperatures and can thus be ascribed to the more prominent kinetics and the consequently more prominent polarization resistances.

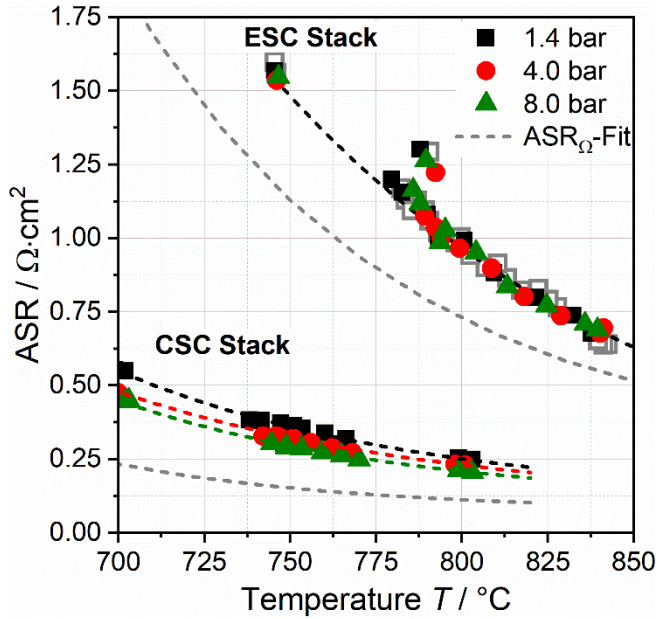


Figure 31: Temperature and pressure dependent total ASR of the CSC and the ESC stack. The ASR of the ESC stack is plotted jointly with values obtained with a different but identically constructed stack used in Article II (unfilled squares). [69].

The dynamically recorded $U(i)$ -curves carried out with both stacks show that the resistance increases by adding CO_2 into the feed. Particularly, the operation of the CSC stack under pure CO_2 -electrolysis shows a more significant bending of the $U(i)$ -curve at high voltages for a $\text{RC} \geq 45\%$. This phenomenon is attributable to a higher diffusion resistance since CO_2 and CO have a larger molecular size and molecular mass than H_2O or H_2 that can lead to more significant mass transport limitations. Furthermore, it is shown by the quantified ASR values that the pure CO_2 electrolysis operation shows an increased pressure dependency when compared to the pure steam or co-electrolysis operation for this stack type. However, a more prominent pressure dependency during CO_2 electrolysis was observed for both the CSC and the ESC stack. This could indicate the existence of a significant different electrochemical reaction mechanism during the reduction process. Hence, EIS was performed in order to investigate the cell resistances of both the CSC and ESC stack during pressurized steam and CO_2 electrolysis mode. Due to the variety of fuel gases used, it was possible to assign the observed peaks in the $-Z''(f)$ diagrams to concrete processes. The EIS spectra related to the CSC stack show that the fuel electrode surface process is located in a frequency range around 10^3 Hz. Thus, this process is found to be located almost two magnitudes higher in frequency than for the ESC stack with its Ni-NGO fuel electrodes. The influence of pressure that leads to a reduced resistance of the fuel electrode process as a consequence of an increase of reactants present at the triple-phase boundary can be shown for the steam electrolysis mode of the CSC (see Figure 32

a and b). However, the same process does not show a significantly reduced resistance during pressurized CO₂ electrolysis. It is hypothesized that this phenomenon indicates a different and less pressure-influenced rate-determining step within the reduction mechanism and/or that adsorption/desorption rates of CO₂ or CO at the TPB significantly differ from the H₂O/H₂ operation for Ni-YSZ electrodes. However, due to the large cell area in a stack, mechanistic details are highly difficult to be elucidated with EIS since temperature gradients, distinct current density and flow distributions generally occur. Nonetheless, the indication of a different electrochemical mechanism for the Ni-YSZ and Ni-CGO fuel electrodes was identified as a topic for perspective research needs. It might be investigated in more detail with segmented cells or even segmented stacks and can thus provide significant scientific knowledge about this specific electrochemical process in dependence of the used material.

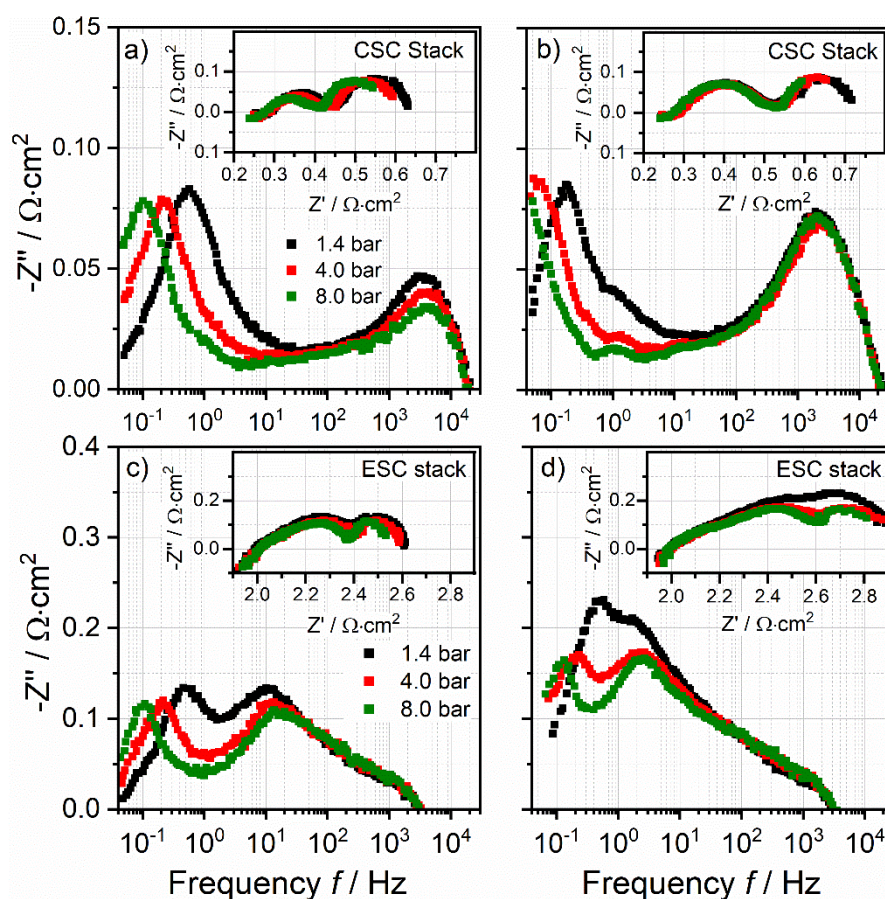


Figure 32: EIS spectra of the CSC during a) pure steam and b) pure CO₂ electrolysis at pressures of 1.4, 4, and 8 bar at 750 °C. c) and d) show the same experiment for the ESC stack at a temperature of 700 °C. [69].

The diffusion resistance is observed to be significantly influenced by both the operating pressure and the type of fuel gas used for the CSC stack. In contrast, the fuel electrode peak of the ESC stack shows a significant decrease indicating a significantly decreasing

electrode resistance during both the steam and CO₂ electrolysis operation. Furthermore, the peak attributed to the gas diffusion and conversion resistance is not affected significantly by pressure. Consequently, the increased pressure effect during CO₂ electrolysis which was evaluated and quantified during the dynamically recorded U(i)-curves of both stacks can possibly be attributed to the diffusion process in case of the CSC stack and possibly more to the fuel electrode process in case of the ESC stack.

To conclude, the research need described in section 2.2 was addressed in Article IV by operating a CSC stack type from Forschungszentrum Jülich for the first time under elevated operating pressures in electrolysis mode. The performance and electrochemical behavior were compared with the ones of the ESC stack. The performances of both stack types were apparently different during steam, co- and CO₂ electrolysis. The CSC stack furthermore showed significantly higher achievable current densities than the ESC stack. Furthermore, a performance gain was achieved with the CSC during its operation at elevated pressures. The total ASR and the ohmic resistance were quantified over a large temperature and pressure range and can thus be used as input parameters for subsequent stack or system studies. The EIS analyses showed considerable differences of the fuel electrode mechanisms between the Ni-YSZ (CSC stack) and Ni-CGO (ESC stack) electrodes during steam and CO₂ electrolysis mode. This aspect furthermore opens up a field for future research activity on the electrochemical mechanisms that occur in different cell types and under different electrolysis modes.

5.6 General context of the results

The results of the Articles I-IV are placed into the general context of the current SOC research within this chapter.

The presented experimental results have shown previously unknown pressure effects for SOC stacks with different cell concepts under various operating modes. At elevated pressure, the ESC stack performance was hardly influenced whereas the CSC stack showed a considerable performance gain. This observed behavior can be used to describe the influence of the elevated operating pressure on the ESC and CSC stack performance in terms of efficiency. Figure 33 shows the pressure dependency of the voltage efficiency η_U for steady state operations in steam and co-electrolysis mode with 70 % conversion for both cell concepts. The calculated efficiencies are based on the resulting temperatures for current densities that lead to similar voltages of the ESC and CSC stack for an endothermal, exothermal and close to thermoneutral operation (CSC: 720-780 °C, ESC: 790-850 °C, see Articles II and IV). The voltage efficiency is calculated by dividing the reactant conversion dependent ideal Nernst voltage ($U_{\text{Nernst, avg}}$, see chapter 4.3.1) by the measured voltage.

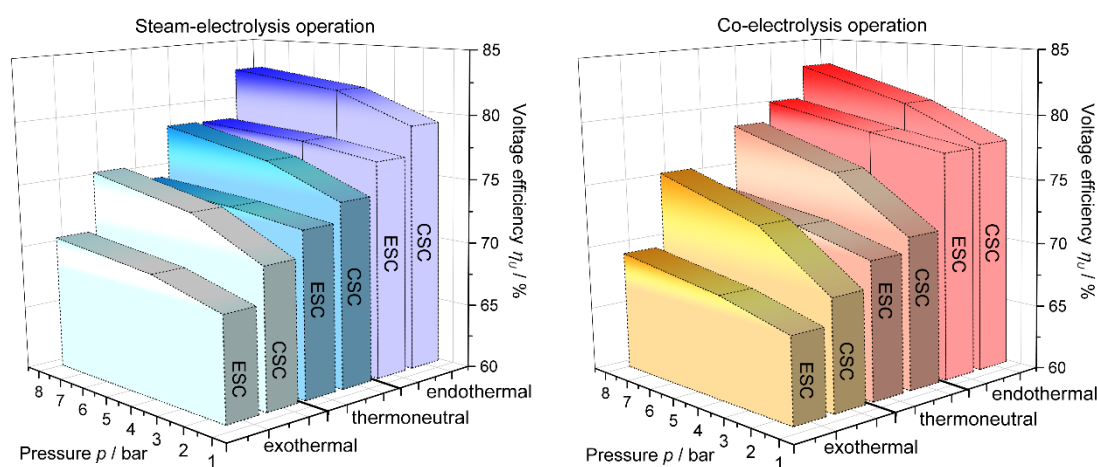


Figure 33: Pressure dependency of the voltage efficiencies of the ESC and CSC stack for an endothermal, exothermal and close to thermoneutral operation during steam and co-electrolysis.

Within the endothermic operating regime, the generally low cell voltages lead to high voltage efficiencies whereas an increased current density and the related more exothermic operation leads to decreasing voltage efficiencies. Furthermore, the CSC stack shows generally higher efficiencies than the ESC stack due to its significantly lower operating temperature and lower ohmic loss. Hence, a low stack voltage in combination with a low operating temperature is favorable for high voltage efficiencies of SOCs. Compared to

steam electrolysis, the endothermic rWGS reaction can additionally reduce the stack temperature. However, a low operating temperature in the pressurized co-electrolysis mode leads to increased exothermic methanation and, in turn, to increased stack temperatures and thus to reduced voltage efficiencies. Furthermore, compared to the steam electrolysis operation, the CSC stack exhibits slightly higher voltages at low pressures in co-electrolysis mode due to increased activation and diffusion resistances that consequently lead to reduced voltage efficiencies. Hence, the dominance of the different effects of operating pressure, occurring rWGS or methanation reaction and stack temperature on the voltage efficiency highly depends on the current density and thus the operating regime of an SOC stack. However, within both steam and co-electrolysis modes, it is shown that the influence of an increased operating pressure on the voltage efficiency is more significant for the operation of the fuel electrode supported cell concept.

Within the current thesis, the degradation rates investigated with the ESC stack were found to increase considerably with higher steam and oxygen partial pressures. Hence, by using the existing SOC materials and cell and stack structures for the pressurized operation, several challenges have been identified.

However, a possible option for adapting existing SOCs for an increased benefit during the pressurized operation can be the usage of a reduced electrolyte thickness or an electrolyte material with increased ionic conductivity. Both would lead to a lower pressure independent ohmic resistance and thus an increased benefit due to more prominent activation and diffusion resistances. As identified for the ESC within Article I, a considerable proportion of contact resistances contribute to the total ohmic resistance, thus offering potential for perspective improvements and increased benefits when operated under pressure.

A challenge by adapting existing SOCs for the pressurized operation was identified to be related with the degradation behavior. Generally, impurities represent an important aspect for the degradation of SOCs within both the atmospheric and the pressurized operation. The post-test analyzes of the fuel electrodes carried out in Article III found silicon, which is known to contribute significantly to the degradation of SOCs. The origin of this species is not yet clearly identified, but there is a high probability that a high proportion originates from the used glass sealings that are placed around the cells and flow channels within the stack. The used liquid water or components of the pressurized test rig could have been excluded as major silicon sources. For the pressurized operation with high partial

pressures of steam, the usage of other type of glass sealants with lower content of silica might be necessary in order to circumvent or reduce the silicon contamination of the fuel electrode and its impact on the degradation behavior [93]. The co-electrolysis operation carried out within Article III showed a higher performance loss compared to steam electrolysis operation. As already stated in literature, sulfur impurities that likely originate from the used CO₂ or CO gas at ppb level can trigger this accelerated degradation as it adsorbs and occupies parts of the reaction surface area of the fuel electrode [91,94]. It can be assumed that for pressurized operation, the higher partial pressure of the specific sulfur containing gas and therefore the increased proportion of pollutants in the electrode compartment lead to a larger deactivated surface area. Hence, an effective desulfurization of the inlet gases is necessary especially for pressurized co-electrolysis operations.

However, one of the predominant degradation phenomena in SOECs that have been observed in literature and which was found within the current thesis to become more significant under elevated operating pressure is the coarsening and depletion of metallic nickel within the fuel electrode. In addition, the degradation of the SOEC operation caused by Ni coarsening has been shown in literature to be highly dependent of other operating parameters such as temperature, current density or fuel electrode overpotential [95]. Hence, a possible option is to operate the electrolyzer within part load regimes and/or at lower temperature in order to decrease the Ni mobility and thus increase the long-term stability. However, this operation strategy might lead to a lower efficiency of SOEC systems.

Within the state-of-the-art fuel electrode materials of Ni-YSZ or Ni-CGO, the nickel content generally leads to two advantages for the cermet of the electrode: it exhibits a high electronic conductivity and is an excellent reforming catalyst and electrocatalyst for the electrochemical reduction. Research is currently being carried out on alternative materials for the use in fuel electrodes that have similar positive properties as the nickel material while achieving an enhanced morphological stability. For instance, promising approaches with ceria-doped lanthanum and strontium chromo-manganite (Ce-LSCM) or CGO with strontium iron molybdenum oxide (SFM) have been shown [50,96]. Another important argument for the development of alternative materials is that it continues to be a challenge to operate continuously in a safe operating regime during the pressurized co- and CO₂ electrolysis modes where carbon deposition within the fuel electrode compartment is prevented. The deposition of solid carbon can lead to mechanical failures via electrode delamination or cracking of the cell. Additionally, it can be assumed that carbon deposition

is favored by the nickel content of state-of-the-art electrode material due to its excellent catalyst properties. Perovskite materials for alternative fuel electrodes in SOCs are promising due to their flexibility in composition which enables to adjust their electrocatalytic properties. For instance, it has been shown that titanate electrodes show a particularly high coking tolerance and promising results for a lanthanum strontium chromite-based perovskite material (L65SCrN) under CO₂ electrolysis operation have been published [97,98]. Hence, the development and usage of alternative Ni-free fuel electrodes for the electrolysis operation is one of the most promising strategies to increase the long-term stability for the pressurized operation.

A potential synergy with the development and usage of alternative electrode materials for the pressurized operation might arise with the aim to prevent internal methanation when the electrolyzer is coupled with specific downstream processes in the PtX context. For instance, the presence of methane can be disadvantageous for a high yield production of a Fischer-Tropsch reactor [99]. Furthermore, it was shown within the Articles II-IV and chapter 5.1 that the methanation has a significant effect on the stack temperature and can lead to significant temperature gradients along the cell length. As the simulation results of Figure 17 in chapter 5.1.3 show, a thermal hotspot is located at approximately three quarters of the cell length in the studied ESC stack. Depending on the operating parameters, the formed temperature gradient can increase and pose a risk to the cell due to thermomechanical stress. In addition to the possible reduction of internal methane production with alternative fuel electrode materials, reducing the thermomechanical stress and achieving a more uniform temperature distribution can help to increase the stability for the pressurized operation. Therefore, stacks with a counterflow or crossflow setup might be considered and investigated for the pressurized operation.

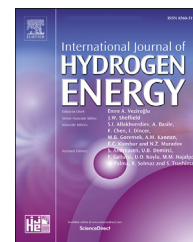
6 Publications

Article I:

Analysis of pressurized operation of 10 layer solid oxide electrolysis stacks.

M. Riedel, M.P. Heddrich, K.A. Friedrich,
International Journal of Hydrogen Energy, Vol. 44 (2019), 4570–4581.

DOI: <https://doi.org/10.1016/j.ijhydene.2018.12.168>.

Available online at www.sciencedirect.com**ScienceDirect**journal homepage: www.elsevier.com/locate/ije

Analysis of pressurized operation of 10 layer solid oxide electrolysis stacks

M. Riedel^{*}, M.P. Heddrich, K.A. Friedrich

German Aerospace Center (DLR), Institute for Engineering Thermodynamics, Pfaffenwaldring 38-40, 70569, Stuttgart, Germany

ARTICLE INFO

Article history:

Received 23 October 2018

Received in revised form

18 December 2018

Accepted 22 December 2018

Available online 22 January 2019

Keywords:

Solid oxide electrolysis

Pressurized SOEC

Pressure

Stack

Electrolysis

ABSTRACT

High temperature steam electrolysis using solid oxide electrolysis cell (SOEC) technology can provide hydrogen as fuel for transport or as base chemical for chemical or pharmaceutical industry. SOECs offer a great potential for high efficiencies due to low overpotentials and the possibility for waste heat use for water evaporation. For many industrial applications hydrogen has to be pressurized before being used or stored. Pressurized operation of SOECs can provide benefits on both cell and system level, due to enhanced electrode kinetics and downstream process requirements. Experimental results of water electrolysis in a pressurized SOEC stack consisting of 10 electrolyte supported cells are presented in this paper. The pressure ranges from 1.4 to 8 bar. Steady-state and dynamically recorded $U(i)$ -curves as well as electrochemical impedance spectroscopy (EIS) were carried out to evaluate the performance of the stack under pressurized conditions. Furthermore a long-term test over 1000 h at 1.4 bar was performed to evaluate the degradation in exothermic steam electrolysis mode. It was observed that the open circuit voltage increases with higher pressure due to well-known thermodynamic relations. No increase of the limiting current density was observed with elevated pressure for the ESC-stacks (electrolyte supported cell) that were investigated in this study. The overall and the activation impedance were found to decrease slightly with higher pressure. Within the impedance studies, the ohmic resistance was found to be the most dominant part of the entire cell resistance of the studied electrolyte supported cells of the stack. A constant current degradation test over 1000 h at 1.4 bar with a second stack showed a voltage degradation rate of 0.56%/kh.

© 2019 The Authors. Published by Elsevier Ltd on behalf of Hydrogen Energy Publications LLC. This is an open access article under the CC BY-NC-ND license (<http://creativecommons.org/licenses/by-nc-nd/4.0/>).

Introduction

Solid Oxide Electrolysis Cells (SOECs) offer a great potential for a highly efficient conversion of renewable electrical energy and the production of fuels for mobility or commodity chemicals for chemical and pharmaceutical industry. High

temperature steam electrolysis (HTSE) using SOECs can therefore function as a key technology for sector coupled energy storage systems. The high operating temperature of SOECs leads to reduced electrochemical losses, fast kinetics and offers the option to use waste heat [1]. Hydrogen, as the product of the HTSE is arguably a versatile, efficient and environmentally friendly fuel [2,3]. It can be stored under

^{*} Corresponding author.

E-mail address: Marc.Riedel@dlr.de (M. Riedel).

<https://doi.org/10.1016/j.ijhydene.2018.12.168>

0360-3199/© 2019 The Authors. Published by Elsevier Ltd on behalf of Hydrogen Energy Publications LLC. This is an open access article under the CC BY-NC-ND license (<http://creativecommons.org/licenses/by-nc-nd/4.0/>).

pressure in gas tanks, injected into the natural gas grid or can further be used directly as a commodity chemical for industrial processes. The operation of the HTSE under elevated pressure offers several benefits. Costs for auxiliary components like compressors for the pressurization of the produced hydrogen in HTSE systems can be omitted or reduced. Furthermore, the operation of the HTSE under elevated pressure has already been published to be energetically even more efficient for fuel electrode supported cells [4–8]. In most of the reported studies single cells have been tested for electrolysis performance and durability under elevated pressure. However, only a limited number of studies focus on the performance of stacks in HTSE mode [9–11].

In this study experimental data of commercially available 10-layer planar stacks with electrolyte supported cells operated at pressures ranging from 1.4 to 8 bar in steam electrolysis mode is presented. Steady-state and dynamically recorded $U(i)$ -curves were performed, as well as electrochemical impedance spectroscopy (EIS) to investigate the pressure effect in more detail. A long-term test over 1000 h at 1.4 bar was furthermore performed to investigate the durability of the stack during steam electrolysis operation.

Test setup

The pressurized SOC stack test facility at DLR is shown in Fig. 1. The experimental test setup offers the opportunity to characterize short stacks in SOEC as well as in SOFC mode in an absolute pressure range between 1.4 and 8 bar. The stack is placed inside a furnace that is installed inside a pressure vessel. During operation the whole setup is pressurized. The pressurization can be conducted with a maximum speed of 1 bar/100 min. The temperature range for the experimental investigations is between 650 and 950 °C. On the fuel side gases like H_2 , N_2 , He, CH_4 , CO and CO_2 can be supplied. Furthermore the test rig offers a stable steam supply for the fuel feed of up to 100%. For the oxygen electrodes air, N_2 and O_2 are available. All gases are controlled by mass flow controllers and preheated via an electric heater before entering the stack. The temperature of the preheater can be controlled independently from the furnace temperature.

A challenge in the operation of SOC stacks on elevated pressure is to keep the pressure differences between anode and cathode gas compartment and the surrounding furnace

atmosphere constantly very low (<20 mbar). Since a large pressure difference may lead to the destruction of the whole stack, all pressures are controlled by a sensitive differential pressure control system of the test rig. The differential pressures between fuel side/air side and air side/vessel are measured at the outlet pipes of the three gas compartments. To enable the precise pressure control, the gas volume of the stack is balanced by equalizing tanks (500 l each) at the anode and cathode outlet to match the furnace volume. Three independently controlled valves for the gas volumes of the two equalizing tanks and the pressure vessel are installed to maintain the set pressure differences between all gas compartments. The released gases are combusted in an off-gas burner. Further information about the setup operated in fuel cell mode are given in Ref. [12].

As well as the possibility to record current-voltage characteristics of the stack and of its individual cells, the test rig offers the opportunity to perform impedance spectroscopy during operation. For determining the gas compositions of the in- and outlet streams a gas analysis system is available.

Since the investigated stacks have an open oxygen electrode design and pure oxygen with its corrosive characteristic is produced during electrolysis, oxygen gas compartment had to be decoupled from the furnace environment to prevent oxidation of the furnace components. Furthermore, in case of a leakage between anode and cathode gas compartment, reactants would stream into the furnace unimpededly and may force oxidation or electric short circuits in the test rig. Due to these aspects, the stack is housed in a gastight steel box with internal gas manifolding (Fig. 2). The necessary compression force is supplied to the stack through a thin transfer metal sheet on the top of the box. Current collectors and voltage wires are lead through the stack box to the designated connection points of the test rig. For measuring the temperatures inside the stack during operation, five thermocouples are placed directly on the oxygen electrodes of the stack. This offers the possibility for an accurate temperature measurement and an investigation of the temperature profile in the stack during operation. One thermocouple is placed on layer one and ten respectively. The three remaining thermocouples are placed at quarter, half and three-fourths of the length of the middle cell of the stack.

The commercially available planar stacks used in this study are co-flow setups and contain 10 electrolyte supported cells, each with an active area of 127.8 cm². Each cell consists of an approximately 55 μm thick lanthanum strontium cobalt ferrite oxide (LSCF) as oxygen electrode, a 90 μm thick 3 mol% yttria-stabilized zirconia (3 YSZ) as electrolyte, gadolinia-doped ceria layer (GDC) between electrolyte/fuel electrode and electrolyte/air electrode, and a 30 μm thick nickel gadolinia-doped ceria (Ni-GDC) as fuel electrode.

Experimental methodology

In this study steady-state as well as dynamically recorded current-voltage curves were performed for characterizing the stacks under pressurized operation in steam electrolysis mode. For steady-state $U(i)$ -curves, current density was



Fig. 1 – Pressurized SOC stack test facility of DLR.

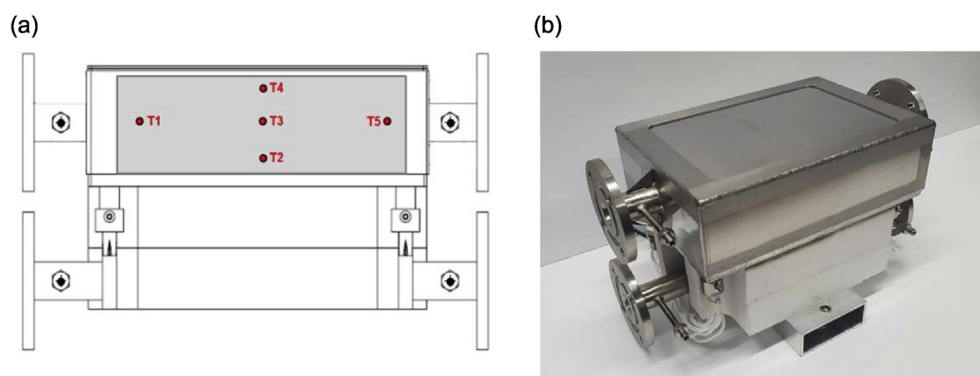


Fig. 2 – (a) Sketch of the steel box with the implemented 10 layer stack and positioning of the five thermocouples. (b) Photo of one manufactured stack box at the beginning of the study.

increased stepwise by 39.12 mA cm^{-2} for every measuring point. The gas flows with a composition of 90% H_2O and 10% H_2 were adjusted at every current density point for a constant steam conversion rate (RC) of 60% at the cells. A flux of 10 slpm air was supplied to the stack on the anode side. Reaching stationary conditions in the stack took at least 90 min depending on operating point. Afterwards cell voltages and temperatures were logged and the experimental parameters were switched to the next measuring point with a higher current density. Due to this method it is possible to record a $U(i)$ -characteristic with a current density dependent temperature profile at a constant steam conversion rate.

In contrast to that, dynamically recorded $U(i)$ -curves were performed with a fast increase of current density of $1.96 \times 10^{-3} \text{ A cm}^{-2} \text{ s}^{-1}$. The gas flows were defined for a steam conversion rate of 60% at 0.8 A cm^{-2} . Air with 10 slpm was supplied to the anode side of the stack. Due to the fast current ramp a quasi-isothermally recorded $U(i)$ -curve with a very

small temperature change over the complete range of current density could be performed.

Electrochemical impedance analysis was performed galvanostatically with a Zahner Zennium at $7.8 \times 10^{-3} \text{ A cm}^{-2}$ with an AC amplitude of 0.38 A. The applied current density leads to a voltage which is very close to OCV at the studied conditions and ensures measuring in pure electrolysis mode. The frequency range for impedance spectroscopy was defined to be in the range of 100 kHz to 50 mHz with single sine wave impedance.

Results and discussion

Steady-state $U(i)$ -curves

Fig. 3 shows the performed steady-state $U(i)$ -curves at a furnace temperature of $800 \text{ }^\circ\text{C}$ and three different operating

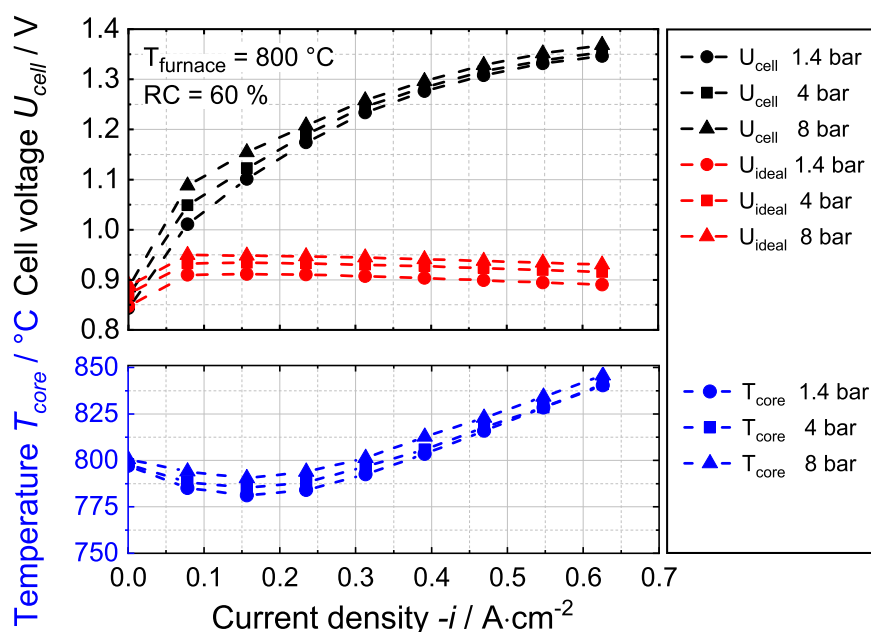


Fig. 3 – Steady-state $U(i)$ -curves recorded with a 10-layer planar SOC stack at a furnace temperature of $800 \text{ }^\circ\text{C}$, air and 90% $\text{H}_2\text{O} + 10\% \text{H}_2$ with a constant steam conversion rate of 60% at every measuring point.

pressures of 1.4, 4 and 8 bar respectively. The showed voltage belongs to the middle cell of the stack. Additionally, the core temperature T3, which is assumed to be the characteristic stack temperature, and the theoretical Nernst voltage for every measuring point are plotted against current density. The recording of the U(i)-curves was aborted before the maximum stack temperature of 860 °C or cell voltages above 1.4 V were reached.

The Nernst voltage was calculated with the following equation by using the definition of the mole fraction $X_i = p_i/p_0$ and by assuming ideal gases ($a_i = p_i/p_0$).

$$U_{ideal} = U_0 + \frac{RT}{zF} \ln\left(\frac{X_{H_2} \cdot X_{O_2}^{0.5}}{X_{H_2O}}\right) + \frac{RT}{2zF} \ln\left(\frac{p}{p_0}\right) \quad (1)$$

Considering the SOC stack to behave as a continuous stirred-tank reactor (CSTR), an averaged gas composition between inlet and outlet of the stack is taken as basis for the calculation of the temperature and conversion rate dependent Nernst voltage (U_{ideal}) [13]. Only at OCV conditions, the gas composition of the inlet is taken for calculating the theoretical values.

As predicted by the Nernst equation, the open circuit voltage was found to increase with increasing operating pressure. The measured cell voltages of Fig. 3 are in good agreement with the theoretical values, indicating an accurate water dosage and hardly any leakage in the stack.

The core temperature of the stack decreases at low current densities due to the endothermic water reduction reaction. At a voltage of 1.28 V for thermoneutral operation, the current density shows values of approximately -0.36 to -0.4 A cm^{-2} depending on operating pressure. Due to the higher OCV and the low influence of kinetics on the stack performance at higher operating pressures, the current density for thermoneutral operation is decreased with higher pressure.

The measured core temperature T3 (characteristic stack temperature; see Section [Ohmic Resistance](#)) shows slightly higher values than the furnace temperature at thermoneutral operation. This behavior could possibly indicate that the thermocouple for the measurement of the core temperature at the middle length of cell 5 measures closer to a hotspot and may not be a well-chosen characteristic stack temperature within these experimental conditions. Nevertheless, the temperature deviation at the thermoneutral operating point between core of the stack and furnace temperature is only in the range of 2–6 K. With higher current densities heat production increases due to the internal resistances of the cells and the stack shows an exothermic behavior.

In the range of low current densities, thermodynamics' influence on the stack and cell performance is bigger than the influence of electrochemical reactions' kinetics. The higher the current density becomes, the more ionic and electronic conduction, activation and diffusion resistances affect the cell performance. At elevated pressure, internal cell resistances are known to decrease due to superior mass transport and decreased diffusion overpotential. Due to this aspect, the impact of pressurization on cell performance becomes bigger with higher current densities. The U(i)-curves recorded at 4 and 8 bar show a slight decrease of the slope with higher

current densities compared to the U(i)-curve recorded at 1.4 bar. Associated is a slight convergence of the U(i)-curves with higher current densities. Nevertheless a crossing of the U(i)-curves, as already reported in literature for fuel electrode supported cells, cannot be observed with the investigated electrolyte supported cell stack up to a cell voltage of 1.4 V and the investigated maximum operating pressure of 8 bar [4,14,15].

During the performed steady-state U(i)-curves, a distinct vertical and horizontal temperature profile forms within the stack. By means of the five thermocouples implemented on certain oxygen electrodes in the 10-layer stack, the temperature distribution depending on the operating point can be described. Fig. 4 shows the current-dependent temperature profile and the voltage of cell 1, 3, 5, 7 and 10 of the stack during the 1.4 bar steady-state U(i)-curve shown in Fig. 3.

The recorded temperatures show a maximum deviation of 5.2 K in the endothermic and 10.4 K in the exothermic operating mode. As expected, the surrounding furnace environment shows the most significant thermal influence on both outer layers of the stack. During endothermic operation both layers have the highest and in exothermic operation the lowest temperature. The temperatures measured along the length of layer 5 show a maximum deviation of 3 K, whereas the thermocouple close to the inlet recorded the lowest values. The temperature profile along the height of the stack leads to the inequality of the cell voltages shown in Fig. 4 b. At high current densities the cell voltages show a maximum deviation of 31 mV. At the operating pressures of 4 and 8 bar, the described behavior of the temperatures and cell voltages were not observed to be significantly different. At 4 bar and 8 bar, a maximum temperature deviation of 4.9 K and 5.2 K in endothermic and 10.8 K and 9 K in the exothermic mode is determined. The cell voltages show a maximum deviation of 35 mV and 29 mV respectively.

Dynamically recorded U(i)-curves

Dynamically recorded U(i)-characteristics are shown in Fig. 5 and Fig. 6. Due to the already mentioned fast current ramp for the dynamically recorded U(i)-curves, only a small temperature deviation in the stack of less than 7 K was observed. The small temperature spread leads to a very low voltage deviation between all 10 cells of the stack. Therefore, the middle cell of the stack with the corresponding core temperature is shown in the following graphs. The voltage shows an almost linear behavior up to the defined maximum voltage of 1.4 V. The slope is slightly decreased with higher operating pressures, which is also indicated by the ASR values shown in the diagrams.

The ASR values are calculated by linearizing the U(i)-curves. Due to the fact that the conversion rate over the current density range is not constant, theoretical Nernst voltage is calculated with the actual current depending gas composition and the actual measured characteristic temperature for every measuring point. By subtracting the theoretical voltage from the measured voltage and dividing it by the current density, ASR values are obtained for every measuring point. The values shown in the diagram of Fig. 5

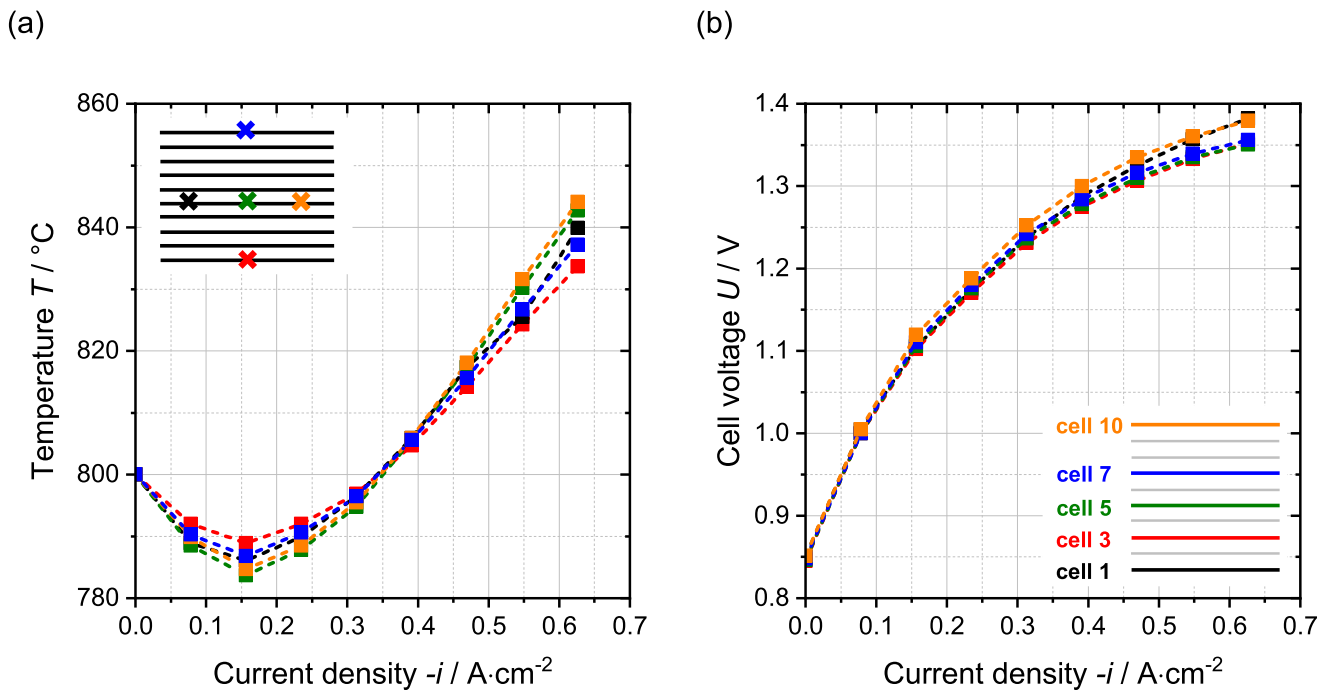


Fig. 4 – During the 1.4 bar steady-state $U(i)$ -curve recorded (a) temperature distribution within the stack. The sensor location is indicated by the colored crosses. (b) shows the cell voltages of specific cells of the same experiment. The cells shown in the graph are indicated by colors. (For interpretation of the references to colour in this figure legend, the reader is referred to the Web version of this article.)

are averaged values over the range of a current density from 0.1 to 0.45 $A\ cm^{-2}$.

The diagrams in Fig. 6 show two different $U(i)$ -curves recorded at furnace temperatures of 750 °C and 850 °C respectively.

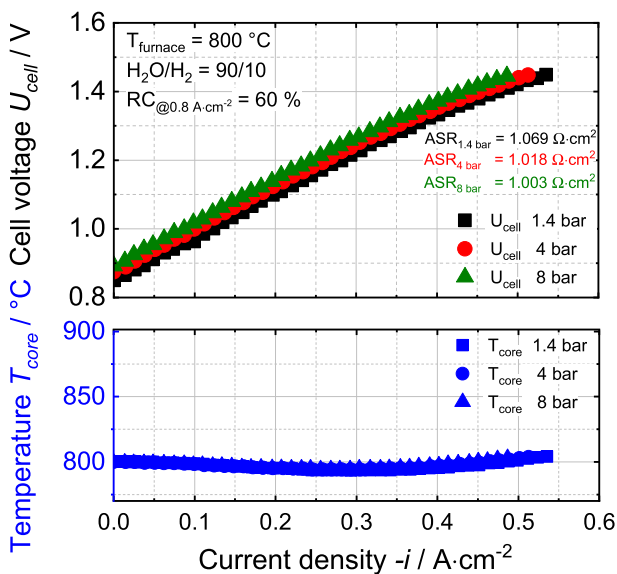


Fig. 5 – Dynamically recorded $U(i)$ -curves at three different operating pressures, a furnace temperature of 800 °C, air and 90% $H_2O + 10\% H_2$ with a steam conversion rate of 60% at 0.8 $A\ cm^{-2}$.

The ASR values shown in diagram (a) are averaged over the range of a current density from 0.1 to 0.25 $A\ cm^{-2}$ and the values in diagram (b) over the range of 0.1–0.6 $A\ cm^{-2}$. At all three operating temperatures shown in Figs. 5 and 6, no positive pressure effect on the achievable current density of the stack could be observed up to a cell voltage of 1.4 V and an operating pressure of up to 8 bar.

Investigation of the pressure effect via EIS

To investigate the pressure influence on the cell performance in more detail, impedance spectra were recorded at operating pressures of 1.4, 4 and 8 bar. As feed gas 1 slpm/cell with a composition of 90% H_2O and 10% H_2 was supplied to the stack. The anode side was flushed with 1 slpm/cell air. A small current density of $7.8 \times 10^{-3} A\ cm^{-2}$ was applied to the stack. Despite the applied small current, cell voltages remained very close to OCV at the studied conditions and recording of the spectra via single sine wave impedance in pure electrolysis mode was ensured.

The inset in Fig. 7 shows the Nyquist plot of the three different impedance spectra. As can be seen, the ohmic resistance is not influenced by pressure and was found to be the most dominant part of entire cell resistance with 0.85 $\Omega\ cm^2$ at 800 °C. The total area specific resistance (ASR_{tot}) shows a very slight decrease with elevated pressures, which explains the already shown $U(i)$ -characteristic with the slightly decreased slope at higher operating pressures. In the frequency dependent plot of Fig. 7 a big resistance in the low frequency part of the spectra could be observed. This resistance is typically attributed to the gas concentration

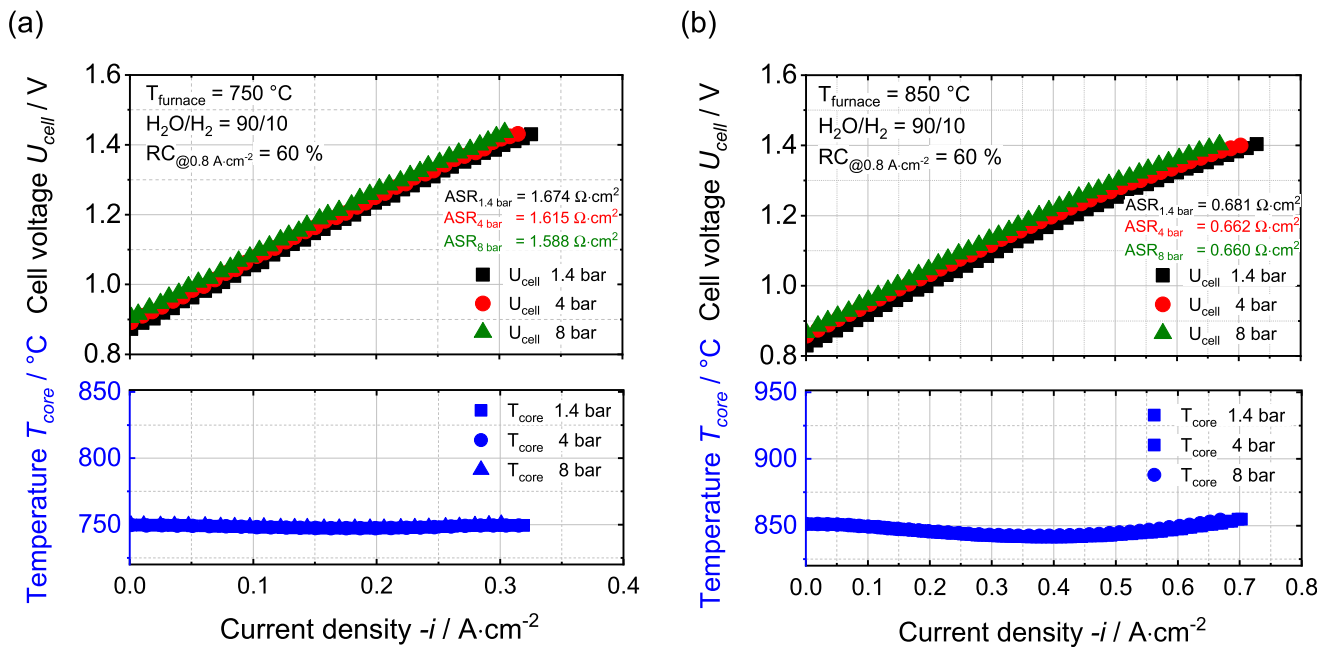


Fig. 6 – Dynamically recorded $U(i)$ -curves at three different operating pressures, gas flows of air and 90% H_2O + 10% H_2 for a steam conversion rate of 60% at 0.8 A cm^{-2} and a furnace temperature of (a) $750 \text{ }^\circ\text{C}$ and (b) $850 \text{ }^\circ\text{C}$.

impedance, the coupled phenomena of gas conversion and gas diffusion. The peak frequency was found to decrease with higher pressures, which is in good agreement with already existing literature about pressurized operations of SOCs [16]. These findings state that as pressure increases, the number of gas molecules in the gas distribution layer and the fuel electrode increases and results in an increase of the gas conversion capacitance and therefore the decrease of the peak frequency.

Next to the lowered peak frequencies, a slight decrease of the resistance could be observed in the described low

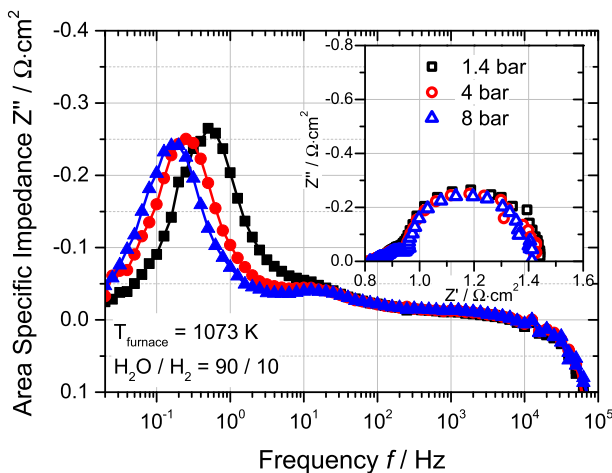


Fig. 7 – EIS recorded at $800 \text{ }^\circ\text{C}$ for 1.4, 4 and 8 bar. For each cell 1 slpm was supplied with 90% H_2O and 10% H_2 at the fuel electrodes. The oxygen side was flushed with 1 slpm/ cell air.

frequency part with increased operating pressure. As stated by Primdahl et al. the resistance related to gas concentration is predicted to be independent of pressure [16,17]. The observed phenomena of a decreasing resistance in the low frequency part with increasing pressure could possibly be explained with a pressure dependent charge-transfer process of the fuel electrode located in that frequency part. Riegraf et al. already observed a charge transfer to be located at very low frequencies for Ni-GDC10 electrodes [18]. With higher pressures, the resistance of charge transfer processes is decreased due to an increased concentration of reactants at active sites of the cells. Accordingly, the resistance of converting the reactants is reduced and could therefore lead to the observed decreased resistance in the low frequency part of the spectra. Furthermore, the change of the diffusion resistance may be negligible for electrolyte supported cells due to the thin electrodes and can therefore not be observed in the recorded impedance spectra [19,20].

Ohmic resistance

Since the ohmic resistance is the most dominant part of the entire cell resistance for electrolyte supported cells, a further investigation of the temperature behavior of the ohmic part was performed. Therefore, impedance spectra were recorded for the middle cell of the stack, at 1.4 bar, OCV and in a temperature range between 650 and 850 $^\circ\text{C}$. Furnace temperature was increased in 20 K steps. To ensure the stack temperature to be equal to furnace temperature at every measuring point, a dwell time of at least 90 min had to expire before EIS was performed. Out of the obtained impedance spectra, the ohmic resistance was analyzed for every temperature step. In Fig. 8 the obtained experimental data for the

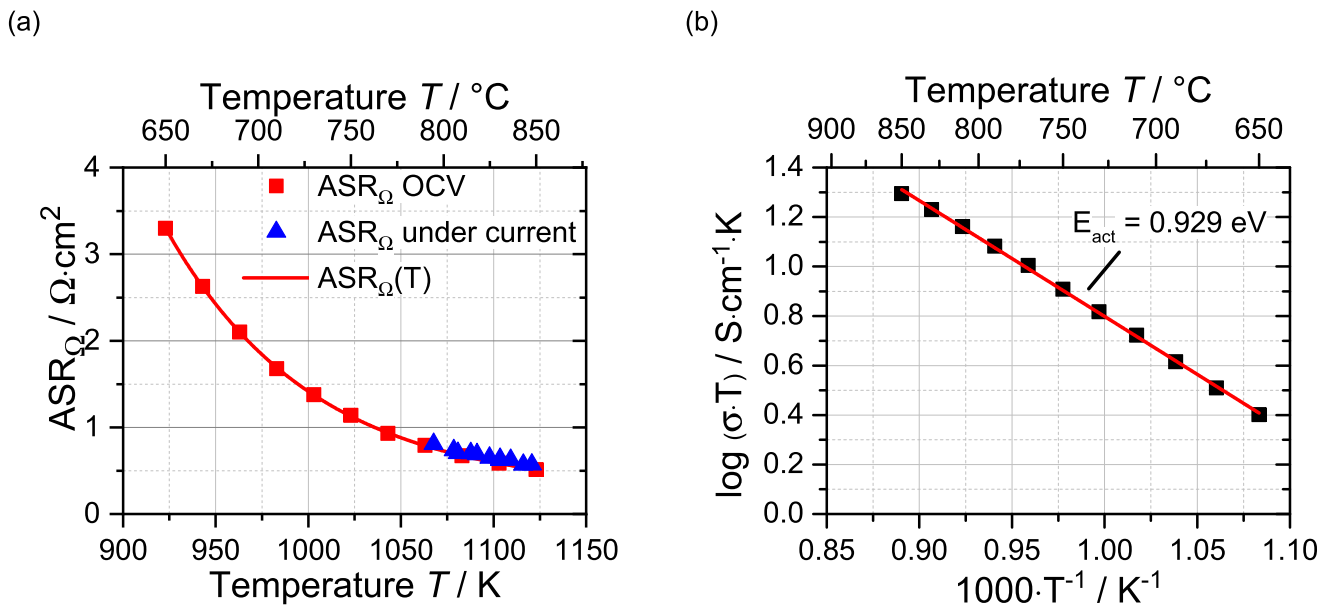


Fig. 8 – (a) Temperature dependency of the ohmic resistance for the middle cell of the stack. (b) Arrhenius plot for the activation energy of the ohmic resistance.

temperature dependent ohmic resistance of the stack is shown.

The resistance was fitted with the exponential expression $ASR_{\Omega} = y_0 + A \cdot \exp(B \cdot T)$. The values obtained for the fit ($R^2 = 0.998$) can be found in Table 1.

The ohmic resistance was further determined for the middle cell of the stack from impedance measurements under load corresponding to the steady state U(i)-curves. T3 was there used as the characteristic stack temperature. In contrast to a measurement at OCV, under operating conditions the cells within the stack will have a distinct horizontal temperature profile that has a significant impact on the local ionic transport conductivity of the cells. Therefore the values of the ohmic resistance obtained out of impedance spectroscopy are an average over the cell area. As can be seen in Fig. 8, these steady-state measured points nevertheless fit very well with the temperature dependent ohmic resistance curve analyzed before. This behavior indicates that the measured core temperature of the stack is a rather good average. It can be used as the characteristic stack temperature.

With the obtained data for the temperature dependent ohmic resistance, values for an Arrhenius plot were calculated. Fig. 8b shows the logarithmic scaled conductivity over the reciprocal temperature. Out of the slope of the curve, an activation energy of 0.929 eV can be calculated. This value is in

good agreement with already published activation energies for YSZ as an electrolyte material [21].

With the detailed information of the temperature dependency of the ohmic resistance, the polarization resistances out of the ASR values of the dynamically recorded U(i)-curves of Section Dynamically recorded U(i)-curves can be calculated by assuming the total ASR to consist of an ohmic (ASR_{Ω}) and a polarization part (ASR_{pol}).

As can be seen in Fig. 9, the polarization resistances decrease with increasing temperature and increasing pressure. The largest influence of the operating pressure on the polarization resistance is found to be at the lowest experimentally performed operating temperature of 750 °C. There, the resistance is reduced by 59 mΩ cm² from 1.4 to 4 bar and by 27 mΩ cm² from 4 to 8 bar. In contrast, at 850 °C the resistance

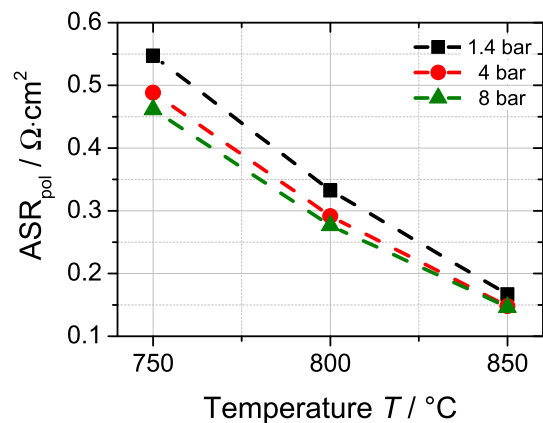


Fig. 9 – Analysis of the temperature and pressure dependency of the polarization resistances obtained out of the three dynamically recorded U(i)-curves shown in Section Dynamically recorded U(i)-curves.

Table 1 – Fit values of the temperature dependent ohmic resistance.

$ASR_{\Omega} = y_0 + A \cdot \exp(B \cdot T)$	
$y_0 / \Omega \text{ cm}^2$	27.266×10^{-2}
$A / \Omega \text{ cm}^2$	35.316×10^4
B / K^{-1}	-1.264×10^{-2}

is merely reduced by 19 mΩ cm² from 1.4 to 4 bar and by 2 mΩ cm² from 4 to 8 bar. Consequently, it can be seen that at lower temperatures the pressure effect plays a more significant role. This behavior can be explained with the slower electrochemical reaction kinetics at lower temperatures and thus the higher sensitivity of the polarization resistance towards changes of the operating pressure affected activation and diffusion resistances. At higher operating temperature, reaction kinetics are inherently faster and the pressure effect on the polarization resistance is reduced. Henke et al. published the pressure dependency of the activation and concentration overvoltages up to a pressure of 20 bar [5]. It was shown that these resistances are following a logarithmic behavior, i.e. the major pressure influence is found at lower pressures. Hence, it can be assumed that the shown U(i)-curves of this study would not show a significant higher pressure dependency by expanding the operating pressure to higher values.

Theoretical analysis of the ohmic resistance

In the following section a simple theoretical analysis of the ohmic resistance of a single repeating unit of a stack is introduced. To the experimentally obtained ohmic cell resistance shown in Fig. 8a, several single resistances as e.g. the ion transfer through the electrolyte, the electrical resistance of the electrochemically active material (anode/cathode functional layer), the protective layers of a single repeating unit, the electrically conductive parts (Nickel mesh, interconnect, wires), contact resistances or delamination effects between the cell layers or eventually occurring oxide layers may contribute. This modeling approach was made to investigate and quantify the proportion of the ohmic resistance coming from (i) the used materials with significant resistance, (ii) the

used materials without significant resistance and (iii) additional contact resistance of one repeating unit.

According to Eq. (2), an idealized ohmic resistance can be calculated using the electrical or ionic conductivities of the individual materials of one single repeating unit of the stack.

$$ASR_{\Omega} = \frac{\delta_{ic}}{\rho_{ic}^{-1}} + \frac{\delta_{mesh}}{\rho_{mesh}^{-1}} + \frac{\delta_{fe}}{\rho_{fe}^{-1}} + \frac{2\delta_{barr}}{\rho_{barr}^{-1}} + \frac{\delta_{el}}{\rho_{el}^{-1}} + \frac{\delta_{ae}}{\rho_{ae}^{-1}} + \frac{\delta_{cl}}{\rho_{cl}^{-1}} + \frac{\delta_{crb}}{\rho_{crb}^{-1}} \quad (2)$$

Here δ stands for the thickness of the specific layer and ρ for the resistivity of the characteristic material. The resistivity of the Nickel mesh (ρ_{mesh}) as the current conductor in the fuel compartment and the stainless steel material of the interconnect (ρ_{ic}) is much lower than the one of the ceramic materials of the electrochemical cell (see Fig. 10). Furthermore, the total resistivities of the materials of the fuel electrode (ρ_{fe}), the air electrode functional layer (ρ_{ae}) and the contact layer at the air side (ρ_{cl}) are generally considered to be much lower than the values for the electrolyte (ρ_{el}) or the GDC barrier layers (ρ_{barr}) between the two electrodes and the electrolyte. The barrier layer on the interconnect to prevent chromium poisoning of the air electrode (ρ_{crb}) is neglected for the presented modeling approach due to its very low thickness. Among the materials under consideration, the total resistivity of GDC is close to the same order of magnitude as the electrolyte material at the regarded operating temperature range for SOECs.

Fig. 10 shows a simplified sketch of one single repeating unit and highlights the simplifications for the presented modeling approach.

Electrical- (ρ_e) and ionic (ρ_{ionic}) resistivities of the different materials (i, ii) as well as the contact resistances (R_{contact}) between each material layer (iii) are represented by arrows. The components with very low total resistivities (<10⁻³ Ω m) were assumed to be negligible for this modeling approach and are

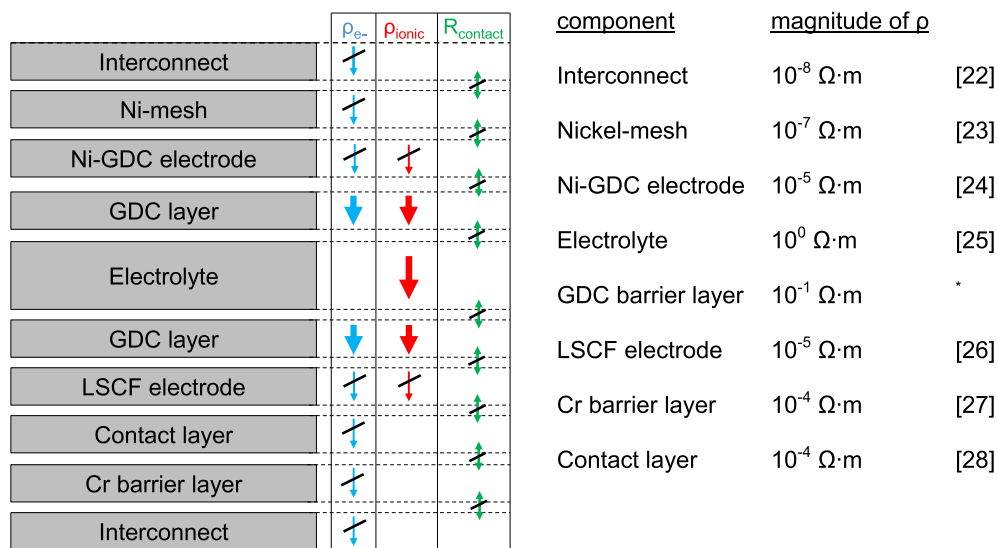


Fig. 10 – Simplified sketch of one single repeating unit of the stack. Arrows represent the electrical- (ρ_e) and ionic (ρ_{ionic}) resistivities of each material and the contact resistances (R_{contact}) between each component. Neglected resistivities and resistances for the presented modeling approach are scored out with diagonal bars. The magnitudes of the material resistivities are shown on the right side [22–28]. *Value experimentally obtained by DLR with a pure GDC pellet in a furnace condition.

scored out with diagonal bars in Fig. 10. Furthermore, the contact resistances between the material layers are neglected, but are assumed to have a significant influence on the overall ohmic resistance.

The temperature dependent specific conductivity, as the reciprocal value of the resistivity of the GDC material, was calculated by the following equation reported by Park et al. [29].

$$\sigma_{GDC} = \frac{1.3 \cdot 10^5 \text{ S} \cdot \text{K} \cdot \text{cm}^{-1}}{T} \cdot \exp\left(-\frac{0.7 \text{ eV}}{k \cdot T}\right) \quad (3)$$

In contrast to the dense electrolyte material, the GDC layer is very porous ($\epsilon = 0.4$). The porosity was taken into account via the equation reported by Wahl et al. [30].

$$\sigma_\epsilon = \sigma \cdot (1 - \epsilon)^{1.5} \quad (4)$$

Out of the conductivities for each material, the ohmic resistances were calculated with the characteristic thickness of the specific layer in the cell. The temperature dependent ohmic resistance of the 3 YSZ electrolyte (data by Kerafol) and GDC material is shown in Fig. 11. The temperature dependency of the resistance of the GDC material was analyzed by DLR in a furnace environment. The modeled area specific resistance of GDC and 3 YSZ material is furthermore compared with the experimentally obtained results for the ohmic resistance of one single repeating unit of the characterized stack (Section Ohmic resistance).

It can be observed that the experimentally obtained values for the ohmic resistances are higher than the calculated ones of the total ASR_Ω (ASR_{Ω,calculated}^{total}). In the considered temperature range from 650 to 850 °C a deviation of 15–20% between the modeled and the experimentally obtained ohmic resistance can be observed. This indicates a noticeable influence of one or more additional resistances in the repeating unit. Most likely this is reasoned by a poor contact between the electrochemically active cell materials and the electronic conductive parts of the repeating unit. It could therefore be a promising

path to investigate the origin and reduce the additional resistance for prospective improvements. As can be seen in this study, a proportion of the ohmic resistance of 15–20% which is not purely driven by the used material in the repeating unit reveals significant potential for an improvement of the performance of prospective stacks.

1000 h durability test at 1.4 bar

For a durability test at 1.4 bar in steam electrolysis mode, a new stack was used. In Fig. 12 the cell voltage of the middle cell of the 10-layer stack and the core temperature as a function of time at constant-current steam electrolysis is shown. The chosen gas composition for the durability test was a mixture of 90% H₂O with 10% H₂ at a furnace temperature of 800 °C. Gas flows were adjusted for a steam conversion rate of 70% at a current density of -0.5 A cm^{-2} . At these experimental conditions the applied current density corresponded to an exothermic operation of the stack ($U_{\text{cell}} > 1.28 \text{ V}$).

Within the 1000 h durability test the voltage degradation per cell was found to be 0.008 V kh^{-1} . This corresponds to a voltage degradation rate of 0.56%/kh and a degradation rate of the ASR of 2.11%/kh. Due to the increasing operating voltage during the test, core temperature increased by 3.13 K over the 1000 h of testing time.

In order to get a deeper insight into the degradation behavior, EIS was performed every 200 h of operating time.

As can be seen in Fig. 13a, the ASR increases over the 1000 h of operation. This behavior can be mainly attributed to an increase of the ohmic resistance. Although the stack temperature is increased due to the increase of the cell voltages, one could see the ohmic resistance of the middle cell of the stack still increases. Fig. 13b shows the change of the ohmic resistance, the ASR and the polarization resistance over 1000 h. The values for the ohmic resistance and the total ASR were obtained out of the Nyquist plots of Fig. 13a. The values for the polarization resistance were obtained by subtracting the ohmic from the total resistance and were found to decrease over the 1000 h of operation. This behavior can be attributed to the increased stack temperature and the related faster electrochemical reaction kinetics. The slight decrease of the polarization resistance points to the fact to be triggered by the increased stack temperature, so that significant microstructural changes in the thin electrodes and an impact on e.g. diffusion resistances are unlikely. Nevertheless, a detailed analysis of the cells is ongoing and will be published subsequently. Due to the increase of the core temperature by 3.13 K over the 1000 h of operation, the temperature independent voltage degradation rate can be calculated with the information of the ohmic resistance given in Section Ohmic Resistance. With an increase of the characteristic temperature by 3.13 K the ASR_Ω is decreased by 2.13%. Assuming a linear change of the gas composition along the length of the cell, the theoretical voltage is reduced due to that temperature effect by 1.0 mV. As a consequence, by neglecting the change of the polarization resistance and by taking the change of the theoretical voltage into account, it leads to a slightly higher temperature independent voltage degradation rate of 0.64%/kh.

To determine the degradation rate at higher operating pressures, long-term experiments at 4 and 8 bar will be

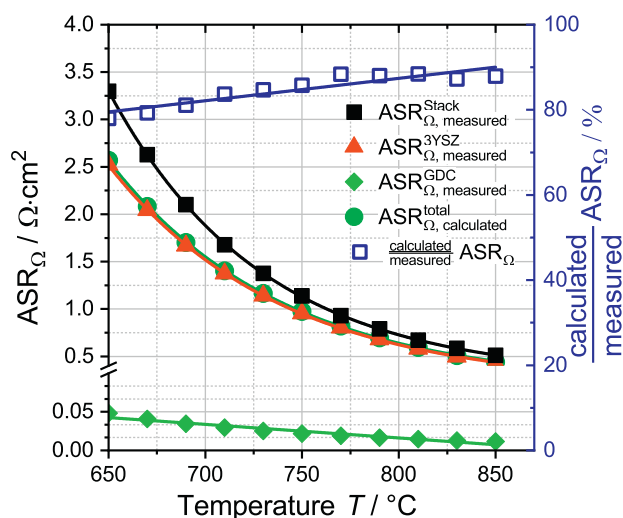


Fig. 11 – Comparison between the ohmic resistance of one cell of the stack (see Section Ohmic resistance) and the ohmic resistance of GDC and 3 YSZ material.

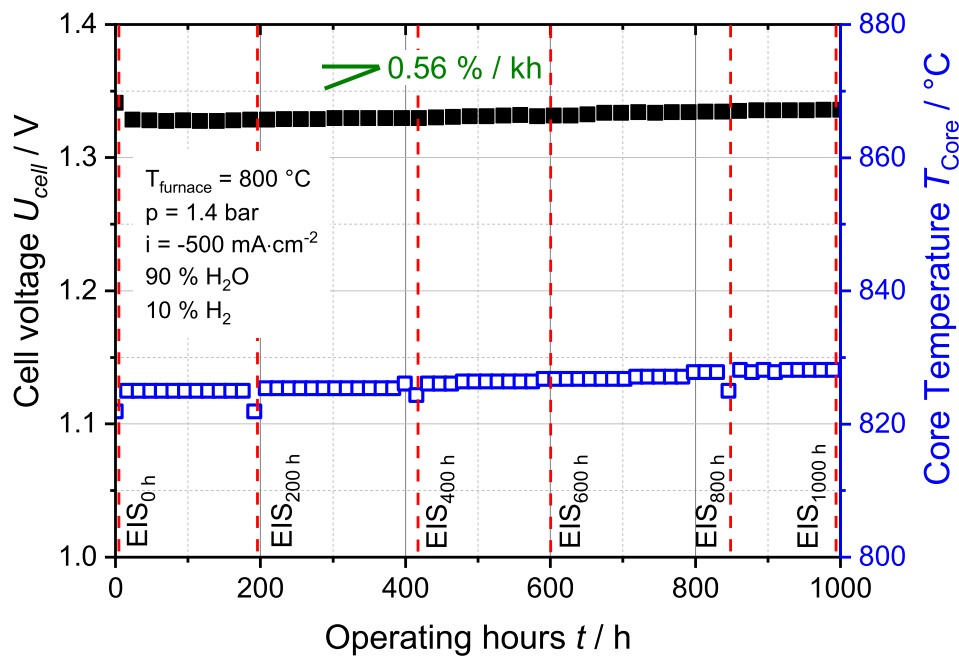


Fig. 12 – 1000 h durability test on 1.4 bar, a furnace temperature of 800 °C, 90% H₂O + 10% H₂ with a steam conversion rate of 70% at -0.5 A cm^{-2} .

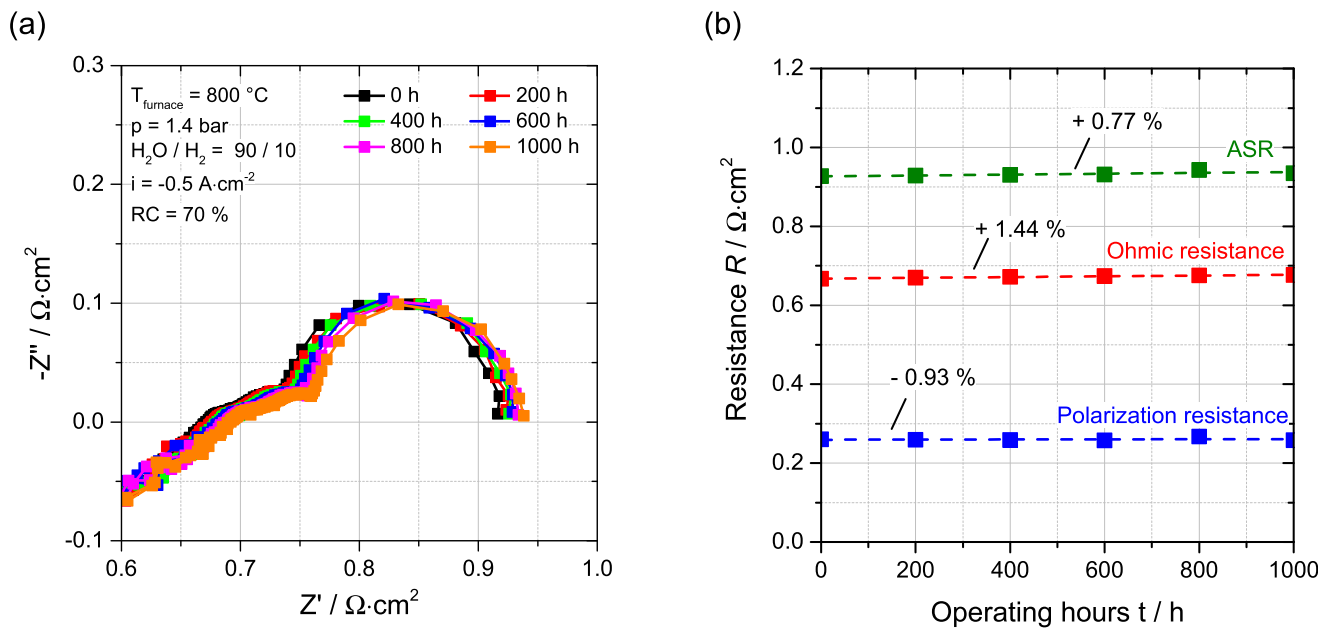


Fig. 13 – (a) EIS recorded at 0, 200, 400, 600, 800 and 1000 h of operating time. (b) Change of the ohmic and polarization resistance and the total ASR over 1000 h of operation.

conducted. A distinctly higher degradation rate at higher operating pressures is expected due to the possible higher mobility of Nickel with higher partial pressures of steam [31]. Furthermore, delamination effects at the air electrode could be observed due to the higher partial pressure of oxygen [32]. The results will be presented in a following publication by the authors.

Conclusion

In this work two commercially available SOC stacks were used for an electrochemical characterization in steam electrolysis mode. The stacks consist of 10 planar electrolyte supported cells. SOC test results for steady-state and dynamic recorded

characterizations were demonstrated under elevated operating pressures up to 8 bar.

The results show that the cell voltages increase with the increase of pressure as predicted by the Nernst equation. Furthermore a slight positive influence on the performance of the stack could be observed in the dynamically and stationary recorded $U(i)$ -curves as well as in the obtained impedance spectra. Due to the dominant and pressure independent ohmic resistance combined with the thin electrodes and the high operating temperature of the electrolyte supported cells, the decrease in the activation and diffusion resistances is low.

Impedance data showed a high resistance at low frequencies which is normally attributed to gas concentration impedance. The peak frequency of this low frequency process decreased with increasing operating pressure. Furthermore the resistance at this low frequency process was slightly decreased. Pure gas concentration impedance should not be affected by pressure [10]. This behavior could possibly be explained with a pressure dependent charge transfer process on the fuel electrode which was already found at quite low frequencies for Ni-GDC electrodes in literature [18].

The most dominant part of the impedance spectra was found to be the ohmic resistance which was closely investigated within a temperature range from 650 °C to 860 °C and was fitted with an exponential expression. A highly simplified model was set up to analyze the ohmic resistance part of the electrolyte supported cells. A comparison between the experimentally obtained data for the ohmic resistance and the values of GDC and 3 YSZ material showed a deviation of 15–20% over the considered temperature range (650–860 °C). This could be reasoned by a poor contact between the electrochemically active cell materials and the electrical conductive parts or by eventually formed oxide layers during the operation on the metal-based components of the repeating unit. The study showed that the proportion of the ohmic resistance which is not purely driven by the used material in the repeating unit reveals significant potential for an improvement of the performance of prospective stack developments, especially because the ohmic resistance is the major part of entire cell resistance for electrolyte supported cells.

The second stack in this study was used for a long term degradation test at 1.4 bar and a steam conversion rate of 70% at 0.5 A cm⁻² over 1000 h. These conditions lead to an exothermic behavior of the stack ($U > 1.28$ V). A voltage increase of 8 mV was observed over the 1000 h of operation which corresponds to a voltage degradation rate of 0.56%/kh. Due to the voltage driven parallel increase of the stack temperature, the actual degradation rate was calculated to be slightly higher. With the performed detailed analysis of the temperature dependency of the ohmic resistance of the stack, the voltage degradation rate was corrected on account of the temperature increase. The actual voltage degradation rate was found to be 0.64%/kh.

Acknowledgement

This work was financially supported by the project “pressurized high temperature electrolysis” (DruHEly) of the Federal

Ministry of Economic Affairs and Energy (BMWi, funding code 03ET6051). The responsibility for the report's contents lies with the authors.

Nomenclature and abbreviations

Abbreviations

SOC	Solid Oxide Cell
SOEC	Solid Oxide Electrolysis Cell
HTSE	High Temperature Steam Electrolysis
EIS	Electrochemical Impedance Spectroscopy
LSCF	Lanthanum Strontium Cobalt Ferrite
YSZ	Yttria-stabilized zirconia
GDC	Gadolinium-doped ceria
Ni	Nickel
OCV	Open Circuit Voltage
CSTR	Continuous Stirred-Tank Reactor

Latin letters

U	Voltage, V
i	Current density, A cm ⁻²
R	Gas constant, J mol ⁻¹ K ⁻¹
z	Number of electrons,
F	Faraday constant = 96485.33, C/mol
slpm	Standard liters per minute, l min ⁻¹
T	Temperature, °C/K
RC	Reactant Conversion, %
p	Pressure, bar
ASR	Area Specific Resistance, Ω m ²

Greek letters

ρ	Resistivity, Ω m
σ	Conductivity, S m ⁻¹
ε	Porosity, %

Subscripts

tot	Total
pol	Polarization
ic	Interconnect
mesh	Mesh
fe	Fuel electrode
barr	Barrier Layer
el	Electrolyte
ae	Air Electrode
cl	Contact Layer
crb	Chromium barrier layer

REFERENCES

- [1] Nguyen VN, Fang Q, Packbier U, Blum L. Long-term tests of a Jülich planar short stack with reversible solid oxide cells in both fuel cell and electrolysis modes. *Int J Hydrogen Energy* 2013;38(11):4281–90.
- [2] Veziroglu TN, Barbir F. Hydrogen: the wonder fuel. *Int J Hydrogen Energy* 1992;17(6):391–404.
- [3] Edwards PP, Kuznetsov VL, David WIF, Brandon NP. Hydrogen and fuel cells: towards a sustainable energy future. *Energy Pol* 2008;36(12):4356–62.
- [4] Jensen SH, Graves C, Chen M, Hansen JB, Sun X. Characterization of a planar solid oxide cell stack operated

- at elevated pressure. *J Electrochem Soc* 2016;163(14):F1596–604.
- [5] Henke M, Willich C, Kallo J, Friedrich KA. Theoretical study on pressurized operation of solid oxide electrolysis cells. *Int J Hydrogen Energy* 2014;39:12434–9.
- [6] Bernadet L, Gousseau G, Chatroux A, Laurencin J, Mauvy F, Reytier M. Influence of pressure on solid oxide electrolysis cells investigated by experimental and modeling approach. *Int J Hydrogen Energy* 2015;40(38):12918–28.
- [7] Sun X, Chen M, Jensen SH, Ebbesen SD, Graves C, Mogens M. Thermodynamic analysis of synthetic hydrocarbon fuel production in PSOEC. *Int J Hydrogen Energy* 2012;37:17101–10.
- [8] Momma A, Takano K, Tanaka Y, Kato T, Yamamoto A. Experimental investigation of the effect of operating pressure on the performance of SOFC and SOEC. *ECS Transaction* 2013;57:699–708.
- [9] O'Brien JE, Stoots CM, Herring JS, Mckellar MG, Harvego EA, Sohal MS, Condie KG. "High Temperature Electrolysis for Hydrogen Production from Nuclear Energy – Technology Summary. 2010.
- [10] Jensen SH, Sun X, Ebbesen SD, Chen M. Pressurized operation of a planar solid oxide cell stack. *Fuel Cell* 2016;16(2):205–18.
- [11] Riedel M, Heddrich MP, Friedrich KA. 1st international conference on electrolysis. In: *Book of abstracts*; 2017. p. 71.
- [12] Seidler S, Henke M, Kallo J, Bessler WG, Maier U, Friedrich KA. Pressurized solid oxide fuel cells: experimental studies and modeling. *J Power Sources* 2011;196(17):7195–202.
- [13] Santhanam S, Heddrich MP, Riedel M, Friedrich KA. Theoretical and experimental study of Reversible Solid Oxide Cell (r-SOC) systems for energy storage. *Energy* 2017;141:202–14.
- [14] Bernadet L, Gousseau G, Chatroux A, Laurencin J, Mauvy F, Reytier M. Assessment of pressure effects on high temperature steam electrolysis based on solid oxide technology. *ECS Trans.* 2015;68(1):3369–78.
- [15] Sun X, Bonaccorso AD, Graves C, Ebbesen SD, Jensen SH, Hagen A, Holtappels P, Hendriksen PV, Mogensen MB. Performance characterization of solid oxide cells under high pressure. *Fuel Cell* 2015;15(5):697–702.
- [16] Primdahl S. Gas conversion impedance: a test geometry effect in characterization of solid oxide fuel cell anodes. *J Electrochem Soc* 1998;145(7):2431.
- [17] Primdahl S. Gas diffusion impedance in characterization of solid oxide fuel cell anodes. *J Electrochem Soc* 1999;146(8):2827.
- [18] Riegraf M, Yurkiv V, Costa R, Schiller G, Friedrich KA. Evaluation of the effect of sulfur on the performance of nickel/gadolinium-doped ceria based solid oxide fuel cell anodes. *ChemSusChem* 2017;10(3):587–99.
- [19] Bessler WG, Gewies S. Gas concentration impedance of solid oxide fuel cell anodes. *J Electrochem Soc* 2007;154:548–59.
- [20] Zhu H, Kee RJ. A general mathematical model for analyzing the performance of fuel-cell membrane-electrode assemblies. *J Power Sources* 2003;117:61–74.
- [21] Nielsen J, Hjelm J. Impedance of SOFC electrodes: a review and a comprehensive case study on the impedance of LSM:YSZ cathodes. *Electrochim Acta* 2014;115:31–45.
- [22] Yang ZG, Paxton DM, Weil KS, Stevenson JW, Singh P. *Materials Properties Database for Selection of High-Temperature Alloys and Concepts of Alloy Design for SOFC Applications*. 2002.
- [23] Abadlia L, Gasser F, Khalouk K, Mayoufi M, Gasser JG. New experimental methodology, setup and LabView program for accurate absolute thermoelectric power and electrical resistivity measurements between 25 and 1600 K: Application to pure copper, platinum, tungsten, and nickel at very high temperatures. *Rev Sci Instrum* 2014;85:095121.
- [24] Infortuna A, Harvey AS, Muecke UP, Gauckler LJ. Nanoporous Ni–Ce_{0.8}Gd_{0.2}O_{1.9–x} thin film cermet SOFC anodes prepared by pulsed laser deposition. *Phys Chem Chem Phys* 2009;11(19):3663–70.
- [25] Brett DJL, Atkinson A, Brandon NP, Skinner SJ. Intermediate temperature solid oxide fuel cells. *Chem Soc Rev* 2008;37:1568–78.
- [26] Yashiro K, Nakano I, Kuhn M, Hashimoto S, Sato K, Miuzusaki J. Electrical conductivity and oxygen diffusivity of perovskite-type solid solution LSCF. In: *219th ESC Meeting*; 2011. p. 739.
- [27] Chen X, Hou PY, Jacobson CP, Visco SJ, De Jonghe LC. Protective coating on stainless steel interconnect for SOFCs: oxidation kinetics and electrical properties. *Solid State Ionics* 2005;176(5–6):425–33.
- [28] Ivers-Tiffée E, Weber A, Herbristrit D. Materials and technologies for SOFC-components. *J Eur Ceram Soc* 2001;21:1805–11.
- [29] Park SH, Yoo HI. Defect-chemical role of Mn in Gd-doped CeO₂. *Solid State Ionics* 2005;176(15–16):1485–90.
- [30] Wahl S, Segarra AG, Horstmann P, Carré M, Bessler WG, Lapique F, Friedrich KA. Modeling of a thermally integrated 10 kW planar solid oxide fuel cell system with anode offgas recycling and internal reforming by discretization in flow direction. *J Power Sources* 2015;279:656–66.
- [31] Mogensen MB, Hauch A, Sun X, Chen M, Tao Y, Ebbesen SD, Hansen KV, Hendriksen PV. Relation between Ni particle shape change and Ni migration in Ni–YSZ electrodes – a hypothesis. *Fuel Cell* 2017;17(4):434–41.
- [32] Moçoteguy P, Brisse A. A review and comprehensive analysis of degradation mechanisms of solid oxide electrolysis cells. *Int J Hydrogen Energy* 2013;38(36):15887–902.

Article II:

Experimental Analysis of the Co-Electrolysis Operation under Pressurized Conditions with a 10 Layer SOC Stack.

M. Riedel, M.P. Heddrich, K.A. Friedrich,

Journal of The Electrochemical Society, 167 (2020), 024504.

DOI: <https://doi.org/10.1149/1945-7111/ab6820>.



Experimental Analysis of the Co-Electrolysis Operation under Pressurized Conditions with a 10 Layer SOC Stack

M. Riedel,^{1,z} M. P. Heddrich,¹ and K. A. Friedrich^{1,2}

¹German Aerospace Center (DLR), Institute for Engineering Thermodynamics, 70569 Stuttgart, Germany

²Institute of Building Energetics, Thermal Engineering and Energy Storage (IGTE), University of Stuttgart, 70569 Stuttgart, Germany

This study examines the performance of a solid oxide cell (SOC) stack during co-electrolysis of CO₂ and H₂O at elevated pressures up to 8 bar. Steady-state and dynamically recorded $U(i)$ -curves were performed in order to evaluate the performance over a wide temperature range and to quantify the area specific resistance (ASR) at different pressure levels. Furthermore, the outlet gas composition at various current densities was analyzed and compared with the thermodynamic equilibrium. The open circuit voltage (OCV) was found to increase with higher pressure due to well known thermodynamic relations. An increase of the limiting current density at elevated pressure was not observed for the investigated stack with electrolyte supported cells. The ASR of the stack was found to decrease slightly with higher pressure. It revealed an increase of the cell resistance with lower H/C ratios in the feed at lower temperatures, whereas the performance of the co-electrolysis was very similar to steam electrolysis for temperatures above 820 °C. Within an impedance study for steam, co- and CO₂ electrolysis operation it was shown that pure CO₂ electrolysis exhibits a higher pressure sensitivity compared to pure steam or co-electrolysis due to significantly increased activation and diffusion resistances.

© 2020 The Author(s). Published on behalf of The Electrochemical Society by IOP Publishing Limited. This is an open access article distributed under the terms of the Creative Commons Attribution Non-Commercial No Derivatives 4.0 License (CC BY-NC-ND, <http://creativecommons.org/licenses/by-nc-nd/4.0/>), which permits non-commercial reuse, distribution, and reproduction in any medium, provided the original work is not changed in any way and is properly cited. For permission for commercial reuse, please email: oa@electrochem.org. [DOI: 10.1149/1945-7111/ab6820]



Manuscript submitted October 2, 2019; revised manuscript received December 12, 2019. Published January 17, 2020.

List of symbols

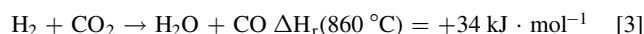
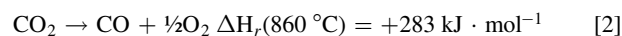
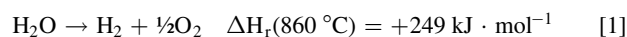
Latin letters

U	Voltage, V
i	Current density, A·cm ⁻²
ASR_{total}	Total area specific resistance, Ω·cm ²
ASR_{pol}	Area specific polarisation resistance, Ω·cm ²
ASR_{Ω}	Area specific ohmic resistance, Ω·cm ²
$slpm$	Standard liters per minute, l·min ⁻¹
RC	Reactant Conversion, %
p	Pressure, bar
R_{MF}	Resistance of the middle frequency process, Ω·cm ²
R_{LF}	Resistance of the low frequency process, Ω·cm ²
J_i	Area specific inlet gas flux with the unit of mol cm ⁻² s ⁻¹
$x_{i,educt}$	Mole fraction of educt in the inlet gas, %
$x_{i,product}$	Mole fraction of product in the inlet gas, %
V	CSTR volume, m ³
A	geometric electrode area, m ²
f	Frequency, Hz
x_b	Mole fraction of product or educt in the bulk, %
D_{eff}	Effective diffusion coefficient, m ² ·s ⁻¹

The goals set by the European Union for the near future until 2050 foresee a stringent reduction of the proportion of fossil fuels in all sectors, in particular also in power, transport and industry.¹ Moreover, the constant increase of electric power from renewables will enable new uses apart from electricity if the technologies for conversion are flexible, efficient and economical.²⁻⁴ Especially cross-sectoral use with a storage function in the area of combined heat and power, transport and chemical industry will be of essential importance. Producing chemicals from steam and CO₂ with solid oxide electrolysis cells (SOECs) as energy converters could become a key technology for expanding the energy transition beyond the electricity sector.^{5,6} Due to the high operating temperature (>700 °C), SOECs offer significant benefits like high thermodynamic efficiency, fast kinetics and reduced electrochemical losses with steam electrolysis. Moreover it is possible to conduct co-electrolysis operation to convert

H₂O and CO₂ simultaneously into synthesis gas (H₂ + CO). This syngas can be used as feedstock for the production of base chemicals or synthetic fuels in downstream processes. Fischer–Tropsch or methanol synthesis reactors are typically operated at elevated pressures in the range of 10 to 60 bar to achieve high conversion or high yield.⁷⁻⁹ Furthermore storage and transportation of gaseous products also require pressurization of the products. Combining a SOEC stack and the catalytical downstream reactor in a pressurized system could therefore be highly beneficial since additional compression work could be significantly reduced or omitted.¹⁰ Furthermore, previous studies have shown that with increasing the pressure, the total area specific resistance (ASR_{total}) decreases significantly with fuel electrode supported cells.¹¹⁻¹⁵

During co-electrolysis operation H₂O and CO₂ reduction occur at the fuel electrode and require energy supply due to the endothermic properties of the reactions shown in Eqs. 1 and 2. Additionally, both reactions are related via the endothermic reverse-water-gas-shift (rWGS) reaction shown in Eq. 3:



The high temperature electrolysis mode requires the enthalpy of formation for the reactions to be provided as electrical and thermal energy. Figure 1 shows the energy demand for the reactions shown in Eqs. 1 and 2 over temperature at standard pressure.

The total energy demand (ΔH) slightly increases for H₂O reduction and is nearly constant for CO₂ reduction respectively whereas for both reduction reactions the electrical energy demand (ΔG) strongly decreases and the thermal energy demand ($T \cdot \Delta S$) increases with temperature accordingly. As depicted in Fig. 1 the CO₂ reduction generally requires a higher amount of thermal (and total) energy supply whereas the electrical energy demand is fairly equal with water reduction at temperatures >750 °C. In literature the co-electrolysis operation is sometimes stated to solely take place via electrochemical steam reduction and CO is purely produced by rWGS reaction.^{16,17} The additional thermal energy demand of the rWGS leads to lower stack temperatures and increased

^zE-mail: Marc.Riedel@dlr.de

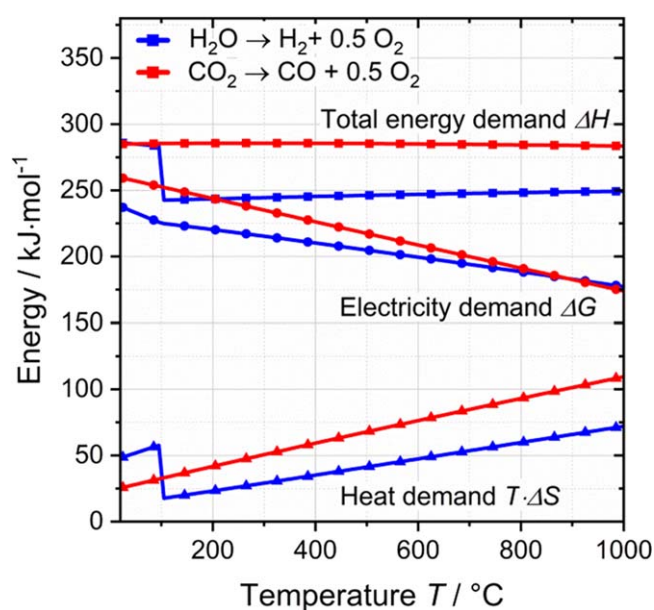


Figure 1. Energy demand of the H₂O and CO₂ reduction reactions depicting the total energy demand (reaction enthalpy ΔH , squares), the electricity demand (Gibbs free reaction energy ΔG , points) and the heat demand ($T \cdot \Delta S$, triangles).

overpotentials. Furthermore, SOECs operated in pure CO₂ electrolysis mode reveal a significantly higher thermoneutral voltage than steam electrolysis operation due to the higher enthalpy of the related reduction reaction.

Test Setup

In this study a commercially available stack with 10 electrolyte supported cells was used. Each cell consists of a Ni-CGO fuel electrode, a 3YSZ electrolyte and a LSCF air electrode. Additionally, CGO barrier layers are implemented between the fuel electrode/electrolyte and the air electrode/electrolyte respectively. Since the stack has an open oxygen electrode design, it is housed in a specially designed gas tight steel box. For measuring the temperatures inside the stack during operation, five thermocouples are placed directly on the air electrodes. One thermocouple is placed on layer one and ten respectively. The three remaining thermocouples are placed at quarter, half and three-fourths of the length of the middle cell of the stack. Further details about the stack and the implementation into the test setup are already published and can be found elsewhere.¹⁸

The experimental test setup at DLR offers the opportunity to characterize short stacks in SOEC as well as in SOFC mode in an absolute pressure range between 1.4 and 8 bar. Figure 2 shows the schematic of the test setup which mainly consists of the media supply (A), the pressurized vessel with an integrated oven (C) and the pressure control combined with two equalizing tanks for the anode and cathode streams (D). A stable and low pulsation steam supply is assured by an evaporator without the use of carrier gas (B). Ultrapure water for evaporation is stored in a water tank with an integrated UV-lamp and is continuously circulated through a self-constructed water purification system with fine filters and a desalination unit in order to prevent any contaminants entering the test rig and/or lead to enhanced degradation of the investigated stacks. Except the steam, all feed gases are supplied via mass flow controllers at the gas supply panel. Before entering the pressure vessel, the feed gases are heated to 300 °C via an electric heater and are mixed with the required steam mass flow in order to prevent condensation and thus caused pressure drops and instable cell voltages. The mixture is led through the vessel wall and is further heated via an electric preheater to the furnace temperature before

entering the stack. However, the carbon containing gases (CO, CO₂ or CH₄) are led directly via a stub to the furnace compartment in order to prevent solid carbon deposition in the preheater due to the possible lower heating rates. The carbon containing gases are mixed with the remaining gases of the preheater upstream of the stack.

In order to maintain very small differential pressures between fuel side, air side and the surrounding furnace atmosphere (<5 mbar), a highly sensitive pressure control system is implemented in the test rig. Differential pressure sensors at the outlet pipes are constantly surveilling the pressure differences between the pressure vessel and the fuel outlet stream and between the fuel side and the air side. To enable a precise pressure control, the gas volumes of the anode and cathode side have to match the vessel volume and are therefore balanced by two equalizing tanks (D, 500 l each). The pressures in the equalizing tanks are controlled by pneumatic valves, which let specific volumes stream into the off-gas burner to match the exact pressure difference between the gas compartments. The fuel side is generally operated at slightly higher pressure in order to prevent gas transition towards the air electrode in case of cell leakages.

The pipe connecting the fuel outlet of the stack and the equalizing tank of the fuel side is constantly heated to 250 °C to prevent condensation of the containing steam content and thus an instable voltage of the upstream-located stack. In order to prevent solid carbon deposition within the outlet pipe of the test setup during co- and CO₂-electrolysis studies, a second water evaporator is installed (B). Generally, solid carbon can deposit during the chilling of the produced hot CO or syngas in the outlet pipes and could clog the whole system with a likely associated damage to the stack. The risk of carbon deposition especially takes place in a temperature range between 500 °C–700 °C and becomes more severe with higher operating pressures. Therefore, the second evaporator injects additional steam directly behind the stack outlet and increases the partial pressure of H₂O in the fuel outlet pipe. Combined with a rather quick cross of the risky temperature window to 250 °C, no carbon deposition occurred during the presented studies of this publication. Due to that configuration, detailed investigations of risky operation conditions can be made without endangering the test facility or the stack. Figure 3 shows a theoretical consideration for the amount of steam need to be injected into the fuel outlet pipe to prevent solid carbon deposition based on thermodynamic equilibrium. $\dot{m}_{H_2O}^{add}$ represents the mass flow of steam to be injected into the outlet pipe and \dot{m}_{react} is the mass flow of gas which is supplied to the stack at the media inlet. The gas inlet composition and the reactant conversion (RC) are in accordance to the experimental parameters used in this study where a considerable risk of solid carbon formation due to the low H/C ratio of 2.44 (inlet gas composition 45% H₂O, 45% CO₂ and 10% H₂) exists. 1.4 bar is the lowest, 8 bar the highest possible operating pressure of the described test rig at DLR. Furthermore, the theoretically needed steam injection to prevent carbon deposition at an operating pressure of 30 bar is shown in the graph. This pressure level represents the operation of a co-electrolysis system with a directly coupled downstream process e. g. Fischer–Tropsch where much higher pressures are needed.

Due to slower reaction kinetics at lower temperatures and the limitation of catalytic reaction sites in the steel pipe, the values given in Fig. 3 can be considered to be maximum values for a safe operation of a pressurized test setup. Experimental investigations showed that the injection of additional steam into the outlet pipe of the test rig does not affect the OCV or performance of the stack in all investigated cases.

In order to constantly monitor the outlet gas composition of the stack, a gas analyzing system is connected to the test rig (Fig. 1e). During the experiments a continuous gas flow of 1 slpm is taken from the fuel outlet pipe and sent to a Rosemount X-Stream analyzer with sensors for H₂, CO, CO₂ and CH₄. Due to the optical measuring principle of this analyzer the steam of the gas mixture is removed via a compressor chiller operated at 3 °C. All gases can be analyzed in a range of 0%–100% with an accuracy of $\leq \pm 1\%$.

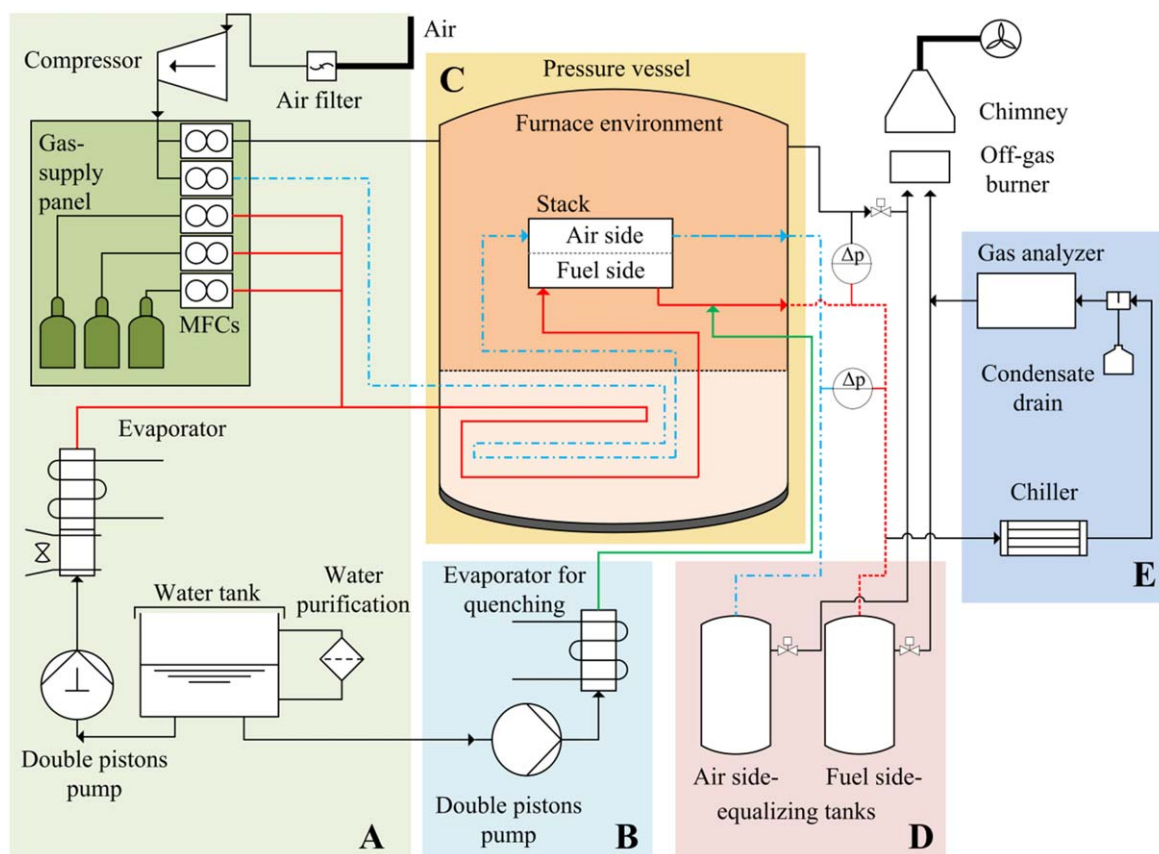


Figure 2. Schematic of the experimental test setup for pressurized SOC stack investigations at DLR.

Experimental Methodology

In this study two inlet gas compositions were used with an H/C ratio of 2.44 (45% H₂O/45% CO₂/10% H₂) and 4.67 (60% H₂O/30%

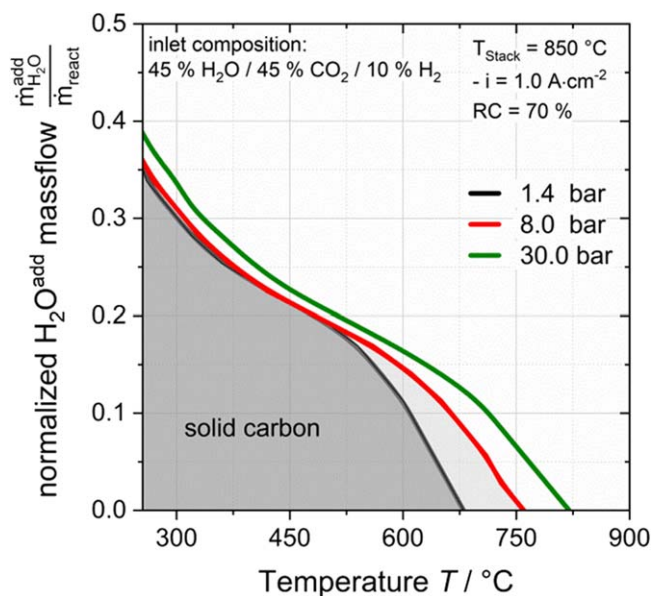


Figure 3. Ratio between mass flow of steam to be injected ($m_{\text{H}_2\text{O}}^{\text{add}}$) and the inlet mass flow of gas supplied to the 10 layer stack (m_{react}) in order to prevent carbon deposition during chilling in the outlet pipe. Calculations are based on thermodynamic equilibrium for an inlet composition of 45% H₂O, 45% CO₂ and 10% H₂ at a stack temperature of 850 °C and a conversion rate of 70% at a current density of $-1.0 \text{ A}\cdot\text{cm}^{-2}$.

CO₂/10% H₂). Steady-state as well as dynamically recorded current-voltage curves were performed for characterizing the stacks under pressurized operation in co-electrolysis mode. For steady-state $U(i)$ -curves, current density was increased stepwise by $78.24 \text{ mA}\cdot\text{cm}^{-2}$ ($\cong 10 \text{ A}$ steps). The gas flows for each composition were adjusted at every current density point for a constant reactant conversion (RC) of 70% at the cells. The RC is always defined according to the overall inlet mass flow of convertible reactants, i.e. the overall amount of H₂O and CO₂ during co-electrolysis operation that can be converted to H₂ and CO (and not further to C). A constant flux of air was supplied to the stack on the anode side. Reaching stationary conditions in the stack took at least 90 min depending on the operating point. The outlet gas composition was constantly monitored during all experiments. Due to this method it is possible to record a $U(i)$ -characteristic with a current density dependent temperature and gas composition profile at a constant reactant conversion rate.

In contrast, dynamically recorded $U(i)$ -curves were performed with a fast increase of current density of $1.96\cdot 10^{-3} \text{ A}\cdot\text{cm}^{-2}\cdot\text{s}^{-1}$ ($\cong 20 \text{ A min}^{-1}$). The gas flows were defined for a reactant conversion of 70% at $-0.47 \text{ A}\cdot\text{cm}^{-2}$. 10 slpm air was supplied to the anode side of the stack. Due to the fast current ramp a quasi-isothermally recorded $U(i)$ -curve with a very small temperature change over the complete range of current density could be performed.

Electrochemical impedance analysis was performed galvanostatically with a Zahner Zennium at $-0.20 \text{ A}\cdot\text{cm}^{-2}$ with an AC amplitude of 380 mA. The frequency range for impedance spectroscopy was defined to be in the range of 20 kHz to 50 mHz with single sine wave impedance. The recorded spectra were analyzed with the commercial software THALES.

The stack was operated over approximately 700 hours for the characterizations of the steam, co-, and CO₂ electrolysis shown in this study. A significant degradation during that operating time was not observed.

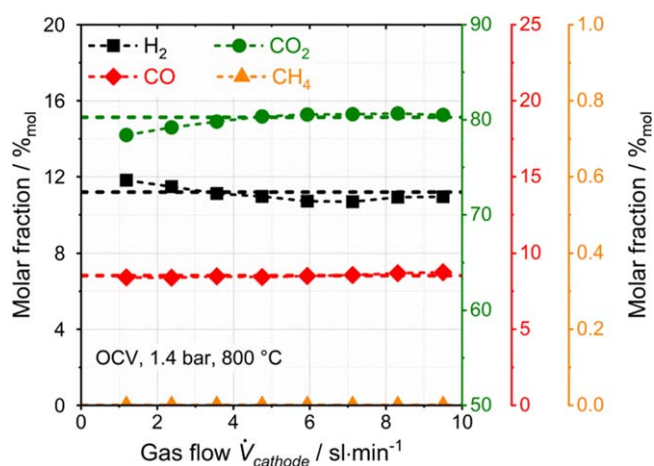


Figure 4. Comparison between thermodynamic equilibrium and the measured outlet gas composition of the stack operated with an inlet composition of 45/45/10 ($\text{H}_2\text{O}/\text{CO}_2/\text{H}_2$), at 1.4 bar and 800 °C over the full range of volume flows for the steady-state $U(i)$ -curves shown in Fig. 5.

Results and Discussion

Steady state $U(i)$ -characteristics and gas analysis.—Before starting the experimental investigations, the stack was operated in non-loaded conditions with a 50/50 mixture of hydrogen and nitrogen at 800 °C. The temperatures measured inside the stack were equal to furnace temperature and the stack voltage was above 12.5 V. Hence, leakages were considered to be negligible.

To exemplify the accuracy of the gas analyzing system, Fig. 4 shows the recorded outlet gas composition during stack measurements at OCV conditions, 1.4 bar, a stack temperature of 800 °C and an inlet gas composition of 45/45/10 ($\text{H}_2\text{O}/\text{CO}_2/\text{H}_2$). At OCV condition and at a constant furnace temperature, an effect of the occurring endothermic rWGS reaction cannot be noticed since the content of reducing gas (H_2 , CO) in the used feed composition is low and the extent of reaction is therefore limited. The outlet gas composition was analyzed over the full range of inlet volume flows according to the steady-state $U(i)$ -curves with 70% reactant conversion presented in Fig. 5. The maximum flow corresponds to a current density of $0.63 \text{ A}\cdot\text{cm}^{-2}$. Note that H_2O is completely removed out of the outlet gas composition by the gas analyzing system due to its measuring principle. The straight lines represent the thermodynamic equilibrium of the gases H_2 , CO, CO_2 and CH_4 respecting a H_2O -free gas composition. Thermodynamic equilibrium was calculated with the CEA tool (Chemical Equilibrium with Applications) and the included gas properties published by the National Aeronautics and Space Administration (NASA).¹⁹

The maximum deviation between the thermodynamic equilibrium and the experimentally recorded measurement points can be found at small gas flows supplied to the stack. The maximum deviation of 1.9%-points (CO_2) can likely be attributed to the increasing inaccuracy of the mass flow controllers at small gas flows. Note that the impact of the inaccuracy on the OCV is marginal due to the present reducing gas content (H_2 , CO) of more than 10%. Generally, the outlet gas composition is in good accordance to the calculated thermodynamic equilibrium over the full range of inlet volume flows. Firstly, this indicates the precise supply of the feed gases and the analytical system to work accurately over a wide range

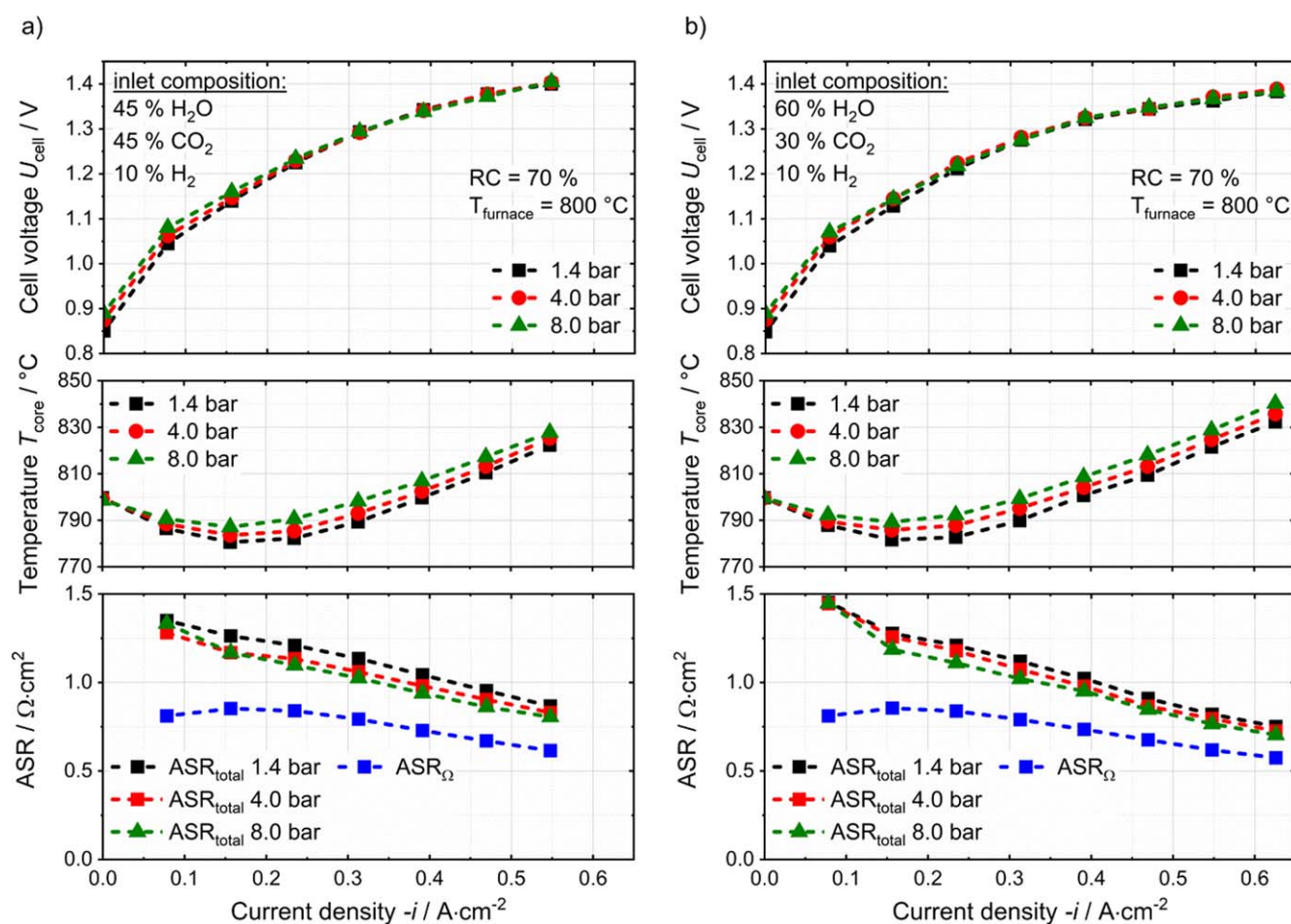


Figure 5. Steady-state $U(i)$ -curves recorded at 1.4, 4 and 8 bar at a furnace temperature of 800 °C. Inlet gas composition is (a) 45/45/10 ($\text{H}_2\text{O}/\text{CO}_2/\text{H}_2$) and (b) 60/30/10 ($\text{H}_2\text{O}/\text{CO}_2/\text{H}_2$) with a reactant conversion of 70% at every measuring point.

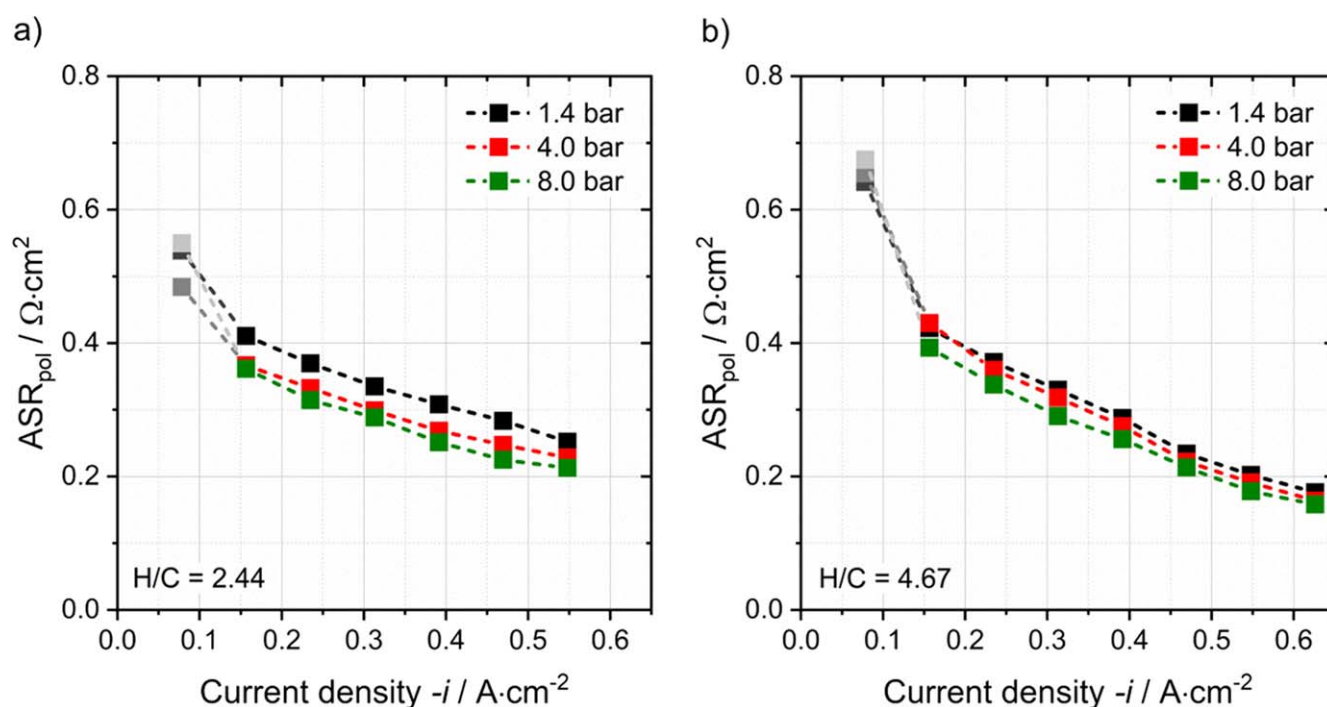


Figure 6. Polarization resistance for the steady-state $U(i)$ -curves recorded at 1.4, 4 and 8 bar at a furnace temperature of 800 °C.

of operation. Secondly, it shows that the chemical reactions are fast and the catalytic surface is sufficiently active and available to equilibrate the inlet gases rapidly within the cells via the reverse water-gas shift reaction (rWGS).

Figure 5 shows steady-state $U(i)$ -curves with the inlet compositions 45/45/10 and 60/30/10 ($\text{H}_2\text{O}/\text{CO}_2/\text{H}_2$) for 1.4, 4 and 8 bar and a furnace temperature of 800 °C. The inlet gas compositions correspond to an H/C ratio of 2.44 and 4.67 respectively. The cell voltage of the middle cell, the core temperature of the stack and the calculated total ASR (ASR_{total}) are plotted against the current density. Furthermore the ohmic ASR (ASR_{Ω}) is plotted based on the core temperature of the stack for the measurements at 1.4 bar. An equation for the temperature-dependency of the ohmic resistance of the studied stack was already published by the authors and can be found in.¹⁸

For calculating the ASR_{total} the conversion is considered to be linear over the cell length. The theoretical voltage at every measuring point is hence calculated with the equilibrated averaged gas composition between inlet and outlet of the stack and the actual measured stack temperature. The justification of that method for calculating the ideal voltage is published elsewhere.²⁰ The ASR_{total} was subsequently calculated by dividing the difference between theoretical and measured voltage by the current density.

As can be seen, both experiments on co-electrolysis show similar performance although the H/C ratio is different by a factor of almost 2. As expected, the open circuit voltages were found to increase with increasing operating pressure. In the range of low current densities, the influence of thermodynamics on the stack and cell performance is more significant than the influence of electrochemical reaction kinetics. The core temperatures of the stack decrease at low current densities due to the endothermic reduction reaction of H_2O (and CO_2), the endothermic rWGS reaction and the comparably low overvoltages at low currents. With higher current densities the stack temperature increases due to the higher heat generation (or higher losses).

By increasing the current density, the cell voltages are found to converge, particularly the $U(i)$ -curves recorded at 4 and 8 bar show a decreased slope in both cases. This could be attributed to the measured stack temperature which increased with higher pressures

due to the occurring internal methanation reaction. The higher temperature lowers the cell voltage due to the reduced cell resistance which may explain the convergence with higher pressures. Furthermore, at elevated pressure internal cell resistances are known to decrease due to superior mass transport and decreased diffusion overpotentials.^{21–24} Hence, the impact of pressurization on cell performance becomes more significant with higher current densities. To exemplify, in Fig. 5a the maximum spread of the characteristic stack temperature between 1.4 and 8 bar is 8.9 K at a current density value of $-0.39 \text{ A} \cdot \text{cm}^{-2}$. According to the relation published in¹⁸ this temperature spread leads to a deviation of the ohmic resistance of $0.055 \Omega \cdot \text{cm}^2$. At this current density point the deviation of the calculated ASR_{total} between 1.4 and 8 bar is $0.110 \Omega \cdot \text{cm}^2$ and thus two times higher than the ohmic resistance spread. At the highest investigated current density of $-0.54 \text{ A} \cdot \text{cm}^{-2}$, the temperature deviation between 1.4 and 8 bar is 5.5 K, which corresponds to $0.023 \Omega \cdot \text{cm}^2$ in ohmic resistance. The ASR deviation at this measuring point is $0.062 \Omega \cdot \text{cm}^2$, thus almost three times higher than the ohmic resistance deviation.

Comparing both experiments with different inlet compositions, Fig. 5a with the higher content of carbonaceous gas in the feed shows a slightly increased cell voltage and subsequently a decreased maximum achievable current density. The performance loss indicates the contribution of an increased diffusion and activation overpotential with increasing CO_2 content in the feed gas. However, the measured stack temperatures show almost same values in both experiments.

The bottom charts in Fig. 5 show the calculated ASR_{total} for each recorded current density step based on the measured characteristic stack temperature. The ASR_{Ω} represents the specific ohmic resistance for the measured temperatures at 1.4 bar and follows the temperature profile shown in the graph above. Due to the fact that for ESC stacks the overall cell resistance is dominated by the ohmic part, the ASR_{total} was expected to follow the shape of the ASR_{Ω} curve. Though, at low current densities the ASR_{total} shows comparably high values for both co-electrolysis experiments at every operating pressure. Most likely this behavior results from the inaccuracy of the mass flow controllers of the test rig at little gas flows as shown in Fig. 4 where a slightly increased molar fraction of H_2 and a

simultaneously decreased CO_2 fraction were found at the outlet. The inaccuracy leads to slightly higher measured voltages and hence to a higher calculated ASR_{total} . With increasing current density and stack temperature, Fig. 5 indicates that the polarization resistance, derived from the difference between ASR_{total} and ASR_{Ω} decrease with current density. In Fig. 6 the polarization resistances are plotted against current density for each pressure. Note, the points related to a current density of $0.08 \text{ A}\cdot\text{cm}^{-2}$ are plotted in grey due to the inaccuracy of the mass flow controllers according to Fig. 4 and will not be part of further analysis.

Comparing both experiments, the polarization resistances show higher values for the lower H/C ratio which is congruent with the findings of the higher ASR_{total} with the higher CO_2 content in the feed gas shown in Fig. 5. With increasing current density, the polarization resistances are found to decrease due to the higher stack temperature and the consequently faster reaction kinetics. Furthermore the activation and diffusion resistances are known to decrease with elevated pressure. However, the pressure dependency was already found to be marginal due to the thin electrodes and the comparably high ohmic resistance of the ESCs used in the studied stack. Hence, the decrease of the polarization resistances at higher pressures is induced by two effects: the faster reaction kinetics due to higher temperature and the decrease of the activation and diffusion resistances due to the elevated operating pressure.

During the co-electrolysis experiments, the outlet gas composition at every stationary current density step was recorded. Figure 7 shows the measured values of H_2 , CO , CO_2 and CH_4 for 1.4 bar (squares), 4 bar (dots), 8 bar (triangles) and the thermodynamic equilibrium based on the measured stack temperature (dashed lines). As described above, the steam content is removed out of the mixture before the analyzer due to its optical measurement principle.

The measured concentrations for the outlet gases are in good accordance with the calculated thermodynamic equilibrium over the full range of current density. As can be seen, in both experiments the major deviation between theoretical and experimentally recorded values can be found at low current densities, especially for H_2 and CO_2 . As mentioned above, this is likely due to an inaccurate dosage of the mass flow controllers of the test rig at little gas flows. The experimental results of the gas analysis indicate that the rWGS and the methanation reactions are fast and shift the gas mixture into equilibrium within the stack even at high flow rates and a RC of 70%.

For high methanation extent of reaction, high pressures, high H_2/CO ratios and low temperatures are favorable. During the experiments a methane content of almost 5% was measured at 8 bar and 790°C for the inlet composition of 60/30/10 ($\text{H}_2\text{O}/\text{CO}_2/\text{H}_2$) with the H_2/CO ratio of 2.5 after 70% conversion. With higher current densities the methane content was found to decrease due to the increased stack temperature and thus a decreasing H_2/CO ratio. Within the conducted experiments, the H_2/CO ratio at the stack outlet is in a range of 1.18-1.27 for the inlet composition of 45/45/10 and between 2.31-2.48 for the 60/30/10 composition.

The measured temperature distribution within the stack during the steady-state co-electrolysis operation with the 45/45/10 mixture at 1.4 and 8 bar is shown in Fig. 8. The nomenclature of the temperatures $T_{i,j}$ in the legend indicate the position of the thermocouple in the stack. i is the specific layer and j the position along the flow direction of the active cell area where the thermocouple is located.

The recorded temperatures show a maximum deviation of 5.9 K at 1.4 bar and 6.3 K at 8 bar in the endothermic operating mode. In the exothermic mode it is 6.1 K and 12.9 K respectively. As expected, the surrounding furnace environment shows the most significant thermal influence on both outer layers of the stack ($T_{L1,1/2}$ and $T_{L10,1/2}$) at both pressures. During endothermic operation both layers have the highest and in exothermic operation the lowest temperature. The temperatures measured along the flow direction of layer 5 show a maximum deviation of 3.9 K at 1.4 bar and 8.7 K at 8 bar, whereas the thermocouple close to the inlet ($T_{L5,1/4}$) always

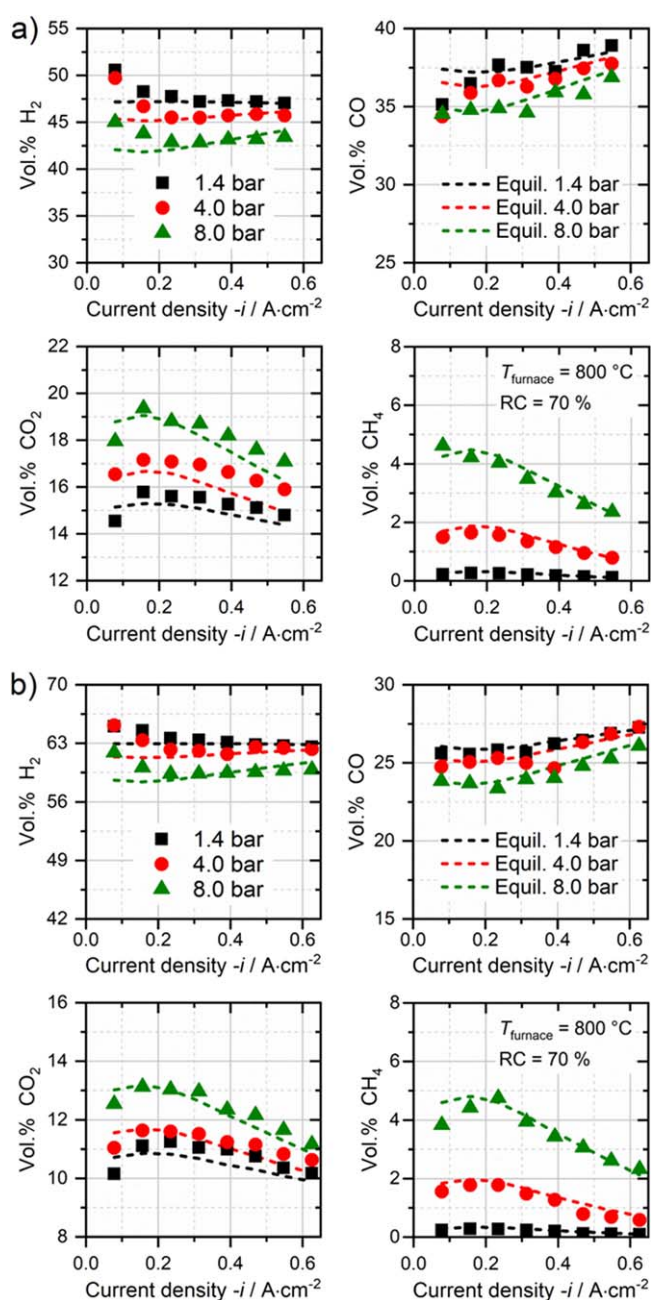


Figure 7. Gas analysis of the stack outlet composition during the steady state co-electrolysis experiments for an inlet composition of (a) 45/45/10 ($\text{H}_2\text{O}/\text{CO}_2/\text{H}_2$) and (b) 60/30/10 ($\text{H}_2\text{O}/\text{CO}_2/\text{H}_2$). The reactant conversion is 70%.

recorded the lowest and the thermocouple close to the outlet ($T_{L5,3/4}$) the highest values. The temperature profile along the height of the stack contributes to the inequality of the cell voltages shown in Fig. 8b. As can be seen, at maximum current density the cell voltage of layer 10 show the maximum deviation of 45 mV.

Dynamically recorded $U(i)$ -characteristics.—The aim of the dynamically recorded $U(i)$ -curves is the quasi-isothermal characterization with only a small temperature deviation within the stack. This ensures determining the performance at a certain stack temperature. Figure 9 shows a comparison between co- and pure steam electrolysis at 800°C and 850°C with a reactant conversion of 70% at $-0.47 \text{ A}\cdot\text{cm}^{-2}$. In both cases, the voltage shows an nearly linear behavior up to the maximum current density with a slightly decreased slope of the $U(i)$ -curves recorded at elevated pressure.

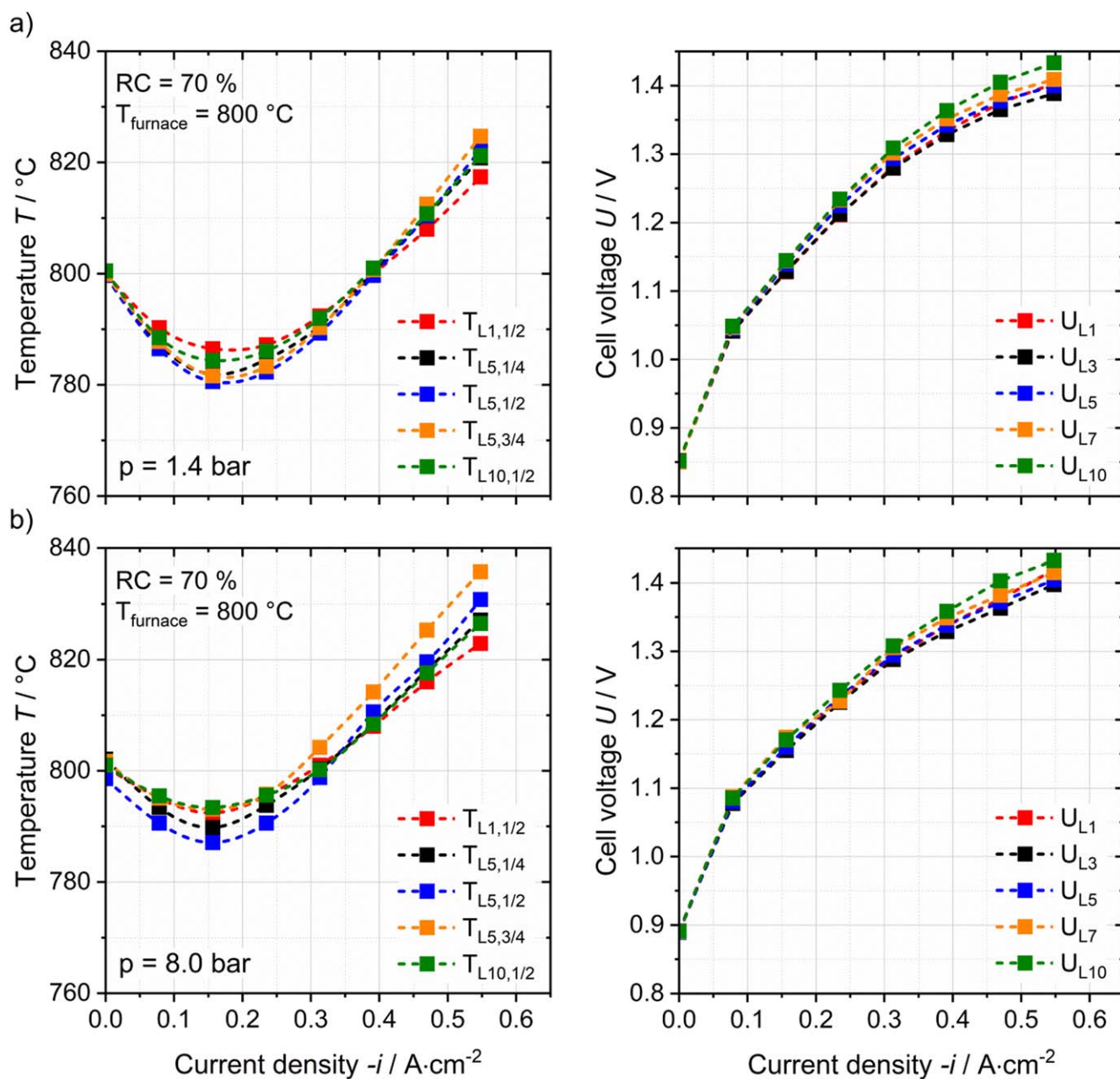


Figure 8. Measured temperatures and cell voltages of the stack during the steady-state co-electrolysis experiment at 1.4 and 8 bar respectively and an H/C ratio of 2.44 in the feed gas (45/45/10 mixture).

However, an overall positive pressure effect on the achievable current density could not be observed for the ESC stack at the studied steam- or co-electrolysis conditions.

Determination of the area specific resistance during co-electrolysis operation.—In order to determine the ASR values, the theoretical Nernst voltage is calculated based on the actual current dependent gas composition and the measured characteristic stack temperature for every measuring point due to the increasing conversion rate over the recorded current density. Note, for co-electrolysis operation the averaged gas composition between the inlet and outlet of the stack is equilibrated before calculating the theoretical voltage. The ASR values shown in the graphs are averaged values in the range of $0.08 \text{ A}\cdot\text{cm}^{-2}$ to the maximum achieved current density of the experiment. As depicted in the graphs, the increase of 50 K furnace temperature leads to a decrease of the ASR by almost 30%.

Due to increased temperature deviations over the range of current density, the recorded $U(i)$ -curves in co-electrolysis mode show slightly higher voltages and ASR values compared to pure steam electrolysis at both furnace temperatures. In co-electrolysis operation the measured temperature deviation is more significant at lower pressures due to the occurring endothermic rWGS reaction and less extent of exothermic methanation. At elevated pressure the voltage increases due to thermodynamics influence and the exothermal methanation reaction becomes more prominent. Hence, increasing heat production at elevated pressure contributes to counterbalance the characteristic of the pure endothermal electrolysis- and rWGS reactions and lead to decreased overvoltages. The described temperature behavior at higher pressures can also be observed for pure steam electrolysis. However the lower temperature deviation at higher pressure is solely caused by the thermodynamically driven higher voltages in that operating mode.

The following Table I shows the temperature deviations for the recorded $U(i)$ -curves:

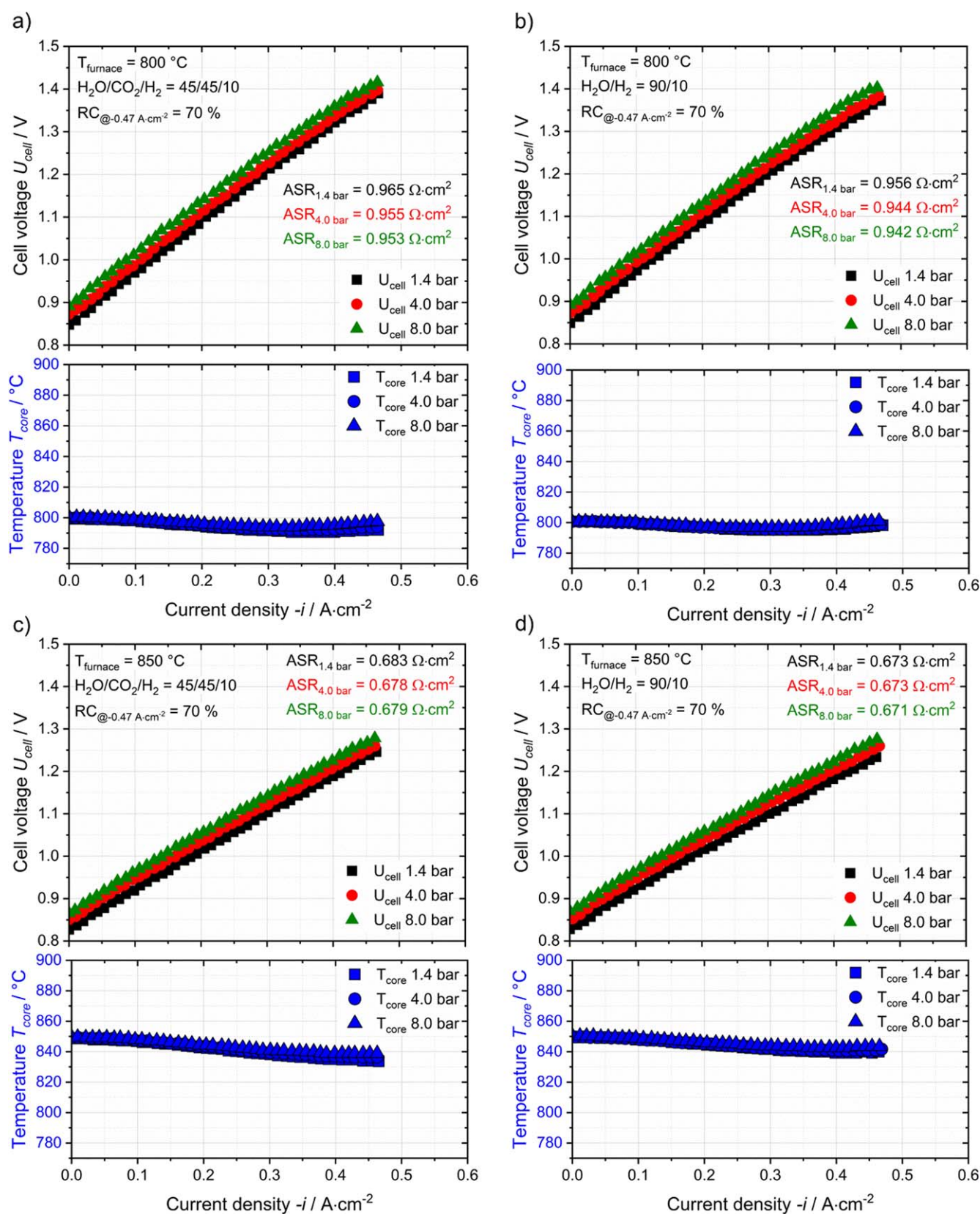


Figure 9. Dynamically recorded $U(i)$ -curves at three different operating pressures a conversion rate of 70% at $-0.47 \text{ A}\cdot\text{cm}^{-2}$ and 800°C and 850°C furnace temperature. (a) and (c) show the results for co-electrolysis, (b) and (d) for pure steam electrolysis operation.

The temperature deviation during co-electrolysis operation at 800°C furnace temperature and 1.4 bar was found to be 8.7 K over the complete range of current density. The $\text{ASR}_{\text{total}}$ was calculated to

be $0.965 \Omega\cdot\text{cm}^2$ accordingly. In pure steam electrolysis operation the $\text{ASR}_{\text{total}}$ was calculated to be $0.950 \Omega\cdot\text{cm}^2$ and a temperature deviation of 5.5 K was observed. Hence, the difference of the

Table I. Temperature deviations between furnace and the measured characteristic stack temperature over the complete current density range during dynamically recorded $U(i)$ -curves in steam- and co-electrolysis operation.

Furnace temperature/°C	Pressure/bar	Temperature deviation in Co-electrolysis 45/45/10 in K	Temperature deviation in H ₂ O-electrolysis 90/10 in K
800	1.4	8.7	5.5
800	4.0	8.0	5.2
800	8.0	6.3	4.2
850	1.4	14.9	10.0
850	4.0	12.9	9.0
850	8.0	10.8	7.6

characteristic stack temperature between steam and co-electrolysis operation is about 3.2 K ($\Delta ASR = 0.015 \Omega\text{-cm}^2$) at this pressure. The lower temperature during co-electrolysis operation leads to an increased ohmic resistance of about $0.017 \Omega\text{-cm}^2$.¹⁸ At 8 bar the ΔASR_{total} was found to be $0.012 \Omega\text{-cm}^2$ with a ΔT of about 2 K. This leads to an increase of the ohmic resistance of $0.013 \Omega\text{-cm}^2$. Therefore it can be concluded that the performance of the stack within the studied dynamical conditions in pure steam- and in co-electrolysis is highly similar and mainly influenced by the stack temperature.

Out of dynamically recorded and steady state measurements for steam- and co-electrolysis operation, detailed characteristics of the ASR_{total} could be obtained for the studied ESC stack. Figs 10a–10c shows the ASR_{total} and the characteristic ASR_{Ω} over a wide temperature range for the inlet gas compositions of 45/45/10, 60/30/10 (H₂O/CO₂/H₂) and 90/10 (H₂O/H₂). The ASR values were fitted to the exponential expression $ASR_{total} = y_0 + A \cdot \exp(B \cdot T)$ and are furthermore plotted for all studied gas compositions in Fig. 10d.

During steam electrolysis operation the ASR_{total} follows the characteristic of the ohmic resistance with an additional and temperature dependent resistance. This additional part indicated by the difference between ohmic and overall resistance can be attributed to the polarization overvoltage. It accounts for approximately 20% of the overall resistance in steam electrolysis over a wide temperature range of the ESC. In case of co-electrolysis operation the polarization resistance shows a higher temperature dependency. At low temperatures the ASR_{total} shows a higher proportion of the polarization resistance while at high temperatures (>820 °C) a significant difference between steam- and co-electrolysis cannot be observed. Thus the increasing partial pressure of CO₂ has a worsening influence on the cell and stack performance during co-electrolysis especially at lower temperatures. This could be related to the decreased partial pressure of steam at the TPB and thus the increased activation and concentration overpotentials. This would imply CO to be solely produced by the rWGS reaction. However it is very likely that for some extent CO₂ is reduced electrochemically which leads to higher overpotentials due to a higher required activation energy of the reduction process at the TPB and a higher diffusion overpotential due to its comparably larger molecular size and molecular mass.^{25–27} Furthermore, the effective diffusion coefficient is proportional to the operating temperature. Both can lead to a higher diffusion overpotential at lower temperatures and thus an increased concentration overpotential.²¹ Since at higher temperatures the influence of reaction kinetics is less prominent, the ASR_{total} of the co-electrolysis operation converges towards the ASR_{total} of steam electrolysis operation.

Impedance analysis during steam, co-, and CO₂ electrolysis operation.—EIS was performed in order to investigate in more detail the pressure influence on the performance of the stack during co-electrolysis mode. Recorded EIS data of the middle cell of the stack were fitted with an equivalent circuit model (ECM) consisting of an inductive unit, a serial resistor and three RQ elements connected in series. Figure 11 shows a comparison of EIS spectra at 1.4 (a) and 8 bar (b) with five different gas compositions. Pure

steam electrolysis with a 90/10 (H₂O/H₂) mixture, co-electrolysis compositions with 60/30/10 and 45/45/10 (H₂O/CO₂/H₂) and CO₂-electrolysis with 90/10 (CO₂/H₂ and CO₂/CO) are investigated. For the co-electrolysis and the CO₂/H₂ compositions rWGS reaction can occur, whereas for the CO₂/CO mixture pure electrochemical reduction of CO₂ is ensured. The measurements were recorded at a stack temperature of 780 °C and a current density of $-0.2 \text{ A}\cdot\text{cm}^{-2}$. The outlet gas composition of the stack was close to a 60/40 reactant/product mixture where the concentration impedance is highly reduced due to the more balanced composition between reactants and products in the cells.²⁸ Due to the different inlet gas compositions, the furnace temperature had to be adjusted in order to ensure an equal stack temperature and thus similar serial resistances for all recorded measurements.

The comparison between the EIS spectra recorded at 1.4 and 8 bar shows an apparent influence of the operating pressure. The peak in the $-Z''(f)$ diagram for the process at 0.1–0.5 Hz becomes less prominent and shows a decreased frequency at elevated pressure. The resistance in this range of frequency can be attributed to gas concentration, the coupled phenomena of diffusion and reactant conversion taking place within the fuel electrode compartment.^{28–32} The conversion impedance itself occurs due to the deviation between the supplied reactant concentrations and the actual gas concentrations at the electrode surface during operation. This resistance becomes generally more significant with an increasing imbalance between H₂O/H₂ or CO₂/CO. Considering the SOC to behave as a continuous stirred tank reactor (CSTR), the resistance of the conversion impedance R_{conv} is pressure independent whereas the capacitance C_{Conv} increases linearly with increasing pressure.^{30,33}

$$R_{conv} = \frac{RT}{4F^2 J_i} \left(\frac{1}{x_{i,educt} + x_{i,product}} \right)$$

$$C_{conv} = \frac{4F^2 p V}{(RT)^2 A} \left(\frac{1}{x_{i,reactant} + x_{i,product}} \right)^{-1}$$

where J_i is the area specific inlet gas flux with the unit of $\text{mol cm}^{-2} \text{ s}^{-1}$, $x_{i,reactant}$ and $x_{i,product}$ are the specific mole fractions in the inlet gas. p is the absolute pressure, V the CSTR volume and A the geometric electrode area. Primdahl et al. showed that the conversion capacitance increases with increasing pressure, since the volumetric density of reactants and products within the fuel electrode compartment increase.^{31,33} Consequently, the frequency f of the conversion process decreases at elevated pressure and follows a p^{-1} dependency due to the relation $f = 1/(2\pi \cdot R \cdot C)$. Due to keeping constant the relevant parameters (flux of gases, stack temperature, 90/10 mixture as inlet composition, current density) for all EIS measurements one can assume the R_{conv} to be equal for all experiments shown in Fig. 11 and only the capacitance C_{Conv} to change due to the operating pressure. As the diffusion of CO₂ compared to H₂O (or CO compared to H₂) through a porous layer or a gas layer is generally more hindered due to its larger molecule size and molecular mass, the change in the observed peak at 0.1–0.5 Hz can most likely be

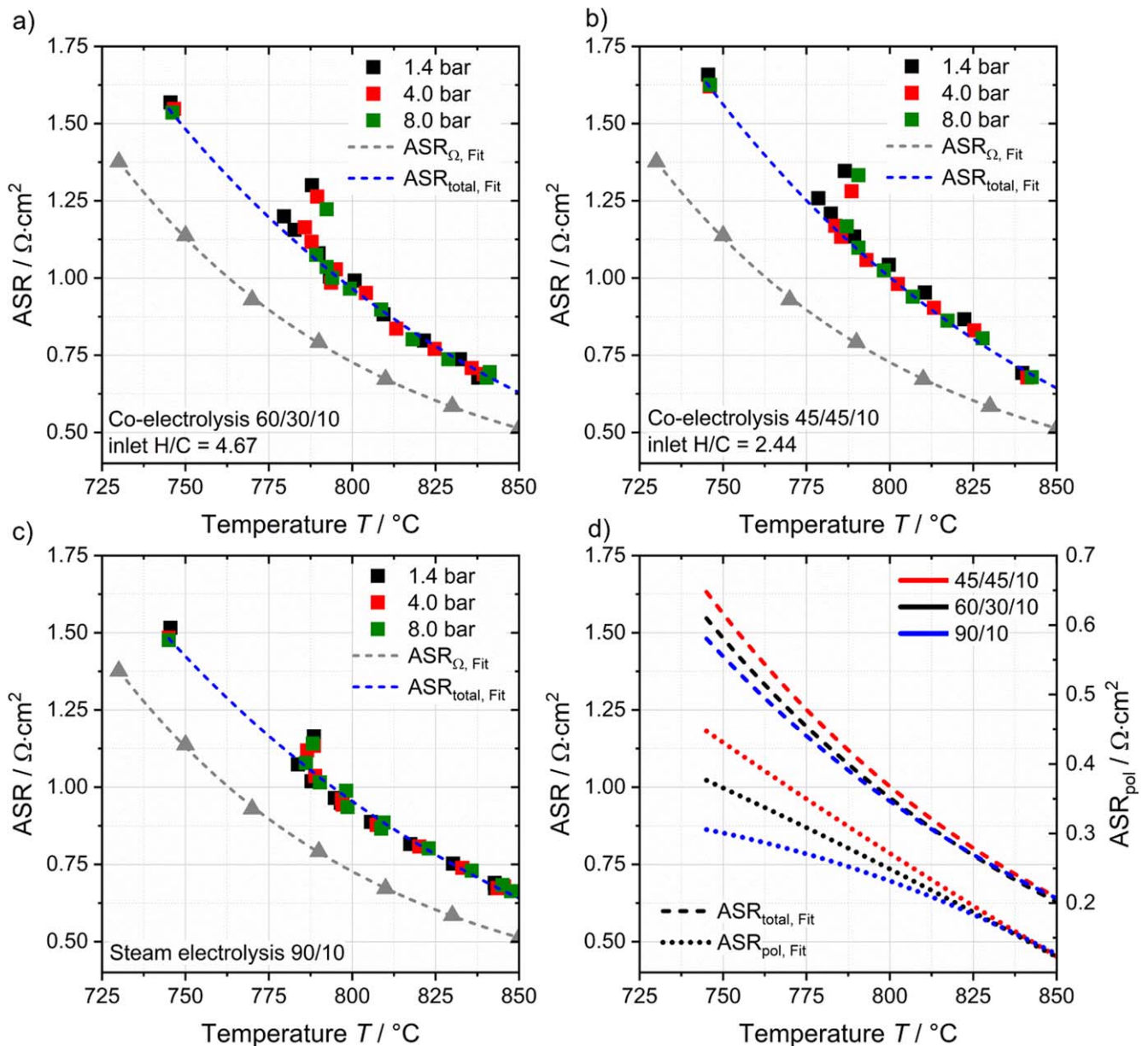


Figure 10. ASR values derived from $U(i)$ characteristics for co-electrolysis (a), (b) and pure steam-electrolysis (c). (d) shows the fitted ASR curves of a-c. Values of the temperature-dependency of the ohmic resistance derived from.¹⁸

attributed to a diffusion process within the fuel electrode compartment. The diffusion resistance $R_{D_{\text{diff}}}$ has the following expression:

$$R_{D_{\text{diff}}} = \left(\frac{RT}{2F} \right)^2 \frac{l}{pD_{\text{eff}}} \left(\frac{1}{x_{b, \text{educt}}} + \frac{1}{x_{b, \text{product}}} \right)$$

with x_b as the mole fraction of reactant and product in the bulk gas outside the diffusion layer or porous electrode and D_{eff} as the effective diffusion coefficient consisting of the Knudsen (D_K) and ordinary diffusion coefficients (D_{ord}). At low pressure, diffusion is governed by Knudsen diffusion mechanism. Knudsen diffusion itself is pressure independent and the diffusive mass flux is therefore governed by the concentration gradient which is directly proportional to pressure. At higher pressure, diffusion becomes governed by ordinary diffusion mechanism which is reciprocally proportional to pressure. Hence, the effective diffusion coefficient D_{eff} decreases nonlinearly with increasing pressure. However, the slight decrease of D_{eff} nevertheless leads to an increase of the term $p \cdot D_{\text{eff}}$ by increasing the pressure. A detailed theoretical study about the operating

pressure dependency of D_{eff} for SOCs can be found elsewhere.^{22,34} In conclusion, $R_{D_{\text{diff}}}$ decreases with increasing pressure according to the above mentioned equation. The lower resistance at elevated pressure consequently leads to a decreased height of the peak around 0.5 Hz in the $-Z'$ (f) diagram of Fig. 11. Jensen et al. conducted stack measurements at elevated pressure and showed that the low frequency peak shifts towards lower frequencies by increasing the operating pressure.¹⁰ This is in good agreement with the EIS measurement shown in Fig. 11 for steam, co- and CO_2 electrolysis where the same phenomenon was observed. However, a decreased resistance of the low frequency process was not observed within the study of Jensen et al. This is most likely due to the fact that the measurements were conducted at OCV, whereas the measurements shown in Fig. 11 were conducted under significant load. The increased extent of reaction leads to a significantly more dominant diffusion of reactants and products and hence to a more dominant pressure effect.

Figure 11 reveals the process-related peak and the resistance at a frequency of 10–20 Hz to become less prominent with higher

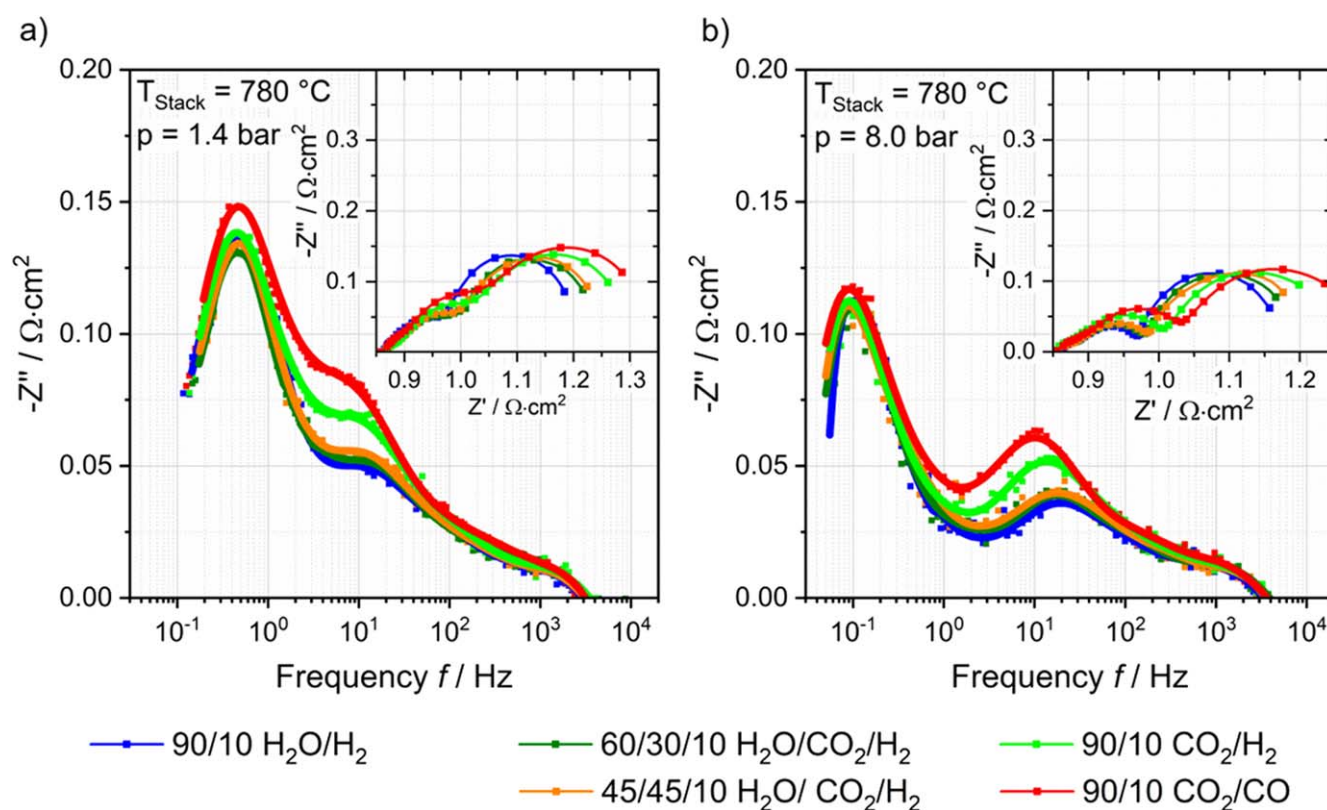


Figure 11. Comparison of five gas compositions for steam, co- and CO₂-electrolysis at 1.4 (a) and 8 bar (b). A reactant conversion of 30% and a current density of $-0.20 \text{ A}\cdot\text{cm}^{-2}$ was chosen for the EIS spectra.

operating pressure. Since this middle frequency process shows a dependency on the partial pressures of the reactants, it can likely be attributed to a surface process at the fuel electrode. With higher pressure the resistance decreases due to the increased concentration of reactants at active sites and the frequency in the EIS spectrum therefore decreases. Additionally the peak and the resistance can be observed to get more prominent with an increasing content of CO₂ in the feed gas for 1.4 and 8 bar respectively. This can be attributed to the decreasing partial pressure of H₂O within the porous electrode and a related increase of the activation resistance. Albeit the activation energy of electrochemical CO₂ reduction is reported to be higher than that for steam reduction, it is nonetheless likely that CO₂ is reduced electrochemically to some extent especially at high conversion rates.^{27,35} Since a low partial pressure of H₂ reduces the rate of the rWGS reaction, it can be assumed that the electrode potential increases locally at the beginning of the cell area due to the increased diffusion and activation resistance of the CO₂ process. With increased cell length, the CO production pathway is then shifted towards the rWGS reaction due to the increased partial pressure of produced H₂. Since the recorded EIS measurements shown in Fig. 11 constitute an average of the SOC performance due to the large cell area of the used stack, the difference between pure steam- and co-electrolysis gas compositions is found to be marginal. Hence, it can be assumed that the main reaction pathway for the production of CO during co-electrolysis operation is via the fast rWGS reaction.^{16,36}

Since the influence of CO₂ in the feed gas on the characteristic performance of the stack was shown to be most dominant at low temperatures, a direct comparison between pure steam and pure CO₂ electrolysis is shown in Fig. 12 for 700 °C and 850 °C. In addition to the EIS spectra plotted in a $-Z''(f)$ diagram, the values for the ASR_{total} and the middle and low frequency resistances (R_{MF} and R_{LF}) are given in Table II according to the ECM with one inductive unit, a serial resistor and three RQ elements connected in series. The high frequency process (10^2 – 10^3 Hz) was not analyzed in detail since it is

most likely attributable to the air electrode and should not differ between H₂O and CO₂ electrolysis due to the same RC.³⁷ However, several studies show that the contribution of a CGO bulk process of the fuel electrode is most likely located additionally within the high frequency range.^{38,39} Hence, the high frequency process cannot be assigned to one single process though the data was fitted with a single RQ element and a constant n-value of 0.5. The authors are aware that the n-value of 0.5 for the high frequency process(es) do physically not make sense and indicate that a Gerischer element could be used for a more physically meaningful fit of the air electrode. However, due to the mentioned overlap (air electrode + CGO bulk) the authors decided to use a single RQ element to reduce the number of fitting parameters. Furthermore, the purpose of this study was to describe the changes in the impedance spectra during H₂O and CO₂ electrolysis for the middle and low frequency processes. The n-values during the fitting procedure were kept constant for all RQ elements according to Table II. Note that the raw data and the fitted spectra are plotted jointly in Fig. 12.

At 700 °C the difference between steam and CO₂ electrolysis is observed to be significant for the middle and low frequency processes attributed to the fuel electrode and the concentration impedance respectively. At 1.4 bar the gas concentration resistance shows significantly higher values during CO₂ electrolysis compared to pure steam electrolysis operation (see Table II). Since the resistance of the gas conversion is considered to be equal due to the same amount of reactant moles and volume flows in both cases, the difference can be attributed to a more significant diffusion resistance for CO₂ electrolysis operation. However, both operation modes show similar frequencies for the respective low frequency peak which indicates a significant change of the capacitance for the CO₂/CO operation. At higher pressure (Fig. 12b) the diffusion resistance decreases due to superior mass transport and the peaks are shifted towards lower resistance values and lower frequencies. The middle frequency peak attributed to the fuel electrode process shows higher values for CO₂ electrolysis and consequently a decreased

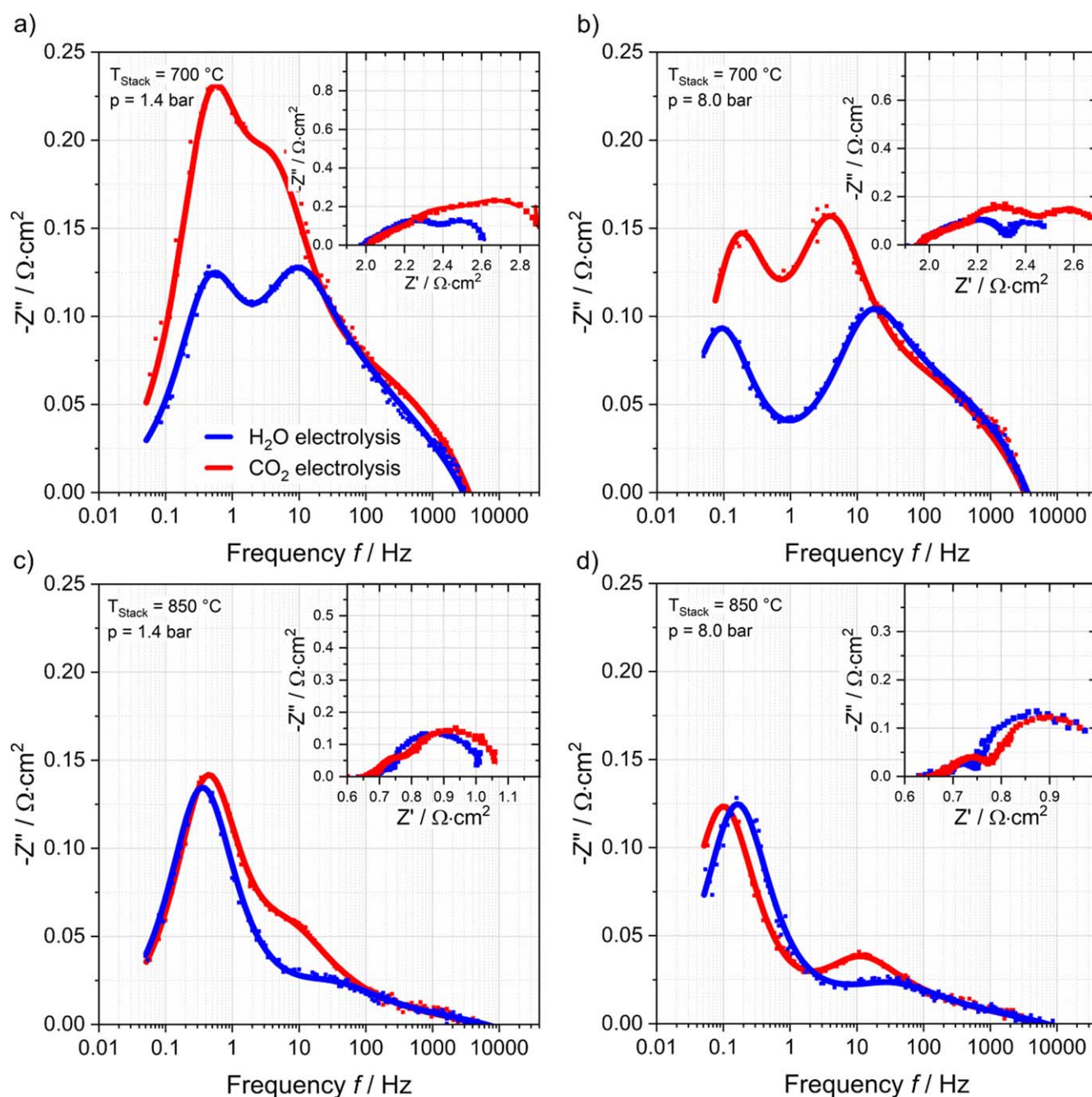


Figure 12. Comparison of EIS spectra during steam and CO₂ electrolysis operation at 700 °C and 850 °C respectively and 1.4 and 8 bar of pressure. *RC* is 30% at a current density of $-0.20 \text{ A} \cdot \text{cm}^{-2}$.

frequency compared to pure steam electrolysis operation. The decrease of the resistance at elevated pressure is observed to be more significant for the CO₂ electrolysis indicating a significantly higher pressure sensitivity compared to pure steam electrolysis.

At a stack temperature of 850 °C the middle frequency resistance at 1.4 and 8 bar show lower values due to the generally faster kinetics at higher temperature. The low frequency process is observed to be similar for steam and CO₂ electrolysis respectively, which could indicate an equal diffusion rate of the reactants through the porous layer. The middle frequency process shows slightly higher resistances for CO₂ reduction compared to steam reduction at both 1.4 and 8 bar. However, in relation to the ASR_{total} , the proportion of R_{MF} is marginal in both operation modes and at both pressures whereas the conversion and diffusion part takes almost a proportion of one fourth of the ASR_{total} at 850 °C in this study. Since

the concentration impedance for steam and CO₂ electrolysis is found to be similar at high temperatures and the influence of the fuel electrode process on the ASR_{total} is marginal, it can be concluded that the overall performance of the ESC stack is similar in both operation modes at high operating temperature. Lower operating temperatures are observed to lead to a more significant influence of the low and middle frequency processes and thus to a more significant performance loss during CO₂ electrolysis operation. This observation is congruent with the findings for the ASR_{total} characteristics of the co-electrolysis operation shown in Fig. 10 where a correlation between a higher CO₂ content in the feed gas and an increased ASR_{total} was observed. However, the current theory based on the equations for R_{diff} and R_{conv} predict both the diffusion and conversion resistances to increase with higher temperatures. While this is in accordance with the impedance results of the low frequency part of the spectra

Table II. Values of the middle and low frequency resistances (R_{MF} and R_{LF}) and the total resistance (ASR_{total}) at the two operating temperatures and pressures according to the spectra shown in Fig. 12. N-values of the RQ elements were kept constant during the fitting procedure.

Pressure	H ₂ O electrolysis				CO ₂ electrolysis			
	700 °C		850 °C		700 °C		850 °C	
	1.4 bar	8 bar	1.4 bar	8 bar	1.4 bar	8 bar	1.4 bar	8 bar
$R_{HF}/\Omega\cdot\text{cm}^2$	0.27	0.25	0.07	0.07	0.29	0.27	0.07	0.07
n value	0.50	0.50	0.50	0.50	0.50	0.50	0.50	0.50
$R_{MF}/\Omega\cdot\text{cm}^2$	0.18	0.16	0.02	0.02	0.29	0.28	0.07	0.06
n value	0.90	0.90	0.90	0.90	0.90	0.90	0.90	0.90
$R_{LF}/\Omega\cdot\text{cm}^2$	0.20	0.19	0.26	0.25	0.37	0.25	0.27	0.25
n value	0.99	0.99	0.99	0.99	0.99	0.99	0.99	0.99
ASR_{total}	2.61	2.55	1.02	0.99	2.93	2.74	1.07	1.03

recorded for steam electrolysis, it is not the case for pure CO₂ electrolysis. Furthermore one would expect the Knudsen diffusion to be more dominant at lower temperature due to the proportionality between the mean free path for the gas molecules and the operating temperature. As described above, Knudsen diffusion itself is pressure independent. Hence, one would expect a higher pressure dependency of the stack at higher operating temperatures. It could be speculated that an additional electrochemical process may be located within the low frequency part of the spectra which could explain the observed behavior. However, this could not be identified within the presented study. Hence, the described temperature behavior during CO₂ electrolysis and the related decrease of the low frequency resistance by increasing the temperature is currently not fully understood and need to be investigated in more detail for the used Ni-CGO electrodes.

Conclusions

Pressurized operation, high conversion rates during co-electrolysis and high partial pressures of CO in the outlet gas composition increase the risk of solid carbon formation in the outlet pipes of SOC test rigs. Since a clogging of the pipe would be related to a damage of the stack, an approach for the prevention of carbon deposition was introduced and could successfully be demonstrated for all measurements shown in this study. A commercially available 10 layer SOC stack was used for an experimental characterization in steam, co- and CO₂-electrolysis mode. The investigated stack consists of electrolyte supported cells with Ni/CGO fuel electrodes and LSCF air electrodes. Test results for steady-state and dynamic operation were demonstrated under elevated operating pressures up to 8 bar. Furthermore EIS analysis was performed in order to investigate the pressure dependency of the SOC performance during co- and CO₂-electrolysis in more detail.

Gas analysis at OCV condition with different inlet volume flows showed that the gas composition at the outlet of the stack was found to be generally in good accordance with the calculated thermodynamic equilibria. Firstly, this indicates the precise supply of the feed gases and the analytical system to work accurately over a wide range of operation in this study. Secondly, it shows that the chemical reactions are fast and the catalytic surface is sufficiently active and available to equilibrate the inlet gases rapidly within the cells via the reverse water-gas shift reaction (rWGS).

Steady-state measurements in co-electrolysis mode with inlet gas compositions with a H/C ratio of 4.67 (60/30/10 H₂O/CO₂/H₂) and 2.44 (45/45/10 H₂O/CO₂/H₂) were performed at 1.4, 4 and 8 bar with a conversion of 70%. The results show that the cell voltages increase at elevated pressure as predicted by the Nernst equation. With increasing current density, the cell voltages of the different pressure levels were found to converge due to decreased activation and diffusion resistances. However, the observed convergence was primarily due to the increased stack temperature which is related to the occurring exothermic methanation reaction

during co-electrolysis operation. Since the polarization resistance of the electrolyte supported cells used in the studied stack are comparably low (pressure independent ohmic resistance ~70% of entire cell resistance), a positive pressure effect on the limiting current density could not be observed. The gas analysis showed a good correlation between experiment and the stack temperature-based calculated thermodynamic equilibrium in all measurements.

Dynamically recorded $U(i)$ -curves were performed both in steam- and co-electrolysis mode. Due to the additionally occurring endothermic rWGS reaction in co-electrolysis, the stack is affected by a more significant cooling effect and shows a slightly lower performance compared to steam electrolysis. However, an estimation of the influence of the reduced temperature on the ohmic resistance indicated that the performance and the ASR within the studied conditions in pure steam- and in co-electrolysis are highly similar.

Out of the steady-state and dynamic measurements, ASR values were derived for both steam and co-electrolysis operation over a wide temperature range. It was clearly observed that the ASR increases with lower H/C ratios at lower temperatures whereas it shows similar values at temperatures above 820 °C. The observation of an increasing ASR with increasing CO₂ content could possibly be explained by a higher resistance caused by the occurrence of direct CO₂ electrolysis during co-electrolysis operation. It could be shown that the CO₂ reduction process reveal a higher activation resistance especially at lower temperatures. Furthermore the diffusion resistance during CO₂ electrolysis was found to show a significantly higher temperature dependence compared to pure steam electrolysis. However, for the studied co-electrolysis operation the difference of the activation and diffusion resistances was found to be marginal indicating that the main reaction pathway for CO production is via the rWGS. Since pure CO₂ electrolysis showed a higher proportion of activation and diffusion resistances compared to the pressure independent ohmic resistance of the cell, the pressure sensitivity was found to be significantly increased for that type of SOC operation mode.

References

- European Commission, *A clean planet for all - A European Strategic Long-Term Vision For a Prosperous, Modern, Competitive and Climate Neutral Economy COM(2018)773* (2018) 1–25 <https://ec.europa.eu/transparency/regdoc/rep/1/2018/EN/COM-2018-773-F1-EN-MAIN-PART-1.PDF>.
- H. Ibrahim, A. Ilinca, and J. Perron, "Energy storage systems-Characteristics and comparisons." *Renew. Sustain. Energy Rev.*, **12**, 1221 (2008).
- A. Evans, V. Strezov, and T. J. Evans, "Assessment of sustainability indicators for renewable energy technologies." *Renew. Sustain. Energy Rev.*, **13**, 1082 (2009).
- P. J. Hall and E. J. Bain, "Energy-storage technologies and electricity generation." *Energy Policy*, **36**, 4352 (2008).
- A. Sternberg and A. Bardow, "Power-to-What?-environmental assessment of energy storage systems." *Energy Environ. Sci.*, **8**, 389 (2015).
- J. C. Koj, C. Wulf, and P. Zapp, "Environmental impacts of power-to-X systems - A review of technological and methodological choices in life cycle assessments." *Renew. Sustain. Energy Rev.*, **112**, p. 865-879 (2019).

7. J. B. Hansen, N. Christiansen, and J. U. Nielsen, "Production of sustainable fuels by means of solid oxide electrolysis." *ECS Trans.*, **35**, 2941-2948 (2011).
8. G. A. Mills, "Status and future opportunities for conversion of synthesis gas to liquid fuels." *Fuel*, **73**, 1243 (1994).
9. X. Sun, M. Chen, S. H. Jensen, S. D. Ebbesen, C. Graves, and M. Mogensen, "Thermodynamic analysis of synthetic hydrocarbon fuel production in pressurized solid oxide electrolysis cells." *Int. J. Hydrogen Energy*, **37**, 17101 (2012).
10. S. H. Jensen, C. Graves, M. Chen, J. B. Hansen, and X. Sun, "Characterization of a planar solid oxide cell stack operated at elevated pressure." *J. Electrochem. Soc.*, **163**, F1596 (2016).
11. S. H. Jensen, X. Sun, S. D. Ebbesen, R. Knibbe, and M. Mogensen, "Hydrogen and synthetic fuel production using pressurized solid oxide electrolysis cells." *Int. J. Hydrogen Energy*, **35**, 9544 (2010).
12. J. E. O. Brien, X. Zhang, and G. K. Housley, *High Temperature Electrolysis Pressurized Experiment Design, Operation, and Results INL/EXT-12-26891* (2012) 1–15 <https://inldigitalibrary.inl.gov/sites/sti/sti/5516323.pdf>.
13. X. Sun et al., "Performance characterization of solid oxide cells under high pressure." *Fuel Cells*, **15**, 697 (2015).
14. E. C. Thomsen, G. W. Coffey, L. R. Pederson, and O. A. Marina, "Performance of lanthanum strontium manganite electrodes at high pressure." *J. Power Sources*, **191**, 217 (2009).
15. G. A. Hughes, J. Railsback, D. M. Butts, and S. A. Barnett, "Electrochemical performance of solid oxide cell oxygen electrodes under pressurization." *ECS Trans.*, **68**, 687 (2015).
16. S. D. Ebbesen, R. Knibbe, and M. Mogensen, "Co-electrolysis of steam and carbon dioxide in solid oxide cells." *J. Electrochem. Soc.*, **159**, F482 (2012).
17. C. Stoots, J. O'Brien, and J. Hartvigsen, "Results of recent high temperature coelectrolysis studies at the Idaho National Laboratory." *Int. J. Hydrogen Energy*, **34**, 4208 (2009).
18. M. Riedel, M. P. Heddrich, and K. A. Friedrich, "Analysis of pressurized operation of 10 layer solid oxide electrolysis stacks." *Int. J. Hydrogen Energy*, **44**, 4570 (2019).
19. B. J. McBride, M. J. Zehe, and S. Gordon, *NASA Glenn Coefficients for Calculating Thermodynamic Properties of Individual Species NASA/TP-2002-211556* (2002) 1–283 <https://www.grc.nasa.gov/WWW/CEAWeb/TP-2002-211556.pdf>.
20. S. Santhanam, M. P. Heddrich, M. Riedel, and K. A. Friedrich, "Theoretical and experimental study of reversible solid oxide cell (r-SOC) systems for energy storage." *Energy*, **141** (2017).
21. M. Henke, J. Kallo, K. A. Friedrich, and W. G. Bessler, "Influence of pressurisation on SOFC performance and durability: A theoretical study." *Fuel Cells*, **11**, 581 (2011).
22. M. Henke, C. Willich, J. Kallo, and K. A. Friedrich, "Theoretical study on pressurized operation of solid oxide electrolysis cells." *Int. J. Hydrogen Energy*, **39**, 12434 (2014).
23. L. Bernadet, G. Gousseau, A. Chatroux, J. Laurencin, F. Mauvy, and M. Reyrier, "Assessment of pressure effects on high temperature steam electrolysis based on solid oxide technology." *ECS Trans.*, **68**, 3369 (2015).
24. M. Henke et al., "A validated multi-scale model of a SOFC stack at elevated pressure." *Fuel Cells*, **13**, 773 (2013).
25. S. D. Ebbesen, X. Sun, and M. B. Mogensen, "Understanding the processes governing performance and durability of solid oxide electrolysis cells." *Faraday Discuss.*, **182**, 393 (2015).
26. X. Yue and J. T. S. Irvine, "Alternative cathode material for CO₂ Reduction by high temperature solid oxide electrolysis cells." *J. Electrochem. Soc.*, **159**, F442 (2012).
27. V. Menon, Q. Fu, V. M. Janardhanan, and O. Deutschmann, "A model-based understanding of solid-oxide electrolysis cells (SOECs) for syngas production by H₂O/CO₂ co-electrolysis." *J. Power Sources*, **274**, 768 (2015).
28. W. G. Bessler and S. Gewies, "Gas concentration impedance of solid oxide fuel cell anodes." *J. Electrochem. Soc.*, **154**, 548 (2007).
29. T. Jacobsen, P. V. Hendriksen, and S. Koch, "Diffusion and conversion impedance in solid oxide fuel cells." *Electrochim. Acta*, **53**, 7500 (2008).
30. M. B. Mogensen, S. D. Ebbesen, S. H. Jensen, X. Sun, A. Hauch, and M. Chen, "Concentration impedance in testing of solid oxide cells revisited." *ECS Trans.*, **78**, 2133 (2017).
31. S. Primdahl, "Gas conversion impedance: a test geometry effect in characterization of solid oxide fuel cell anodes." *J. Electrochem. Soc.*, **145**, 2431 (1998).
32. Y. Tanaka, M. P. Hoerlein, and G. Schiller, "Numerical simulation of steam electrolysis with a solid oxide cell for proper evaluation of cell performances." *Int. J. Hydrogen Energy*, **41**, 752 (2016).
33. S. Primdahl, "Gas diffusion impedance in characterization of solid oxide fuel cell anodes." *J. Electrochem. Soc.*, **146**, 2827 (1999).
34. M. Henke, J. Kallo, K. A. Friedrich, and W. G. Bessler, "Influence of pressurisation on SOFC performance and durability: a theoretical study." *Fuel Cells*, **11**, 581 (2011).
35. J. Aicart, M. Petitjean, J. Laurencin, L. Talloire, and L. Dessemond, "Accurate predictions of H₂O and CO₂ co-electrolysis outlet compositions in operation." *Int. J. Hydrogen Energy*, **40**, 3134 (2015).
36. J. Wei and E. Iglesia, "Isotopic and kinetic assessment of the mechanism of reactions of CH₄ with CO₂ or H₂O to form synthesis gas and carbon on nickel catalysts." *J. Catal.*, **224**, 370 (2004).
37. Q. Fang, C. E. Frey, N. H. Menzler, and L. Blum, "Electrochemical performance and preliminary post-mortem analysis of a solid oxide cell stack with 20,000 h of operation." *J. Electrochem. Soc.*, **165**, F38 (2018).
38. S. Primdahl and M. Mogensen, "Mixed conductor anodes: Ni as electrocatalyst for hydrogen conversion." *Solid State Ionics*, **152–153**, 597 (2002).
39. M. Riegraf, R. Costa, G. Schiller, K. A. Friedrich, S. Dierickx, and A. Weber, "Electrochemical impedance analysis of symmetrical Ni/gadolinium-doped ceria (CGO10) electrodes in electrolyte-supported solid oxide cells." *J. Electrochem. Soc.*, **166**, F865 (2019).

Article III:

Investigation of the Long-term Stability of Solid Oxide Electrolysis Stacks under Pressurized Conditions in Exothermic Steam and Co-electrolysis Mode.

M. Riedel, M.P. Heddrich, K.A. Friedrich,
Fuel Cells, Vol. 20 (2020), 592-607.

DOI: <https://doi.org/10.1002/fuce.202000011>.



Investigation of the Long-term Stability of Solid Oxide Electrolysis Stacks under Pressurized Conditions in Exothermic Steam and Co-electrolysis Mode

M. Riedel¹*, M. P. Heddrich¹, K. A. Friedrich^{1,2}

¹ German Aerospace Center (DLR), Institute of Engineering Thermodynamics, Pfaffenwaldring 38–40, 70569 Stuttgart, Germany

² University of Stuttgart, Institute of Building Energetics, Thermal Engineering and Energy Storage (IGTE), Pfaffenwaldring 31, 70569 Stuttgart, Germany

Received February 11, 2020; accepted May 18, 2020; published online September 01, 2020

Abstract

In this study three identically constructed ten-layer stacks with electrolyte supported cells were tested in exothermic steam and co-electrolysis mode at elevated pressures of 1.4 and 8 bar. Investigations during constant-current operation at a current density of -0.5 A cm^{-2} and a reactant conversion of 70% over 1,000–2,000 h were carried out. The inlet gas composition for steam electrolysis was 90/10 ($\text{H}_2\text{O}/\text{H}_2$) and 63.7/31.3/3.3/1.7 ($\text{H}_2\text{O}/\text{CO}_2/\text{H}_2/\text{CO}$) for co-electrolysis operation. All stacks showed highly similar resistances at the beginning of the tests indicating a high level of accuracy and repeatability during manufacturing. The stack operated in steam electrolysis mode at 1.4 bar showed comparably low degradation of $8 \text{ mV kh}^{-1} \text{ cell}^{-1}$, whereas the stack operated at 8 bar showed an approximately four times higher degrada-

tion. The third stack was operated in co-electrolysis mode at 1.4 and 8 bar and showed noticeably higher degradation rates than during steam electrolysis mode. The predominant increase of the ohmic resistance during operation was identified to be mainly responsible for the observed degradation of all three stacks, whereas the increase of the polarization resistances played a subordinate role. Within the post-test analysis, noticeably high nickel depletion was observed for the stack operated at the highest pressure in steam electrolysis mode. Furthermore, partial delamination of electrodes was observed. The degradation is discussed with relation to phenomena and experimental parameters during operation.


Keywords: Degradation, Pressure, Solid Oxide Electrolysis Cell, SOEC, 10-cell Stack

1 Introduction

Solid oxide electrolyzers are known as efficient energy converters for producing hydrogen or synthesis gas (H_2+CO) from steam and/or CO_2 . Due to the high operating temperatures, solid oxide electrolysis cells (SOECs) offer significant benefits in terms of fast kinetics, reduced electrochemical losses and high electrical-to-chemical conversion efficiencies. Furthermore, the produced hydrogen or synthesis gas can be used as feedstock for the production of base chemicals or synthetic fuels in downstream processes like Fischer-Tropsch or methanol synthesis. However, the respective downstream reactors are typically operated at elevated pressures in the range of 10 to 60 bar to achieve high conversion or high yield. Since the cell performance was already shown to improve due

to reduced overpotentials the combination of SOEC stacks and the downstream reactors in one pressurized system could be highly beneficial [1–3]. However, studies investigating the performance of stacks with electrolyte supported cells showed that the influence of pressurized operation on the electrochemical performance is low [4–7]. The decrease of overpotentials

[*] Corresponding author, Marc.Riedel@dlr.de

 This is an open access article under the terms of the Creative Commons Attribution-NonCommercial License, which permits use, distribution and reproduction in any medium, provided the original work is properly cited and is not used for commercial purposes.

may not be high compared to the pressurized operation of cathode supported cell concepts. Nevertheless, the direct coupling of SOECs to downstream processes can lead to additional advantages on system level. For instance, liquid water and CO₂ compression need significantly less energy than steam, hydrogen or syngas compression [1,8]. Furthermore, the coupling of the electrolysis and synthesis processes enable close process integration and intensification synergies like significantly reduced or omitted compression work of the produced hydrogen or syngas before entering the downstream synthesis. However, certain challenges related to the design and the operation of pressurized SOECs and combined systems have to be considered. Increased pressure differences between anode, cathode or the surrounding atmosphere have to be avoided since it can lead to the destruction of the electrochemical device [9]. Furthermore, the produced oxygen on the anode side has to be flushed from the electrode and individual safety restrictions related to the maximum oxygen concentration in the outlet can lead to significant use of air, N₂ or CO₂ for dilution. A compression of the flushing medium and its recirculation could be required in order to avoid severe losses in process efficiency. These criteria have to be considered and evaluated for each individual system need.

However, both pressurized and non-pressurized SOEC systems with relevant power output are still under development and need to fulfill certain criteria to become of broad economic and commercial interest. The performance stability of the stacks in long-term operation is one of the key factors for competitiveness and the feasibility to enter into mass market.

On cell level several experimental studies were carried out and degradation mechanisms were already proposed [10–15]. However, the reported degradation data are mostly hard to compare since cell concepts, materials and experimental conditions such as reactant flows, gas composition, conversion, voltage or current density strongly differ from one study to the other. Experimental investigations on the long-term stability of SOEC stacks are less available but highly required to identify and promote potential developments on cell, stack or system level [5, 16–23].

In this study, three identically constructed ten-layer stacks with electrolyte supported cells were tested in exothermic steam and co-electrolysis mode at elevated pressures of 1.4 and 8 bar. Investigations during constant-current operation over 1,000–2,000 h were carried out. Electrochemical impedance spectroscopy (EIS) and post-test analysis (PTA) *via* scanning electron microscopy (SEM) and energy-dispersive X-ray spectroscopy (EDX) was used, in order to identify the influence of the operating pressure on the performance stability and microstructural changes of the cells in more detail.

2 Experimental

In order to investigate the long-term stability of SOCs operated at different pressures, three commercially available stacks with ten electrolyte supported cells (ESC) were evaluated.

Each cell has an active area of 127.8 cm² and consists of an approximately 55 μm thick lanthanum strontium cobalt ferrite oxide (LSCF) oxygen electrode, a 90 μm thick yttria-stabilized zirconia (3YSZ) electrolyte and a 30 μm thick nickel gadolinia-doped ceria (Ni-GDC) composite as fuel electrode. Additionally, a thin GDC layer is used between the electrolyte/fuel electrode and the electrolyte/air electrode, respectively.

Within this study, constant-current long-term tests were performed both in steam electrolysis and co-electrolysis mode. The pure steam electrolysis operation was examined with two stacks over 1,000 h at 1.4 bar, and over 2,000 h at 8 bar. Within these experiments an inlet gas composition with molar fractions of 90% H₂O and 10% H₂ was used. The third stack was mainly investigated in co-electrolysis mode at two different pressures (1.4 and 8 bar) with an inlet gas composition with molar fractions of 63.7% H₂O, 31.3% CO₂, 3.3% of H₂, and 1.7% CO. However, the first 160 h were conducted in steam electrolysis mode to enable comparability. All experiments were performed at a furnace temperature of 800 °C and a current density of -0.5 A cm^{-2} . The inlet mass flows were set for a constant reactant conversion (RC) of 70%. Table 1 gives an overview about the stacks A–C used in this study and the associated experiments.

The stacks are housed into gas tight steel boxes due to the open oxygen electrode design of each repeating unit. Each repeating unit of the stack consists of two fuel gas inlets and two fuel gas outlets. Along the cell length, gas channels within the fuel electrode and air electrode compartment distribute the media in co-flow condition. More details about the stack configuration with modeling and experimental results of the temperature distribution along and across the stack and its repeating units can be found elsewhere [24–26]. During the experiments the oxygen electrodes of each stack were flushed with 1 slpm per cell air to prevent the accumulation of pure oxygen with its corrosive characteristic in the outlet pipes of the testing facility. This led to an oxygen outlet content of 36% at the defined operating point with 70% of reactant conversion. For measuring the temperatures inside the stack during operation, an overall number of five thermocouples with a diameter of 0.25 mm are placed directly on certain oxygen electrode layers. However, the thin thermocouples sometimes fail due to mechanical stress inside the steel box. As Figure 1 shows, one thermocouple each is placed at the middle length of layer one and layer ten. The remaining three thermocouples are placed at quarter, half and three-quarter lengths of layer five. Due to test housing restrictions, the ten cells within the stacks of this study are electrically packaged into five cell

Table 1 Overview of the experiments conducted with the three stacks A–C.

Description	Operation mode	Pressure / bar	Duration / h
Stack A	Steam electrolysis	1.4	1,000
Stack B	Steam electrolysis	8	2,000
Stack C	Steam & Co-electrolysis	1.4 and 8	1,000

Fuel Cells

Riedel et al.: Investigation of the Long-term Stability of Solid Oxide Electrolysis Stacks

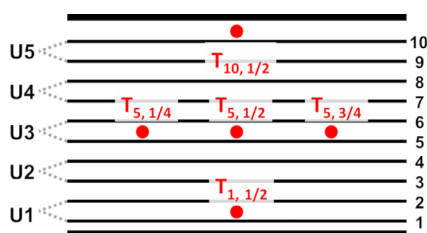


Fig. 1 Sketch of the 10-layer stack with the positioning of the five thermocouples ($T_{i,j}$) and a depiction of the electrical packaging into five cell blocks.

blocks. Hence, the cell voltages of two cells are measured in series. A further description of the pressurized test facility as well as the design of the stack housing can be found elsewhere [5, 7].

In order to monitor the outlet gas composition during the co-electrolysis experiment, a Rosemount X-Stream analyzer with sensors for H_2 , CO , CO_2 , and CH_4 is connected to the test facility. Due to the measuring principle of this analyzer, the steam of the gas mixture is removed *via* a compressor chiller operated at $3^\circ C$. All gases can be analyzed in a range of 0–100% with an accuracy of $\leq \pm 1\%$ points.

At the beginning of the tests and several times within the experiment, electrochemical impedance spectroscopy (EIS) was carried out at the operating point, in order to evaluate the time-dependent change of the resistances. The frequency range was from 0.05 Hz to 20 kHz with ten points per decade and an amplitude of 0.96 A. The impedance spectra were recorded using a Zahner Zennium impedance analyzer. After the degradation tests, the three stacks were disassembled and the middle cells of the stacks were used for post-test analysis *via* scanning electron microscopy (SEM) and energy-dispersive X-ray spectroscopy (EDX).

3 Results and Discussion

The increased partial pressure of the reactants under pressurized operation leads to an increased Nernst voltage, due to well-known thermodynamic relations [2]. In order to secure exact measurements, the open circuit voltages (OCV) of all the three stacks were monitored and compared with the theoretical Nernst voltages (U_{Nernst}) at $800^\circ C$ before starting the long-term experiments. For stack A and B a gas composition of 90/10 (H_2O/H_2), for stack C the co-electrolysis mixture of 63.7/31.3/3.3/1.7 ($H_2O/CO_2/H_2/CO$) was used. Note that the table presents the voltages of two layers due to the described electrical series connection of two cells within the stacks.

As shown within Table 2, the OCVs of all stacks are in good agreement with the theoretical (doubled) Nernst voltage indicating an exact dosage of the gas flows for all experiments and negligible leakages inside the

studied stacks. However, stack A shows an apparent deviation of the four upper layers with a significantly decreased OCV. Though these cells showed low voltages during non-loaded conditions, the measured temperatures within the stack did not exceed furnace temperature. This would be clearly noticeable in case of a cell crack and corresponding oxidation of the hydrogen content of the feed in the anode or cathode compartment. Furthermore, the four upper layers did not show any negative influence on the overall stack performance during operation over 1,000 h (see Section 3.1). Hence, one can assume that the apparent low voltages of the cells were caused by electrical wiring problems within the testing facility. Apart from these layers of stack A, the maximum deviation between the experimentally obtained and theoretically calculated block voltage is 1 mV for stack A, 4 mV for stack B, and 6 mV for stack C.

Figure 2 shows the ohmic resistance of each stack at the operating current density of $-0.5 A cm^{-2}$ with its predefined gas composition before the start of the long-term tests. The depicted temperature was measured with the thermocouple placed at the middle length of the air electrode of layer 5 ($T_{5,1/2}$). It was already shown by the authors that this temperature can be taken as the characteristic stack temperature in steam electrolysis mode [5]. The ohmic resistance of stack A showed a value of $0.670 \Omega cm^2$ at a characteristic temperature of $825.3^\circ C$. Stack B and stack C showed characteristic

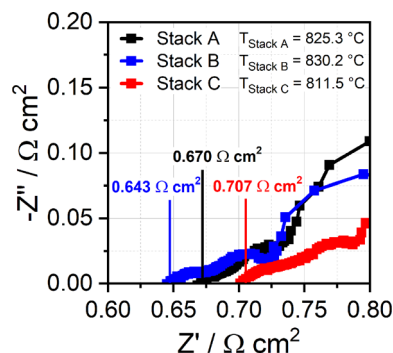


Fig. 2 Impedance spectra of the three stacks at constant-current operation ($-0.5 A cm^{-2}$) before the long-term tests. Stack A is operated at 1.4 bar, stack B at 8 bar in steam electrolysis mode and stack C is operated in co-electrolysis mode at 1.4 bar.

Table 2 OCV values of the three stacks with an inlet gas composition of 90/10 (H_2O/H_2) for stack A (1.4 bar) and B (8 bar) and 63.7/31.3/3.3/1.7 ($H_2O/CO_2/H_2/CO$) for stack C (1.4 bar). The values in brackets indicate the (averaged) single cell voltages.

	Voltage stack A / V (single cell voltage / V)	Voltage stack B / V (single cell voltage / V)	Voltage stack C / V (single cell voltage / V)
Theoretical voltage	1.695 (0.848)	1.776 (0.888)	1.628 (0.814)
Layer 1+2	1.694 (0.847)	1.779 (0.890)	1.623 (0.812)
Layer 3+4	1.695 (0.848)	1.779 (0.890)	1.622 (0.811)
Layer 5+6	1.694 (0.847)	1.780 (0.890)	1.624 (0.812)
Layer 7+8	0.820 (0.410)*	1.778 (0.889)	1.624 (0.812)
Layer 9+10	0.748 (0.374)*	1.780 (0.890)	1.623 (0.812)

temperatures of 830.2 °C and 811.5 °C, and ohmic resistances of 0.643 Ω cm² and 0.707 Ω cm², respectively. The measured ohmic resistances of the stacks at the defined operating point correlate well with the temperature dependency published in [5].

The differences of the ohmic resistances can be attributed to the different operating conditions of the stacks. In particular, stack B is operated at higher pressure leading to a higher voltage and consequently a higher temperature. Stack C operates at a reduced temperature due to the additionally occurring endothermic reversed water-gas shift (rWGS) reaction while operating in co-electrolysis mode. Hence, it can be concluded that all the studied stacks show highly similar resistances at the beginning of the tests indicating a decent level of accuracy and repeatability during manufacturing.

3.1 1,000 h Steam Electrolysis Operation at 1.4 bar

Figure 3 shows the result of the first long-term test over 1,000 h at an operating pressure of 1.4 bar in steam electrolysis mode. At the current density of -0.5 A cm^{-2} and a furnace temperature of 800 °C the ESC stack is operated exothermically at approximately 1.33 V per cell at the start of the test. The values shown for the single cell voltage are derived from the layers 5+6 of the ten-layer stack, whereas the measured temperature was derived from $T_{5,1/2}$. The total area specific resistance (ASR_{total}) was calculated at steady state condition based on the single cell voltage and the averaged theoretical Nernst voltage ($U_{\text{Nernst, avg}}$) at the applied current density:

$$ASR_{\text{total}} = (U_{\text{measured}} - U_{\text{Nernst, avg}}) / i \quad (1)$$

The Nernst voltage is determined according to the averaged gas composition between the inlet and the outlet of the

stack [4]. Due to the analysis shown in Table 1 and the derived negligibility of leakages inside the stacks, assuming the outlet gas composition to be defined purely by current and thermodynamic equilibrium is valid. $U(t)$ and $T(t)$ over 1,000 h can be found in a previous analysis by the authors [5]. However, the authors will focus on the analysis of the ASR behavior under the different experimental conditions shown within the current study and the comparison with the long-term tests of the identically constructed stacks B and C. As regards the completeness, the normalized ohmic resistance (ASR_{Ω}) and normalized polarization resistance (ASR_{pol}) are shown within the diagram according to the related results of the impedance study of Figure 5. The values of the ohmic resistance were obtained from the EIS data, whereas the polarization resistance was calculated as the difference between ASR_{total} and ASR_{Ω} , thus not considering the conversion recorded in EIS. The small voltage and temperature peaks which can be observed at every 200 h of operation are due to the switch between EIS analyzer and the load of the test rig. In contrast to the previous analysis, the time for the switch and the recording of the EIS spectra was not considered for the time of operation shown in Figure 3.

The voltage shows a nearly linear increase of 8 mV over the 1,000 h of operation. Accordingly, the ASR_{total} increases by 18 mΩ cm². Due to the increasing voltage, the characteristic cell temperature increases by 3.13 K kh⁻¹. The authors want to point out that contrary to the authors' previous studies and many other publications the degradation rates will not be given in percentages, since this specification is highly dependent on the operating voltage and can lead to wrong interpretation of the degradation [5, 14, 16–20, 27–31]. The indication of the shift in voltage and ASR during the operating time leads to much better comparability of experimental studies.

Figure 4a shows the behavior of the layers within this long-term experiment. As already shown by the results during OCV operation in Table 2, lower voltages of the layers 7+8 and 9+10 over the complete operating time were observed. Furthermore, the respective layers show a highly instable voltage behavior with a volatility of more than 200 mV. However, the remaining layers showed stable voltages over the complete operating time favoring the assumption of an electrical wiring issue within the testing facility of the layers 7+8 and 9+10. Layer 1+2 showed a rapidly decreasing voltage at around 400 h of operation. However, Figure 4b supports the hypothesis that this behavior was not caused by a crack in one of the cells or of some glass sealing since the thermocouple at the middle length of layer 1 ($T_{1,1/2}$) did not show any unduly behavior of the temperature. This indicates that the voltage decrease was likely caused by a loss of contact or a short circuit within the testing facility. The thermocouple $T_{1,1/2}$ broke completely approximately 100 h later. If the sensor failure of $T_{1,1/2}$ and the earlier observed decreased voltage of layer 1+2 may be related to each other, could not be finally clarified within the PTA. However, all remaining measured temperatures within the stack increased according to the cell voltages linearly over the 1,000 h of operation.

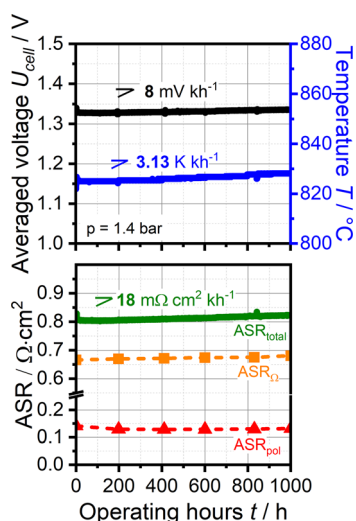


Fig. 3 Constant-current steam electrolysis operation over 1,000 h at 1.4 bar and 800 °C furnace temperature with stack A. The gas inlet composition was 90% H₂O with 10% H₂. The mass flow on the fuel side was set for a reactant conversion of 70% at a current density of -0.5 A cm^{-2} . $U(t)$ and $T(t)$ were taken from [5], normalized ohmic and polarization resistances were added according to the EIS and ASR analysis.

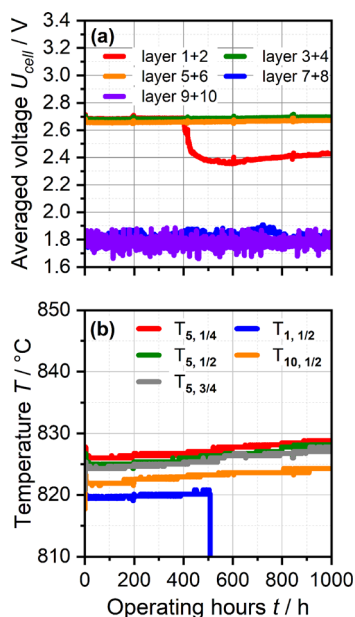


Fig. 4 a) Voltage behavior of the ten layers, and b) measured temperature trend within the stack A over 1,000 h of operation at 1.4 bar in constant-current steam electrolysis mode.

Table 3 gives an overview of the voltage and ASR shifts of stack A. As described earlier, the layers 1+2, 7+8, and 9+10 showed a conspicuous voltage behavior during the test and were not considered for evaluating the degradation rates (labelled with *). Hence, the averaged voltage shift per cell was 8 mV kh^{-1} and the ASR per cell increased by $18 \text{ m}\Omega \text{ cm}^2 \text{ kh}^{-1}$.

The increasing stack temperature over the operating time leads to an improved ionic conductivity of the electrolyte material. Since its temperature dependency was already studied in detail by the authors, a temperature corrected ASR shift can be calculated according to [5]. The increase of 3.13 K leads to a decrease of the ohmic resistance by $13 \text{ m}\Omega \text{ cm}^2$. Hence, the temperature corrected ASR shift is $30 \text{ m}\Omega \text{ cm}^2 \text{ kh}^{-1}$ and $31 \text{ m}\Omega \text{ cm}^2 \text{ kh}^{-1}$, respectively.

Impedance spectra were recorded every 200 h of operation during the long-term experiment at the operating point. The $-Z(f)$ spectra do not show a significant change within the recorded frequency range indicating a minor effect on the electrodes and their resistances. However, the Nyquist plots in the inset of Figure 5 show that the ohmic resistance increases with

Table 3 Overview of the degradation rates of the respective layers of stack A.

Layer	Voltage at 0 h / V (single cell voltage at 0 h / V)	Voltage at 1,000 h / V (single cell voltage at 1,000 h / V)	Voltage shift / $\text{mV kh}^{-1} \text{ cell}^{-1}$	ASR increase / $\text{m}\Omega \text{ cm}^2 \text{ kh}^{-1} \text{ cell}^{-1}$
1+2	2.686 (1.343)	2.435* (1.218*)	*	*
3+4	2.682 (1.341)	2.698 (1.349)	8	18
5+6	2.657 (1.329)	2.672 (1.336)	8	17
7+8	1.769* (0.885*)	1.751* (0.876*)	*	*
9+10	1.799* (0.900*)	1.793* (0.897*)	*	*

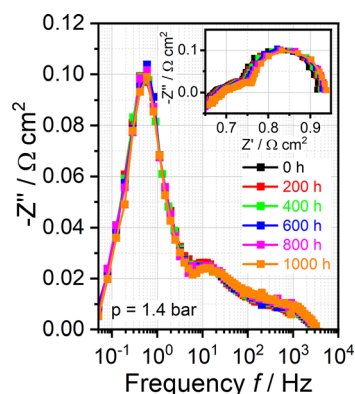


Fig. 5 Impedance data of the 1,000 h experiment conducted at 1.4 bar in steam electrolysis at -0.5 A cm^{-2} with stack A. The data showing the Nyquist plots in the inset is taken from [5].

increasing operating time, as shown within a previous study [5]. The averaged ohmic resistance increased about $18 \text{ m}\Omega \text{ cm}^2$ compared to the begin of the study which is in agreement with the calculated ASR increase shown in Table 3 for the analyzed layers. Hence, it can be concluded that the observed overall degradation of the stack can be mainly ascribed to an increase of the ohmic resistance and the polarization resistances to be affected marginally within this experiment.

3.2 2,000 h Steam Electrolysis Operation at 8 bar

Figure 6 shows the result of the long-term test over 2,000 h at an operating pressure of 8 bar in steam electrolysis mode. The higher pressure leads to higher voltages due to well-known thermodynamic relations. However, activation and diffusion resistances are known to decrease with increasing pressure and could lead to an overall better performance of the stack [32,33]. As already shown by the authors, the studied ESC stack does not show a significant pressure effect since the performance is majorly influenced by the pressure independent ohmic resistance [5,7]. Due to this aspect, the increased pressure led to a higher voltage of the stack and hence to a more significant exothermic operation behavior than the experiment conducted at 1.4 bar. In particular, stack B showed a temperature of 830°C and a voltage of the middle cell of 1.351 V at the beginning of the test. Thus, stack B was operated at a 5 K higher characteristic temperature and a 22 mV higher voltage per cell than stack A.

The voltage shows a nearly linear increase of 31 mV over the first 1,000 h of operation. The ASR increases with $68 \text{ m}\Omega \text{ cm}^2$ during this operating time. Due to the increasing voltage, the characteristic cell temperature increased by 10.4 K. According to the temperature relation of the ohmic resistance presented in [5], the temperature corrected ASR shift is $107 \text{ m}\Omega \text{ cm}^2$. After 1,450 h of steam electrolysis operation, the experiment was conducted in fuel cell mode for 150 h with a gas composition of 75/25 H_2/N_2 at a current

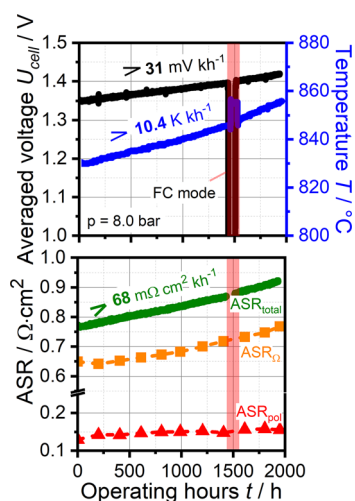


Fig. 6 Constant-current steam electrolysis operation over 2,000 h at 8 bar and 800 °C furnace temperature with stack B. The gas inlet composition was 90% H₂O with 10% H₂. The mass flow on the fuel side was set for a reactant conversion of 70% at a current density of -0.5 A cm^{-2} . Additionally, fuel cell mode was performed over 150 h.

density of 0.21 A cm^{-2} and a RC of 33%. The low current and RC was chosen to operate the stack in the approved temperature range below 860 °C while the same furnace temperature as in steam electrolysis mode (800 °C) could be used. Consequently, the stack showed an averaged cell voltage of 0.867 V and a characteristic temperature of 855.5 °C due to the exothermic fuel cell operation. The fuel cell mode was conducted in order to test the influence of the reversed operation on the stack degradation. Publications showing both a positive and a negative influence of a reversible cycling operation on the long-term performance of a SOC can be found in literature [15, 21, 34]. In case of an observed superior stability, it was hypothetically achieved due to eliminating the microstructural degradation mechanism that occurs when a high oxygen partial pressure near the oxygen-electrode/electrolyte interface is present [34]. However, a study over 2,000 h with a 30-layer stack conducted at DLR showed the SOFC/SOEC cycling to lead to a higher degradation than during stationary steam electrolysis operation [21]. The authors are aware that whichever the outcome, the experimental conditions within the present study are different since extensive cycling was not performed. The degradation of stack B during the short fuel cell operation was observed to be similar to the electrolysis mode. However, the degradation during the subsequent 450 h of steam electrolysis operation increased significantly with 19 mV (42 mV kh^{-1}), $43 \text{ m}\Omega \text{ cm}^2$ ($95 \text{ m}\Omega \text{ cm}^2 \text{ kh}^{-1}$), and a stack temperature increase of 8 K (18 K kh^{-1}). Consequently, the operation in fuel cell mode turned out to lead to an accelerated degradation within this experiment.

Figure 7a shows the behavior of all layers within this long-term experiment over 2,000 h at 8 bar. Layer 1+2 and 9+10, i.e., the outer layers of the stack, show the highest voltage since their performance is influenced by heat losses towards the lower furnace temperature and the consequently higher resistance of these cells.

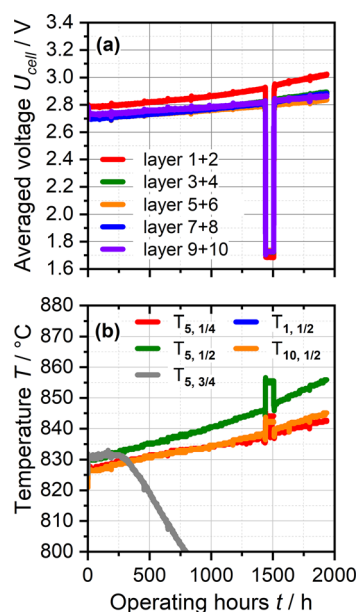


Fig. 7 a) Voltage behavior of the ten layers, and b) measured temperature trend within the stack B over 2,000 h of operation at 8 bar in constant-current steam electrolysis mode.

In particular, layer 1+2 showed an apparently higher voltage over the complete range of operating time. This is in agreement with observations within the 1.4 bar test over 1,000 h where layer 1+2 showed the lowest temperature and accordingly the highest voltage. This phenomenon can most likely be attributed to a slightly lower temperature at the bottom of the furnace environment. At higher pressure the heat losses from the stack box towards the furnace environment become more prominent due to increased convection and lead to an even lower temperature of the bottom cells of the stack. Unfortunately, the sensor of $T_{1,1/2}$ failed already during the heat-up of the stack. Moreover a slight exponential voltage growth of layer 1+2 can be observed whereas the other layers show a more linear characteristic. The measured temperatures plotted in Figure 7b also show a linear increase, though $T_{5,1/2}$ increases with a higher slope than the other temperatures measured within the stack. The thermocouple placed at quarter-length of layer five showed an increase of 15.6 K ($T_{5,1/4}$) and the sensor placed at the middle length of layer ten of 18.1 K over the complete 2,000 h of operation. $T_{5,1/2}$ increased with 25.7 K. Since this thermocouple also showed an offset of 6 K after the long-term test under 95/5 N₂/H₂ forming gas, the slightly increased slope of the measured temperature can be attributed to a drift of $T_{5,1/2}$. However, the impact of the drift (<10 K) on the calculated ASR is rather small. By taking $T_{10,1/2}$ for the ASR calculation the resistance would solely increase $6 \text{ m}\Omega \text{ cm}^2$ less.

Table 4 gives an overview of the voltage and ASR shifts of stack B. Note that the voltage and ASR shift rates are shown in the specific unit per cell for the first kh.

The average voltage shift per cell was 33 mV kh^{-1} , and the ASR per cell increased by $72 \text{ m}\Omega \text{ cm}^2 \text{ kh}^{-1}$ over the first

Fuel Cells

Riedel et al.: Investigation of the Long-term Stability of Solid Oxide Electrolysis Stacks

Table 4 Overview of the degradation rates of the ten layers of stack B.

Cell layer	Voltage at 0 h / V (single cell voltage at 0 h / V)	Voltage at 1,000 h / V (single cell voltage at 1,000 h / V)	Voltage shift / mV kh ⁻¹ cell ⁻¹	ASR increase / mΩ cm ² kh ⁻¹ cell ⁻¹
1+2	2.788 (1.394)	2.864 (1.432)	38	82
3+4	2.703 (1.352)	2.780 (1.390)	39	82
5+6	2.701 (1.351)	2.763 (1.382)	31	68
7+8	2.701 (1.351)	2.772 (1.386)	36	77
9+10	2.739 (1.370)	2.786 (1.393)	24	53

1,000 h. The average temperature corrected ASR shift is 101 mΩ cm² kh⁻¹. Consequently, the experiment conducted at 8 bar showed both in voltage and ASR an almost four times higher degradation than at 1.4 bar. The authors are aware that this has no statistical significance, but both experiments conducted at 1.4 and 8 bar indicate a significant impact of the operating pressure on the long-term stability. Furthermore, after the operation in fuel cell mode the average voltage shift for the remaining 450 h in electrolysis mode was 26 mV per cell (58 mV kh⁻¹) and the ASR per cell increased by 55 mΩ cm² (122 mΩ cm² kh⁻¹). Hence, it can be concluded that the fuel cell mode had a significantly worsening effect on the performance stability of the stack since the degradation accelerated by almost 60%. One possible explanation for the higher degradation might be the increased transversal and longitudinal temperature gradients within the stack during the highly exothermic fuel cell operation. These temperature gradients cause thermomechanical stress within the cell structure and might lead to contact losses of the fuel or the air electrode from the electrolyte [35,36]. The weakened contact at the electrode/electrolyte interface could consequently lead to extended contact losses in the subsequent full loaded electrolysis operation and increased ohmic resistances.

Impedance spectra were recorded every 200 h of operation during the long-term experiment at -0.5 A cm⁻².

The -Z(f) diagram in Figure 8 shows the visible peaks at approximately 10 and 1,500 Hz to shift towards higher values on the imaginary axis with increasing operating time. Though the peaks in a -Z(f) diagram generally do not fully describe resistances, higher imaginary values nevertheless indicate increasing resistances. In particular, the processes around 10³ Hz and 10¹ Hz can be attributed to the air electrode and fuel electrode of the ESC stack, respectively [7]. Consequently, both electrodes show a considerable performance loss during the experiment. However, the Nyquist plots in the inset of Figure 8 show that the increased electrode resistances play a subordinate role compared to the predominant change of the ohmic resistance. The primarily increased ohmic resistance could be attributed to Nickel depletion and the consequently longer O²⁻ pathway as it was already described in literature [14, 27, 37, 38] (see Section 3.5.2).

3.3 Co-electrolysis over 1,000 h

Figure 9 shows the result of the long-term test over 1,000 h at operating pressures of 1.4 and 8 bar in steam and co-electrolysis mode. During the first 160 h of operation, steam electrolysis at 1.4 bar was conducted in order to enhance the comparability with the test of stack A. An averaged voltage increase of 3 mV for the layer 5+6 was observed for stack C. This is in good agreement with the experiment of stack A where a voltage increase of 2 mV was measured during the first 160 h.

The authors are aware that this short period of testing in steam electrolysis mode at 1.4 bar does not allow a profound forecast of the degradation over 1,000 h. However, it strongly indicates that the long-term stability of the ESC stacks A and C in steam electrolysis is similar and the recorded data is valid.

After the 160 h of steam electrolysis, co-electrolysis operation at 1.4 bar was conducted for 500 h. Due to the operation with CO₂ in the feed gas and the additional occurrence of the endothermic reverse water-gas shift (rWGS) reaction, the stack operating temperature was significantly lower which subse-

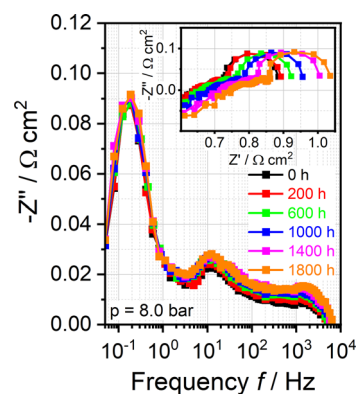


Fig. 8 Impedance data of the 2,000 h steam electrolysis experiment conducted at 8 bar with stack B.

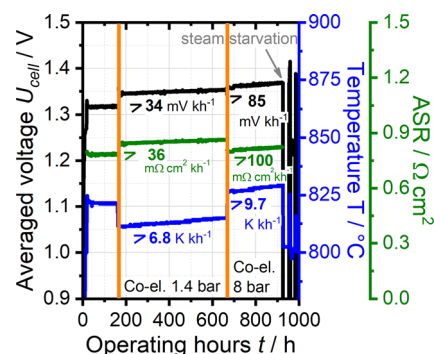


Fig. 9 Constant-current operation in steam and co-electrolysis mode over 1,000 h at 1.4 bar and 8 bar with stack C. The gas inlet composition was 90/10 (H₂O/H₂) in case of steam electrolysis and 63.7/31.3/3.3/1.7 (H₂O/CO₂/H₂/CO) during co-electrolysis operation. The mass flow on the fuel side was set for a constant reactant conversion of 70% at a current density of -0.5 A cm⁻².

quently led to a higher voltage. An accelerated degradation was observed during this operational regime. The voltage increased by 17 mV which corresponds to a voltage shift rate of 34 mV kh^{-1} and an increase of the ASR of $36 \text{ m}\Omega \text{ cm}^2 \text{ kh}^{-1}$. Due to the increasing voltage the temperature increased by 3.4 K (6.8 K kh^{-1}). The temperature corrected ASR can be calculated to $68 \text{ m}\Omega \text{ cm}^2 \text{ kh}^{-1}$. Compared to steam electrolysis operation conducted at the same pressure with stack A, the performance loss during co-electrolysis mode almost doubled.

Figure 9 shows that the co-electrolysis operation at an elevated pressure of 8 bar led to an even more significant degradation than at 1.4 bar. During the 260 h of operation, the voltage increased by 85 mV kh^{-1} and the ASR by $100 \text{ m}\Omega \text{ cm}^2 \text{ kh}^{-1}$. This implies an approximately three times higher degradation compared to the low pressure operation.

Figure 10a shows the behavior of the stack layers within this long-term experiment over 1,000 h. Layer 1+2 and 9+10, i.e., the outer layers of the stack, showed the highest voltage since their performance is majorly influenced by the heat losses towards the lower furnace temperature and the consequently higher resistances of these cells. It can be seen, that the operation at the higher voltage led to a significantly increased degradation within this study.

Furthermore, a comparison between the recorded temperatures at 1.4 and 8 bar showed the stack temperature gradients to increase significantly at higher pressure. This phenomenon is caused by (i) an increase of internal heat production due to the increased extent of exothermic methanation reaction, and (ii) caused by increased heat losses of the stack towards the lower furnace temperature due to a higher ΔT and the increase of convection at higher operating pressure. As can be seen in Figure 10, the thermocouples $T_{1,1/2}$ measuring close to the bottom and $T_{10,1/2}$ measuring close to the top of the stack

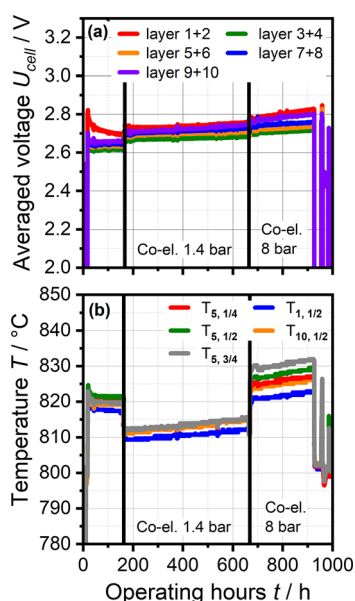


Fig. 10 a) Voltage behavior of the ten layers, and b) measured temperature trend within the stack over 1,000 h at both 1.4 and 8 bar in constant-current steam and co-electrolysis mode.

show the lowest temperature. In contrary, at three-quarter length of layer 5 ($T_{5,3/4}$) the highest temperature and probably the hotspot within these experimental conditions was observed. The location of this hotspot is in good agreement with a thermal 3D simulation of the stack in exothermic fuel cell mode [25].

During the co-electrolysis operation at both 1.4 and 8 bar, the outlet gas composition of the stack was monitored *via* a gas analyzer and showed the molar fractions to follow the thermodynamic equilibrium. This behavior has already been shown within detailed co-electrolysis studies by the authors [7, 29, 39].

At 930 h, a malfunction of the water pump for the steam supply occurred and the automated safety procedures of the test rig triggered a load shedding. Figure 11 shows the behavior of the voltages and the simultaneously recorded analysis of the outlet gas composition in detail. Note that the molar fraction of H_2O is not analyzed since H_2O is removed from the gas mixture upstream of the analyzer.

The malfunction of the water pump led to steam starvation and in turn to a voltage increase as well as a voltage fluctuation of almost 20 mV per cell. In particular, the outer layers of the stack showed the most significant influence and voltage increase since their temperature was lowest during operation. The authors assume a small gas bubble entered and remained in one piston of the liquid water pump of the test rig and considerably decreased the mass flow for evaporation. The gas analysis in Figure 11b shows the outlet gas composition during this time period with decreasing fractions of CO_2 and H_2 and increasing fractions of CO and CH_4 , respectively. Based on the gas analysis, a decrease of the steam supply by almost 40% could be calculated which led to a RC of 94% within the stack. Due to this high conversion, the H_2O fraction decreases to a minimum within this scenario while a higher amount of CO_2 is shifted towards CO by the rWGS reaction and simultaneously a higher extent of electrochemical CO_2 reduction

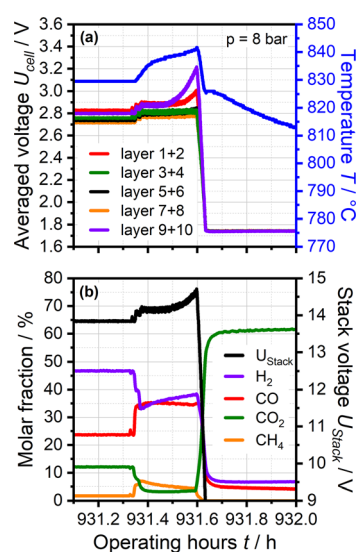


Fig. 11 a) Characteristic stack temperature depicted with the voltage behavior of the ten layers; b) recorded analysis of the outlet gas composition during the operating time of the water pump's malfunction.

occurs. Hence, the increased amount of produced CO could be consumed by a higher extent of the exothermic methanation reaction which led to the observed increased stack temperature. By calculating the thermodynamic equilibrium with the reduced H₂O supply and the accordingly high conversion, a H₂/CO ratio of approximately 1.5 can be found for this scenario. A reduction of 40% of the steam supply in combination with the related high conversion of >90% leads to approximately 5% of solid carbon formation according to the thermodynamic equilibrium at these experimental conditions. The thermodynamic equilibrium was calculated with the software of the Glenn Research Center [40]. Since the outer layers of the stack showed the lowest temperature due to the heat losses towards the furnace environment, the risk and amount of solid carbon deposition increases. Additionally, a slightly unequal distribution of reactants between the different stack layers could lead to the observed more significant voltage increase of the outer layers.

When steam starvation occurred, the characteristic temperature of the stack increased due to the considerable rise of the RC and the higher extent of methanation. The increased temperature led to a higher H₂ concentration due to thermodynamic relations and intensified the voltage increase until the automated safety procedure of the test rig intervened. After this event a continuation of operation was attempted twice but was impeded since the stack exceeded the maximum voltage. Most likely the high RC and carbon deposition irreversibly damaged the cell structure since the ohmic resistance showed a considerable increase after the steam starvation event (see Figure 12).

During the operation of stack C in steam and co-electrolysis mode, impedance spectra were recorded in the same manner as conducted with stack A and B in order to quantify the influence of the operating mode on the performance loss in more detail. Figure 12 shows the measured ohmic resistance, the temperature dependent ohmic resistance of one layer according to [5], the calculated polarization resistance and the characteristic stack temperature during the 1,000 h test. Note that the measured ohmic resistance shown in the graph is an aver-

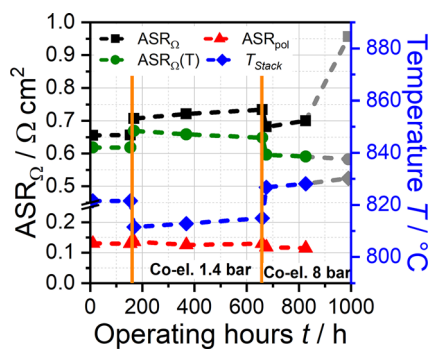


Fig. 12 Measured ohmic resistance (ASR_{Ω}), temperature-dependent ohmic resistance according to [5] ($ASR_{\Omega}(T)$) and measured characteristic stack temperature (T_{Stack}) during the steam and co-electrolysis experiment at 1.4 and 8 bar.

age of the cell layers 5+6 since the depicted characteristic stack temperature is measured on layer 5.

EIS was performed before and after the operation in pure steam electrolysis mode at 1.4 bar. A significant increase neither of the voltage nor of the ohmic resistance was observed. This is in good agreement with the results of the pure steam electrolysis mode performed with stack A, where a minor degradation over 1,000 h at the same operating condition was observed (see Figure 3). The measured ASR_{Ω} was $0.655 \Omega \text{ cm}^2$ at a characteristic stack temperature of $821.5 \text{ }^{\circ}\text{C}$ at the beginning of the test. After 160 h the measured ASR_{Ω} was $0.657 \Omega \text{ cm}^2$ and thus showed an insignificant increase over the operating time. A small deviation of the measured ohmic resistance under load and the temperature-dependent resistance according to [5] ($ASR_{\Omega}(T)$) can be seen. However, it solely accounts for $16 \text{ m}\Omega \text{ cm}^2$. The small deviation can be explained by the fact that the resistance at the inlet and the outlet of the stack is highly influenced by heat losses towards the lower furnace temperature in exothermic operating mode which leads to slightly higher averaged resistances recorded by EIS.

The measurements during the co-electrolysis operation at 1.4 bar show the ohmic resistance and the temperature to increase simultaneously. The deviation between the measured ASR_{Ω} and the $ASR_{\Omega}(T)$ becomes more significant, due to the more dominant degradation of the stack. As can be seen in the graph, the performance loss increases at 8 bar since the slope of the measured ohmic resistance increases. After the incident of steam starvation at 930 h of operation the ohmic resistance showed a major increase which led to the abortion of the test.

3.4 Comparison of the Experiments

In order to compare the results obtained from the experiments with stack A–C, Figure 13 shows the degradation based on the increase of the measured ohmic resistance. All conducted experiments showed the performance loss to be majorly caused by an increase of the ohmic part in the EIS spectra. Stack A and the first 160 h of stack C were operated at

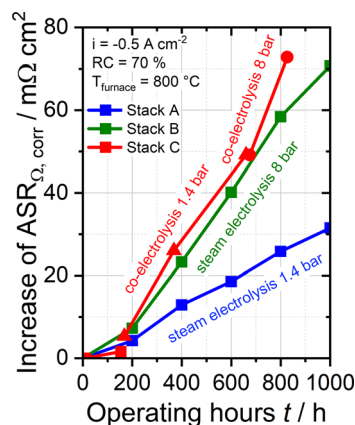


Fig. 13 Increase of the ohmic resistance during the conducted experiments in steam and co-electrolysis with stack A–C.

the same condition in steam electrolysis mode and show a comparable increase of the measured ASR_{Ω} . Stack B which was operated in steam electrolysis at 8 bar and thus at a higher voltage and temperature showed an apparently more significant increase of the ohmic resistance. Compared to the operation of stack A at 1.4 bar, the rise of the ohmic resistance of stack B almost doubled after 1,000 h. The co-electrolysis operation at 1.4 bar with stack C showed a considerable increase of the ohmic resistance. Furthermore, the operation at the elevated pressure of 8 bar led to an even more significant increase of the resistance.

Table 5 summarizes the conducted experiments with the averaged voltage of the middle cell, the averaged characteristic stack temperature and the corresponding increase of the total and ohmic resistances over the operating time. Note that all resistances are normalized or extrapolated to 1 kh. The ASR is additionally shown with the specific temperature correction according to the discussion of the related experiments. As shown before, the polarization resistances are in similar ranges to each other and play a subordinate role compared to the ohmic resistance increase. Hence, the polarization resistances are not considered here. Stack A showed a voltage shift of 8 mV over the 1000 h of testing at 1.4 bar and a RC of 70% at -0.5 A cm^{-2} . Experiments in atmospheric conditions with a similar ESC single cell configuration have already shown a voltage shift of approximately 7 mV kh^{-1} at current densities between -0.5 and -0.9 A cm^{-2} [13, 41]. Both the steam content (75%) and the reactant conversion (51%) were lower than the ones of the presented study whereas the temperature was slightly higher ($\sim 850 \text{ }^{\circ}\text{C}$). The electrolyte material of the cell

was 6Sc1CeSZ which has a generally higher conductivity than the 3YSZ material used in the stacks of the current study, hence higher current densities could be achieved while operating in long-term endothermic mode [30]. The same ESC architecture with a 3YSZ electrolyte on single cell level was used in another long-term study at atmospheric conditions [15]. A voltage shift of 5 mV kh^{-1} was shown for a current density of -0.7 A cm^{-2} and 60% conversion which corresponded to a temperature corrected ASR increase of $7 \text{ m}\Omega \text{ cm}^2$. Both ESC single cell studies also observed a predominant increase of the ohmic contribution and only a minor contribution from the electrodes during the operation which is in agreement with the findings of the current study. One major difference between the single cell and stack experiments is the additional contribution of contact resistances (i.e., bipolar plates) to the overall measured ohmic resistance of a stack [5]. Since these resistances additionally increase during the operation time, long-term stack experiments tend to show higher performance losses [19]. Furthermore, temperature gradients, current density-, gas-, and conversion distribution can highly differ from single cell to stack experiments. Moreover, the impacts of piping and seals can lead to further degradation contributions to stacks [19, 42].

On stack level, the long-term behavior was mainly investigated on stacks with cathode supported cells (CSC) at atmospheric operating pressures [16–18, 20, 43, 44]. Fang et al. investigated a two-layer stack (Ni8YSZ/8YSZ/LSCF) over more than 10,000 h of steady state electrolysis operation at $800 \text{ }^{\circ}\text{C}$ and observed a voltage shift of approximately $4\text{--}5 \text{ mV kh}^{-1}$. The stack was operated in endothermic mode

Table 5 Overview of the experimental conditions of the conducted studies with the three stacks A–C. The averaged voltage of the middle cell, the averaged characteristic stack temperature and the increase of the total and ohmic resistances are given per kh.

	Stack A	Stack B	Stack C	Stack C	Stack C
Operating mode	H ₂ O-electrolysis	H ₂ O-electrolysis	H ₂ O-electrolysis	Co-electrolysis	Co-electrolysis
Time / h	1,000	2,000	160	500	260
Pressure / bar	1.4	8	1.4	1.4	8
Stack temperature at start / °C	825.3	830.2	823.1	811.5	827
Stack temperature increase / K	3.13	10.4	2.4	6.8	9.7
Voltage at start / V	1.329	1.351	1.325	1.35	1.369
Voltage increase / mV	8	31	12	34	85
p _{H₂O} / bar	1.26	7.2	1.26	0.89	5.10
p _{H₂} / bar	0.14	0.8	0.14	0.05	0.27
p _{CO₂} / bar	–	–	–	0.44	2.50
p _{CO} / bar	–	–	–	0.02	0.13
ASR _{total} at start / mΩ cm ²	808	767	797	843	804
ASR _{total} increase / mΩ cm ² kh ⁻¹	18	68	15	36	100
ASR _{total} increase with temperature correction / mΩ cm ² kh ⁻¹	32	107	26	68	137
ASR _Ω increase / mΩ cm ² kh ⁻¹	18	32	12	56	72
ASR _Ω increase with temperature correction / mΩ cm ² kh ⁻¹	32	71	23	88	109 (157 if incident considered)

and with 50% of H₂O content at -0.5 A cm^{-2} . Lang et al. investigated a 30 layer stack at atmospheric pressure with identical cells as used within the current study and observed a voltage shift of approximately 6 mV kh^{-1} and a ASR shift of approximately $13 \text{ m}\Omega \text{ cm}^2$ (without temperature correction) during steady state electrolysis operation at -0.5 A cm^{-2} and a conversion of 70% [21]. The stack temperature increased with about 3 K kh^{-1} which leads to an temperature corrected ASR shift of approximately $26 \text{ m}\Omega \text{ cm}^2$ by assuming the temperature dependency of the stack measured by the authors [5]. The cell voltages and the inlet gas composition were similar to the current study. Latest published results of a 30 layer ESC stack test showed an ASR shift of $13 \text{ m}\Omega \text{ cm}^2$ (with temperature correction) for thermoneutral operation at ambient pressure [45]. However, the stack design was slightly improved compared to the one used within the current study. Consequently, the observed degradation of stack A is in a similar range to relevant stack investigations at ambient pressure, though it shows slightly higher voltage and ASR shifts. Furthermore, both the CSC and the ESC investigations showed that the ohmic resistance predominantly increased [20,21].

The number of publications related to long-term stack performances under pressurized operation is limited due to the limited presence of pressurized stack test rigs. Jensen et al. investigated an 11-cell CSC stack at elevated operating pressure of 10 bar over a duration of 200 h in steady state steam electrolysis [22]. The applied current density was in a range between -0.18 and -0.25 A cm^{-2} . The voltage shift was found to be around $90\text{--}270 \text{ mV kh}^{-1}$ though several incidents during the operation raised uncertainties about the meaningfulness of the achieved results. In comparison, a similar stack tested at ambient pressure condition and higher temperature led to a voltage shift of 40 mV kh^{-1} [46]. Despite the uncertainties, these results might also indicate higher stack degradation at higher operating pressures. Stack B of the current study showed a voltage shift of 31 mV kh^{-1} and a temperature corrected ASR shift of $107 \text{ m}\Omega \text{ cm}^2$ at 8 bar. However, both the voltage and ASR shift are approximately four times higher than during the experiment conducted with stack A at 1.4 bar.

The co-electrolysis experiment conducted with stack C at 1.4 bar showed a noticeably higher degradation than stack A. This indicates a negative influence of the used CO₂ or CO on the long-term performance. A higher degradation during co-electrolysis operation was already observed within single cell and stack tests and was ascribed to additional contaminants like sulfur which can be brought in by the carbonaceous gas leading to an inactivation of the catalyst [46–48]. Schäfer et al. showed a degradation of $19 \text{ m}\Omega \text{ cm}^2 \text{ kh}^{-1}$ with a four layer CSC stack under co-electrolysis conditions at ambient pressure and -0.5 A cm^{-2} . In comparison, stack C of the current study showed a higher ASR shift ($36 \text{ m}\Omega \text{ cm}^2 \text{ kh}^{-1}$; $68 \text{ m}\Omega \text{ cm}^2 \text{ kh}^{-1}$ with temperature correction) whereas it was operated at a significantly higher voltage. The increase of the operating pressure up to 8 bar caused an additional increase of the degradation of stack C, which is in agreement with the comparison of the results of stack A and B.

3.5 Post-test Analysis (PTA)

All stacks were disassembled after the long-term experiments in order to examine the influence of the different operating conditions on the stack components and cell microstructure. Samples from the inlet, middle and outlet of layer five of each stack including the bipolar plate (BPP) was embedded in resin for cross-section preparation and investigations *via* SEM and EDX while the rest of the stacks were inspected visually.

3.5.1 Investigation of the Bipolar Plates

Within stack A and B no cell cracks or traces of burning on either the anode or the cathode side were observed. This is in good agreement with the recorded data since prominent increases in temperature were not measured during both experiments. Figure 14 shows the cross section of the two BPPs close to the air outlet of stack A and B. The pictures show the steel of the BPP (upper part in light gray), the marked oxide layer and the porous contact paste towards the air electrode underneath. Generally, a growing oxide layer at the BPP leads to an increasing ohmic resistance of the specific repeating unit and of the whole stack.

A different extent of oxide layer formation and a chromium accumulation at the interface was found within the analysis. The oxide layer at the BPP of stack B was almost twice as thick as the one of stack A. This can most likely be attributed to the doubled operating time of stack B since an oxide layer growth in Ni-Cr steel generally follows a parabolic time law in the temperature range of $750\text{--}950 \text{ }^\circ\text{C}$ [49]. Consequently, the significantly higher partial pressure of oxygen within the experiment of stack B plays a subordinate role for the oxide layer growth at the BPP. Furthermore a loss of contact between the oxide layer and the contact paste of stack B was observed.

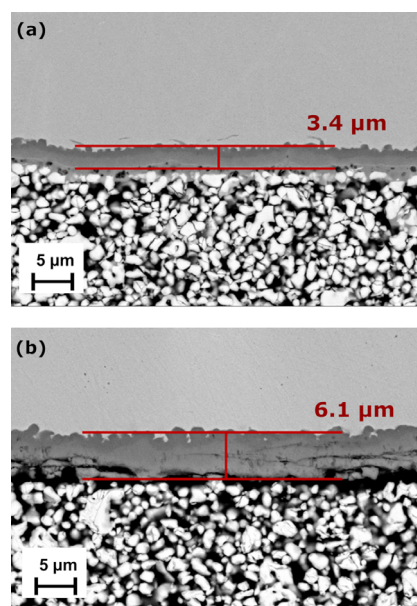


Fig. 14 Cross section of the bipolar plates close to the air outlet with the formed oxide layers.

However, the related experimental results of stack B do not lead to the expectation that this loss of contact happened during operation since the compression weight on top of the stack effectively presses on these contact spots between BPP and air electrode. It is assumed that the slight delamination consequently occurred during the stack disassembly and sample preparation. Within the PTA cross sections of the BPP at the air inlet and at the middle length were prepared and investigated *via* SEM but did not show different results than the one shown in Figure 14. The significant difference in ohmic resistance between stack A and B hence did not originate from the oxide layer formation at the investigated BPPs.

3.5.2 Investigation of the Electrodes

Figure 15 shows the cross section of the fuel electrode (Ni-GDC) and partly of the electrolyte (3YSZ) of stack A and B. The samples were taken close to the inlet of the stacks. Ni coarsening and depletion is conspicuous in the fuel electrode of stack B and a comparably denser layer of Nickel on the surface of the electrode was observed. These observations were particularly made at the inlet of the stack whereas significantly less Ni depletion was observed towards the stack outlet. This observation is in agreement with other studies related to long-term SOEC investigations [17, 50]. Since the partial pressure of H₂O is highest at the inlet, this observation indicates a direct correlation between steam content and Ni depletion. Though stack B was operated over a longer operating time, it is unlikely that a high amount of Ni depletion and accumulation on the surface considerably occurs only within the second half of the 2,000 h test.

In literature a direct correlation between the partial pressure of H₂O and Ni mobility and depletion was already dis-

cussed for steam electrolysis operation, though no mechanism has been proven so far [10, 11, 27, 51–55]. However, the studies mostly focus on fuel electrode supported single cells with Ni-YSZ electrodes. Furthermore, the cells were operated at a significantly higher current density leading to high overpotential and temperature gradients perpendicular to the electrode/electrolyte interface. It is hypothesized that these gradients are the driving force for the loss of contact between Ni and YSZ and the related depletion of Ni *via* volatile Ni(OH)_x species [10, 17, 27, 51, 55–57]. However, in the present study a composite electrode of Ni-GDC in an electrolyte supported cell was used in the stacks. Ni-GDC is a wellknown mixed ionic and electron conducting material which can offer a significantly broader triplephase boundary (TPB) and reaction region than Ni-YSZ material. Consequently, all potential and temperature gradients within the porous electrode decrease and should lead to less Ni evaporation [11, 56]. In the present study the operating voltage of the middle cell of stack B was 22 mV higher than the one of stack A at the beginning of the tests. Furthermore, the temperature difference between both stacks was approximately 5 K whereas the reactant conversion of 70% was constant. Hence, the difference of the potential and temperature gradients of stack A and B were marginal and cannot be responsible for the apparently higher Ni depletion in stack B. However, the partial pressure of H₂O at the inlet of stack A was 1.26 bar (H₂ 0.14 bar) whereas it was 7.2 bar (H₂ 0.8 bar) during the operation of stack B. The molar fraction of Ni(OH)₂ as the predominantly occurring hydroxide species was calculated based on thermodynamic equilibrium to 9·10⁻¹¹ by using the experimental conditions for stack A and the averaged gas composition. The equilibrium was calculated with FactSage software [58]. The calculation of the thermodynamic equilibrium shows a linear dependency of the partial pressure of Ni(OH)₂ with the operating pressure. The high partial pressures of H₂O and H₂ in stack B can consequently lead to a significantly higher Ni mobility *via* a high partial pressure of the hydroxide species. Additionally, the decreased diffusion resistance during pressurized operation and the high reactant conversion of 70% might contribute to an increased Ni(OH)_x output and depletion rate. However, it is difficult to assess how operating parameters influence the formation and the diffusive characteristic of Ni(OH)_x species during pressurized operation, due to insufficient knowledge of the underlying mechanisms [10, 11, 17, 52]. But as a consequence, the loss of Ni in the porous electrode structure leads to an increased ohmic resistance since the ionic conduction pathway of the O²⁻ ions becomes longer. This correlation was already shown by publications where the long-term behavior of Ni-YSZ fuel electrodes was investigated [37, 59–61]. Though GDC with its electro-catalytic characteristic is present in the used electrodes, the ohmic resistance might increase since the electrical conductivity of GDC is lower than the one of Ni [5, 62]. Furthermore, the electrical contact between the GDC particles within the porous electrode could become worse, due to the loss of highly conductive Ni material and relatedly formed cavities. Hence, the predominant electrochemical reaction zone moves

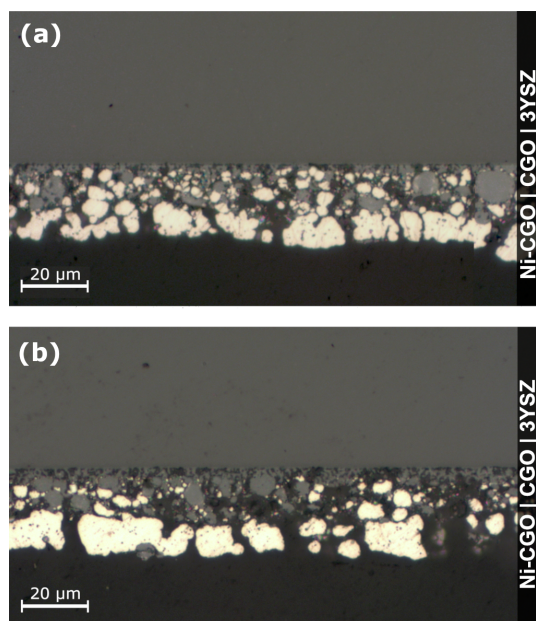


Fig. 15 Cross section showing the fuel electrode and electrolyte of stack A and B.

to the outer part of the electrode layer [30,63]. Additionally, the loss of Ni leads to an increased polarization resistance of the fuel electrode which is in good agreement with the experimental results shown in the EIS spectra of Figure 8. However, the magnitude of the increase in ohmic and polarization resistance might be lower than it would be for Ni-YSZ electrodes, since ions and electrons can be distributed *via* the GDC material and can still participate in the electrochemical reaction.

Within the fuel electrodes of both stacks traces of silicon contamination were observed *via* EDX. The possible major origin of this contaminant is both the liquid water for evaporation and the glass sealants of the stack. Silicon in the form of silicon dioxide is known to be solved in liquid water and very difficult to remove. Though ultrapure water was used for the experiments, a concentration of 4 to 7 $\mu\text{g L}^{-1}$ was measured in several analyses of the liquid phase at DLR. The contamination was observed to be highest close to the inlet of the cells, whereas significantly less silicon was found at the outlet of the cells. Figure 16 a and b show representative EDX images of the stacks A and B at the inlet of the cells where the maximum concentration of silicon was observed. In case of stack A, an averaged silicon contamination of approximately 2.3 mass-% was found across the fuel electrode thickness at the inlet whereas spots with a maximal concentration of 5.5 mass-% were found close to the Ni/CGO-CGO interface (Figure 16 a spots 9, 10). In contrast, spots with a maximum silicon contamination of 0.9 mass-% were found close to the outlet of the cell.

The maximum silicon contamination of stack B was found with 13.4 mass-% at the inlet close to the Ni/CGO-CGO interface (Figure 16 b spots 8, 9), whereas a maximum silicon contamination of 1.4 mass-% was found at the outlet of the cell. Please note that the EDX analysis is used for a qualitative comparison between stack A and B and showed that stack B was significantly more contaminated with silicon than stack A. This observation can be attributed to the doubled operating

time and most likely to the higher partial pressure of silicon within the electrode compartment during operation. However, the low degradation of stack A is promising although the cells were contaminated with silicon. To quantify the impact of silicon contamination on the actual degradation rate of a stack has to be subject of further investigations.

A partial delamination of the air electrode from the electrode/electrolyte interface was observed for stack B. This phenomenon could significantly contribute to the predominant increase of the ohmic resistance during the experiment. In particular the partial delamination was observed close to the outlet, i.e., within the cell area with the highest partial pressure of oxygen (p_{O_2}) during operation. It cannot be fully clarified if this delamination happened during or after the operation or during the disassembly of the stack. Unfortunately, a preparation of a cross-sectional sample of a spot close to the outlet of the cell was not possible due to the instability of the cell during the disassembly. However, since it was not observed at the inlet or middle length of the cell there is a strong indication that it happened already during operation. In accordance with the experimental conditions, the p_{O_2} of stack B was 2.9 bar at the outlet. In literature the delamination of the air electrode was extensively investigated for electrolysis operation with LSM electrodes and was mostly assigned to the high p_{O_2} at the interface or the formation of a secondary phase [64–66]. The latter was not observed within the PTA of stack B for the samples prepared of the inlet or the middle length of the cell. The high p_{O_2} within the air electrode compartment and at the electrode/electrolyte interface might have led to a weakening of the interface between YSZ and the GDC barrier layer and consequently to the observed delamination [67].

Stack C which was mostly operated in co-electrolysis mode at 1.4 and 8 bar showed an apparent delamination of the fuel electrode from the electrolyte, as can be seen in Figure 17. The experiment was aborted, due to steam starvation accompanied by a reactant conversion >90%. After the incident the stack showed a significantly higher ohmic resistance which could be caused by the observed delamination of the fuel electrode.

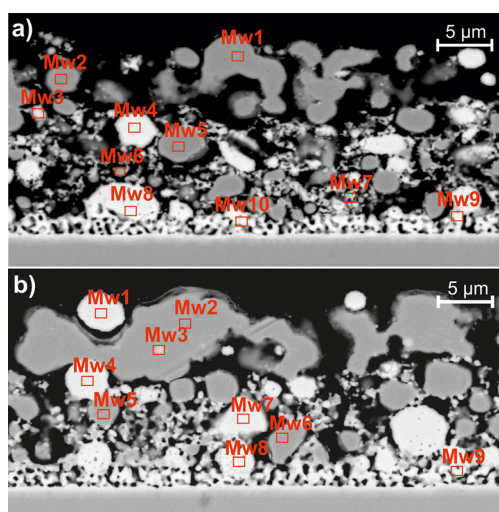


Fig. 16 Representative cross-section of the Ni-CGO fuel electrode from a spot close to the inlet of the middle cell of a) stack A; and b) stack B for a qualitative comparison of the silicon contamination *via* EDX.

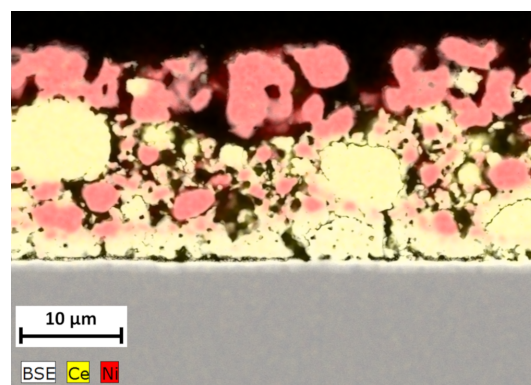


Fig. 17 Backscattered electrons image of the fuel side of cell 5 of stack C. Ceria (Ce) is marked in yellow, Ni in red.

As mentioned within Section 3.3, it is expected that solid carbon formed close to the electrode/electrolyte interface where the lowest H/C ratio is present during the operation at high conversion rates. Furthermore, the solid carbon could have been oxidized when the current decreased and enough steam or CO₂ was present due to a lower reactant conversion. Both, the reduction and oxidizing process are associated with a volume change within the microstructure of the electrode which can lead to a damage of the electrode structure and consequently to the observed delamination. However, if the delamination of the fuel electrode already began before the incident of steam starvation could not be fully clarified within the PTA. Furthermore, thermomechanical stress might have contributed to the structural defect since the stack temperature dropped by approximately 15 K within 1 minute after load shedding (see Figure 11 a).

Electroreduction of the 3YSZ electrolyte and related conduction loss due to high reactant conversion can generally lead to significantly increased ohmic resistances. However, since the cell voltage (except layer 9+10) stayed below 1.5 V during the steam starvation incident, it can be assumed that the electrolyte itself was not irreversibly damaged within the current study [68].

Nickel depletion was observed at the fuel electrode, though to a much lesser extent than observed in stack B (see Figure 17). The lower depletion can be attributed to the shorter operating time under elevated pressure and the lower partial pressure of H₂O at the inlet during the co-electrolysis mode. However, the ohmic resistance of stack C showed a significantly higher increase at 1.4 bar than during the steam electrolysis operation of stack A. Experimental data about the long-term behavior during co-electrolysis operation can be found in literature [69–71]. Compared to steam electrolysis, the operation with CO₂ in the inlet led to increased degradation rates in all studies. The higher performance loss was mostly ascribed to the adsorption of impurities like sulfur at active sites. Partly inactivation of the electrode with that respective contaminant leads to locally increased current densities, higher overpotentials and hence a decreased long-term performance. Contamination with silicon was also observed for stack C but qualitatively compared slightly less than within the PTA of stack A. More specifically, an averaged contamination of 2.9 mass-% across the fuel electrode thickness at the inlet with a maximum contamination of 4.3 mass-% close to the Ni/CGO-CGO interface was found. This could be attributed to the lower steam content during the co-electrolysis operation. Except for the fuel electrode delamination, no suspicious observations of the stack and/or cell microstructure were made.

4 Conclusion

In this study three identically constructed ten-layer stacks (A–C) with electrolyte supported cells were tested in exothermic steam and co-electrolysis mode at elevated pressures of 1.4 and 8 bar. Investigations during constant-current operation

at a current density of -0.5 A cm^{-2} and a reactant conversion of 70% were carried out over 1,000–2,000 h. The inlet gas molar fractions for steam electrolysis was 90/10 (H₂O/H₂) and 63.7/31.3/3.3/1.7 (H₂O/CO₂/H₂/CO) for co-electrolysis operation.

All stacks showed highly similar resistances according to their respective temperature dependency at the beginning of the tests, indicating a high level of accuracy and repeatability during manufacturing. Stack A was operated in steam electrolysis mode at 1.4 bar over 1,000 h and showed a low degradation of 8 mV kh^{-1} per cell and an ASR shift of $18 \text{ m}\Omega \text{ cm}^2 \text{ kh}^{-1}$ per cell. The main reason for the observed performance loss could be ascribed to the time-dependent increase of the ohmic resistance whereas the polarization resistances remained almost constant.

Stack B was operated at 8 bar over 2,000 h and showed an almost four times higher voltage and ASR shift than stack A. Impedance analysis showed increased resistances for both the air electrode and the fuel electrode. However, the major part of the observed degradation could be attributed to the ohmic resistance. A short period of fuel cell operation of about 150 h was also performed with stack B in the second half of the testing time. The degradation became noticeably higher during the subsequent constant steam electrolysis operation. Within the post-test analysis of the two stacks (A and B), a significantly higher extent of Ni depletion in the fuel electrode was observed for stack B. This phenomenon indicates that the operating pressure has a considerable influence on the nickel mobility and could lead to a decrease in the effective conductivity of the fuel electrode. Furthermore, a partial delamination of the air electrode was observed particularly at the outlet of the stack. However, delamination attributed to high partial pressure of oxygen at the outlet cannot be confidently confirmed, since delamination is also possible to occur during the disassembly of the stack.

Stack C was operated in steam electrolysis mode for the first 160 h and showed a highly similar degradation as stack A. Afterwards, the stack was operated in co-electrolysis mode for 500 h at 1.4 bar. The performance loss increased noticeably and the ohmic resistance was identified again to be the dominant cause of the degradation. The voltage shifted by 34 mV kh^{-1} and the ASR by $36 \text{ m}\Omega \text{ cm}^2 \text{ kh}^{-1}$. The stack was operated for another 260 h (930 h total operating time) in co-electrolysis mode at 8 bar until it unfortunately failed due to a short steam starvation incident. After this event a continuation of operation was attempted twice but was impeded since the stack exceeded the maximum voltage due to a highly increased ohmic resistance. Within the PTA a delamination of the fuel electrode was observed which might be attributable to formed and reoxidized solid carbon within the microstructure of the electrode and thus a weakening of the mechanical property due to volume changes within the substrate.

Finally, the authors would like to point out that the conducted experiments indicate that a higher degradation is associated with the higher operating pressure, but a general statement about the long-term stability is truly not possible at this time. The authors are aware that neither 1,000 nor 2,000 h are

sufficient in order to forecast the degradation of a SOEC and much longer operating times are needed [13,20]. However, in order to be able to investigate the general consequence of a higher operating pressure on the long-term stability, an increased number of experiments have to be conducted in order to reproduce the results shown in this study and in order to increase the statistical significance.

List of Abbreviations and Symbols

ASR _{pol}	Area specific polarization resistance / $\Omega \text{ cm}^2$
ASR _{total}	Total area specific resistance / $\Omega \text{ cm}^2$
ASR _{Ω}	Area specific ohmic resistance / $\Omega \text{ cm}^2$
EDX	Energy-dispersive X-ray spectroscopy
EIS	Electrochemical impedance spectroscopy
ESC	Electrolyte supported cell
f	Frequency / Hz
i	Current density / A cm^{-2}
GDC	Gadolinium-doped ceria
LSCF	Lanthanum strontium cobalt ferrite
Ni	Nickel
OCV	Open circuit voltage
p	Pressure / bar
PTA	Post-test analysis
RC	Reactant conversion / %
SEM	Scanning electron microscopy
slpm	Standard liters per minute / L min^{-1}
SOC	Solid oxide cell
SOEC	Solid oxide electrolysis cell
U	Voltage / V
YSZ	Yttria-stabilized zirconia

References

- [1] S. H. Jensen, C. Graves, M. Chen, J. B. Hansen, X. Sun, *J. Electrochem. Soc.* **2016**, *163*, F1596.
- [2] M. Henke, C. Willich, J. Kallo, K. A. Friedrich, *Int. J. Hydrogen Energy* **2014**, *39*, 12434.
- [3] X. Sun, A. D. Bonaccorso, C. Graves, S. D. Ebbesen, S. H. Jensen, A. Hagen, P. Holtappels, P. V. Hendriksen, M. B. Mogensen, *Fuel Cells* **2015**, *15*, 697.
- [4] S. Santhanam, M. P. Heddrich, M. Riedel, K. A. Friedrich, *Energy* **2017**, *141*, 202.
- [5] M. Riedel, M. P. Heddrich, K. A. Friedrich, *Int. J. Hydrogen Energy* **2019**, *44*, 4570.
- [6] D. M. A. Dueñas, M. Riedel, M. Riegraf, R. Costa, K. A. Friedrich, *Chemie Ing. Tech.* **2020**, *92*, 45.
- [7] M. Riedel, M. P. Heddrich, K. A. Friedrich, *J. Electrochem. Soc.* **2020**, *167*, 024504.
- [8] L. Bernadet, G. Gousseau, A. Chatroux, J. Laurencin, F. Mauvy, M. Reytier, *ECS Trans.* **2015**, *68*, 3369.
- [9] S. Seidler, M. Henke, J. Kallo, W. G. Bessler, U. Maier, K. A. Friedrich, *J. Power Sources* **2011**, *196*, 7195.
- [10] M. P. Hoerlein, M. Riegraf, R. Costa, G. Schiller, K. A. Friedrich, *Electrochim. Acta* **2018**, *276*, 162.
- [11] M. B. Mogensen, A. Hauch, X. Sun, M. Chen, Y. Tao, S. D. Ebbesen, K. V. Hansen, P. V. Hendriksen, *Fuel Cells* **2017**, *17*, 434.
- [12] R. Knibbe, M. L. Traulsen, A. Hauch, S. D. Ebbesen, M. Mogensen, *J. Electrochem. Soc.* **2010**, *157*, B1209.
- [13] J. Schefold, A. Brisse, H. Poepke, *Int. J. Hydrogen Energy* **2017**, *42*, 13415.
- [14] P. Moçoteguy, A. Brisse, *Int. J. Hydrogen Energy* **2013**, *38*, 15887.
- [15] J. Schefold, A. Brisse, A. Surrey, C. Walter, *Int. J. Hydrogen Energy* **2020**, *45*, 5143.
- [16] C. E. Frey, Q. Fang, D. Sebold, L. Blum, N. H. Menzler, *J. Electrochem. Soc.* **2018**, *165*, F357.
- [17] D. Schäfer, Q. Fang, L. Blum, D. Stolten, *J. Power Sources* **2019**, *433*, 126666.
- [18] Q. Fang, L. Blum, N. H. Menzler, *J. Electrochem. Soc.* **2015**, *162*, F907.
- [19] V. N. Nguyen, Q. Fang, U. Packbier, L. Blum, *Int. J. Hydrogen Energy* **2013**, *38*, 4281.
- [20] Q. Fang, C. E. Frey, N. H. Menzler, L. Blum, *J. Electrochem. Soc.* **2018**, *165*, F38.
- [21] M. Lang, S. Raab, M. S. Lemcke, C. Bohn, M. Pysik, *ECS Trans.* **2019**, *91*, 2713.
- [22] S. H. Jensen, X. Sun, S. D. Ebbesen, M. Chen, *Fuel Cells* **2016**, *16*, 205.
- [23] J. Brabandt, O. Posdziech, *ECS Trans.* **2017**, *78*, 2987.
- [24] M. Preininger, B. Stoeckl, V. Subotić, F. Mittmann, C. Hochenauser, *Appl. Energy* **2019**, *254*, 113695.
- [25] B. E. Mai, T. Heller, D. Schimanke, J. Lawrence, C. Wunderlich, *ECS Trans.* **2009**, *25*, 187.
- [26] S. Srikanth, M. P. Heddrich, S. Gupta, K. A. Friedrich, *Appl. Energy* **2018**, *232*, 473.
- [27] A. Hauch, S. D. Ebbesen, S. H. Jensen, M. Mogensen, *J. Electrochem. Soc.* **2008**, *155*, 1184.
- [28] X. Zhang, J. E. O'Brien, R. C. O'Brien, J. J. Hartvigsen, G. Tao, G. K. Housley, *Int. J. Hydrogen Energy* **2013**, *38*, 20.
- [29] M. Riedel, M. P. Heddrich, K. A. Friedrich, *Proc. 13th Eur. SOFC SOE Forum*, Lucerne, Switzerland, **2018**, B1504.
- [30] M. B. Mogensen, *Curr. Opin. Electrochem.* **2020**, *21*, 265.
- [31] J. Schefold, A. Brisse, F. Tietz, *J. Electrochem. Soc.* **2011**, *159*, A137.
- [32] M. Henke, C. Willich, J. Kallo, K. A. Friedrich, *Int. J. Hydrogen Energy* **2014**, *39*, 12434.
- [33] L. Bernadet, G. Gousseau, A. Chatroux, J. Laurencin, F. Mauvy, M. Reytier, *Int. J. Hydrogen Energy* **2015**, *40*, 12918.
- [34] C. Graves, S. D. Ebbesen, S. H. Jensen, S. B. Simonsen, M. B. Mogensen, *Nat. Mater.* **2015**, *14*, 239.
- [35] M. Mori, T. Yamamoto, H. Itoh, H. Inaba, H. Tagawa, *J. Electrochem. Soc.* **1998**, *145*, 1374.
- [36] J. Malzbender, W. Fischer, R. W. Steinbrech, *J. Power Sources* **2008**, *182*, 594.

- [37] M. P. Hoerlein, G. Schiller, F. Tietz, K. A. Friedrich, in *Proc. 14th Int. Symp. Solid Oxide Fuel Cells*, Glasgow, Scotland, **2015**, pp. 3553.
- [38] M. P. Hoerlein, V. Yurkiv, G. Schiller, K. A. Friedrich, in *Proc. 12th Eur. SOFC SOEC Forum*, Lucerne, Switzerland, **2016**.
- [39] M. Riedel, M. P. Heddrich, K. A. Friedrich, in *Proc. 1st Int. Conf. Electrolysis*, Copenhagen, Denmark, **2017**, pp. 71.
- [40] B. J. McBride, M. J. Zehe, S. Gordon, *NASA Glenn Coefficients for Calculating Thermodynamic Properties of Individual Species*, **2002**.
- [41] J. Schefold, A. Brisse, H. Poepke, *Electrochim. Acta* **2015**, 179, 161.
- [42] H. Nabilek, L. Blum, H. P. Buchkremer, V. Haanappel, L. G. J. B. de Haart, W. J. Quadackers, R. Steinberger-Wilckens, R. W. Steinbrech, U. Reisinger, F. Tietz, *Adv. in Solid Oxide Fuel Cells III: Ceramic and Engineering Science Proceedings*, **2009**, 28, 65.
- [43] J. E. O'Brien, C. M. Stoots, J. S. Herring, M. G. McKellar, E. A. Harvego, M. S. Sohal, K. G. Condie, *High Temperature Electrolysis for Hydrogen Production from Nuclear Energy Technology Summary*, Idaho National Laboratory, February 2010.
- [44] S. Diethelm, J. Van herle, D. Montinaro, O. Bucheli, *Fuel Cells* **2013**, 13, 631.
- [45] C. Geipel, K. Hauptmeier, K. Herbrig, F. Mittmann, M. Münch, M. Pötschke, L. Reichel, T. Strohbach, T. Seidel, A. Surrey, C. Walter, *ECS Trans.* **2019**, 91, 123.
- [46] S. D. Ebbesen, J. Høgh, K. A. Nielsen, J. U. Nielsen, M. Mogensen, *Int. J. Hydrogen Energy* **2011**, 36, 7363.
- [47] T. L. Skafte, P. Blennow, J. Hjelm, C. Graves, *J. Power Sources* **2018**, 373, 54.
- [48] G. Jeanmonod, S. Diethelm, J. Van Herle, *J. Phys. Energy* **2020**, 2, 034002.
- [49] T. Brylewski, T. Maruyama, M. Nanko, K. Przybylski, *J. Therm. Anal. Calorim.* **1999**, 55, 681.
- [50] Y. Tao, S. D. Ebbesen, M. B. Mogensen, *J. Power Sources* **2016**, 328, 452.
- [51] F. Tietz, D. Sebold, A. Brisse, J. Schefold, *J. Power Sources* **2013**, 223, 129.
- [52] M. Hubert, J. Laurencin, P. Cloetens, B. Morel, D. Montinaro, F. Lefebvre-Joud, *J. Power Sources* **2018**, 397, 240.
- [53] A. Zekri, M. Knipper, J. Parisi, T. Plaggenborg, *Phys. Chem. Chem. Phys.* **2017**, 19, 13767.
- [54] J. Mason, I. Celik, S. Lee, H. Abernathy, G. Hackett, *J. Electrochem. Soc.* **2018**, 165, F64.
- [55] L. Kröll, L. G. J. De Haart, I. Vinke, R. A. Eichel, *Phys. Rev. Appl.* **2017**, 7, 044007.
- [56] M. B. Mogensen, M. Chen, H. L. Frandsen, C. Graves, A. Hauch, T. Jacobsen, S. H. Jensen, T. L. Skafte, X. Sun, *ECS Trans.* **2019**, 91, 613.
- [57] A. Gubner, H. Landes, J. Metzger, H. Seeg, R. Stübner, *ECS Proc. Vol.* **1997**, 1997–40, 844.
- [58] C. W. Bale, E. Bélisle, P. Chartrand, S. A. Decterov, G. Eriksson, A. E. Gheribi, K. Hack, I. H. Jung, Y. B. Kang, J. Melançon, A. D. Pelton, S. Petersen, C. J. Sangster, P. Spencer, M. A. Van Ende, *Calphad Comput. Coupling Phase Diagrams Thermochem.* **2016**, 54, 35.
- [59] A. Hauch, K. Brodersen, M. Chen, M. B. Mogensen, *Solid State Ionics* **2016**, 293, 27.
- [60] M. B. Mogensen, A. Hauch, X. Sun, M. Chen, Y. Tao, S. D. Ebbesen, P. V. Hendriksen, *Proc. 12th Eur. SOFC Forum* **2016**, A0902.
- [61] A. Hauch, M. Mogensen, A. Hagen, *Solid State Ionics* **2011**, 192, 547.
- [62] L. Abadlia, F. Gasser, K. Khalouk, M. Mayoufi, J. G. Gasser, *Rev. Sci. Instrum.* **2014**, 85, 951211.
- [63] M. Riegraf, A. Zekri, M. Knipper, R. Costa, G. Schiller, K. A. Friedrich, *J. Power Sources* **2018**, 380, 26.
- [64] T. Jacobsen, M. Mogensen, *ECS Trans.* **2008**, 13, 259.
- [65] S. N. Rashkeev, M. V. Glazoff, *Int. J. Hydrogen Energy* **2012**, 37, 1280.
- [66] J. R. Mawdsley, J. David Carter, A. Jeremy Kropf, B. Yildiz, V. A. Maroni, *Int. J. Hydrogen Energy* **2009**, 34, 4198.
- [67] S. J. Kim, G. M. Choi, *Solid State Ionics* **2014**, 262, 303.
- [68] M. A. Laguna-Bercero, R. Campana, A. Larrea, J. A. Kilner, V. M. Orera, *J. Power Sources* **2011**, 196, 8942.
- [69] C. Graves, S. D. Ebbesen, M. Mogensen, *Solid State Ionics* **2011**, 192, 398.
- [70] M. Chen, J. V. T. Høgh, J. U. Nielsen, J. J. Bentzen, S. D. Ebbesen, P. V. Hendriksen, *Fuel Cells* **2013**, 13, 638.
- [71] S. D. Ebbesen, R. Knibbe, M. Mogensen, *J. Electrochem. Soc.* **2012**, 159, F482.

Article IV:

Pressurized operation of solid oxide electrolysis stacks : An experimental comparison of the performance of 10-layer stacks with fuel electrode and electrolyte supported cell concepts.

M. Riedel, M.P. Heddrich, A. Ansar, Q. Fang, L. Blum, K.A. Friedrich,
Journal of Power Sources, Vol. 475 (2020), 228682.

DOI: <https://doi.org/10.1016/j.jpowsour.2020.228682>.



Contents lists available at ScienceDirect

Journal of Power Sources

journal homepage: www.elsevier.com/locate/jpowsour

Pressurized operation of solid oxide electrolysis stacks: An experimental comparison of the performance of 10-layer stacks with fuel electrode and electrolyte supported cell concepts

M. Riedel^{a,*}, M.P. Heddrich^a, A. Ansar^a, Q. Fang^b, L. Blum^b, K.A. Friedrich^{a,c}

^a German Aerospace Center (DLR), Institute for Engineering Thermodynamics, Pfaffenwaldring 38-40, 70569, Stuttgart, Germany

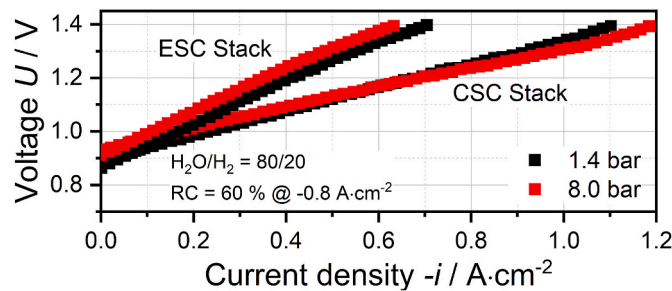
^b Institute of Energy and Climate Research (IEK-14), Forschungszentrum Jülich GmbH, 52425, Jülich, Germany

^c University of Stuttgart, Institute of Building Energetics, Thermal Engineering and Energy Storage (IGTE), Pfaffenwaldring 31, 70569, Stuttgart, Germany

HIGHLIGHTS

- Pressurized cathode-/electrolyte supported planar stacks characterized between 750 and 850 °C.
- Performance gain of the CSC stack up to 3% at 8 bar, ESC hardly affected by pressure.
- Significant extent of internal methanation during pressurized operation.
- Higher pressure dependency during pure CO₂ electrolysis with both stack concepts.

GRAPHICAL ABSTRACT



ARTICLE INFO

Keywords:

Pressurized operation
Solid oxide stack
Electrolysis
Syngas production

ABSTRACT

The electrochemical behavior of two different types of planar 10-layer solid oxide cell (SOC) stacks with having either fuel electrode supported cells or electrolyte supported cells, are examined under steam, co- and CO₂ electrolysis at elevated pressures of up to 8 bar. Experiments with steady-state and dynamically recorded U(i)-characteristics are performed in order to evaluate the performances over a wide temperature range and for different operating conditions. Furthermore, the influence of the operating pressure is quantified via the temperature and pressure dependency of the related ASR values of each stack. Impedance analysis is conducted in order to investigate the major differences and the pressure effect on the specific process resistances during steam and CO₂ electrolysis.

In case of the stack with fuel electrode supported cells, the ASR is found to decrease significantly at elevated pressure leading to an overall performance gain, whereas the stack with electrolyte supported cells shows a minor pressure effect. An impedance study shows that the diffusion and activation resistances are significantly affected when conducting CO₂ instead of H₂O electrolysis for both stack concepts. Furthermore, the pressure sensitivity is found to be more dominant during CO₂ electrolysis than during pure steam electrolysis operation.

* Corresponding author.

E-mail address: Marc.Riedel@dlr.de (M. Riedel).

<https://doi.org/10.1016/j.jpowsour.2020.228682>

Received 1 June 2020; Received in revised form 16 July 2020; Accepted 21 July 2020

Available online 8 August 2020

0378-7753/© 2020 The Authors.

Published by Elsevier B.V. This is an open access article under the CC BY-NC-ND license

(<http://creativecommons.org/licenses/by-nc-nd/4.0/>).

1. Introduction

Solid oxide electrolysis cells (SOECs) offer significant advantages in terms of fast kinetics, reduced electrochemical losses and high electrical-to-chemical conversion efficiencies. Especially by integrating SOECs into cross-sectoral storage technologies, essential benefits for a successful energy transition within the areas of transport and chemical industry can be achieved. The synthesis of gaseous and liquid fuels like methane, methanol or diesel with an SOEC based system requires downstream processes for the conversion of H₂ (and CO) into the desired products. Since the respective downstream processes are typically operated at elevated pressures in a range between 10 and 60 bar, pressurized operation of the SOEC electrolyser could be beneficial due to significantly reduced or omitted interposed compression work [1]. Furthermore, previous studies have shown that by increasing the operating pressure of an SOEC, the overall area specific resistance (ASR) can decrease significantly leading to a decreased power consumption of the electrolyzer for constant H₂, syngas or CO production [2–8].

The SOEC technology heading towards commercial use is currently mainly based on planar stack designs with two different cell concepts [9–12]. The cell developments mainly differ in the respective cell component which is used as the mechanically stabilizing layer. Fuel electrode supported cells use a thick and porous structure of the fuel electrode substrate and are also known as anode supported cells (ASC) when publications discuss the fuel cell mode [13–15]. Since the anode turns into the cathode within electrolysis mode, the term CSC (cathode supported cell) is commonly used and will also be used within this publication [16–18]. Electrolyte supported cells (ESC) use the dense electrolyte as the mechanically stabilizing layer of the cell. Generally, the thickness of the respective layer of each cell concept dominates the performance during the operation and leads to a comparably high ohmic resistance in case of the ESC whereas diffusion and activation resistances are significantly more important for the performance of the CSC.

This study examines the differences in performance during the pressurized operation of 10-layer stacks with CSC and ESC concepts. The pressure effect on dynamically recorded and steady-state U(i)-curves is discussed during steam, co- and CO₂ electrolysis as well as within an impedance study.

The purpose of this study is to provide experimental data about a quantified temperature and pressure dependent ASR and the general performance data for both cell concepts on stack level during different operating modes under elevated pressure. These data can be used for SOEC models and pressurized system studies where the parametrization and validation of the models is generally crucial for the reliability of the simulation results. The impedance study provides scientific knowledge about the influence of an elevated operating pressure during steam and CO₂ electrolysis related to the different cell concepts and electrode materials used within the stacks.

It should be noted that though the study compares the performances, both cell concepts have their own strengths and weaknesses in terms of maximum performance, mechanical-, redox- or long-term stability that should always be considered for individual system needs. These aspects will not be discussed within this manuscript.

2. Experimental

The F10-design stack from Forschungszentrum Jülich used in this study consists of 10 CSCs, each with an active area of 80 cm². The cells consist of a Ni-8YSZ fuel electrode, an 8YSZ electrolyte and a screen printed thin GDC layer attached to the electrolyte beneath the LSCF air electrode. More details about the stack materials with the electrode thicknesses can be found in Ref. [19,20]. The CSC stack with its internal manifold was operated in counter-flow mode. In order to match the media inlet and outlet connection points of the test rig, a specially designed adapter plate was used and integrated into the test bench (see Fig. 1a). Three thermocouples were inserted 40 mm deep into the central

interconnector whereas one thermocouple was inserted into the top and bottom plate of the stack respectively. Within the central interconnector the temperatures were measured at 1/4, 1/2 and 3/4 of the cell length in flow direction. A weight of 100 kg was used for clamping during operation of the stack.

The commercially available ESC stack used in this study has a co-flow setup and contains 10 cells, each with an active area of 127.8 cm². The cells consist of a Ni-GDC fuel electrode, a 3YSZ electrolyte and an LSCF air electrode. Thin GDC layers are implemented between the fuel electrode and the electrolyte and between the air electrode and the electrolyte respectively. Due to the open air external manifold design, the stack is housed into a gastight steel box with open gas manifolding (see Fig. 1 b). For measuring the temperatures inside the stack during operation, five thermocouples are placed directly on the air electrodes of the stack. One thermocouple is placed on layer one and ten respectively. The three remaining thermocouples are placed at 1/4, 1/2 and 3/4 of the length of the middle cell of the stack in flow direction. More details about the stack, the stack box and the electrode thicknesses can be found in Ref. [21–24].

The test rig used in this study offers the possibility to operate SOC stacks in a pressure range between 1.4 and 8 bar. The CSC stack as well as the ESC stack is placed inside a furnace environment which is installed inside a pressure vessel. A schematic of the test rig with a detailed description of the opportunities during operation was already published by the authors and can be found in Ref. [22].

During steady state U(i)-curves, the fuel gas flows for a constant reactant conversion of 70% at each current density point was used. The RC is defined according to the overall inlet mass flow of convertible reactants. Steam electrolysis operation was conducted with a molar ratio of 90/10 (H₂O/H₂), co-electrolysis operation with a molar ratio of 60/30/10 (H₂O/CO₂/H₂) and CO₂ electrolysis operation with a molar ratio of 90/10 (CO₂/CO). Steady state U(i)-curves were performed in order to obtain a current density dependent temperature, ASR and gas composition profile at a constant reactant conversion rate. During dynamically recorded U(i)-curves the fuel gas flows were set according to a reactant conversion of 70% at a current density of -0.75 A cm^{-2} for each gas composition. Due to a fast current ramp of $-0.16 \text{ A cm}^{-2} \cdot \text{min}^{-1}$ a quasi-isothermally recorded U(i)-curve with a very small temperature change over the complete range of current density could be performed. This method gives the possibility to characterize the stacks at a defined temperature. Impedance measurements were recorded galvanostatically with a Zahner Zennium at -0.2 A cm^{-2} and a current amplitude of 0.38 A. For all experiments a constant air flow of 1 slpm air per cell was used for the air side of the stacks. The gas analysis system used within the study is a nondispersive infrared sensor analyzer from Rosemount with sensors for H₂, CO, CO₂ and CH₄.

3. Results and discussion

3.1. Characterization of the ohmic resistance and the performance of both stacks

As a preliminary characterization of the CSC stack, the ohmic resistance was investigated over a wide temperature range between 650 and 820 °C. For this purpose, impedance spectra were recorded for the middle cell of the stack close to OCV condition at 1.4 bar. The furnace temperature was increased in 20 K steps. To ensure the stack temperature to be equal to furnace temperature at every measuring point, a dwell time of at least 90 min had to expire before electrochemical impedance spectroscopy (EIS) was performed. Out of the obtained impedance spectra, the ohmic resistance was extracted for every temperature step. In Fig. 2a) the obtained experimental data for the temperature dependent ohmic resistance of the CSC stack is shown. The values are plotted jointly with data of the ESC stack published in Ref. [21]. The ohmic resistance of the ESC stack was characterized between 650 and 850 °C. The shown curves are fitted based on the

measured values in order to receive an equation for the ohmic resistance over the complete temperature range. Since the electrolyte of the cells used in the ESC stack is the thickest and mechanically stabilizing layer, the overall performance is majorly influenced by the ohmic resistance and correspondingly by the temperature dependency of the electrolyte material. The increased thickness of the electrolyte within the ESCs leads to a higher ohmic resistance compared to the CSC. Furthermore, the 3YSZ material used in the ESC is known to show less oxide ion conductivity than the 8YSZ material of the CSC [25,26]. Consequently, the ohmic resistance of the ESC stack shows a significantly higher temperature dependency and generally higher resistance values.

The ohmic resistance of the cells used in the ESC and CSC stack was fitted with the exponential expression $ASR_{\Omega} = y_0 + A \cdot \exp(B \cdot T)$ where y_0 , A and B are constant parameters as shown in Table 1 and T is the temperature in Kelvin. The obtained values of the CSC stack are as follows whereas the values of the ESC stack are taken from Ref. [21]:

Dynamically recorded $U(i)$ -curves were performed with both stacks and an inlet gas composition of 80/20 H_2O/H_2 . The inlet mass flows were defined for a reactant conversion rate (RC) of 60% at a current density of -0.8 A cm^{-2} . The current density was increased with a ramp of $-0.16 \text{ A cm}^{-2} \text{ min}^{-1}$. The ESC stack was operated at a furnace temperature of $850 \text{ }^\circ\text{C}$ which is a relevant operating temperature for the used commercially available stack [27]. In contrast, the CSC stack was operated at a furnace temperature of $750 \text{ }^\circ\text{C}$. Within both operating conditions shown in Fig. 2 b) the OCV increased at elevated pressure due to the well-known thermodynamic relation between elevated pressure and a related higher Gibbs energy demand of the reaction [4].

In case of the ESC stack the shown averaged cell voltage ($U_{\text{cell,avg}}$) increased almost linearly with current density for 1.4 and 8 bar respectively. Consequently, thermodynamics' influence and the related higher OCV at 8 bar led to a reduced maximum current density at the same voltage of 1.4 V. Thus, the achieved conversion decreased from 53% to 49%. The reason for the almost linear behavior of the voltage and the minor pressure dependency can be attributed to the ohmic resistance as the major part of the overall cell resistance of the ESC. The ohmic resistance itself is pressure independent and the thin electrodes do not lead to significant pressure influences on the diffusion or activation resistances. The ESC stack was already investigated extensively in pressurized steam and co-electrolysis operation by the authors and further results can be found in Ref. [21,22].

Overall, the CSC stack shows a much higher achievable current density at a 100 K lower furnace temperature. The stack showed a RC of 82% at 1.4 bar and at 1.4 V. Furthermore, the operation at elevated pressure led to a reduced slope of the $U(i)$ -curve and an increased

maximum current density. The RC increased by 6%–88% accordingly. Due to the reduced slope of the current-voltage characteristic recorded at 8 bar, a crossing of the $U(i)$ -curves can be observed within the endothermic operating region ($<1.28 \text{ V}$) of the CSC stack. The crossing of the $U(i)$ -curves can be found at a current density of approximately -0.7 A cm^{-2} . Furthermore, the high conversion at 8 bar led to a significantly visible bending of the $U(i)$ -curve at a voltage $>1.3 \text{ V}$ which can be attributed to mass transport limitations [28–30].

3.2. Steady state $U(i)$ -characteristics during pressurized steam electrolysis operation

Fig. 3 shows steady state $U(i)$ -curves of the CSC and ESC stack with an inlet gas composition of 90/10 (H_2O/H_2) for 1.4, 4 and 8 bar. Mass flows were set for a constant RC of 70% at every current density step. The furnace temperature was $750 \text{ }^\circ\text{C}$ during the operation of the CSC stack and $800 \text{ }^\circ\text{C}$ for the ESC stack. Both graphs in Fig. 3 show the voltage of the middle cell of the respective stack. According to the construction of the two stacks described earlier, the core temperature of the CSC stack is measured within the central bipolar plate whereas in case of the ESC stack the temperature is directly measured at the middle length of the air electrode of layer 5. The ASR shown in Fig. 3 is calculated according to the equation $ASR = (U_{\text{measured}} - U_{\text{Nernst,avg}})/i$ where U_{measured} represents the measured cell voltage. $U_{\text{Nernst,avg}}$ represents the theoretical voltage at the corresponding current density i by assuming a linear conversion over the cell length and an averaged gas composition between inlet and outlet [31]. Additionally the area specific ohmic resistance (ASR_{Ω}) is shown according to the values given in Table 1. Note that the y-axes of the compared plots related to the temperature and ASR results shown in Fig. 3 have different scales.

As predicted by the Nernst equation, the open circuit voltage was found to increase with increasing operating pressure within both experimental investigations. The measured open circuit voltages shown in Fig. 3 are in good agreement with the theoretical values, indicating an accurate dosage of the inlet media. However, the measured OCV of the CSC stack when using the small volume flows related to the first measuring point showed a slightly too low voltage (7 mV/cell). This phenomenon could indicate a very small leakage inside or outside of the stack. However, an effect on any stack temperature was not observed. With higher volume flows, the OCVs were in good agreement with the theory. By increasing the current density, the measured core temperature of the stacks decreased at low current densities due to the endothermic reaction. At 1.4 bar and a voltage of 1.28 V for thermoneutral operation, the current density shows values of approximately -0.85 A

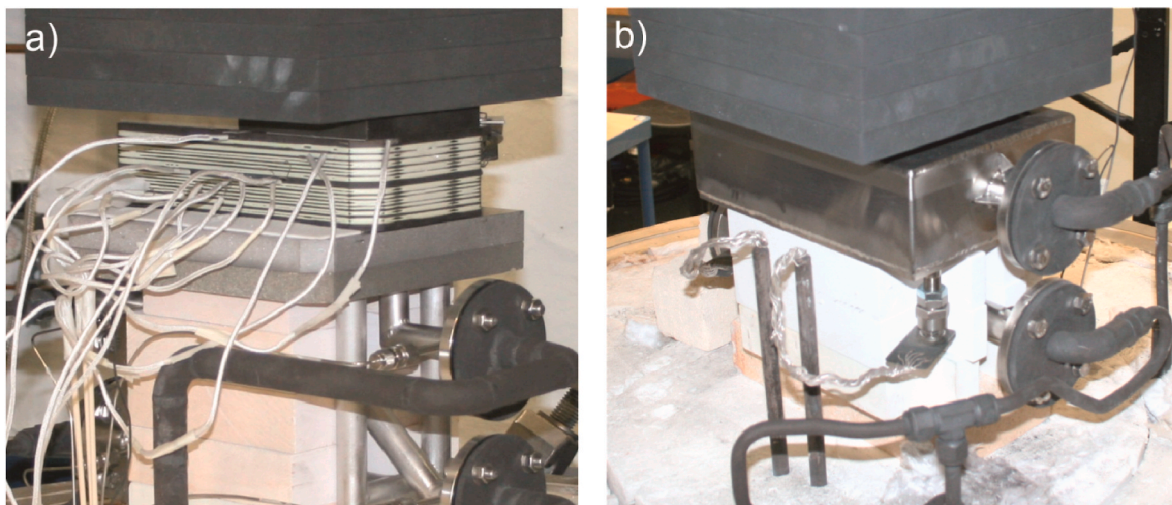


Fig. 1. a) Implementation of the Jülich F10-design stack into the test rig using a specially designed adapter plate. b) Stainless steel box containing the 10-layer ESC stack implemented into the pressurized test rig.

cm^{-2} for the CSC and -0.40 A cm^{-2} for the ESC stack respectively. However, the measured core temperature showed slightly higher values than the furnace temperature indicating that the placed thermocouple probably measures more close to a hotspot within both stack experiments. Nevertheless, the temperature deviation at the thermoneutral operating point between measured core temperature and furnace temperature is only in the range of 2–7 K.

Comparing the U(i)-characteristics of the CSC stack at different operating pressures, the significance of the pressure influence can be clearly observed. The voltages recorded at 4 and 8 bar show a convergence towards the U(i)-curve recorded at 1.4 bar until the characteristics cross each other at approximately -0.6 A cm^{-2} . At this current density, thermodynamics' influence on the cell voltage is compensated by reduced activation and diffusion resistances within the cell. By further increasing the current density, the operation changes towards an exothermic behavior and the difference between the voltages recorded at 1.4 and 8 bar becomes more dominant. Although the stack was operated with a constant RC, the quantity of electrochemical reactions increase with higher current densities and the pressure effect becomes more apparent. Hence, at 8 bar and at the maximum current density within this experiment, the voltage decreased by 39 mV. As a consequence, the lower voltage leads to a decreased power consumption of 35 W (performance gain of approximately 3%) for the 10-layer CSC stack. Furthermore, due to the lower voltage at higher pressure and the related lowered heat production, the measured temperature showed slightly lower values during the exothermic operation regime. The overall cell resistance shown in the lower graph of Fig. 3 a) furthermore demonstrates the apparent pressure dependency of the CSC stack performance. At 1.4 bar, the overall cell resistance shows a value of approximately $0.39 \Omega \text{ cm}^2$ at -0.75 A cm^{-2} , whereas it reduced by 15% to approximately $0.32 \Omega \text{ cm}^2$ at 8 bar. At this current density, the ohmic resistance takes a proportion of approximately 40% at 1.4 bar and 50% at 8 bar. Thus, the influence of changing the operating pressure on the polarization resistance is around 60% at 1.4 bar and reduced from approximately $240 \text{ m}\Omega \text{ cm}^2$ to $170 \text{ m}\Omega \text{ cm}^2$ (8 bar). However, the ASR of the first measuring point at -0.1 A cm^{-2} shows a conspicuous behavior since the calculated values are seemingly too low. This behavior could be associated with a small leakage inside or outside of the stack and a corresponding lower hydrogen proportion since the measured voltage

Table 1

Fit values of the temperature dependent ohmic resistance of the CSC and ESC stack respectively. The variable T is the operating temperature in K.

$\text{ASR}_{\Omega} = y_0 + A \cdot \exp(B \cdot T)$	CSC	ESC
$y_0 / \Omega \cdot \text{cm}^2$	$7.181 \cdot 10^{-2}$	$27.266 \cdot 10^{-2}$
$A / \Omega \cdot \text{cm}^2$	$12.854 \cdot 10^4$	$35.316 \cdot 10^4$
B / K^{-1}	$-1.397 \cdot 10^{-2}$	$-1.264 \cdot 10^{-2}$

and as a consequence the ASR calculated from this would be too low. Though the measured OCV was in good agreement with the theoretical value at higher volume flows, a small leakage could have a significant effect at low current densities with the related small volume flows and the generally low hydrogen content in the feed during electrolysis operation. Compared to the CSC stack performance, the ESC stack shows a significantly lower achievable current density for the same RC of 70%. Further investigations for the steady state steam electrolysis operation of an ESC stack were already published by the authors, however the RC was lower and a different stack was used for the conducted experiments [21]. Nevertheless the experimental investigations show similar results which indicate a high level of accuracy during stack manufacturing and a minor dependency of the RC for this kind of stack. As shown within Fig. 3 b), the cell voltage shows a slight convergence of the U(i)-characteristics, but no crossing or overall performance gain. Consequently, the stack shows similar temperature values at different operating pressures throughout the entire current density range. The plotted ASR shows a significantly smaller pressure dependency compared to the CSC stack and a generally much higher (pressure independent) ohmic resistance. As mentioned before, this phenomenon can be attributed to the much thicker electrolyte (ESC: $90 \mu\text{m}$ 3YSZ; CSC: $10 \mu\text{m}$ 8YSZ) and the related more dominant ohmic loss. Since the cermet of the porous fuel electrode of the CSC possesses a significant proportion of highly conducting Nickel material, the ohmic resistance is comparably small and the performance more dependent on activation and diffusion processes. Consequently, it leads to a generally higher overall ASR of the ESC stack and in turn to a more significant pressure dependency of the CSC stack.

However, the authors want to point out that the higher achievable current density and increased pressure dependency of the CSC stack concerns only one aspect within the comparison of a CSC with an ESC.

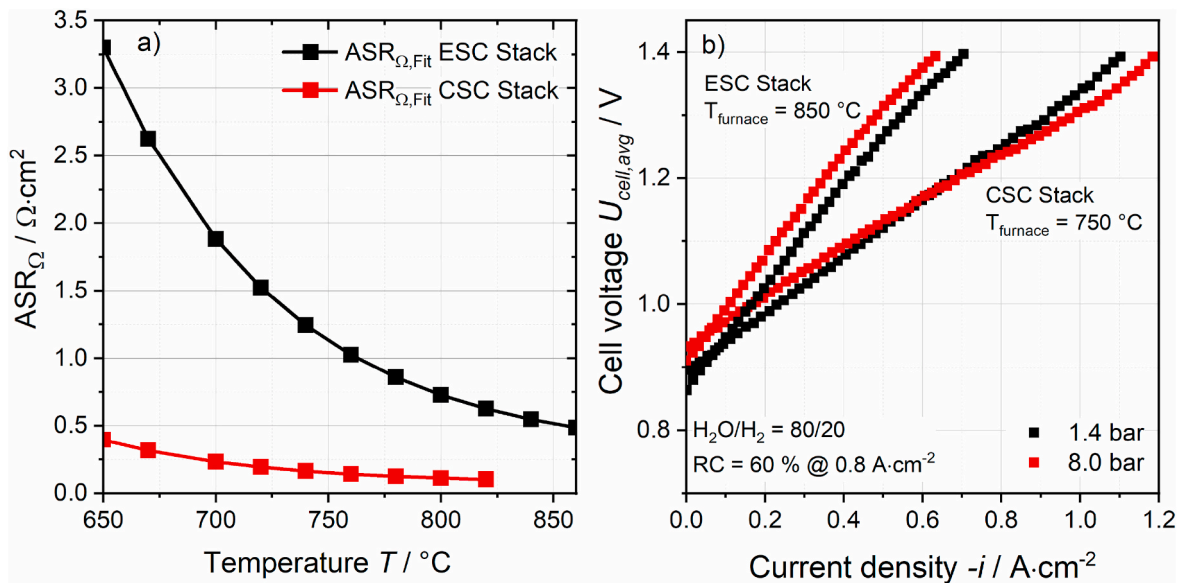


Fig. 2. a) Characterization of the ohmic resistance of the ESC and CSC stacks. The values were obtained from impedance measurements at OCV and 1.4 bar for the middle cell of each stack over a wide temperature range. Data of the ESC can be found in Ref. [21]. b) dynamically recorded U(i)-curves of the CSC stack operated at $750 \text{ }^\circ\text{C}$ in comparison with the ESC stack operated at $850 \text{ }^\circ\text{C}$ during steam electrolysis operation. Inlet mass flows with a 80/20 $\text{H}_2\text{O}/\text{H}_2$ mixture were defined for a RC of 60% at -0.8 A cm^{-2} .

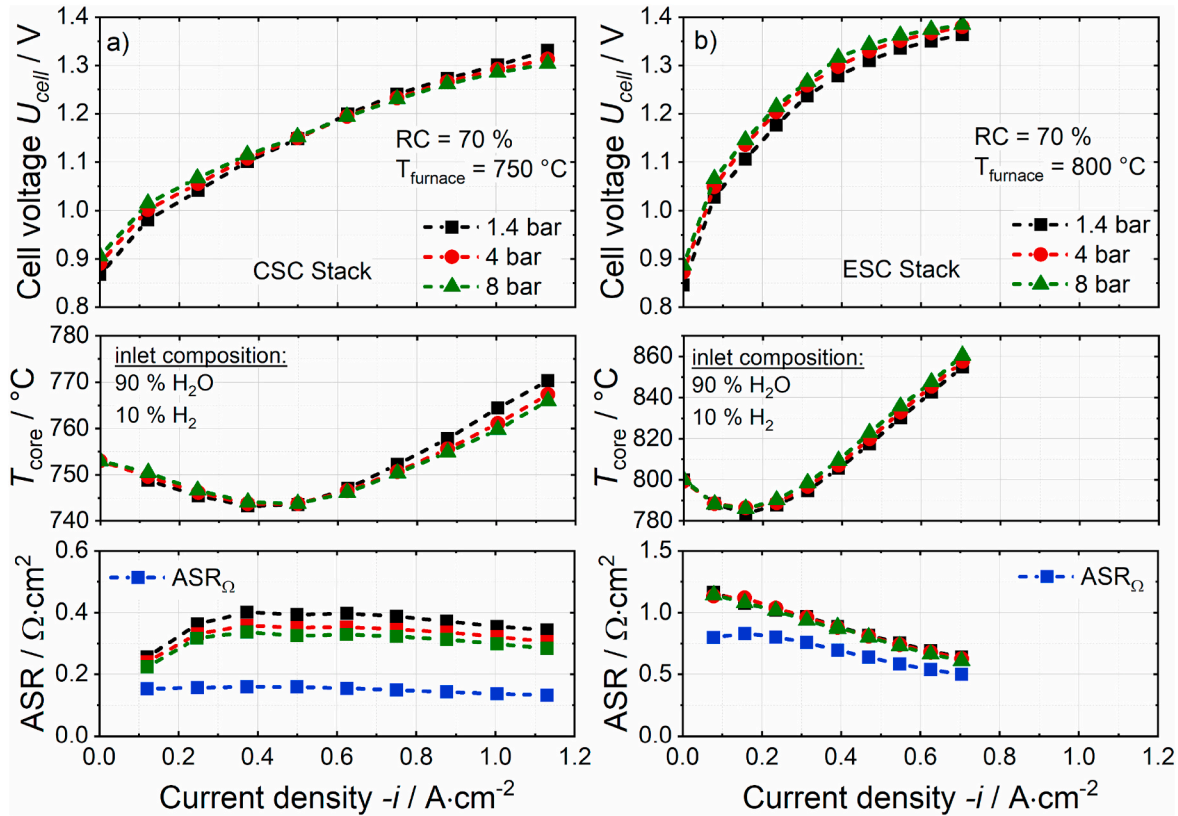


Fig. 3. Steady-state $U(i)$ -curves for a) the CSC stack and b) the ESC stack recorded at 1.4, 4 and 8 bar. The furnace temperatures were 750 °C (CSC) and 800 °C (ESC) respectively. Inlet gas composition is 90/10 H_2O/H_2 with a reactant conversion of 70% at every measuring point. Note that the y-axes of the temperature and ASR plot differ between a) and b) due to the relevant operating temperatures of the stacks.

Although the electrochemical performance of a CSC stack is higher, other aspects like mechanical robustness or redox stability have to be taken into account for system relevant considerations.

3.3. Steady state $U(i)$ -characteristics during pressurized co-electrolysis operation

According to the steady-state experiments conducted for pure steam electrolysis, co-electrolysis performance of the CSC and ESC stack was furthermore compared. A gas inlet composition of 60/30/10 ($H_2O/CO_2/H_2$) was chosen to evaluate the performance and to determine the outlet gas composition throughout the entire current density range at three operating pressures. The voltages of the CSC stack recorded at 4 and 8 bar show a convergence towards the $U(i)$ -curve recorded at 1.4 bar until the characteristics cross each other within the endothermic operating mode. The crossing and the related performance gain occurred already at approximately -0.4 A cm^{-2} , whereas it could be observed at approximately -0.6 A cm^{-2} in case of pure steam electrolysis. The decrease of the voltage with higher pressure was additionally found to be more significant during the co-electrolysis operation. Furthermore, in contrast to the conducted steam electrolysis operation shown in Fig. 3 a), the temperature of the CSC stack shows an apparent influence of the operating pressure during co-electrolysis. Although the voltage decreased with higher pressure, the temperature increased significantly due to internal exothermic methanation reaction. The performance gain found in the $U(i)$ -characteristics can also be seen in the lower plot of the same diagram where the ASR shows a prominent decrease of the overall resistance with higher pressure.

The ESC stack shows a significantly lower achievable current density for the same RC of 70%. As can be seen in Fig. 4b, a slight convergence of the $U(i)$ -characteristics was observed, but no crossing or overall performance gain. However, the convergence of the voltages was found to

be more prominent than during steam electrolysis operation. Furthermore, the temperatures show an apparent difference between the three pressures which was observed for the operation of the CSC stack as well. The plotted ASR shows a significantly smaller pressure dependency compared to the CSC stack and a generally much higher ohmic resistance. Similar results for the ESC stack operation during co-electrolysis can be found in Ref. [22], whereas a different stack was used. Since the results of both studies are in good agreement, it indicates a high level of accuracy and repeatability during manufacturing of the ESC cells and stacks. This attribute is one of the major interests of SOC technology suppliers since similar stack performances are important for efficient operating strategies of larger stack units.

The gas analysis conducted during the co-electrolysis operation of the CSC and the ESC stack is shown in Fig. 5. Due to the measuring principle of the analyzer, water was condensed and was not part of the analyzed composition. The dashed lines in the figure represent the thermodynamic equilibrium of the dry gas composition after a reactant conversion of 70% whereas the dots represent the measured values. The general equation for calculating the molar fraction of one component in a dry gas composition is $X_{i, \text{dry}} = X_i \cdot (1 - X_{H_2O})^{-1}$ with X_i as the measured molar fraction of one component.

The measured concentrations for the outlet gases are generally in good accordance with the calculated thermodynamic equilibrium over a wide range of current density. Within both experiments, the major deviation between theoretically and experimentally recorded values can be found at low current densities, especially for H_2 and CO . As mentioned above, this is likely due to the comparably large impact and uncertainties regarding of flow or leakages at little gas flows. However, the deviation of the measured concentrations is in a range of 3–7% at the lowest current density point. In comparison to the ESC stack, the lower operating temperature of the CSC stack leads to a significantly higher proportion of CH_4 in the outlet at elevated pressure. For a high extent of

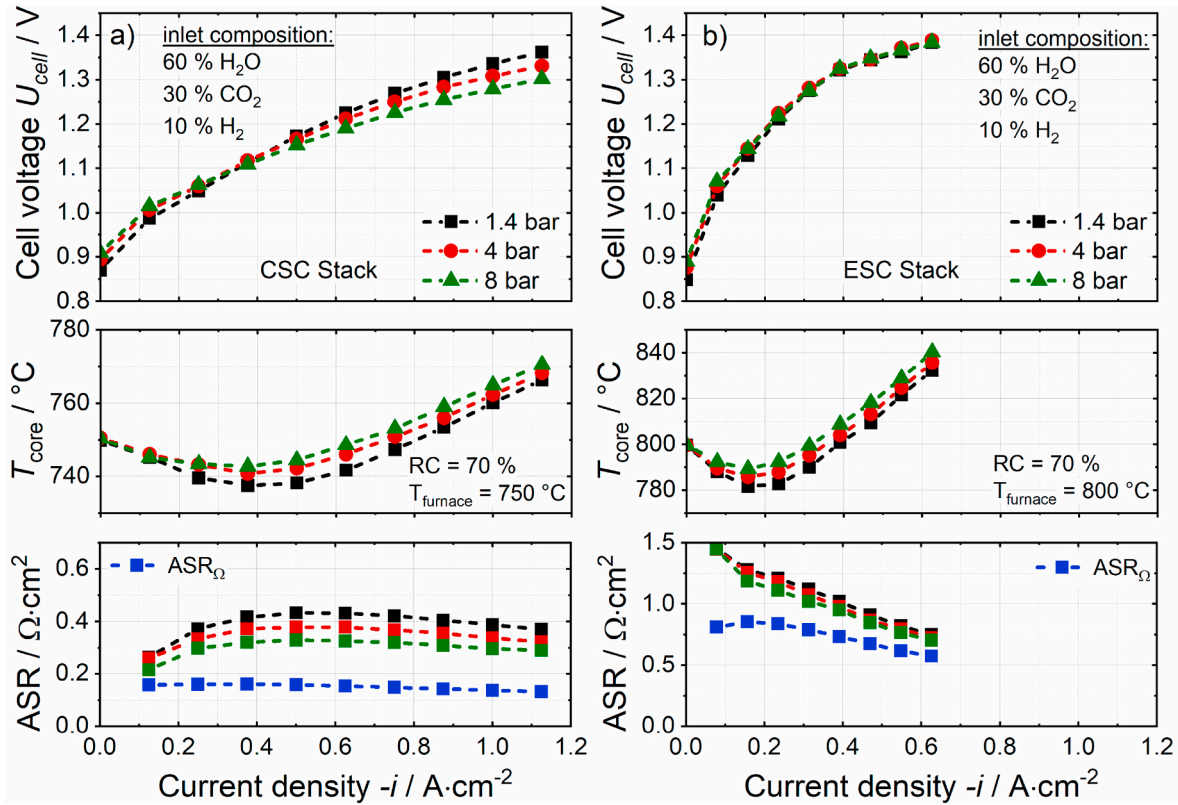


Fig. 4. Steady-state $U(i)$ -curves during co-electrolysis for a) the CSC stack and b) the ESC stack recorded at 1.4, 4 and 8 bar. The furnace temperature was 750 °C (CSC) and 800 °C (ESC) respectively. Inlet gas composition is 60/30/10 (H₂O/CO₂/H₂) with a reactant conversion of 70% at every measuring point. Note that the axes of the temperature and ASR plot differ between a) and b) due to the relevant operating temperatures of the stacks.

methanation reaction, high pressures, high H₂/CO ratios and low temperatures are generally favorable. During the experiments conducted with the CSC stack, a methane content of approximately 7% was measured at 8 bar and 743 °C. Since the ESC stack was operated at a 50 K higher furnace temperature, the extent of the methanation reaction was lower and a proportion of approximately 5% was achieved at 790 °C. Due to the exothermic characteristic of the methanation process, the extent of this reaction has a distinct impact on the thermal behavior of the stack. This can be assigned to the phenomenon observed during the recording of the $U(i)$ -curves of both stacks where a higher temperature was measured while the voltage reduced at elevated pressure. The increased temperature led to a reduced ohmic resistance and faster kinetics and consequently to a more significant reduction of the voltage and the ASR at higher pressures.

3.4. Dynamically recorded $U(i)$ -characteristics of steam, co- and CO₂ electrolysis

Fig. 6 shows dynamically recorded $U(i)$ -curves of the CSC stack operated at 1.4 and 8 bar with a gas composition of 90/10 (H₂O/H₂) for steam electrolysis operation, a 60/30/10 (H₂O/CO₂/H₂) for co-electrolysis operation and a 90/10 (CO₂/CO) for CO₂ electrolysis operation. The general aim of the dynamically recorded $U(i)$ -curves is the quasi-isothermal characterization with only a small temperature deviation within the stack over the complete current range. This allows to determine the performance at a certain stack temperature. The gas flows for the experiments shown in **Fig. 6** were set according to an RC of 70% at a current density of -0.75 A cm^{-2} . Due to the risk of carbon deposition within the stack and the outlet pipes of the test rig during pure CO₂ electrolysis operation, the experiments were not conducted towards reactant conversions larger than 70% [22].

The operation of the CSC stack at 1.4 bar shows a nearly linear

behaviour of the $U(i)$ -curve during pure steam electrolysis. Added CO₂ into the gas inlet composition led to a higher resistance and thus to an increased slope especially at higher RC. At -0.75 A cm^{-2} , the stack showed a 170 mV higher voltage. The operation for pure CO₂ electrolysis shows a more significant bending of the $U(i)$ -curve towards a higher voltage for a RC $\geq 45\%$ ($\triangleq -0.5 \text{ A cm}^{-2}$). This behaviour indicates a higher diffusion resistance during the operation of the CSC at higher current densities since CO₂ has a larger molecular size and molecular mass compared to steam leading to higher mass transport limitations [32–34]. The ASR values given in **Fig. 6** represent an average and were linearized over the current density range of $-0.13 \dots -0.55 \text{ A cm}^{-2}$. The values calculated for the $U(i)$ -curves recorded at 1.4 bar show an increase of the resistance of approximately $20 \text{ m}\Omega \text{ cm}^{-2}$ at 70% RC by switching from pure steam to pure CO₂ electrolysis operation. **Fig. 6 b)** shows the recorded $U(i)$ -characteristics at 8 bar. It is apparent, that the current-voltage curves show a more similar behavior, i.e. more similar resistances compared to the ones observed for the lower operating pressure. The calculated averaged ASR of pure CO₂ electrolysis shows an increase of the resistance of approximately $13 \text{ m}\Omega \text{ cm}^{-2}$. Consequently, the ASR values indicate that the CO₂ electrolysis operation shows a higher pressure dependency than pure steam or co-electrolysis operation.

In comparison to the CSC stack, the $U(i)$ -characteristics of the ESC stack of **Fig. 6 c** and **d** were found to show a more linear behavior for all three operating modes at both pressures. However, the temperature characteristics over the complete current density range were more unequal and a more significant endothermic effect was observed for co- and CO₂ electrolysis operation. According to **Fig. 6**, the maximum temperature spread is 10 K at the highest current density point. Since the thermocouples used in the ESC stack were placed directly at the air electrodes and the thermocouples used in the CSC stack were placed within a hole of the bipolar plate, one can assume that the more

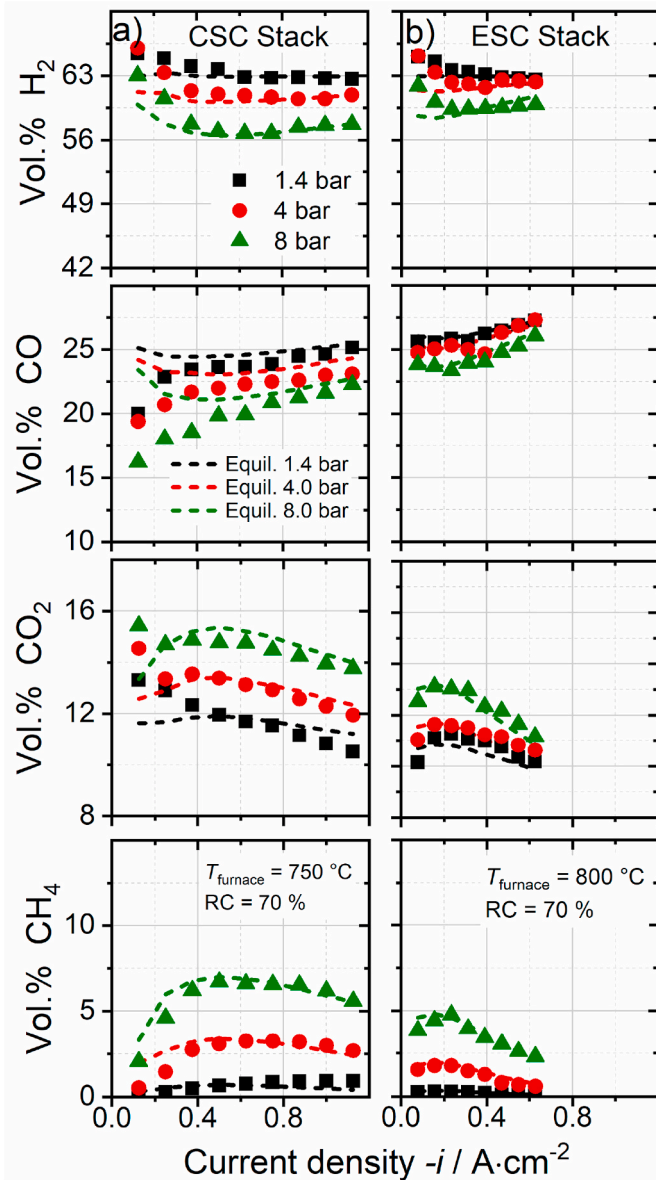


Fig. 5. Gas analysis of the a) CSC and b) the ESC stack according to the steady state co-electrolysis experiments of Fig. 4. The CSC stack was operated at 750 °C furnace temperature whereas the ESC stack was operated at a furnace temperature of 800 °C.

significant endothermic effect observed for the ESC stack operation could not be recorded for the CSC stack due to the dynamical operation and the high heat capacity of the bipolar plate material. It is likely that the same temperature behavior also took place within the CSC stack operation and was most likely more significant since a higher current density could be achieved. However, due to the comparably low temperature dependency and the generally lower influence of the ohmic resistance on the overall performance of the CSC stack the influence of this temperature spread is likely marginal.

Although the ESC stack was operated close to its typical operating temperature, the calculated ASR values were found to be more than twice as high as the values of the CSC stack. Comparing both operating pressures shows that a considerable pressure dependency during steam, co- or CO₂ electrolysis is not observed. Due to the high proportion of the pressure independent ohmic resistance in addition to the thin electrodes with minor diffusion contribution, the pressure dependency of an ESC is considerably small. This phenomenon was already found and discussed

for experimental studies published by the authors using ESC stacks [21, 22, 35, 36]. However, the calculated ASR values of the U(i)-curves of the ESC stack show a slightly higher pressure dependency of the CO₂ electrolysis operation compared to steam and co-electrolysis. Assuming the diffusion resistance to play a subordinate role during the pressurized operation of ESCs, the higher ASR can likely be attributed to the generally higher activation resistance which is necessary for electrochemical CO₂ reduction [34]. However, for both the CSC and the ESC stack a higher pressure dependency during CO₂ electrolysis was observed. Hypothetically, this observation could indicate the existence of a significantly different electrochemical reaction mechanism during the CO₂ reduction process (see section 3.6) [37, 38].

3.5. Quantification of the ASR

Fig. 7 shows the direct comparison of the temperature and pressure dependent overall resistances of the CSC and ESC stack. The ASR values were obtained out of dynamically recorded and steady-state U(i)-characteristics for steam and co-electrolysis operation at 1.4, 4 and 8 bar. The ASR values of the ESC stack for different inlet gas compositions can furthermore be found in Refs. [22]. CO₂ electrolysis was not considered for the analysis due to the limited number of experiments conducted. However as shown within the dynamically recorded characteristics, the ASR of the CO₂/CO operation can be assumed to behave similarly to the characteristics of the one of the steam and co-electrolysis operation with slightly higher resistance values and a slightly higher pressure dependency. Besides the experimentally obtained ASR values, Fig. 7 shows the ohmic resistance for both stacks according to the equations given in Table 1. The ASR of the ESC stack is plotted jointly with values obtained with a different but identically constructed stack used in another study with the same gas composition (unfilled squares) [22].

The pressure effect on both stacks is found to be more prominent at lower temperatures and can be ascribed to the more prominent kinetics and the consequently more prominent polarization resistances at lower temperatures. As already observed for the steady-state and dynamically recorded U(i)-characteristics, the CSC stack performance shows a noticeably higher pressure influence. Furthermore, the pressure effect is more significant between 1.4 and 4 bar than between 4 and 8 bar which is in good agreement with a theoretical study published by Henke et al. [4]. The phenomenon is mainly caused by a change in diffusion mechanisms from Knudsen to ordinary diffusion with increasing pressure and the consequently decreased activation resistance due to the increased number of reactants available at the triple-phase boundary. The phenomenon of the changed diffusion mechanism was already discussed by the authors in detail elsewhere [22]. In case of the ESC stack, the pressure effect on the performance was observed to be marginal. The fitted ASR curves of the ESC and CSC stack follow the equation $ASR = A \cdot \exp(B \cdot T)$ with the parameters shown in Table 2. The ASR curve of the ESC stack is plotted jointly with values obtained with a different but identically constructed stack used in another study with the same gas composition in order to show the reproducibility of the results and the good agreement between these overall resistances [22]. As mentioned before, the reproducibility of the electrochemical performance across different stacks is one of the major interests of SOC technology providers and furthermore required for the efficient operation of larger stack modules.

3.6. Electrochemical impedance study during steam and CO₂ electrolysis operation

EIS was performed in order to investigate the cell resistance of the CSC and ESC in more detail at elevated pressure during steam and CO₂ electrolysis mode. Fig. 8a and b) show a comparison of the H₂O and CO₂ electrolysis operation recorded at -0.2 A cm^{-2} for the CSC stack at three different pressures. In order to minimize the risk of solid carbon formation, the conversion at this operating point was chosen to be 30%.

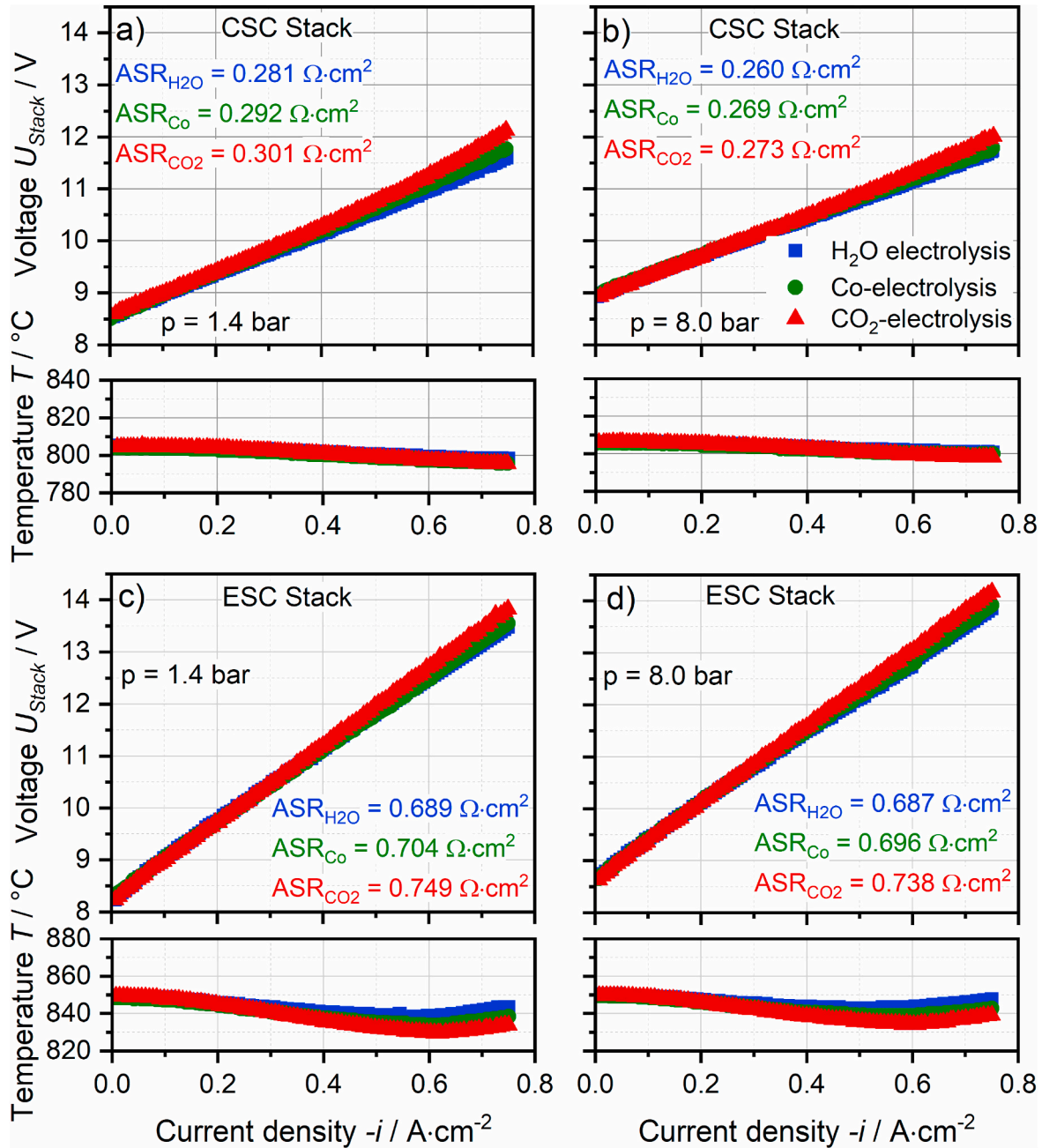


Fig. 6. a)+b) show dynamically recorded $U(i)$ -curves of the CSC stack operated at a) 1.4 and b) 8 bar with steam, co- and CO₂ electrolysis at a furnace temperature of 800 °C. c)+d) show dynamically recorded $U(i)$ -curves of the ESC stack operated at c) 1.4 and d) 8 bar at a furnace temperature of 850 °C.

Due to the different gas mixtures and the related electrolysis modes, the furnace temperature was adjusted to have a constant stack temperature of 750 °C, thus close to a system relevant operating temperature of the CSC stack. The inlet streams were set to match a constant ratio of 60/40 between reactant and product at the outlet of the stack within both electrolysis modes.

By comparing the recorded spectra of the CSC stack, a number of at least four peaks can be observed within the frequency ranges of 0.05–1 Hz (P1), 1–10 Hz (P2), 50–200 Hz (P3) and $1 \cdot 10^3$ – $3 \cdot 10^3$ Hz (P4). P1 and P4 are clearly visible within the impedance spectra of Fig. 8 a and b. The process P2 becomes apparent during steam electrolysis operation at higher pressure and becomes more apparent during CO₂ electrolysis operation within the same frequency range. A process P3 is in the frequency range of 50–200 Hz and becomes apparent in steam electrolysis operation at higher pressure. However, during CO₂ electrolysis

operation this process is overlapped by the high resistance of P4 and cannot be clearly observed within the raw data of the impedance. The characteristic frequencies significantly change with the operating pressure and the provided gas. Although the peak height within a $-Z''(f)$ diagram does not fully describe a resistance, it clearly indicates that there is an apparent difference of the respective resistances between pure steam and pure CO₂ electrolysis operation within the frequency ranges of P1, P2 and P4.

Within the range of P4, a significantly higher peak can be observed for CO₂ electrolysis which is much less dominant for H₂O electrolysis operation. Since the reduction of CO₂ requires a higher activation energy than the reduction of H₂O, P4 located within the high frequency range of the spectra can most likely be attributed to the reduction process with the corresponding charge-transfer reaction occurring at the fuel electrode of the CSC [34]. With higher pressure, the imaginary part

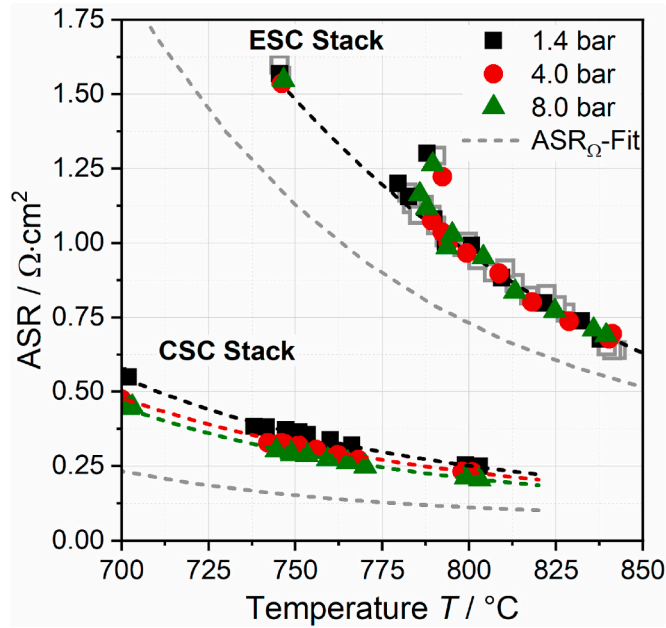


Fig. 7. Temperature and pressure dependent total ASR of the CSC and the ESC stack. The values were obtained out of dynamically recorded and steady-state U (i)-characteristics. The ASR of the ESC stack is plotted jointly with values obtained with a different but identically constructed stack used in another study with the same gas composition (unfilled squares) [22].

Table 2

Parameters for the fitted pressure and temperature dependency of the overall resistance of the CSC and ESC stack.

	CSC			ESC
	1.4 bar	4 bar	8 bar	1.4, 4 and 8 bar
A / $\Omega \cdot \text{cm}^2$	$1.60 \cdot 10^2$	$0.94 \cdot 10^2$	$1.17 \cdot 10^2$	$7.28 \cdot 10^2$
B / $^\circ\text{C}^{-1}$	$-8.11 \cdot 10^{-3}$	$-7.54 \cdot 10^{-3}$	$-7.96 \cdot 10^{-3}$	$-8.29 \cdot 10^{-3}$

of P4 decreases which indicates a decreasing resistance for the steam electrolysis operation. This phenomenon can be ascribed to a decreased activation resistance due to the increased number of reactants present and available at the triple phase boundary at elevated pressure [4,8,22]. However, for CO₂ electrolysis operation a decrease of the height of this peak and subsequently a decrease of the corresponding resistance cannot be clearly observed. The phenomenon of a comparably less significant pressure effect on the fuel electrode process of P4 during CO₂ electrolysis is currently not fully understood but the observation indicates that the respective reduction mechanism on Ni-YSZ is most likely dominated by a different rate-determining step compared to pure steam electrolysis operation. According to the findings of Leonide et al., the process P4 within the corresponding frequency range is overlapped with gas diffusion, charge transfer and ionic transport processes in the fuel functional layer [39,40]. The influence of the additional processes should be almost negligible and should not be affected by using CO₂/CO or H₂O/H₂ since the thickness of the porous fuel electrode functional layer is < 10 μm and the ionic transport in the YSZ independent of the used fuel gas [39]. The limited influence of the operating pressure on the process of P4 during CO₂ electrolysis could hypothetically be connected with different adsorption and/or desorption rates of CO₂ or CO at the TPB and a related limited pressure influenced frequency of reactants available at the active area. Consequently, the pressure effect on the process P4 would be significantly decreased. However, the authors want to point out that the purpose of the presented EIS study was not to analyze any electrode mechanism in detail but rather show the general difference between steam and CO₂ electrolysis operation with a CSC

(Ni/YSZ fuel electrode) and an ESC stack (Ni-GDC fuel electrode) under pressurized conditions. A better insight into the mechanistic details of electrode processes for H₂O or CO₂ electrolysis can likely be done with half-cell or button cell experiments but are highly limited for stack investigations due to the large cell area and the corresponding significant influences of temperature, gas and current distribution on the EIS analysis.

By comparing the spectra a) and b) of Fig. 8 recorded under H₂O and CO₂ electrolysis conditions, an apparent difference of P3 cannot be observed. Hence, this process is likely related to the air electrode since the air electrode process is not dependent on the fuel gas mixture provided to the stack. Thus one can assume that the characteristic frequency of the oxygen evolution reaction and the O²⁻ bulk diffusion within the air electrode is most likely located within the frequency range around 50–200 Hz.

By operating the CSC stack under CO₂ electrolysis conditions, the process P2 is clearly observable whereas under H₂O electrolysis conditions the process is overlapped by P1 and difficult to observe as a single peak especially at low pressures. However, at higher pressure the peak of P2 gets more apparent within the spectra. Since P1 and P2 are both affected by the operating pressure and the type of gas provided to the stack, it can be assumed that the processes are attached to the fuel side of the CSC. In more detail, both processes can be attributed to the gas diffusion (P2) and gas conversion (P1) resistance occurring within an SOC [20,39]. The gas conversion describes the impedance which is caused by a decrease of a reactant concentration due to the conversion of the reactant by the electrode reaction. While applying a current (or current amplitude), the gas concentration within the electrode changes. This change becomes less significant the more the reactant/product ratio approaches a value of 1 since the sensitivity of the (Nernst) voltage decreases with more equally weighted reactant/product gas mixtures [41]. At ambient pressure, the diffusion and conversion resistance oftentimes overlaps which makes it nearly impossible to distinguish between both processes and find their individual resistance. However, at higher pressures, the gas conversion process shows a significant decrease of its characteristic frequency. This phenomenon occurs due to a change of the capacitance of the process and was also shown within an experimental study of Jensen et al. for a CSC stack [3].

However, in case of pure CO₂ electrolysis operation, the gas conversion resistance was observed to be shifted towards slightly lower characteristic frequencies. The maximum of the peak during H₂O electrolysis was at 0.6 Hz whereas it was at 0.2 Hz during CO₂ electrolysis at 1.4 bar. Consequently, the diffusion resistance of the fuel electrode becomes clearly visible around 1 Hz. Furthermore, the gas diffusion resistance becomes smaller due to improved gas transport through the porous substrate of the fuel electrode. Compared to H₂O electrolysis, the slight shift of P1 during CO₂ electrolysis operation towards a lower frequency has to be investigated in more detail, since according to Mogensen et al. a change of the characteristic conversion frequency at a constant pressure with a constant reactant/product ratio can only be influenced by the supplied gas flux, the electrode area, the reactor volume or the temperature [41]. However, these parameters should not differ by using H₂O/H₂ or CO₂/CO gas mixtures and were certainly constant for both operating modes.

The found processes with their related frequency ranges and the derived assignment to the specific electrode processes are in good agreement with other studies investigating Ni/YSZ fuel electrode supported cells or stacks [20,37,39].

Fig. 8c and d shows the EIS spectra recorded during H₂O and CO₂ electrolysis at different pressures of the ESC stack. The stack temperature was kept constant at 700 $^\circ\text{C}$ in order to record significant cell and process resistances. At temperatures close to the system relevant operating temperature (~ 860 $^\circ\text{C}$), the electrode resistances are significantly lower since the kinetics are faster, which makes it much more difficult to distinguish between the pressure-influenced phenomena occurring during H₂O and CO₂ electrolysis. However, a detailed EIS study by the

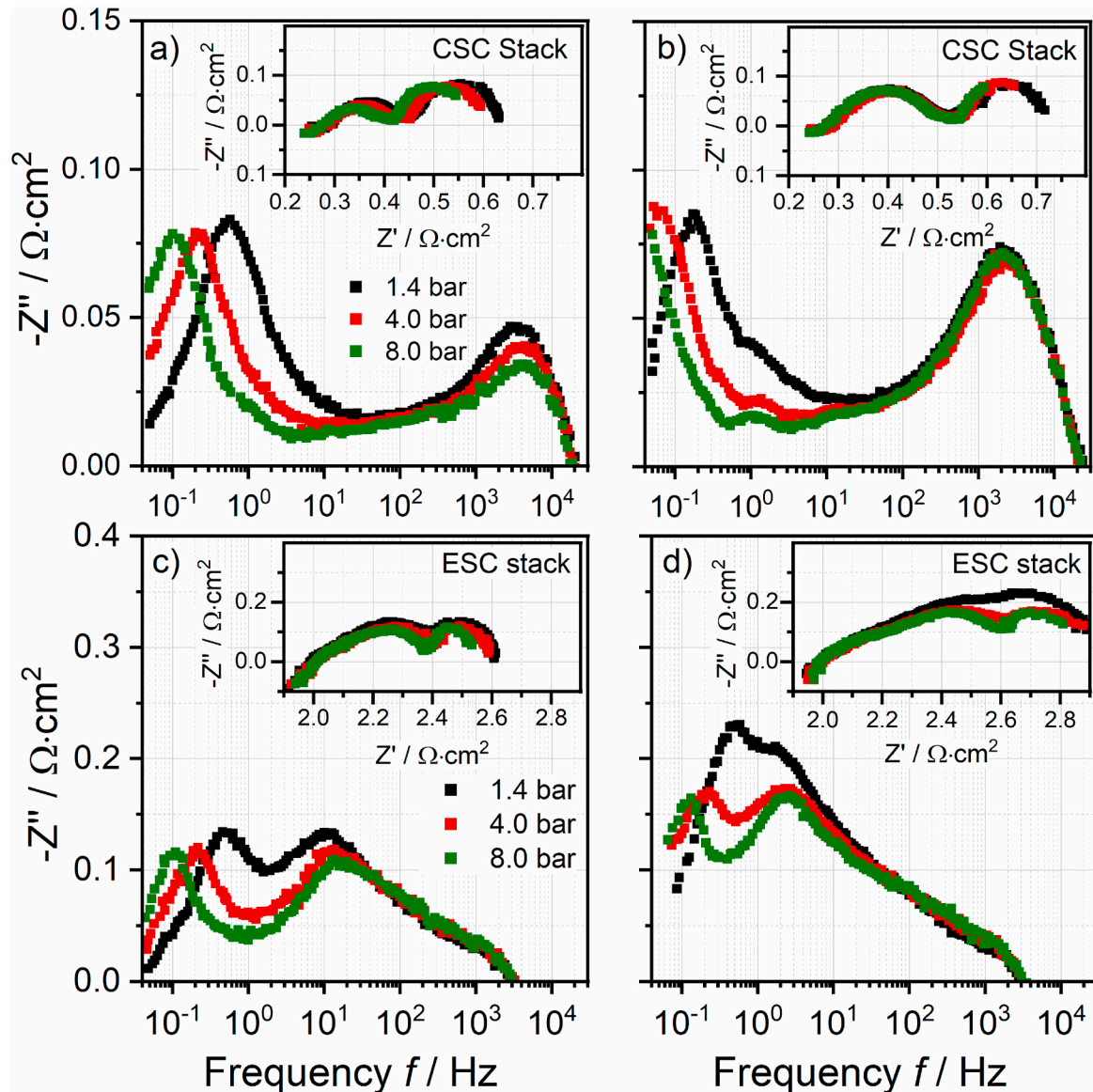


Fig. 8. EIS spectra of the CSC stack recorded at a current density of approximately -0.2 A cm^{-2} during a) pure steam and b) pure CO_2 electrolysis at pressures of 1.4, 4, and 8 bar at 750°C . c) and d) show the same experiment for the ESC stack at a temperature of 700°C . Reactant/product ratio at the outlet was set to 60/40 for both experiments.

authors on the ESC stack comparing H_2O , co- and CO_2 electrolysis at higher temperature can be found elsewhere [22]. Within the two $-Z''(f)$ plots of Fig. 8, two prominent peaks can be observed within a frequency range of 0.1–1 Hz (P1) and 1–20 Hz (P2). Although present, the detailed frequency ranges of further apparent processes cannot be clearly observed within the recorded EIS spectra of the ESC stack.

Since the process around 10–20 Hz decreases with increasing the operating pressure, it can be attributed to a surface process of the fuel electrode. Furthermore, it clearly depends on the type of fuel gas which is provided to the stack and shows significantly higher peaks for CO_2 electrolysis operation. Both observations lead to the assumption that this surface process is the one of the Ni-GDC fuel electrode.

Contrary to the CSC stack with its Ni/YSZ electrodes, the fuel electrode process of the ESC stack was observed at a frequency roughly two magnitudes lower. The low frequency process which is attributed to the gas concentration impedance shows almost the same frequency compared to the CSC stack. During H_2O electrolysis operation, the frequency of the gas concentration resistance decreases due to the before mentioned change of the capacitance at higher operating pressures.

However, since the peak height (corresponding to the resistance of the process) decreases at elevated pressure, it is likely that a gas diffusion contribution is overlapping with the process at around 0.1–1 Hz. During CO_2 electrolysis operation, gas diffusion becomes more prominent due to the comparably larger molecular size and molecular mass. Consequently, the pressure effect during CO_2 electrolysis operation of the ESC is found to be more dominant than during H_2O electrolysis which is in good agreement with the observations of the dynamically recorded U(i) characteristics shown in Fig. 6.

4. Conclusion

In this study, two stacks with different cell types were investigated experimentally in steam, co- and CO_2 electrolysis mode at elevated pressures of up to 8 bar. The stacks consist of 10 layers with fuel electrode supported cells (CSC) and electrolyte supported cells (ESC) respectively. The CSC stack from Forschungszentrum Jülich uses Ni-8YSZ fuel electrodes and $10 \mu\text{m}$ 8YSZ electrolyte whereas the commercially available ESC stack consists of Ni-GDC fuel electrodes and $90 \mu\text{m}$

3YSZ electrolyte.

The experimental investigation of this study mainly concentrated on the comparison of the pressure influence on the performance of each stack during different electrolysis modes. As expected, the overall performance and the impact of an elevated operating pressure were significantly different due to the different cell types. The performance of the ESC stack is mainly influenced by the ohmic resistance related to the thick electrolyte used within the cells. Hence, the ohmic resistance was found to be four times higher at the relevant operating temperature of 850 °C compared to the ohmic resistance of the CSC stack at its relevant operating temperature of 750 °C.

Steady-state characterization of both stacks was conducted for steam and co-electrolysis mode over a wide current density range. Within this study, a performance gain for the operation of the CSC stack under pressurized conditions was found for current densities higher than 0.5 A cm⁻². A significant pressure effect for the ESC stack could not be observed due to the dominant and pressure independent ohmic resistance. During co-electrolysis operation, the gas analysis showed that the outlet gas compositions of the stacks are in good agreement with thermodynamic equilibrium and furthermore showed methane contents of up to 7% at 8 bar.

Dynamically recorded U(i)-curves were recorded for steam, co- and CO₂ electrolysis in order to characterize both stacks at a nearly constant reactor temperature over a wide current density range at different pressures. Although the CSC stack was operated at a 100 K lower temperature, the achieved current density was almost twice as high as the one of the ESC stack. Furthermore the U(i)-curve recorded at higher pressure was found to cross the one recorded at lower pressure within the endothermic region, thus a significant performance gain could be observed for the pressurized operation. However, again only a small pressure effect could be observed for the ESC stack. The transient operation of both stacks furthermore showed that the pressure influence on the ASR becomes significantly more dominant during CO₂ electrolysis.

Out of the steady-state and dynamically recorded U(i)-characteristics, the pressure and temperature dependent ASR values were calculated and can be used for stack and system modeling.

EIS was performed in order to investigate the cell resistances of the CSC and ESC in more detail at elevated pressure in steam and CO₂-electrolysis mode. Due to the different fuel gases used, the observed peaks in the $-Z''(f)$ diagrams could be assigned to concrete processes and the influence of the operating pressure was discussed. The EIS spectra related to the CSC stack showed that the fuel electrode surface process can be assumed to be located in a frequency range around 10³ Hz. The influence of pressurization leading to a reduced resistance of this process could be shown for steam electrolysis and was assigned to a higher frequency of reactants available at the TPB. However, the same process does not show a significantly reduced peak height during pressurized CO₂ electrolysis. This phenomenon could indicate that a different and less pressure-influenced rate-determining step is present within the reduction mechanism and/or adsorption/desorption rates of CO₂ or CO at the TPB significantly differ from the H₂O/H₂ operation. However, the diffusion resistance was observed to be significantly influenced by the operating pressure and furthermore by the type of fuel gas used in the study for the CSC stack.

In contrast, the fuel electrode peak of the ESC stack showed a significant decrease indicating a significantly decreasing electrode resistance. Furthermore, the peak attributed to the gas diffusion and conversion resistance was not affected significantly by pressure. Consequently, the increased pressure effect during CO₂ electrolysis which was shown for the dynamical operation of both stacks could possibly be attributed to the diffusion process in case of the CSC stack and possibly more to the fuel electrode process of the ESC stack. However, these phenomena should be investigated in more detail with half or button cells under pressurized operation conditions due to the existing limitations of EIS stack investigations.

CRediT authorship contribution statement

M.P. Heddrich: Methodology, Funding acquisition, Writing - review & editing. **A. Ansar:** Funding acquisition, Writing - review & editing. **Q. Fang:** Validation, Writing - review & editing. **L. Blum:** Writing - review & editing. **K.A. Friedrich:** Writing - review & editing, Supervision.

Declaration of competing interest

The authors declare that they have no known competing financial interests or personal relationships that could have appeared to influence the work reported in this paper.

Acknowledgements

The authors would like to thank the IEK-14 of Forschungszentrum Jülich for supplying the 10-layer CSC stack for this study. Furthermore, the authors appreciate the funding for studies of the ESC stack from the Federal Ministry for Economic Affairs and Energy (BMWi) under grant agreement 03ET6051 and 03EIV031C.

List of symbols / glossary

8YSZ	8 mol-% yttria-stabilized zirconia
3YSZ	3 mol-% yttria-stabilized zirconia
GDC	Ce _{0.8} Gd _{0.2} O _{1.9}
ESC	Electrolyte supported cell
CSC	Cathode supported cell
LSCF	La _{0.58} Sr _{0.4} Co _{0.2} Fe _{0.8} O _{3-δ}
ASR	Area specific resistance/Ω·cm ²
RC	Reactant conversion/%
EIS	Electrochemical impedance spectroscopy

References

- [1] S.H. Jensen, C. Graves, M. Chen, J.B. Hansen, X. Sun, Characterization of a planar solid oxide cell stack operated at elevated pressure, *J. Electrochem. Soc.* 163 (2016) F1596–F1604, <https://doi.org/10.1149/2.1171614jes>.
- [2] X. Sun, A.D. Bonaccorso, C. Graves, S.D. Ebbesen, S.H. Jensen, A. Hagen, P. Holtappels, P.V. Hendriksen, M.B. Mogensen, Performance characterization of solid oxide cells under high pressure, *Fuel Cell.* 15 (2015) 697–702, <https://doi.org/10.1002/fuce.201500020>.
- [3] S.H. Jensen, X. Sun, S.D. Ebbesen, M. Chen, Pressurized operation of a planar solid oxide cell stack, *Fuel Cell.* 16 (2016) 205–218, <https://doi.org/10.1002/fuce.201500180>.
- [4] M. Henke, C. Willich, J. Kallo, K.A. Friedrich, Theoretical study on pressurized operation of solid oxide electrolysis cells, *Int. J. Hydrogen Energy* 39 (2014) 12434–12439, <https://doi.org/10.1016/j.ijhydene.2014.05.185>.
- [5] A.A. Burke, L.G. Carreiro, J.R. Izzo, Pressurized testing of a planar solid oxide fuel cell stack, *Int. J. Hydrogen Energy* 38 (2013) 13774–13780, <https://doi.org/10.1016/j.ijhydene.2013.08.058>.
- [6] S.H. Jensen, X. Sun, S.D. Ebbesen, R. Knibbe, M. Mogensen, Hydrogen and synthetic fuel production using pressurized solid oxide electrolysis cells, *Int. J. Hydrogen Energy* 35 (2010) 9544–9549, <https://doi.org/10.1016/j.ijhydene.2010.06.065>.
- [7] A. Momma, K. Takano, Y. Tanaka, T. Kato, A. Yamamoto, Experimental investigation of the effect of operating pressure on the performance of SOFC and SOEC, *ECS Trans.* 57 (1) (2013) 699–708, <https://doi.org/10.1149/05701.0699ecst>.
- [8] L. Bernadet, G. Gousseau, A. Chatroux, J. Laurencin, F. Mauvy, M. Reyrier, Assessment of pressure effects on high temperature steam electrolysis based on solid oxide technology, *ECS Trans.* 68 (2015) 3369–3378, <https://doi.org/10.1149/06801.3369ecst>.
- [9] O. Posdziech, K. Schwarze, J. Brabant, Efficient hydrogen production for industry and electricity storage via high-temperature electrolysis, *Int. J. Hydrogen Energy* 44 (2019) 19089–19101, <https://doi.org/10.1016/j.ijhydene.2018.05.169>.
- [10] T. Strohbach, F. Mittmann, C. Walter, D. Schimanke, C. Geipel, Sunfire industrial SOEC stacks and modules, *ECS Trans.* 68 (1) (2015) 125–129, <https://doi.org/10.1149/06801.0125ecst>. Electrochemical Society Inc.
- [11] R. Küngas, Review—electrochemical CO₂ reduction for CO production: comparison of low- and high-temperature electrolysis technologies, *J. Electrochem. Soc.* 167 (2020), <https://doi.org/10.1149/1945-7111/ab7099>, 044508.
- [12] S. Diethelm, J. Van herle, D. Montinaro, O. Bucheli, Electrolysis and Co-electrolysis performance of a SOE short stack, *Fuel Cell.* 13 (2013) 631–637, <https://doi.org/10.1002/fuce.201200178>.

- [13] S. Seidler, M. Henke, J. Kallo, W.G. Bessler, U. Maier, K.A. Friedrich, Pressurized solid oxide fuel cells: experimental studies and modeling, *J. Power Sources* (2011) 7195–7202, <https://doi.org/10.1016/j.jpowsour.2010.09.100>.
- [14] M. Henke, C. Willich, C. Westner, F. Leucht, J. Kallo, W.G. Bessler, K.A. Friedrich, A validated multi-scale model of a SOFC stack at elevated pressure., *Fuel Cell* 13 (2013) 773–780, <https://doi.org/10.1002/fuce.201300076>.
- [15] C. Willich, C. Westner, M. Henke, F. Leucht, J. Kallo, K.A. Friedrich, Pressurized solid oxide fuel cells with reformat as fuel, *J. Electrochem. Soc.* 159 (2012) F711–F716, <https://doi.org/10.1149/2.031211jes>.
- [16] J. Udagawa, P. Aguiar, N.P. Brandon, Hydrogen production through steam electrolysis: model-based steady state performance of a cathode-supported intermediate temperature solid oxide electrolysis cell, *J. Power Sources* 166 (2007) 127–136, <https://doi.org/10.1016/j.jpowsour.2006.12.081>.
- [17] J. Udagawa, P. Aguiar, N.P. Brandon, Hydrogen production through steam electrolysis: control strategies for a cathode-supported intermediate temperature solid oxide electrolysis cell, *J. Power Sources* 180 (2008) 354–364, <https://doi.org/10.1016/j.jpowsour.2008.01.069>.
- [18] A. Nechache, A. Mansuy, M. Petitjean, J. Mougin, F. Mauvy, B.A. Boukamp, M. Cassir, A. Ringuedé, Diagnosis of a cathode-supported solid oxide electrolysis cell by electrochemical impedance spectroscopy, *Electrochim. Acta* 210 (2016) 596–605, <https://doi.org/10.1016/j.electacta.2016.05.014>.
- [19] D. Schäfer, Q. Fang, L. Blum, D. Stolten, Syngas production performance and degradation analysis of a solid oxide electrolyzer stack, *J. Power Sources* 433 (2019), <https://doi.org/10.1016/j.jpowsour.2019.05.072>, 126666.
- [20] Q. Fang, L. Blum, N.H. Menzler, Performance and degradation of solid oxide electrolysis cells in stack, *J. Electrochem. Soc.* 162 (2015) F907–F912, <https://doi.org/10.1149/2.0941508jes>.
- [21] M. Riedel, M.P. Heddrich, K.A. Friedrich, Analysis of pressurized operation of 10 layer solid oxide electrolysis stacks, *Int. J. Hydrogen Energy* 44 (2019) 4570–4581, <https://doi.org/10.1016/j.ijhydene.2018.12.168>.
- [22] M. Riedel, M.P. Heddrich, K.A. Friedrich, Experimental analysis of the Co-electrolysis operation under pressurized conditions with a 10 layer SOC stack, *J. Electrochem. Soc.* 167 (2020), <https://doi.org/10.1149/1945-7111/ab6820>, 024504.
- [23] B.E. Mai, T. Heller, D. Schimanke, J. Lawrence, C. Wunderlich, Influence of operating conditions on the reliable performance of stacks and integrated stack modules, *ECS Trans.* 25 (2009) 187–194, <https://doi.org/10.1149/1.3205524>.
- [24] C. Geipel, K. Hauptmeier, K. Herbrig, F. Mittmann, M. Münch, M. Pötschke, L. Reichel, T. Strohbach, T. Seidel, A. Surrey, C. Walter, Stack development and industrial scale-up, *ECS Trans.* 91 (2019) 123–132, <https://doi.org/10.1149/09101.0123ecst>.
- [25] E. Ivers-Tiffée, A. Weber, D. Herbstritt, Materials and technologies for SOFC-components, *J. Eur. Ceram. Soc.* 21 (2001) 1805–1811, [https://doi.org/10.1016/S0955-2219\(01\)00120-0](https://doi.org/10.1016/S0955-2219(01)00120-0).
- [26] M.B. Mogensen, Materials for reversible solid oxide cells, *Curr. Opin. Electrochem.* 21 (2020) 265–273, <https://doi.org/10.1016/j.coelec.2020.03.014>.
- [27] B.E. Mai, T. Heller, D. Schimanke, J. Lawrence, C. Wunderlich, Influence of operating conditions on the reliable performance of stacks and integrated stack modules, *ECS Trans.* 25 (2009) 187–194, <https://doi.org/10.1149/1.3205524>.
- [28] A. Mahmood, S. Bano, J.H. Yu, K.H. Lee, Effect of operating conditions on the performance of solid electrolyte membrane reactor for steam and CO₂ electrolysis, *J. Memb. Sci.* 473 (2015) 8–15, <https://doi.org/10.1016/j.memsci.2014.09.002>.
- [29] A. Mahmood, S. Bano, J.H. Yu, K.H. Lee, Performance evaluation of SOEC for CO₂/H₂O co-electrolysis: considering the effect of cathode thickness, *J. CO₂ Util.* 33 (2019) 114–120, <https://doi.org/10.1016/j.jcou.2019.05.014>.
- [30] L. Bernadet, G. Gousseau, a. Chatroux, J. Laurencin, F. Mauvy, M. Reyrier, Influence of pressure on solid oxide electrolysis cells investigated by experimental and modeling approach, *Int. J. Hydrogen Energy* 40 (2015) 12918–12928, <https://doi.org/10.1016/j.ijhydene.2015.07.099>.
- [31] S. Santhanam, M.P. Heddrich, M. Riedel, K.A. Friedrich, Theoretical and experimental study of Reversible Solid Oxide Cell (r-SOC) systems for energy storage, *Energy* 141 (2017), <https://doi.org/10.1016/j.energy.2017.09.081>.
- [32] S.D. Ebbesen, X. Sun, M.B. Mogensen, Understanding the processes governing performance and durability of solid oxide electrolysis cells, *Faraday Discuss* 182 (2015) 393–422, <https://doi.org/10.1039/c5fd00032g>.
- [33] X. Yue, J.T.S. Irvine, Understanding of CO₂ electrochemical reduction reaction process via high temperature solid oxide electrolyzers, *ECS Trans* 68 (1) (2015) 3535–3551, <https://doi.org/10.1149/06801.3535ecst>. Electrochemical Society Inc.
- [34] V. Menon, Q. Fu, V.M. Janardhanan, O. Deutschmann, A model-based understanding of solid-oxide electrolysis cells (SOECs) for syngas production by H₂O/CO₂ co-electrolysis, *J. Power Sources* 274 (2015) 768–781, <https://doi.org/10.1016/j.jpowsour.2014.09.158>.
- [35] M. Riedel, M.P. Heddrich, K.A. Friedrich, Performance and Durability of a 10 layer SOE Stack operated under pressurized conditions, in: *Proc. 13th Eur. SOFC SOE Forum*, 2018, pp. 110–115. B1504.
- [36] M. Riedel, M.P. Heddrich, K.A. Friedrich, Electrochemical characterization of a 10-layer solid oxide electrolysis stack operated under pressurized conditions, in: *Proc. 1st Int. Conf. Electrolysis, Copenhagen*, 2017, p. 71.
- [37] A. Utz, A. Leonide, A. Weber, E. Ivers-Tiffée, Studying the CO-CO₂ characteristics of SOFC anodes by means of patterned Ni anodes, *J. Power Sources* 196 (2011) 7217–7224, <https://doi.org/10.1016/j.jpowsour.2010.10.056>.
- [38] V. Yurkiv, D. Starukhin, H.-R. Volpp, W.G. Bessler, Elementary reaction kinetics of the CO/CO₂ Ni/YSZ electrode, *J. Electrochem. Soc.* 158 (2011) B5, <https://doi.org/10.1149/1.3505296>.
- [39] A. Leonide, Y. Apel, E. Ivers-Tiffée, SOFC modeling and parameter identification by means of impedance spectroscopy, *ECS Trans.* 19 (20) (2009) 81–109, <https://doi.org/10.1149/1.3247567>.
- [40] A. Leonide, V. Sonn, A. Weber, E. Ivers-Tiffée, Evaluation and modeling of the cell resistance in anode-supported solid oxide fuel cells, *J. Electrochem. Soc.* 155 (2008) B36–B41, <https://doi.org/10.1149/1.2801372>.
- [41] M.B. Mogensen, S.D. Ebbesen, S.H. Jensen, X. Sun, A. Hauch, M. Chen, Concentration impedance in testing of solid oxide cells revisited, *ECS Trans.* (2017) 2133–2139, <https://doi.org/10.1149/07801.2133ecst>. Electrochemical Society Inc.

7 Conclusion

The SOEC is expected to be a promising technology for electrically powered production of chemicals due to its high efficiency, flexibility and modularity. Steam or carbon dioxide can be converted into valuable molecules like hydrogen or carbon monoxide that can be used in chemical industry processes. Furthermore, both steam and CO₂ electrolysis reactions can take place simultaneously to generate a synthesis gas with highly flexible H₂/CO ratios. However, for storage or transportation of the produced gases a certain compression is required. Furthermore, downstream synthesis reactors for the production of more complex chemicals or fuels like methane, methanol, ammonia, DME or jet fuel are typically operated at elevated pressures in the range of 10-60 bar [12–18]. Hence, a pressurized operation of the SOEC can be beneficial in terms of system integration and efficiency since compression work can be significantly reduced or omitted [22]. However, the research associated with the pressurized operation of SOECs and thus the influence of elevated partial pressures of the media on the electrochemical behavior, characteristic performance or long-term stability is rare. Hence, this thesis aims to close the research gaps that were identified by providing experimental results and scientific knowledge about the pressurized steam, co- and CO₂ electrolysis operation of SOEC stacks.

A unique test rig for the pressurized investigation of SOEC stacks was adapted in order to be able to operate in steam, co- and CO₂ electrolysis mode at elevated pressures of up to 8 bar. The adaptations mainly included installing a water treatment system with an evaporator for a stable steam supply, the sensitive pressure control and a method to prevent carbon deposition within the fuel outlet pipes. Furthermore, a gas analysis and impedance measurement setup were integrated. Two 10-layer stacks with fuel electrode supported cells and eight 10-layer stacks with electrolyte supported cells were used for the experimental analyses of their electrochemical behavior under pressurized conditions in this thesis. Due to the higher availability of ESC stacks, this stack type was investigated with a considerably higher number of experiments.

The first step within the scientific approach was to quantify the ohmic resistance of both the ESC and CSC stacks with electrochemical impedance spectra recorded under different operating temperatures. The experimentally obtained temperature dependencies were fitted to mathematical expressions and were provided to the literature. For the ESC, the

ohmic resistance was found to be the dominant cell resistance since the electrolyte is the thickest and mechanically stabilizing layer. When current is applied, a distinct horizontal temperature profile forms along the flow direction which has a significant impact on the local ionic transport conductivity of the cells. However, the experiments showed that the ohmic resistance measured during steady-state points fit very well with the temperature dependent ohmic resistance curve that was analyzed. Hence, a practical finding is that the measured core temperature of the ESC stack can be used as a characteristic stack temperature for the electrolysis mode. This observation can be and is already being applied to larger SOEC modules that contain multiple stacks. Instead of measuring temperatures via thermocouples that have generally to be implemented and distributed in many stacks, the ohmic resistance value could be obtained with the available electronic loads. This opens up a possibility for a significant saving of costs and working time which are incurred for the placement and manual installation of the temperature measurement sensors of larger modules, also helping greatly with temperature control concepts. In contrast, the electrolyte of the CSC is significantly thinner leading to significantly lower ohmic resistance values.

A simplified theoretical study of the predominant ESC resistance showed that 15-20 % of the measured ohmic contribution does not originate from the used electrolyte material. This indicates that a noticeable contribution might originate from additional contact resistances within the repeating unit, thus opening a possible path for prospective improvements.

Detailed electrochemical characterizations were carried out by examining steady-state and dynamically recorded current-voltage curves. The influence of the operating pressure on the voltage and performance and on the occurring temperature gradients within the stacks was analyzed for steam and co-electrolysis operation. As expected, the overall performance and the impact of the operating pressure were significantly different when comparing the ESC and the CSC stack types. Despite both being operated at their relevant operating temperature, the latter achieved current densities twice as high as the ESC stack. Furthermore, a performance gain of up to 5 % (based on voltage) at elevated pressure in both operating modes was achieved with the CSC stack whereas a noticeable pressure effect for the ESC stack was generally not observed due to its dominant and pressure independent ohmic resistance. The ASR of the CSC stack becomes significantly reduced at higher pressures due to less ohmic and a comparably a more significant influence of the pressure dependent polarization resistance. Furthermore, the generally high operating

temperature of the ESC results in a small pressure effect since reaction kinetics are fast at high temperatures. Despite the fact that the ESC stack does not show a significantly increased performance at elevated pressure, the required electrical power for electrolysis at high pressure showed to be almost the same as at low pressure due to a convergence of the $U(i)$ -curves at high currents. Hence, the advantage of produced hydrogen at elevated pressure that can be directly used or stored at the outlet of the SOEC remains.

The analyses of the outlet gas compositions carried out during the pressurized co-electrolysis studies showed that thermodynamic equilibrium is reached even when high mass flow rates are used. Methane contents of up to 7 % at 8 bar were shown that led to significantly increased stack temperatures due to the highly exothermic reaction. Consequently, both the methanation and the endothermic reverse water-gas shift reaction occur stack-internally and shift the gases rapidly into equilibrium. In addition to the steady-state characterizations, dynamically recorded $U(i)$ -curves were carried out for steam, co- and CO_2 electrolysis. Hence, both stack types were characterized at constant reactor temperatures over a wide current density range and at different operating pressures. ASR values were derived out of both the steady-state and dynamically recorded characterizations so that detailed temperature and pressure relations for the ESC and CSC stack were quantified and are now available in literature.

Further co-electrolysis experiments that were carried out with the ESC stack with different CO_2 contents in the feed showed that the ASR increases with lower temperatures. An investigation with EIS revealed that the electrochemical CO_2 reduction process leads to a generally higher fuel electrode resistance than steam reduction. Furthermore, the diffusion resistance during CO_2 electrolysis was found to show a significantly higher temperature dependency compared to pure steam electrolysis. Both effects can lead to a higher overall resistance at high conversions and low operating temperatures. The scientific question whether CO_2 reduction occurs electrochemically or via the rWGS in the SOEC is greatly researched and currently discussed controversially. Although not fully clarifying the processes, this thesis provides a strong indication that for the production of relevant synthesis gas compositions with H_2/CO ratios higher than one, the main reaction pathway for CO production can be assumed to occur via the rWGS reaction and only a minor part coming from electrochemical CO_2 reduction.

CO_2 electrolysis showed noticeably higher pressure sensitivity for both the ESC and the CSC stack due to increased diffusion and activation resistances. However, the pressure

influence on the CO₂ electrolysis operation showed apparent differences within the impedance spectra of the CSC and the ESC stack. It was found that the pressure effect can be ascribed to a reduced diffusion resistance for the CSC stack operation, whereby an influence on the fuel electrode process was not observed. However, the fuel electrode showed a significant influence of pressure during steam electrolysis. This observation indicates that the respective reduction mechanism on Ni-YSZ is most likely dominated by a different rate-determining step compared to pure steam electrolysis operation. In comparison, the pressure effect of the ESC stack was found to be related to a reduced fuel electrode resistance that can be attributed to the increased number of reactants at active sites at higher pressure. On the other hand, the diffusion is hardly affected due to the low thickness of the fuel electrode.

The long-term stability was investigated under constant-current conditions with three ESC stacks in pressurized steam and co-electrolysis mode over 1,000-2,000 hours. Therefore, these experiments represent the longest stack operation in pressurized electrolysis modes published to date. The steam electrolysis operation at 1.4 bar showed a degradation behavior that is comparable with published results of atmospheric operations. The stack that was operated at a pressure of 8 bar over 2,000 hours showed a performance loss almost four times higher than at 1.4 bar. For both stacks, the major part of the observed degradation could be attributed to the ohmic resistance. Within the post-test analyses of the cells, a significantly higher extent of nickel depletion in the fuel electrode was observed for the stack operated at 8 bar. This phenomenon indicates that the operating pressure has a considerable influence on the nickel mobility and leads to a decrease in the effective conductivity of the fuel electrode. Observed delamination of the air electrodes were difficult to attribute certain operating conditions since these phenomena are also possible to occur during the disassembly of stacks. The third ESC stack was operated in co-electrolysis at 1.4 and 8 bar over 1,000 hours. The performance loss was shown to noticeably increase from steam to co-electrolysis operation. Furthermore, the ohmic resistance was identified again to be the dominant cause of the degradation. However, the increased performance loss observed during co-electrolysis operation could finally not be confidently assigned to the operating condition. A contamination with sulfur by the used CO₂ or CO is likely, as similar observations had previously also been made for single-cell operations [90–92]. Although Ni-CGO electrodes have been shown to be more tolerant towards sulfur contamination, an irreversible degradation due to a partially

deactivated cell surface is likely to be nevertheless associated [100]. Hence, a suitable desulfurization unit should therefore be used for the co-electrolysis operation.

Based on an available numerical model of one repeating unit, a 1D+1D stack model was developed and parameterized with experimentally obtained data to predict the performance and temperature gradients during the pressurized stack operation of the ESC. The activation energy of the fuel electrode reaction and the exponents for the partial pressure dependencies of the exchange current density used in the Butler-Volmer equation were determined experimentally. Furthermore, the properties of the used materials, heat transfers and dimensions within the experimental setup were implemented. The stack model was validated with experimental results for pressurized steam and co-electrolysis operations. The simulations generally show a good agreement with the experiments with regard to cell voltages and temperature gradients. Consequently, the model offers the possibility to investigate operating conditions that go beyond the experimental feasibilities. It is already in use within DLR's research on SOEC modules and can thus serve as a basis for the development and optimization of safe operating strategies or control concepts as described within the next chapter.

8 Future work

The current thesis aims to supplement and close several scientific gaps of the pressurized electrolysis operation of different SOEC stack types. The number of scientific publications has increased significantly with the provided experimental data and performed investigations of this work. However, several aspects for future research directions as a continuation of this work are provided below.

The performance of the ESC stack was shown to be lower compared to the CSC stack due to a significantly higher ohmic resistance. Furthermore, significant potential for a performance improvement of prospective ESC stacks was observed, since contact resistances considerably contribute to the ohmic proportion. Reducing the electrolyte thickness and/or reducing the contact resistances within the cells could therefore lead to a significant increase in performance of the electrochemical device. However, the mechanical stability of the cells must be considered and preserved since it is one of the major advantages of ESCs compared to CSCs.

The stack performance was shown to be dependent on the CO₂ content in the feed and an occurrence of electrochemical CO₂ reduction was indicated by the stack experiments during co-electrolysis operation. The quantification of this proportion for different operating conditions would be scientifically interesting as it would expand our knowledge of the mechanism of the co-electrolysis process. A suitable device for these investigations could be a segmented cell (or even a stack) in which several small active areas can be examined more closely for the electrochemical processes. Furthermore, an analysis of the gas composition in each small cell section could help understand the current density and reactant conversion distribution across a large cell. Hence, temperature gradients or the probability of carbon deposition can be estimated for different conditions and a safe operation of cells and stacks can be derived.

Within the CO₂ electrolysis investigations carried out in this thesis, a significantly different pressure influence was observed when Ni-YSZ or Ni-CGO electrodes were used. The phenomenon and mechanistic details behind the low pressure influence on the Ni-YSZ fuel electrode process during CO₂ electrolysis could not be elucidated with the stack measurements due to the large cell area. However, the measurements indicate that the occurring rate-determining steps and the electrochemical reduction mechanisms are different for Ni-YSZ and Ni-CGO fuel electrodes. A better insight into the mechanistic

details of electrode processes for H₂O or CO₂ electrolysis can likely be done with half-cell or button cell experiments.

Three long-term operations under pressurized conditions were shown in this thesis. Firstly, the experimental results and post-test analyses have to be reproduced to achieve a profound statistical significance. Secondly, the operating durations have to be extended in order to predict the degradation of stacks over much longer operating times, as it would be the case for pressurized SOEC systems. Thirdly, a contamination with silicon was found in the stacks during the post-test analyses. However, the origin of this species is not yet clearly identified, as it could come from the used liquid water, the used glass within the stack sealings or other test rig components. In addition, the influence of the mass of silicon on the stack degradation has not yet been quantified in literature. The co-electrolysis operation showed a significantly higher degradation that might be related to sulfur contamination of the cells originating from the used CO or CO₂ gas. To eliminate this potential contaminant could be a next step for the long-term co-electrolysis investigation, although ppb levels of sulfur are difficult to quantify in the gas phase and furthermore not trivial to precipitate with desulfurization units [101–103].

The developed and parameterized stack model revealed generally a good accordance between the experimental and simulated data. However, a deviation for the highly exothermic operation was observed that can be attributed to inaccuracies of the modeled heat transfers. An improvement is currently being worked on. Furthermore, the electrochemical CO₂ reduction process should be implemented into the model in order to provide the possibility to accurately simulate the pressurized CO₂ electrolysis operation. The kinetics of the occurring stack-internal methanation is currently based on literature values. Hence, an experimental determination of the activation energy required for the methanation process might bring additional accuracy for the pressurized co-electrolysis mode. Lastly, the ability to model different stack types would be of high value for subsequent scientific studies of pressurized SOEC stack operations.

The validated stack model is already being used as a basic building block for extended studies with regard to the modeling of stacks, stack towers, stack modules and even the simulation of SOEC systems. The model will be used to investigate and the development of suitable operating strategies and system control concepts. For instance, a possible application of the model can be the sensor equipment of stack modules, where each stack is currently monitored individually for its voltage and temperature. The model can help to

reduce the number of sensors and thus the costs in perspective by identifying the most meaningful and relevant measurement spots while a safe operation of all stacks is ensured.

9 References

- [1] S.R. Sinsel, R.L. Riemke, V.H. Hoffmann, Challenges and solution technologies for the integration of variable renewable energy sources—a review, *Renew. Energy*. 145 (2020) 2271–2285. <https://doi.org/10.1016/j.renene.2019.06.147>.
- [2] B.N. Stram, Key challenges to expanding renewable energy, *Energy Policy*. 96 (2016) 728–734. <https://doi.org/10.1016/j.enpol.2016.05.034>.
- [3] N. Phuangpornpitak, S. Tia, Opportunities and challenges of integrating renewable energy in smart grid system, *Energy Procedia*. 34 (2013) 282–290. <https://doi.org/10.1016/j.egypro.2013.06.756>.
- [4] T. Brown, D. Schlachtberger, A. Kies, S. Schramm, M. Greiner, Synergies of sector coupling and transmission reinforcement in a cost-optimised, highly renewable European energy system, *Energy*. 160 (2018) 720–739. <https://doi.org/10.1016/j.energy.2018.06.222>.
- [5] Y. Wang, J. Kowal, M. Leuthold, D.U. Sauer, Storage system of renewable energy generated hydrogen for chemical industry, *Energy Procedia*. 29 (2012) 657–667. <https://doi.org/10.1016/j.egypro.2012.09.076>.
- [6] K. Hemmes, J.M. Guerrero, T. Zhelev, Highly efficient distributed generation and high-capacity energy storage, *Chem. Eng. Process. Process Intensif.* 51 (2012) 18–31. <https://doi.org/10.1016/j.cep.2011.09.012>.
- [7] A. Sternberg, A. Bardow, Power-to-What?-Environmental assessment of energy storage systems, *Energy Environ. Sci.* 8 (2015) 389–400. <https://doi.org/10.1039/c4ee03051f>.
- [8] H. Chen, T.N. Cong, W. Yang, C. Tan, Y. Li, Y. Ding, Progress in electrical energy storage system: A critical review, *Prog. Nat. Sci.* 19 (2009) 291–312. <https://doi.org/10.1016/j.pnsc.2008.07.014>.
- [9] T.M. Gür, Review of electrical energy storage technologies, materials and systems: Challenges and prospects for large-scale grid storage, *Energy Environ. Sci.* 11 (2018) 2696–2767. <https://doi.org/10.1039/c8ee01419a>.
- [10] S.R. Foit, I.C. Vinke, L.G.J. de Haart, R.A. Eichel, Power-to-Syngas: An Enabling Technology for the Transition of the Energy System?, *Angew. Chemie - Int. Ed.* 56 (2017) 5402–5411. <https://doi.org/10.1002/anie.201607552>.

- [11] D.J. Roddy, A syngas network for reducing industrial carbon footprint and energy use, *Appl. Therm. Eng.* 53 (2013) 299–304.
<https://doi.org/10.1016/j.applthermaleng.2012.02.032>.
- [12] G.A. Mills, Status and future opportunities for conversion of synthesis gas to liquid fuels, *Fuel*. 73 (1994) 1243–1279. [https://doi.org/10.1016/0016-2361\(94\)90301-8](https://doi.org/10.1016/0016-2361(94)90301-8).
- [13] S.H. Jensen, X. Sun, S.D. Ebbesen, R. Knibbe, M. Mogensen, Hydrogen and synthetic fuel production using pressurized solid oxide electrolysis cells, *Int. J. Hydrogen Energy*. 35 (2010) 9544–9549.
<https://doi.org/10.1016/j.ijhydene.2010.06.065>.
- [14] M.E. Dry, The Fischer-Tropsch process: 1950-2000, *Catal. Today*. 71 (2002) 227–241. [https://doi.org/10.1016/S0920-5861\(01\)00453-9](https://doi.org/10.1016/S0920-5861(01)00453-9).
- [15] B. Todic, L. Nowicki, N. Nikacevic, D.B. Bukur, Fischer-Tropsch synthesis product selectivity over an industrial iron-based catalyst: Effect of process conditions, *Catal. Today*. 261 (2016) 28–39.
<https://doi.org/10.1016/j.cattod.2015.09.005>.
- [16] Ø. Borg, S. Eri, E.A. Blekkan, S. Storsæter, H. Wigum, E. Rytter, A. Holmen, Fischer-Tropsch synthesis over γ -alumina-supported cobalt catalysts: Effect of support variables, *J. Catal.* 248 (2007) 89–100.
<https://doi.org/10.1016/j.jcat.2007.03.008>.
- [17] S. Jürgens, P. Oßwald, M. Selinsek, P. Piermartini, J. Schwab, P. Pfeifer, U. Bauder, S. Ruoff, B. Rauch, M. Köhler, Assessment of combustion properties of non-hydroprocessed Fischer-Tropsch fuels for aviation, *Fuel Process. Technol.* 193 (2019) 232–243. <https://doi.org/10.1016/j.fuproc.2019.05.015>.
- [18] G.P. Van Der Laan, A.A.C.M. Beenackers, Kinetics and Selectivity of the Fischer-Tropsch Synthesis: A Literature Review, *Catal. Rev. - Sci. Eng.* 41 (1999) 255–318. <https://doi.org/10.1081/CR-100101170>.
- [19] J.B. Hansen, N. Christiansen, J.U. Nielsen, Production of sustainable fuels by means of solid oxide electrolysis, in: *ECS Trans.*, 2011: pp. 2941–2948.
<https://doi.org/10.1149/1.3570293>.
- [20] S.H. Jensen, C. Graves, M. Chen, J.B. Hansen, X. Sun, Characterization of a planar solid oxide cell stack operated at elevated pressure, *J. Electrochem. Soc.*

- 163 (2016) F1596–F1604. <https://doi.org/10.1149/2.1171614jes>.
- [21] J. Hartvigsen, S. Elangovan, L. Frost, A. Nickens, C. Stoots, J. O'Brien, J.S. Herring, Carbon dioxide recycling by high temperature co-electrolysis and hydrocarbon synthesis, *TMS Annu. Meet.* (2008) 171–182. <https://doi.org/10.1149/1.2921588>.
- [22] D. Todd, M. Schwager, W. Mérida, Thermodynamics of high-temperature, high-pressure water electrolysis, *J. Power Sources.* 269 (2014) 424–429. <https://doi.org/10.1016/j.jpowsour.2014.06.144>.
- [23] J. Brabandt, O. Posdziech, System Approach of a Pressurized High-Temperature Electrolysis, *ECS Trans.* 78 (2017) 2987–2995. <https://doi.org/10.1149/07801.2987ecst>.
- [24] C. Willich, A. Tomaszewski, M. Henke, J. Kallo, K.A. Friedrich, Temperature effect due to internal reforming in pressurized SOFC, in: *ECS Trans.*, Electrochemical Society Inc., 2013: pp. 401–409. <https://doi.org/10.1149/05701.0401ecst>.
- [25] L. Bernadet, G. Gousseau, A. Chatroux, J. Laurencin, F. Mauvy, M. Reytier, Assessment of Pressure Effects on High Temperature Steam Electrolysis Based on Solid Oxide Technology, *ECS Trans.* 68 (2015) 3369–3378. <https://doi.org/10.1149/06801.3369ecst>.
- [26] L. Bernadet, J. Laurencin, G. Roux, D. Montinaro, F. Mauvy, M. Reytier, Effects of Pressure on High Temperature Steam and Carbon Dioxide Co-electrolysis, *Electrochim. Acta.* 253 (2017) 114–127. <https://doi.org/10.1016/j.electacta.2017.09.037>.
- [27] L. Bernadet, G. Gousseau, a. Chatroux, J. Laurencin, F. Mauvy, M. Reytier, Influence of pressure on solid oxide electrolysis cells investigated by experimental and modeling approach, *Int. J. Hydrogen Energy.* 40 (2015) 12918–12928. <https://doi.org/10.1016/j.ijhydene.2015.07.099>.
- [28] A. Momma, K. Takano, Y. Tanaka, T. Kato, A. Yamamoto, Experimental Investigation of the Effect of Operating Pressure on the Performance of SOFC and SOEC, *ECS Trans.* 57 (2013) 699–708. <https://doi.org/10.1149/05701.0699ecst>.
- [29] X. Sun, A.D. Bonaccorso, C. Graves, S.D. Ebbesen, S.H. Jensen, A. Hagen, P.

- Holtappels, P. V. Hendriksen, M.B. Mogensen, Performance characterization of solid oxide cells under high pressure, *Fuel Cells*. 15 (2015) 697–702.
<https://doi.org/10.1002/fuce.201500020>.
- [30] S.H. Jensen, H. Langnickel, N. Hintzen, M. Chen, Pressurized reversible operation of a 30-cell solid oxide cell stack using carbonaceous gases, *Proc. Eur. Fuel Cell Technol. Appl. Conf. (EFC2017)*; (2017) 413–414.
- [31] E.C. Thomsen, G.W. Coffey, L.R. Pederson, O.A. Marina, Performance of lanthanum strontium manganite electrodes at high pressure, *J. Power Sources*. 191 (2009) 217–224. <https://doi.org/10.1016/j.jpowsour.2009.02.057>.
- [32] O. Posdziech, K. Schwarze, J. Brabandt, Efficient hydrogen production for industry and electricity storage via high-temperature electrolysis, *Int. J. Hydrogen Energy*. 44 (2019) 19089–19101.
<https://doi.org/10.1016/j.ijhydene.2018.05.169>.
- [33] R. Küngas, P. Blennow, T. Heiredal-Clausen, T. Holt Norby, J. Rass-Hansen, S. Primdahl, J.B. Hansen, eCOs – A Commercial CO₂ Electrolysis System Developed by Haldor Topsoe, *ECS Trans.* 78 (2017) 2879–2884.
<https://doi.org/10.1149/07801.2879ecst>.
- [34] J.B. Hansen, Solid oxide electrolysis - a key enabling technology for sustainable energy scenarios, *Faraday Discuss.* 182 (2015) 9–48.
<https://doi.org/10.1039/c5fd90071a>.
- [35] C. Geipel, K. Hauptmeier, K. Herbrig, F. Mittmann, M. Münch, M. Pötschke, L. Reichel, T. Strohbach, T. Seidel, A. Surrey, C. Walter, Stack Development and Industrial Scale-Up, *ECS Trans.* 91 (2019) 123–132.
<https://doi.org/10.1149/09101.0123ecst>.
- [36] T. Strohbach, F. Mittmann, C. Walter, D. Schimanke, C. Geipel, Sunfire industrial SOC stacks and modules, in: *ECS Trans.*, Electrochemical Society Inc., 2015: pp. 125–129. <https://doi.org/10.1149/06801.0125ecst>.
- [37] W. Dönitz, E. Erdle, High-temperature electrolysis of water vapor-status of development and perspectives for application, *Int. J. Hydrogen Energy*. 10 (1985) 291–295. [https://doi.org/10.1016/0360-3199\(85\)90181-8](https://doi.org/10.1016/0360-3199(85)90181-8).
- [38] A.O. Isenberg, Energy conversion via solid oxide electrolyte electrochemical cells at high temperatures, *Solid State Ionics*. 3–4 (1981) 431–437.

- [https://doi.org/10.1016/0167-2738\(81\)90127-2](https://doi.org/10.1016/0167-2738(81)90127-2).
- [39] K. Eguchi, T. Hatagishi, H. Arai, Power generation and steam electrolysis characteristics of an electrochemical cell with a zirconia- or ceria-based electrolyte, *Solid State Ionics*. 86–88 (1996) 1245–1249. [https://doi.org/10.1016/0167-2738\(96\)00295-0](https://doi.org/10.1016/0167-2738(96)00295-0).
- [40] A. Momma, T. Kato, Y. Kaga, S. Nagata, Polarization behavior of high temperature solid oxide electrolysis cells (SOEC), *J. Ceram. Soc. Japan*. 105 (1997) 369–373. <https://doi.org/10.2109/jcersj.105.369>.
- [41] Y. Luo, W. Li, Y. Shi, X. Ye, S. Wang, N. Cai, Methane Synthesis Characteristics of H₂O/CO₂ Co-Electrolysis in Tubular Solid Oxide Electrolysis Cells, *ECS Trans*. 68 (2015) 3465–3474. <https://doi.org/10.1149/06801.3465ecst>.
- [42] R. Küngas, Review—Electrochemical CO₂ Reduction for CO Production: Comparison of Low- and High-Temperature Electrolysis Technologies, *J. Electrochem. Soc*. 167 (2020) 044508. <https://doi.org/10.1149/1945-7111/ab7099>.
- [43] C. Stoots, J. O’Brien, J. Hartvigsen, Results of recent high temperature coelectrolysis studies at the Idaho National Laboratory, *Int. J. Hydrogen Energy*. 34 (2009) 4208–4215. <https://doi.org/10.1016/j.ijhydene.2008.08.029>.
- [44] Y. Song, X. Zhang, K. Xie, G. Wang, X. Bao, High-Temperature CO₂ Electrolysis in Solid Oxide Electrolysis Cells: Developments, Challenges, and Prospects, *Adv. Mater*. 31 (2019) 1–18. <https://doi.org/10.1002/adma.201902033>.
- [45] Y. Zheng, J. Wang, B. Yu, W. Zhang, J. Chen, J. Qiao, J. Zhang, A review of high temperature co-electrolysis of H₂O and CO₂ to produce sustainable fuels using solid oxide electrolysis cells (SOECs): Advanced materials and technology, *Chem. Soc. Rev*. 46 (2017) 1427–1463. <https://doi.org/10.1039/c6cs00403b>.
- [46] A. Hauch, R. Küngas, P. Blennow, A.B. Hansen, J.B. Hansen, B. V. Mathiesen, M.B. Mogensen, Recent advances in solid oxide cell technology for electrolysis, *Science (80-.)*. 370 (2020) 1–8. <https://doi.org/10.1126/science.aba6118>.
- [47] M.A. Laguna-Bercero, Recent advances in high temperature electrolysis using solid oxide fuel cells: A review, *J. Power Sources*. 203 (2012) 4–16. <https://doi.org/10.1016/j.jpowsour.2011.12.019>.

- [48] P. Moçoteguy, A. Brisse, A review and comprehensive analysis of degradation mechanisms of solid oxide electrolysis cells, *Int. J. Hydrogen Energy*. 38 (2013) 15887–15902. <https://doi.org/10.1016/j.ijhydene.2013.09.045>.
- [49] A. Pandiyan, A. Uthayakumar, R. Subrayan, S.W. Cha, S.B. Krishna Moorthy, Review of solid oxide electrolysis cells: a clean energy strategy for hydrogen generation, *Nanomater. Energy*. 8 (2019) 2–22. <https://doi.org/10.1680/jnaen.18.00009>.
- [50] M.B. Mogensen, Materials for reversible solid oxide cells, *Curr. Opin. Electrochem.* 21 (2020) 265–273. <https://doi.org/10.1016/j.coelec.2020.03.014>.
- [51] O. Posdziech, T. Geißler, K. Schwarze, R. Blumentritt, System Development and Demonstration of Large-Scale High-Temperature Electrolysis, *ECS Trans.* 91 (2019) 2537–2546. <https://doi.org/10.1149/09101.2537ecst>.
- [52] R. Küngas, P. Blennow, T. Heiredal-Clausen, T. Holt Nørby, J. Rass-Hansen, J.B. Hansen, P.G. Moses, Progress in SOEC Development Activities at Haldor Topsøe, *ECS Trans.* 91 (2019) 215–223. <https://doi.org/10.1149/09101.0215ecst>.
- [53] J.B. Hansen, N. Christiansen, J.U. Nielsen, Production of Sustainable Fuels by Means of Solid Oxide Electrolysis, *ECS Trans.* 35 (2019) 2941–2948. <https://doi.org/10.1149/1.3570293>.
- [54] Q. Zhu, Developments on CO₂-utilization technologies, *Clean Energy*. 3 (2019) 85–100. <https://doi.org/10.1093/ce/zkz008>.
- [55] A. Tremel, Chemical and Biological Synthesis—Basis for Gaseous and Liquid Fuels, in: *SpringerBriefs Appl. Sci. Technol.*, Springer, 2018: pp. 33–45. https://doi.org/10.1007/978-3-319-72459-1_3.
- [56] R. Kikuchi, T. Yano, T. Takeguchi, K. Eguchi, Characteristics of anodic polarization of solid oxide fuel cells under pressurized conditions, *Solid State Ionics*. 174 (2004) 111–117. <https://doi.org/10.1016/j.ssi.2004.05.029>.
- [57] J.E. O'Brien, X. Zhang, G.K. Housley, K. Dewall, L. Moore-McAteer, G. Tao, High Temperature Electrolysis Pressurized Experiment Design, Operation and Results, 2012. <http://www.inl.gov>.
- [58] S.H. Jensen, X. Sun, S.D. Ebbesen, M. Chen, Pressurized Operation of a Planar Solid Oxide Cell Stack, *Fuel Cells*. 16 (2016) 205–218.

- <https://doi.org/10.1002/fuce.201500180>.
- [59] S.H. Jensen, H. Langnickel, N. Hintzen, M. Chen, X. Sun, A. Hauch, G. Butera, L.R. Clausen, Reversible operation of a pressurized solid oxide cell stack using carbonaceous gases, *J. Energy Storage*. 22 (2019) 106–115.
<https://doi.org/10.1016/j.est.2019.02.003>.
- [60] Y. Cao, Z. Gao, J. Jin, H. Zhou, M. Cohron, H. Zhao, H. Liu, W. Pan, Synthesis gas production with an adjustable H₂/CO ratio through the coal gasification process: Effects of coal ranks and methane addition, *Energy and Fuels*. 22 (2008) 1720–1730. <https://doi.org/10.1021/ef7005707>.
- [61] A. Faes, A. Hessler-Wyser, A. Zryd, J. Van Herle, A review of RedOx cycling of solid oxide fuel cells anode, *Membranes (Basel)*. 2 (2012) 585–664.
<https://doi.org/10.3390/membranes2030585>.
- [62] S. Santhanam, Process systems analysis of reversible Solid Oxide Cell (rSOC) reactors for electricity storage and sector coupling, Stuttgart, 2018.
<https://doi.org/http://dx.doi.org/10.18419/opus-10210>.
- [63] M. Riedel, M.P. Heddrich, K.A. Friedrich, Experimental Analysis of the Co-Electrolysis Operation under Pressurized Conditions with a 10 Layer SOC Stack, *J. Electrochem. Soc.* 167 (2020) 024504. <https://doi.org/10.1149/1945-7111/ab6820>.
- [64] T. Aloui, K. Halouani, Analytical modeling of polarizations in a solid oxide fuel cell using biomass syngas product as fuel, *Appl. Therm. Eng.* 27 (2007) 731–737.
<https://doi.org/10.1016/j.applthermaleng.2006.10.011>.
- [65] F. Yang, J. Gu, L. Ye, Z. Zhang, G. Rao, Y. Liang, K. Wen, J. Zhao, J.B. Goodenough, W. He, Justifying the significance of Knudsen diffusion in solid oxide fuel cells, *Energy*. 95 (2016) 242–246.
<https://doi.org/10.1016/j.energy.2015.12.022>.
- [66] S. Gewies, W.G. Bessler, V. Sonn, E. Ivers-Tiffée, Experimental and Modeling Study of the Impedance of Ni/YSZ Cermet Anodes, *ECS Trans.* 7 (2007) 1573–1582. <https://doi.org/10.1149/1.2729264>.
- [67] W. Lehnert, J. Meusinger, F. Thom, Modelling of gas transport phenomena in SOFC anodes, *J. Power Sources*. 87 (2000) 57–63.
[https://doi.org/10.1016/S0378-7753\(99\)00356-0](https://doi.org/10.1016/S0378-7753(99)00356-0).

- [68] D. Simwonis, F. Tietz, D. Stöver, Nickel coarsening in annealed Ni/8YSZ anode substrates for solid oxide fuel cells, *Solid State Ionics*. 132 (2000) 241–251. [https://doi.org/10.1016/s0167-2738\(00\)00650-0](https://doi.org/10.1016/s0167-2738(00)00650-0).
- [69] M. Riedel, M.P. Heddrich, A. Ansar, Q. Fang, L. Blum, K.A. Friedrich, Pressurized operation of solid oxide electrolysis stacks : An experimental comparison of the performance of 10-layer stacks with fuel electrode and electrolyte supported cell concepts, *J. Power Sources*. 475 (2020) 228682. <https://doi.org/10.1016/j.jpowsour.2020.228682>.
- [70] Q. Fang, L. Blum, R. Peters, M. Peksen, P. Batfalsky, D. Stolten, SOFC stack performance under high fuel utilization, *Int. J. Hydrogen Energy*. 40 (2015) 1128–1136. <https://doi.org/10.1016/j.ijhydene.2014.11.094>.
- [71] S. Santhanam, M.P. Heddrich, M. Riedel, K.A. Friedrich, Theoretical and experimental study of Reversible Solid Oxide Cell (r-SOC) systems for energy storage, *Energy*. 141 (2017) 202–214. <https://doi.org/10.1016/j.energy.2017.09.081>.
- [72] R. Lin, 1D + 1D modeling of reversible Solid Oxide Cell (rSOC) reactors for steady state and dynamic process analyses of electricity storage systems, TU Berlin, 2018. <https://elib.dlr.de/126289/>.
- [73] S. Wahl, A.G. Segarra, P. Horstmann, M. Carré, W.G. Bessler, F. Lapique, K.A. Friedrich, Modeling of a thermally integrated 10 kW planar solid oxide fuel cell system with anode offgas recycling and internal reforming by discretization in flow direction, *J. Power Sources*. 279 (2015) 656–666. <https://doi.org/10.1016/j.jpowsour.2014.12.084>.
- [74] J.-C. Njodzefon, D. Klotz, A. Kromp, A. Weber, E. Ivers-Tiffée, Electrochemical Modeling of the Current-Voltage Characteristics of an SOFC in Fuel Cell and Electrolyzer Operation Modes, *J. Electrochem. Soc.* 160 (2013) F313–F323. <https://doi.org/10.1149/2.018304jes>.
- [75] S. Srikanth, M.P. Heddrich, S. Gupta, K.A. Friedrich, Transient reversible solid oxide cell reactor operation – Experimentally validated modeling and analysis, *Appl. Energy*. 232 (2018) 473–488. <https://doi.org/10.1016/j.apenergy.2018.09.186>.
- [76] P. Aguiar, C.S. Adjiman, N.P. Brandon, Anode-supported intermediate

- temperature direct internal reforming solid oxide fuel cell. I: Model-based steady-state performance, *J. Power Sources*. 138 (2004) 120–136.
<https://doi.org/10.1016/j.jpowsour.2004.06.040>.
- [77] I. Benko, Energy Conservation Through Increased Emissivity in Furnaces, *Period. Polytech. Mech. Eng.* 35 (1991) 235–245–245.
- [78] A.G. Turnbull, Thermal Conductivity of Refractory Materials, *J. Chem. Eng. Data*. 7 (1962) 251–256. <https://doi.org/10.1021/je60013a029>.
- [79] A. Leonide, Y. Apel, E. Ivers-Tiffée, SOFC modeling and parameter identification by means of impedance spectroscopy, in: *ECS Trans.*, 2009: pp. 81–109. <https://doi.org/10.1149/1.3247567>.
- [80] M. Riedel, M.P. Heddrich, K.A. Friedrich, Analysis of pressurized operation of 10 layer solid oxide electrolysis stacks, *Int. J. Hydrogen Energy*. 44 (2019) 4570–4581. <https://doi.org/10.1016/j.ijhydene.2018.12.168>.
- [81] P. Kazempoor, R.J. Braun, Hydrogen and synthetic fuel production using high temperature solid oxide electrolysis cells (SOECs), *Int. J. Hydrogen Energy*. 40 (2015) 3599–3612. <https://doi.org/10.1016/j.ijhydene.2014.12.126>.
- [82] J. Aicart, M. Petitjean, J. Laurencin, L. Tallobre, L. Dessemond, Accurate predictions of H₂O and CO₂ co-electrolysis outlet compositions in operation, *Int. J. Hydrogen Energy*. 40 (2015) 3134–3148.
<https://doi.org/10.1016/j.ijhydene.2015.01.031>.
- [83] M. Riedel, M.P. Heddrich, K.A. Friedrich, Investigation of the Long-term Stability of Solid Oxide Electrolysis Stacks under Pressurized Conditions in Exothermic Steam and Co-electrolysis Mode, *Fuel Cells*. 20 (2020) 592–607.
<https://doi.org/10.1002/fuce.202000011>.
- [84] M. Lang, S. Raab, M.S. Lemcke, C. Bohn, M. Pysik, Long Term Behavior of Solid Oxide Electrolyser (SOEC) Stacks, *ECS Trans.* 91 (2019) 2713–2725.
<https://doi.org/10.1149/09101.2713ecst>.
- [85] Q. Fang, C.E. Frey, N.H. Menzler, L. Blum, Electrochemical performance and preliminary post-mortem analysis of a solid oxide cell stack with 20,000 h of operation, *J. Electrochem. Soc.* 165 (2018) F38–F45.
<https://doi.org/10.1149/2.0541802jes>.

- [86] T. Brylewski, T. Maruyama, M. Nanko, K. Przybylski, TG measurements of the oxidation kinetics of Fe-Cr alloy with regard to its application as a separator in SOFC, *J. Therm. Anal. Calorim.* 55 (1999) 681–690.
<https://doi.org/10.1023/A:1010130910850>.
- [87] M.P. Hoerlein, G. Schiller, F. Tietz, K.A. Friedrich, Systematic parameter study on the influence of humidification and current density on SOEC degradation, in: *Proc. 14th Int. Symp. Solid Oxide Fuel Cells*, 2015: pp. 3553–3561.
<https://doi.org/10.1149/06801.3553ecst>.
- [88] A. Hauch, K. Brodersen, M. Chen, M.B. Mogensen, Ni/YSZ electrodes structures optimized for increased electrolysis performance and durability, *Solid State Ionics.* 293 (2016) 27–36. <https://doi.org/10.1016/j.ssi.2016.06.003>.
- [89] M.B. Mogensen, A. Hauch, X. Sun, M. Chen, Y. Tao, S.D. Ebbesen, K. V. Hansen, P. V. Hendriksen, Relation Between Ni Particle Shape Change and Ni Migration in Ni-YSZ Electrodes – a Hypothesis, *Fuel Cells.* 17 (2017) 434–441.
<https://doi.org/10.1002/fuce.201600222>.
- [90] S.D. Ebbesen, J. Høgh, K.A. Nielsen, J.U. Nielsen, M. Mogensen, Durable SOC stacks for production of hydrogen and synthesis gas by high temperature electrolysis, *Int. J. Hydrogen Energy.* 36 (2011) 7363–7373.
<https://doi.org/10.1016/j.ijhydene.2011.03.130>.
- [91] T.L. Skafte, P. Blennow, J. Hjelm, C. Graves, Carbon deposition and sulfur poisoning during CO₂ electrolysis in nickel-based solid oxide cell electrodes, *J. Power Sources.* 373 (2018) 54–60.
<https://doi.org/10.1016/j.jpowsour.2017.10.097>.
- [92] G. Jeanmonod, S. Diethelm, J. Van Herle, The effect of SO₂ on the Ni-YSZ electrode of a solid oxide electrolyzer cell operated in co-electrolysis, *J. Phys. Energy.* 2 (2020) 034002. <https://doi.org/10.1088/2515-7655/ab8b55>.
- [93] A. Hauch, S.D. Ebbesen, S.H. Jensen, M. Mogensen, Solid oxide electrolysis cells: Microstructure and degradation of the Ni/yttria-stabilized zirconia electrode, *J. Electrochem. Soc.* 155 (2008) 1184–1193.
<https://doi.org/10.1149/1.2967331>.
- [94] S.D. Ebbesen, M. Mogensen, Exceptional durability of solid oxide cells, *Electrochem. Solid-State Lett.* 13 (2010) 106–108.

- <https://doi.org/10.1149/1.3455882>.
- [95] M.P. Hoerlein, M. Riegraf, R. Costa, G. Schiller, K.A. Friedrich, A parameter study of solid oxide electrolysis cell degradation: Microstructural changes of the fuel electrode, *Electrochim. Acta.* 276 (2018) 162–175.
<https://doi.org/10.1016/j.electacta.2018.04.170>.
- [96] E. Lay, G. Gauthier, L. Dessemond, Preliminary studies of the new Ce-doped La/Sr chromo-manganite series as potential SOFC anode or SOEC cathode materials, *Solid State Ionics.* 189 (2011) 91–99.
<https://doi.org/10.1016/j.ssi.2011.02.004>.
- [97] L. Ye, M. Zhang, P. Huang, G. Guo, M. Hong, C. Li, J.T.S. Irvine, K. Xie, Enhancing CO₂ electrolysis through synergistic control of non-stoichiometry and doping to tune cathode surface structures, *Nat. Commun.* 8 (2017) 1–10.
<https://doi.org/10.1038/ncomms14785>.
- [98] D.M. Amaya Duenas, M. Riegraf, A. Nenning, A.K. Opitz, K.A. Friedrich, La_{0.65}Sr_{0.3}Cr_{0.85}Ni_{0.15}O₃ perovskite electrocatalyst for high temperature steam and dry CO₂ electrolysis, in: 14th Eur. SOFC SOEC Forum, www.EFCF.com/Lib, 2020: p. A0606.
- [99] J. Yang, W. Ma, D. Chen, A. Holmen, B.H. Davis, Fischer-Tropsch synthesis: A review of the effect of CO conversion on methane selectivity, *Appl. Catal. A Gen.* 470 (2014) 250–260. <https://doi.org/10.1016/j.apcata.2013.10.061>.
- [100] M. Riegraf, A. Zekri, M. Knipper, R. Costa, G. Schiller, K.A. Friedrich, Sulfur poisoning of Ni/Gadolinium-doped ceria anodes: A long-term study outlining stable solid oxide fuel cell operation, *J. Power Sources.* 380 (2018) 26–36.
<https://doi.org/10.1016/j.jpowsour.2018.01.067>.
- [101] R. Mukundan, E.L. Brosha, F.H. Garzon, Sulfur Tolerant Anodes for SOFCs, *Electrochem. Solid-State Lett.* 7 (2004) 5–8. <https://doi.org/10.1149/1.1627452>.
- [102] S. Hernández, L. Solarino, G. Orsello, N. Russo, D. Fino, G. Saracco, V. Specchia, Desulfurization processes for fuel cells systems, *Int. J. Hydrogen Energy.* 33 (2008) 3209–3214. <https://doi.org/10.1016/j.ijhydene.2008.01.047>.
- [103] Y. Shen, P. Li, X. Xu, H. Liu, Selective adsorption for removing sulfur: A potential ultra-deep desulfurization approach of jet fuels, *RSC Adv.* 2 (2012) 1700–1711. <https://doi.org/10.1039/c1ra00944c>.